MEASUREMENT AND MODELING OF FRAGMENTS AND NEUTRONS PRODUCED FROM PROJECTILE FRAGMENTATION REACTIONS

By

Krystin Elizabeth Stiefel

A DISSERTATION

Submitted to
Michigan State University
in partial fulfillment of the requirements
for the degree of

Chemistry — Doctor of Philosophy

2018

ABSTRACT

MEASUREMENT AND MODELING OF FRAGMENTS AND NEUTRONS PRODUCED FROM PROJECTILE FRAGMENTATION REACTIONS

By

Krystin Elizabeth Stiefel

Projectile fragmentation has been used to produce rare and short-lived nuclei for study at a variety of isotope production beam facilities such as the National Superconducting Cyclotron Laboratory (NSCL). Relatively few exclusive measurements of the final fragments from projectile fragmentation reactions have been made, even though these types of measurements can provide more insight into the production process by comparing the measurements to models that simulate collisions and reactions on nuclei. The present work examines exclusive measurements of neutrons in coincidence with isotopically identified products. Two intermediate-energy (55.5 MeV/u) projectile fragmentation beams of ^{30}S and ^{40}S nuclei were produced and reacted with beryllium targets at the NSCL to produce a wide range of projectile fragments. Resulting heavy residue fragments were measured with the Sweeper magnet charged particle detectors and neutrons were detected in coincidence using the Modular Neutron Array and Large-area multi-Institutional Scintillator Array (MoNA LISA) detectors. A broad range of fragments was identified in each reaction for elements with $Z = 6 - 11$. To explore the projectile fragmentation process, the present results were compared to predictions from two different nuclear reaction models. The hit multiplicity distributions observed in MoNA LISA for the summed elemental and individual isotopic products were compared to the two models. The first calculational approach involved the Liège Intranuclear Cascade (INCL++) model, a microscopic model and Monte Carlo based code that considers the reaction as a two-step process with collisions between individual nucleons followed by a

de-excitation process of the intermediate and highly excited residue. The second approach involved the Constrained Molecular Dynamics (CoMD) model, a more macroscopic quantum mechanical model that follows the dynamical evolution of nuclear matter using the nuclear equation of state with three options for the symmetry energy term. The output of the CoMD model was coupled to GEMINI++ to de-excite any remaining hot fragments. Results from both simulations were passed through the GEANT4 code to model the neutron response of MoNA LISA to produce simulated hit multiplicity distributions that could be compared to the experimental hit multiplicity distributions. The majority of identified fragments were measured in coincidence with no neutron hits. Because the INCL++ model prediction better matched the proportion of fragments with zero hits and the CoMD + GEMINI++ simulations under-predicted the proportion of fragments produced with zero hits, INCL++ did an overall better job at predicting the observed hit multiplicity proportions. However, INCL++ failed to generate enough events with higher hit counts in MoNA LISA. Furthermore, the three CoMD + GEMINI++ symmetry energy options did not appear to produce noticeably different hit multiplicity distributions and no constraint on the symmetry energy could be made with this experimental data set. The distributions of precursor fragments in both the INCL++ and CoMD models were also examined. Many of the precursor fragments contained more nucleons than the projectile, indicating that both models predict that the projectile picks up nucleons from the target during the initial encounter. This prediction differs from common descriptions of these reactions.

To everyone who called this my “paper.”

ACKNOWLEDGMENTS

I regret to announce- this is the end of my time at Michigan State University. I am going now. But before I leave, I must acknowledge those who have helped me along the way.

Thanks to Dave Morrissey, my ever-patient and thoughtful advisor who has provided calm and constructive guidance for this work. I appreciate that you took on my half-baked project and stayed with me until the very end.

My committee members, Sean Liddick, Paul Mantica, and Michael Thoennessen, went above and beyond their committee responsibilities. Sean, my second reader, was always willing to provide some outside perspective, whether it was research-based or career-related. Michael oversaw some of my most challenging transitions and problems throughout the years and continuously offered his help. I would not be at Michigan State University if it was not for Paul, who spoke about all the wonderful work being done at MSU while I was attending Nuclear Chemistry Summer School.

A special thanks is due to Zach Kohley, who guided me in the first few years of graduate school and proposed the initial design of this project with the MoNA Collaboration. It has been an honor to work with the MoNA Collaboration, especially the local members (and former members) Thomas Baumann, Artemis Spyrou, Anthony Kuchera, Jesse Snyder, Jenna Smith, Michael Jones, Thomas Redpath, Han Liu, Daniel Votaw, and Dayah Chrisman.

This material is based upon work supported by the Department of Energy National Nuclear Security Administration through the Nuclear Science and Security Consortium and by the National Science Foundation. Without funding, this dissertation would not have been possible.

It takes a community to raise a scientist, and I am glad to have spent this time at the National Superconducting Cyclotron Laboratory. You cannot find a more commendable group of faculty, staff, and students than the ones found at the NSCL. In particular, I'd like to thank my officemate Becky Lewis for putting up with all my muttering at my desk and my former roommate Kalee Hammerton for putting up with all my muttering at our place. There are some things you can't share without ending up liking each other, and getting through graduate school is one of them.

I would not be where I am without the unending encouragement from my family: my parents, Dana and Kathy; my little sister, Breanna; my extended family- Dushanes, Masserants, Morgans, Stiefels, Twynhams, and every other branch in my enormous family tree; and my "GoodStief" family, Dianne, Geary, Lydia, and Brett Goodman. You have all pushed and inspired me to *keep moving forward*, even when I felt like my odds of success were 3,720 to 1, and for that, I am eternally grateful.

And finally, to Richard Morgan, my husband, I'm afraid I don't quite have enough words to thank you for the loving and patient support you've given me through the years. You'll have to settle for just a few: Thanks for the adventure. Let's go have a new one.

TABLE OF CONTENTS

LIST OF TABLES

LIST OF FIGURES

Chapter 1

Introduction

The field of nuclear science is concerned with studying the nuclei of atoms, or the building blocks that make up everything in the universe. The atomic nucleus is composed of protons and neutrons, and the number of protons and neutrons within the nucleus defines the identity of that nucleus as an isotope. The number of protons and neutrons can be used to organize nuclei in a chart, as shown in Figure 1.1.

While more than 3000 different isotopes have been observed experimentally, over 7000 different isotopes are predicted to exist [1], indicating that there is much more work to be done to fill the nuclear landscape. However, producing these rare isotopes is a challenge. One of the important mechanisms to produce unknown isotopes is the subject of this work.

1.1 Projectile Fragmentation

Only a small percentage of known nuclei are stable. Most nuclei are unstable and decay, with some of the more exotic species having half-lives of less than a second. Because these rare nuclei exist for such a short time, rapid production, separation, and detection is necessary in order to observe their properties. To produce rare nuclei for study, isotope production beam facilities such as the National Superconducting Cyclotron Laboratory use a technique called projectile fragmentation. This technique relies on reacting a high-energy beam of nuclei in a relatively thin target.

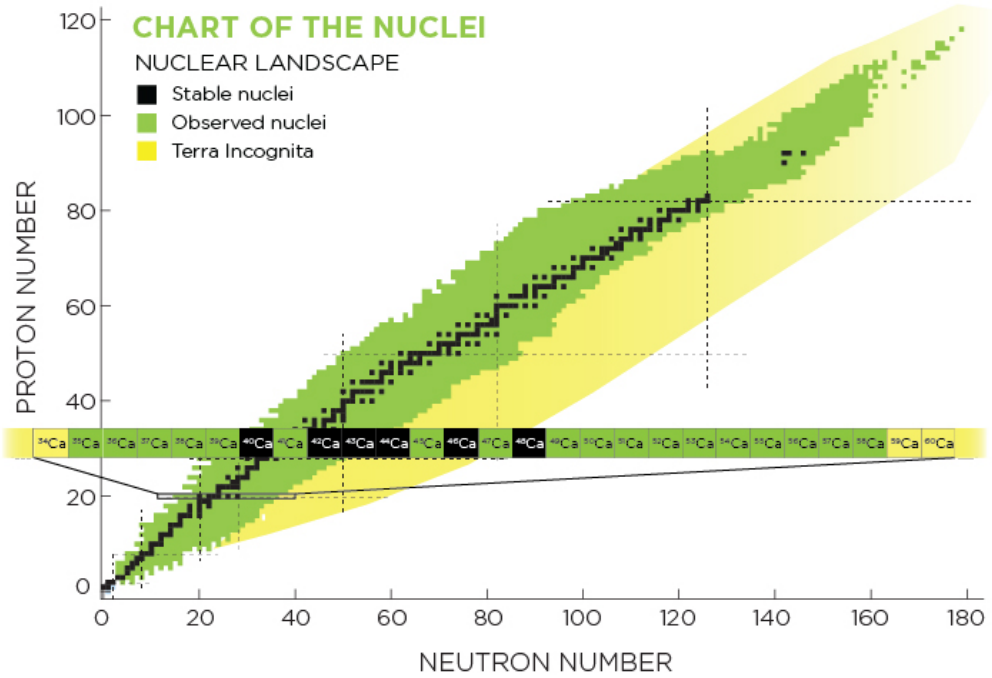

Figure 1.1: Chart of the nuclei displaying the nuclear landscape. The black squares indicate stable nuclei, the green squares indicate unstable nuclei that have been observed, and the yellow "terra incognito" region indicates predicted nuclei that have not yet been observed experimentally. The dashed lines follow nuclear magic numbers. Figure taken from Ref. [2].

Projectile fragmentation reactions have often been described as a two-step process originally referred to as the abrasion-ablation or fireball model [3–5]. Figure 1.2 shows a schematic picture of the abrasion-ablation model. In the first step, the projectile rapidly collides and passes by the target. The overlapping area is abraded or scraped away, creating a "fireball" of participants that releases nucleons and/or fragments. The collision produces two excited precursors, a projectile-like fragment and a target-like fragment. The excited fragments then undergo ablation, a slower de-excitation process, by releasing nucleons, other light particles, and energy. The end results are two "cold" nuclear residues, one moving very fast in the lab frame and another nearly at rest.

Products from a projectile fragmentation reaction may be studied in inclusive or exclusive experiments. In an inclusive measurement, only one product is measured from the collision.

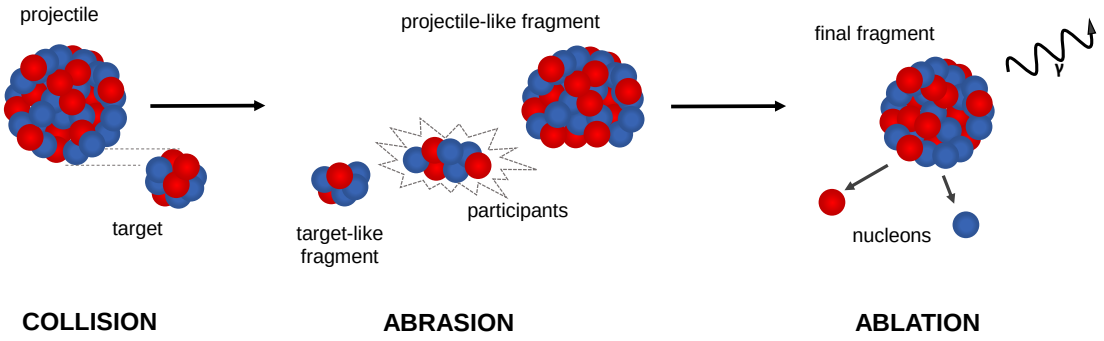

Figure 1.2: Projectile fragmentation reaction depicted as a two-step abrasion-ablation process.

In an exclusive measurement, two or more products from one collision are measured in coincidence. Consider the example of a projectile fragmentation reaction producing a final fragment residue as well as several nucleons and gamma rays, as shown for example in Figure 1.2. If only the residue fragment was measured, an inclusive measurement was made. Measuring the residue fragments in coincidence with the gamma rays or neutrons would be an example of an exclusive measurement.

If measured in an exclusive experiment, the final fragments can provide more insight into the projectile fragmentation process than just measuring the production of individual residues alone. The final fragments can be compared to models that simulate collisions and reactions on nuclei. If the experimental data matches the model, then the model could be considered a fair representation of the fragmentation process. A poor match between data and simulation would indicate that the model has made incorrect assumptions or is missing a piece of the puzzle. One goal of the present work is the use of exclusive measurements of projectile fragmentations products to test nuclear reaction models.

1.2 Nuclear Equation of State

Some models of nuclear reactions treat the nuclei as fluid nuclear matter with a macroscopic equation of state for the total energy. For ground state nuclei, or cold nuclei at saturation density ($\rho_0 = 0.16$ fm^3), the nuclear binding energy is described through the Bethe-Weizsäcker formula for a charged liquid drop model [6]. The nuclear binding energy is then written in a semi-empirical mass formula as

$$BE(Z,N) = a_V A - a_S A^{(2/3)} - a_C \frac{Z^2}{A^{(1/3)}} - a_A \frac{(N-Z)^2}{A} \pm \delta_{pairing} \tag{1.1}$$

where the binding energy, BE, is calculated with a volume term (a_V), a surface term (a_S), a Coulomb term (a_C), an asymmetry term (a_A), and a pairing term ($\delta_{pairing}$). The coefficients are then determined by empirically fitting the equation to experimentally known masses [6].

While ground state nuclei are relatively well-described with the Bethe-Weizsäcker formula, determining the properties of nuclear matter with temperature, densities, and neutron-to-proton ratios away from ground-state nuclei has been a challenge. The nuclear equation of state is often used to describe how the energy per nucleon of infinite nuclear matter changes as a function of the density (ρ) and isospin asymmetry (δ). Isospin asymmetry is often given as

$$\delta = \frac{(\rho_n - \rho_p)}{(\rho_n + \rho_p)} \approx \frac{(N-Z)}{A} \tag{1.2}$$

where ρ_n is the neutron density and ρ_p is the proton density of the matter. (As the difference in proton mass and neutron mass is negligible, the approximation to terms of N, Z, and A is valid.)

1.2.1 Isospin Symmetry Energy

The nuclear equation of state for infinite nuclear matter can be connected to the Bethe-Weizsäcker formula [6] for finite matter. (The connection is summarized below. Intermediate steps are shown in Part 1 of Appendix A.) Consider the Bethe-Weizsäcker formula for the case of an infinitely large mass, A. As infinite matter has no surface, the surface term must be zero. The Coulomb term is removed, as some infinite nuclear matter studies exclude the term and including Coulomb forces makes the liquid drop unstable in this form [7–9]. (Similar derivations of the nuclear equation of state exclude the Coulomb term [10–15].) The pairing term can also be excluded due to its small contribution in this case. Thus, the Bethe-Weizsäcker formula reduces to the following relation for matter with infinitely large mass:

$$\left.\frac{BE(Z,N)}{A}\right|_{A\to\infty} = a_V - a_A\frac{(N-Z)^2}{A^2} \tag{1.3}$$

where the volume and asymmetry terms are the only remaining parts.

The asymmetry term can be further broken into volume and surface terms. As before, the surface term for the asymmetry term can be excluded in infinite matter. The binding energy per nucleon for infinitely large nuclear matter is then written as:

$$\left.\frac{BE(Z,N)}{A}\right|_{A\to\infty} \approx a_V - a_A^v\delta^2 \tag{1.4}$$

where a_A^v is the asymmetry-volume term. For symmetric nuclear matter ($\delta = 0$), the second part of the above equation ($a_A^v\delta^2$) becomes zero. Thus, the first term, a_V, represents the bulk part of the nuclear equation of state, while the second term represents the isospin

asymmetric part. When discussing the nuclear equation of state, the above equation is often written as $E(\rho, \delta)$ in terms of the density and isospin:

$$E(\rho, \delta) = E(\rho, 0) + E_{sym}(\rho)\delta^2 + \mathcal{O}(\delta^4) \tag{1.5}$$

The first term in the expression, $E(\rho, 0)$, represents the binding energy for symmetric nuclear matter ($N = Z$) as a function of density and is independent of δ. The second term contains the symmetry energy, $E_{sym}(\rho)$, or the difference in energy between pure neutron matter ($\delta = 1$) and symmetric nuclear matter ($\delta = 0$). (The third term, $\mathcal{O}(\delta^4)$, is considered negligible and often omitted in current symmetry energy work.) As nuclear matter becomes more asymmetric, this second term becomes more important due to the δ^2 dependence.

While the nuclear equation of state of symmetric nuclear matter is thought to be well-understood and constrained by various measurements, the same is not true of asymmetric matter [10, 16]. For example, the binding energies of ground state nuclei are well-known and the binding energy of symmetric nuclear matter is well-defined at the nuclear saturation density ($\rho_0 = 0.16$ fm^3) [17]. Furthermore, the nuclear equation of state symmetric term, $E(\rho, 0)$, is relatively well-defined from heavy-ion collision transverse flow measurements and giant monopole resonances [18–23].

However, there are large discrepancies among the predictions for the isospin dependence of the nuclear equation of state, in particular in the low and high density regions [10, 16, 17]. Different nucleon-nucleon interactions contain various parameters that are adjusted to fit a variety of experimental data that have led to a variety of predictions. Thus, theoretical models show inconsistencies in predicting the density dependence of the symmetry energy [24, 25].

Determining the form of the symmetry energy and how it behaves in relation to a variety of conditions such as density, temperature, and pressure remains a major objective in understanding nuclear properties, astrophysical processes, and the fundamental nucleon-nucleon interaction [26–37]. In particular, the properties of neutron-rich matter are clearly dependent on the symmetry energy term. For example, neutron stars are thought to have a very asymmetric proton-to-neutron ratio [38, 39]. Adjusting the symmetry energy term has implications for predictions of the mass-to-radius ratios, density, and cooling timescale, among other characteristics, of neutron stars [10, 29, 36, 40–42]. Furthermore, because the characteristics of neutron stars are affected by the nuclear equation of state, the properties of neutron stars can be used to constrain the symmetry energy term [43, 44].

While more sophisticated calculations of the equation of state have produced better constraints of the symmetry energy [45, 46], it is important to continue to test these new predictions of the symmetry energy and neutron matter by experimentally constraining the form of the symmetry energy, establishing tighter and consistent constraints.

The form of the symmetry energy is often described as "soft" or "stiff" based on how the symmetry energy evolves with density. Stiffer forms of the symmetry energy have a more constant increase in symmetry energy as density increases, becoming increasingly larger beyond the nuclear saturation density. Soft forms of the symmetry energy show larger magnitude below the saturation density, with slower increase or even decrease beyond ρ_0. A comparison of three plausible forms of the symmetry energy is displayed in Figure 1.3 [47].

In order to quantitatively describe the form of the symmetry energy, the density dependence of the symmetry energy form can be written as a Taylor expansion of the symmetry energy:

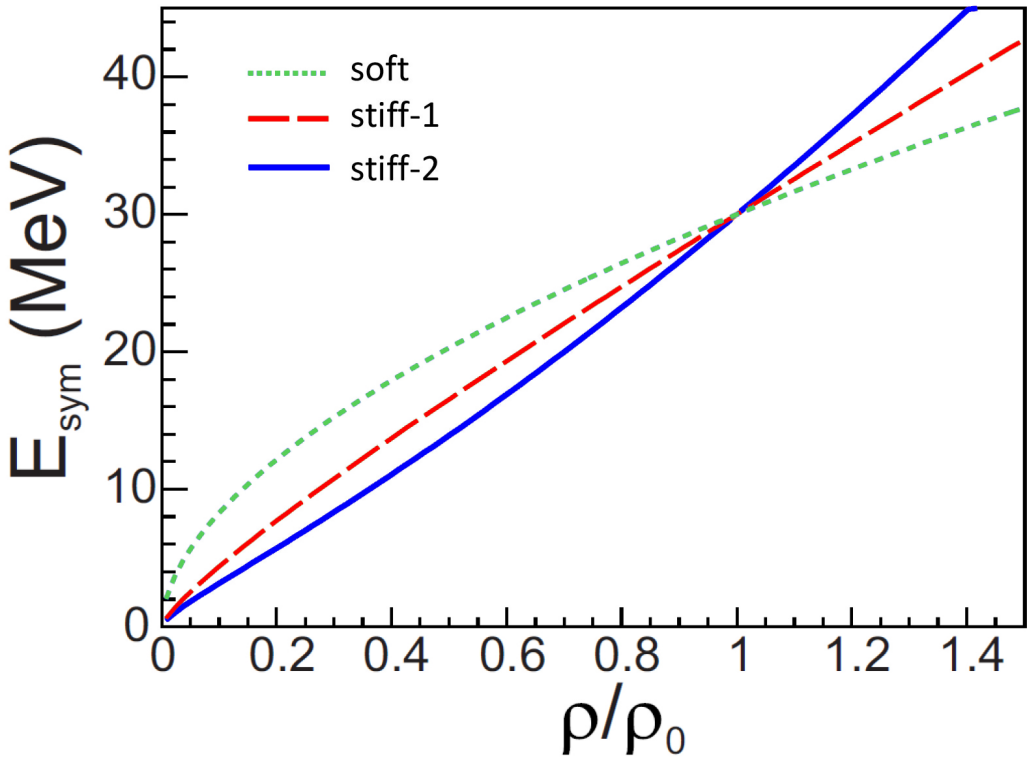

Figure 1.3: The three different forms of the density dependence of the symmetry energy used within CoMD calculations. Figure adapted from [47].

$$E_{sym}(\rho) = E_{sym}(\rho_0) + \frac{L_{sym}}{3}(\frac{\rho - \rho_0}{\rho_0}) + \frac{K_{sym}}{18}(\frac{\rho - \rho_0}{\rho_0})^2 + ... \tag{1.6}$$

where $E_{sym}(\rho_0)$, L_{sym}, and K_{sym} are the magnitude, slope, and curvature parameters, respectively. (The expansion of the symmetry energy term to Equation 1.6 is shown in Part 2 of Appendix A.) These parameters provide quantitative values of the constraints, allowing comparison of the derived constraints from different studies and models.

1.2.2 Constraining Symmetry Energy with Heavy-Ion Collisions

The density dependence of the symmetry energy has been constrained by the results from several studies, including neutron skin measurements, giant dipole resonances, nuclear masses,

astrophysical mass-radius observations, and dipole polarizability studies [48–50]. A comparison of a selection of constraints from diverse experimental studies can be seen in Figure 1.4 [38]. The magnitude of the symmetry energy form is relatively constrained compared to the slope. As an example, the finite-range droplet model (FRDM) was fit using experimental masses to find that $E_{sym}(\rho_0) = 32.5 \pm 0.5$ MeV, a fairly restricted range ($\pm 2\%$), yet L_{sym} had a much larger range of 70 ± 15 MeV ($\pm 21\%$) [50], indicating that it has been more difficult to constrain the slope parameter relative to the magnitude.

Another method that can constrain the symmetry energy involves the use of heavy-ion collisions (HICs), which probe nuclear matter at densities, temperatures, and pressures away from those of ground state nuclei [36, 59]. Heavy-ion collisions produce fragments and other light particles, which can be compared to models containing an adjustable symmetry energy term. Several constraints obtained from experiments using heavy-ion collisions are shown in Figure 1.5 [59] and the green HIC band in Figure 1.4 [38].

Heavy-ion collisions with radioactive ion beams may be a key to placing better constraints on the form of symmetry energy. Compared to the limited possible stable beams, radioactive ion beams can introduce larger asymmetries into the reaction, and thus a larger asymmetry parameter, δ^2. Thus, with these larger asymmetries comes an enhanced sensitivity to symmetry energy.

Unconstrained parameters and differences in modeling the dynamics are the main uncertainty in obtaining constraints from these reactions. There are two main classes of models used in these evaluations: molecular dynamics models and mean-field models. In molecular dynamics models, each nucleon is described as a Gaussian distribution to represent its quantum wave packet with its characteristic nucleon properties. On the other hand, in mean-field approaches, each nucleon is represented by a set of test particles distributed in a cell array.

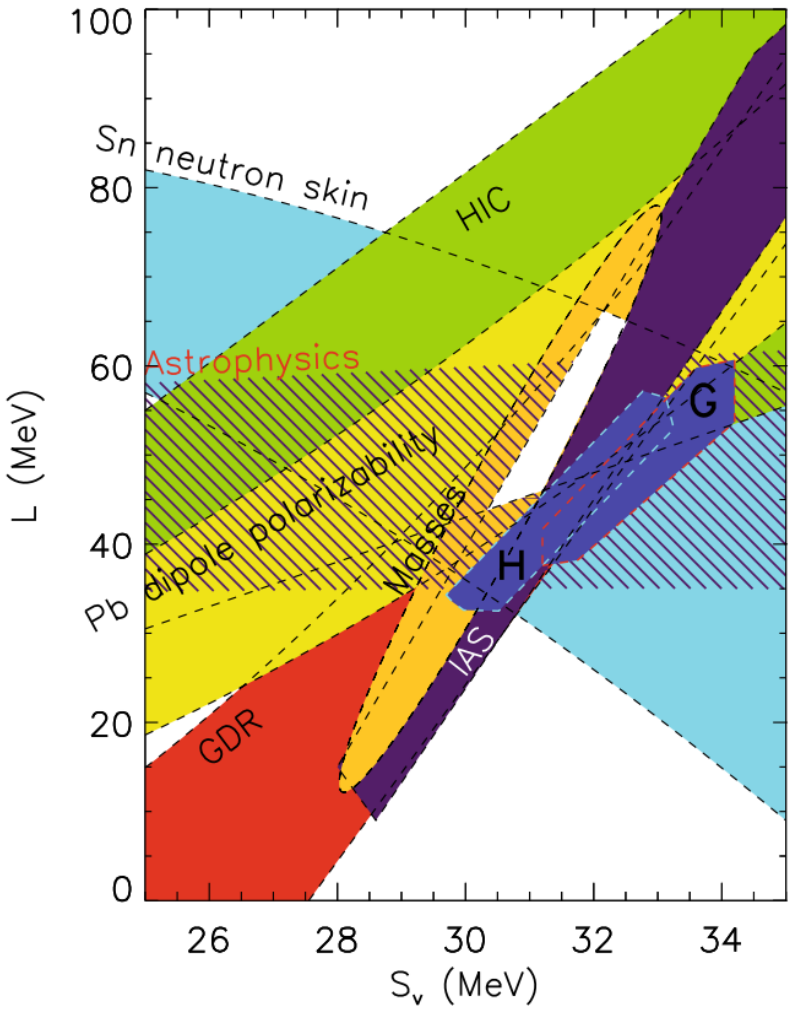

Figure 1.4: Comparison of a selection of experimental constraints for symmetry energy parameters. S_V is equivalent to $E_{sym}(\rho_0)$ and L is equivalent to L_{sym}. Filled bands indicate constraints from neutron skin thicknesses of tin isotopes [49], dipole polarizability of ^{208}Pb [51, 52], giant dipole resonances (GDR) [53], isotope diffusion in heavy-ion collisions (HIC) [54], and energies of excitations to isobaric analog states (IAS) [55]. The filled oval shows constraints from nuclear masses [56]. G and H refer to neutron matter studies of Gandolfi *et al.* [57] and Hebeler *et al.* [58], respectively. The hatched rectangle gives constraints from fitting astrophysical mass-radius observations [43, 44]. The overlap region of the former constraints is indicated by the enclosed white area. Figure taken from [38] with kind permission of *The European Physical Journal* (EPJ).

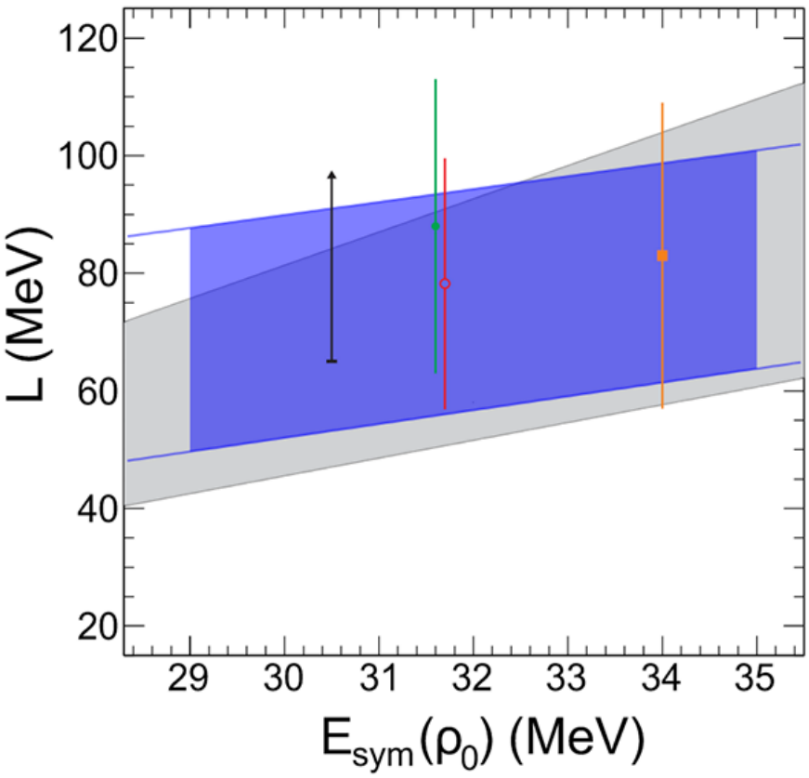

Figure 1.5: Constraints on the slope (L) and magnitude ($E_{sym}(\rho_0)$) in Equation 1.6 of the symmetry energy from heavy-ion collision studies. The shaded light gray and dark purple area are shown from [54] and [60], respectively. Constraints at given values of $E_{sym}(\rho_0)$ are shown from [61], [10], [36], and [62] as the black lower-limit, solid green circle, open red circle, and solid orange square, respectively. For clarity and to avoid overlap, the red circle was offset by 0.1 MeV. Figure taken from [59] with kind permission of *The European Physical Journal* (EPJ).

Nucleons and fragments are formed by phase-space coalescence, in which test particles within an adjustable position range are grouped together.

The differences in the approaches of the models can produce different outcomes. For example, Colonna *et al.* [63] compared multifragmentation reaction simulations from the anti-symmetrized molecular dynamics (AMD) model [64] and the momentum-dependent stochastic mean-field (SMF) model [65]. The study showed that the models gave different results in that more free nucleons were produced in the SMF model compared to AMD model, while light intermediate mass fragments ($A = 5 - 15$) were more abundant in the AMD model

compared to the SMF model. These differences were attributed to early clustering effects and many-body correlations in the AMD model. The clustering grouped nucleons into light intermediate mass fragments, reducing the amount of mass available for generating free nucleons. The constraints made on the symmetry energy are thus model dependent, as the reaction model chosen may affect predictions for the heavy-ion collisions, particularly for particle emission.

1.3 Dissertation Overview

This experiment examined two different approaches to describe the fragment and neutron distributions from projectile fragmentation reactions. In one approach, the experimental data set compared to the Liège Intranuclear Cascade (INCL++) model, a Monte Carlo based code that first simulates the fast part of the reaction to create an excited remnant that is then "cooled" through a statistical de-excitation code. The second approach involved the Constrained Molecular Dynamics (CoMD) model, a dynamical model that contains three versions of the symmetry energy term. The two models are described in Chapter 2.

The experimental data set was collected at the National Superconducting Cyclotron Laboratory, where intermediate-energy (55.5 MeV/u) beams of ^{30}S and ^{40}S were reacted with beryllium targets. Fast neutrons from the reaction were measured in coincidence with heavy residue fragments using the MoNA LISA (Modular Neutron Array and Large-area multi-Institutional Scintillator Array) detectors and Sweeper magnet charged particle detectors [66–68]. Experiment techniques are described in Chapter 3, while analysis of the data is outlined in Chapter 4. Results and comparisons of the two models with the experimental data are discussed in Chapter 5, and final remarks and conclusions are given in Chapter 6.

Chapter 2

Modeling and Simulations

2.1 Constrained Molecular Dynamics Model

The Constrained Molecular Dynamics (CoMD) model [69,70] is a dynamical simulation used to describe the interaction (collision) of two heavy-ions over a given length of time. The length of time can be adjusted to encompass the full evolution of the collision. In CoMD, each nucleon is described as a Gaussian wave-function to represent the quantum wave packet with the distribution function:

$$f_i(r,p) = \frac{1}{(2\pi\sigma_r\sigma_p)^3} \times exp\left[-\frac{(r-\langle r_i\rangle)^2}{2\sigma_r^2} - \frac{(p-\langle p_i\rangle)^2}{2\sigma_p^2} \right] \tag{2.1}$$

where $\langle r_i\rangle$ is the central position, $\langle p_i\rangle$ is the central momentum, σ_r is the width of the position distribution, and σ_p is the width of the momentum distribution of the i^{th} nucleon. Nucleons were propagated according to the relevant equations of motion and a momentum-independent Skyrme interaction. The symmetry term in the Skyrme interaction could be changed, providing a probe to the form of the density dependence of the symmetry energy.

The CoMD model gives special care to the Pauli principle in respect to constraining the equations of motion. In general quantum molecular dynamics models, a Pauli potential is used to prevent nucleons of the same isospin and spin state from occupying the same phase-space. This Pauli potential adds a repulsive force that does not exist in the nucleus. Within

the present CoMD calculations, the occupation density in phase space of each nucleon is calculated every 1 fm/c time step. If an occupation density is found to be greater than one, the nucleon is considered to be in violation of the Pauli principle. To correct the violation, the momenta of the neighboring particles are randomly changed while the total momentum and total kinetic energy of the subset are conserved. If the occupation density drops below one after the change, the configuration is accepted. If the occupation density requirement is not met, the nucleon-nucleon collision is rejected. This allows a faster simulation of heavy-ion collisions compared to other molecular dynamics models. For example, in the antisymmetrized molecular dynamics model (AMD) [64, 71], computation time scales with A^3 (where A is the number of nucleons). In CoMD, computation time scales with A^2 [72]. The decreased computation time allows the simulation to be run for a longer time, enabling the system to be followed as it dynamically evolves.

The CoMD model is an adjustable model in that it includes three different symmetry energy parameterizations: stiff-2, stiff-1, and soft. Each parameter gives a distinct slope for the form of the symmetry energy at a given magnitude. The variation of the equation of state with these parameters was displayed in Figure 1.3 from Chapter 1.

2.1.1 GEMINI++

The CoMD model does not always produce the final products unless the code is run for a very long time. In the present case, the dynamical process was stopped at 2000 fm/c. At this time, the system had, in general, stabilized with very little evolution in fragment distributions, and fewer than 2% of fragments remained excited. (The fragment distributions and their evolutions over time are discussed in Chapter 5.) A list of the excited prefragments were passed to another code to calculate the final distributions by statistical decay.

GEMINI is a statistical decay and evaporation code used to de-excite hot nuclei [73, 74]. The excitation energy, angular momentum, charge, and mass of a hot fragment is used to calculate its decay path in the nuclear landscape to the final, cold product. A Monte Carlo method is used to calculate the most probable series of sequential binary decay steps from the initial hot fragment. The Hauser-Feshbach formalism is used to calculate the decay widths of the light charged particles (including n, p, d, t, ^{3}He, α, ^{6}He, and $^{6\text{-}8}$Li fragments), while the fission channel is calculated with the Bohr-Wheeler formalism. The original GEMINI code was converted to C++ and updated to improve the calculation of the width of the charge and mass distributions from fission of heavy fragments. This revised code was renamed GEMINI++ and was used in the present work.

GEMINI and GEMINI++ are often used as so-called "afterburner codes" that are coupled to molecular dynamics models to decay any remaining hot fragments from the dynamical model [72, 75–78]. Passing the leftover hot fragments from CoMD through GEMINI++ mimics a two-step reaction, with CoMD covering both the abrasion and initial ablation period and GEMINI++ completing the ablation period leading to the final de-excited state. However, it should be emphasized that CoMD attempts to reach a final de-excited state without connection to an afterburner code. In the present case it was found that after a few thousand fm/c, only a small percentage of fragments remain hot for GEMINI++ to de-excite. For each of the three symmetry energy options within both simulated reactions, only 2% or fewer of the fragments were passed to GEMINI++. While the percent of fragments affected was small, it was important to cool the fragments to their final states.

In using the GEMINI++ code as an evaporation code with CoMD simulations, some assumptions had to be made. When the CoMD simulation is stopped at an arbitrary point, hot fragments are likely deformed and at a density below normal nuclear density (ρ_0 =

0.16 fm^{-3}). The GEMINI++ code assumes that the hot fragment is at normal nuclear density when calculating the de-excitation of the hot fragment. This difference in shape and density could potentially affect the decay process. Furthermore, GEMINI++ decays each of the hot fragments independently so final trajectories of the fragments are locked in and no further external nuclear or Coulomb forces are considered. While these assumptions are necessary in using GEMINI++ to cool remaining hot fragments, dynamical models connected to GEMINI and GEMINI++ have produced results with reasonable agreement to a variety of experimental observables [72, 75–79].

2.1.2 Previous CoMD Comparison to MoNA LISA-Sweeper Data

A similar analysis of CoMD predictions for prior MoNA LISA-Sweeper data from another reaction system has been carried out. The original experiment [80,81] was designed to study neutron-unbound states of ^{27}F and ^{28}F populated from direct nucleon knock-out reactions from a ^{29}Ne beam on a ^{9}Be target. The experiment made exclusive measurements of final residue fragments, neutrons, and gamma rays.

While ^{29}Ne was the desired projectile in the proposed experiment, 87% of the beam delivered to the experiment was actually ^{32}Mg contaminant due to the difficulty of separating the very weakly produced ^{29}Ne ions. The more prevalent ^{32}Mg + ^{9}Be contaminant reaction was simulated in the CoMD framework by Kohley *et al.* [60]. The 73 MeV/u reaction was run in CoMD up to 1500 fm/c with no coupling to a de-excitation code. Their results indicated that the N/Z of the final fragment residue may be sensitive to the form of the symmetry energy.

While the neutron yield was partially explored in the work, there were a few limitations in fully exploring neutron multiplicities. The experiment was designed to detect gamma

rays with the CAESAR (CAESium iodide ARray) detector [82]. The inclusion of CAESAR forced the target to be set farther upstream of the normal target position typical for a MoNA LISA-Sweeper configuration, resulting in a lower angular acceptance in the neutron detector array. The present work did not include the CAESAR detector so that neutron distributions were more complete and could be compared to CoMD simulations. Furthermore, the prior experiment required neutron coincidence events detected in MoNA LISA with charged particle fragments measured in the Sweeper detectors. Thus, no fragments with zero hits in MoNA LISA were examined. The present work, as described in Chapter 3, did not require hits in MoNA LISA to measure charged fragments.

2.1.3 CoMD Model Parameters

In this analysis, CoMD simulations of the ^{30,40}S + ^{9}Be reactions were run at 55 MeV/u with each of the three symmetry energy options.

A magnitude ($E_{sym}(\rho_0)$) of 32 MeV was chosen for this experiment due to its relatively well-known constraint from [50] and [59]. The calculated slopes (L_{sym}) at the saturation density for this magnitude are 105 MeV (stiff-2), 78 MeV (stiff-1), and 51 MeV (soft). These values for slope and magnitude lie within the bounds of current potential constraints [38,59].

For comparison with the current set of experimental data, the CoMD heavy-ion collisions were propagated to 2000 fm/c, allowing the system to evolve dynamically relatively far and become relatively cool. Any hot fragments left at 2000 fm/c were further de-excited using GEMINI++. The combined model will be referred to as CoMD + GEMINI++ in this work.

2.1.4 Isotope Production Output

The isotope production distributions taken directly from the CoMD + GEMINI++ simulations are shown in Figures 2.1-2.6. Figures 2.1 and 2.2 contain the distributions from the stiff-2 option, Figures 2.3 and 2.4 contain the distributions from the stiff-1 option, and Figures 2.5 and 2.6 contain the distributions from the soft option. The stiff-2 distributions are skewed slightly more in neutron-rich fragments relative to the distributions from the soft simulations. (Stiff-1 falls in the middle.) Below the saturation density, the soft symmetry potential is more repulsive for neutrons than the stiff potential. Thus, the soft symmetry energy option should result in an increase in neutron emission, which leads to a decreased average N/Z of the residues. The stiffer option was less repulsive, resulting in increased average N/Z of the residues.

It should be noted that the fragment distributions presented here represent the complete inclusive distributions. Filtering the fragments and coincident neutrons through a set of conditions which mimicked the treatment of the experimental data was necessary to compare the simulated results to experimental results. The filtering procedure is described in Chapter 4 and filtered results of hit multiplicities will be presented in Chapter 5.

2.2 Liège Intranuclear Cascade Model

2.2.1 INCL++

The Liège Intranuclear Cascade (INCL) model is a Monte Carlo based code used to simulate nucleon, pion, and light-ion induced reactions on heavy nuclei. The energy of these collisions can range from a few tens of MeV to a few GeV. The latest release of the code, INCL4.6 [83],

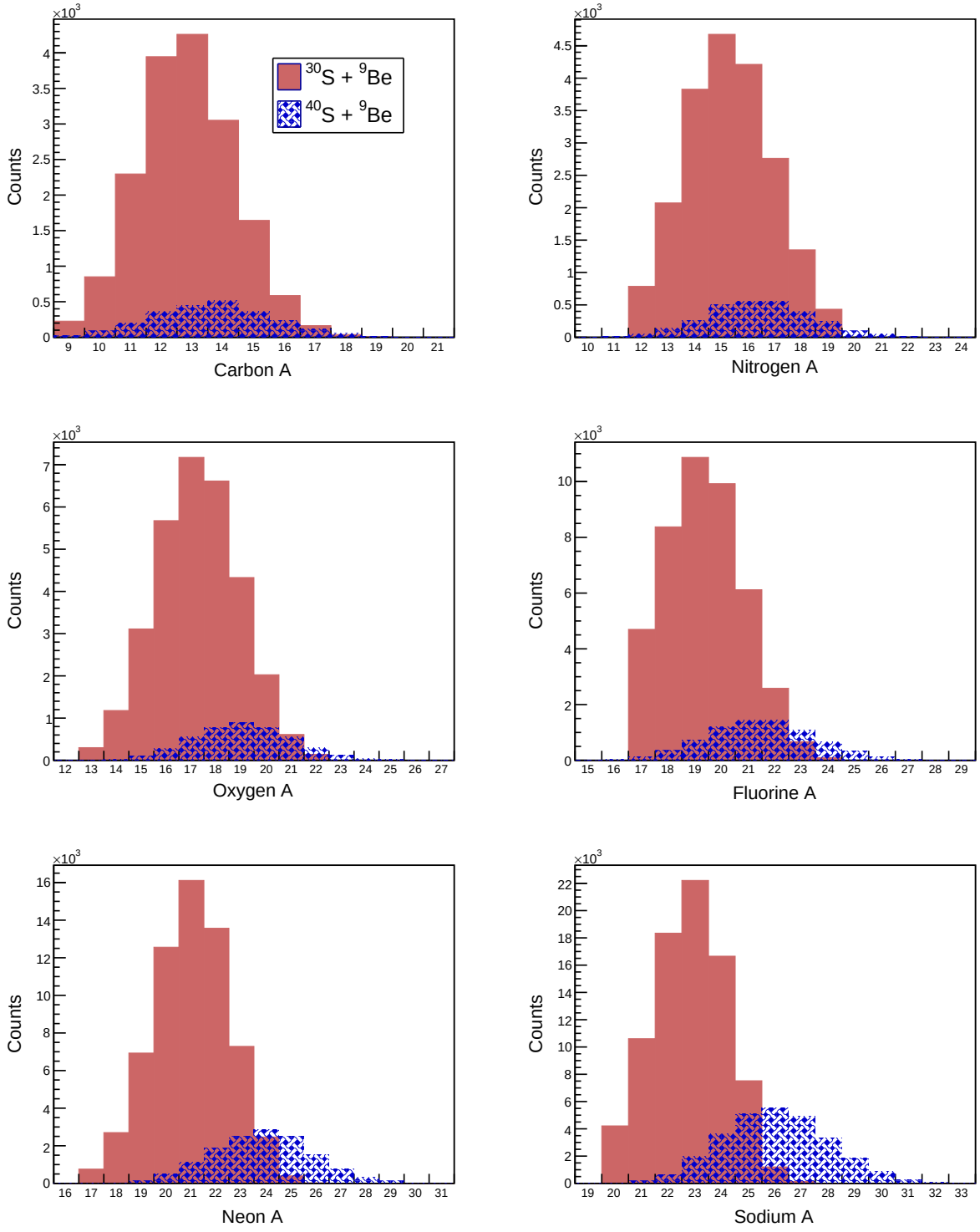

Figure 2.1: Inclusive isotope distributions from the stiff-2 CoMD + GEMINI++ simulations for elements $Z = 6 - 11$.

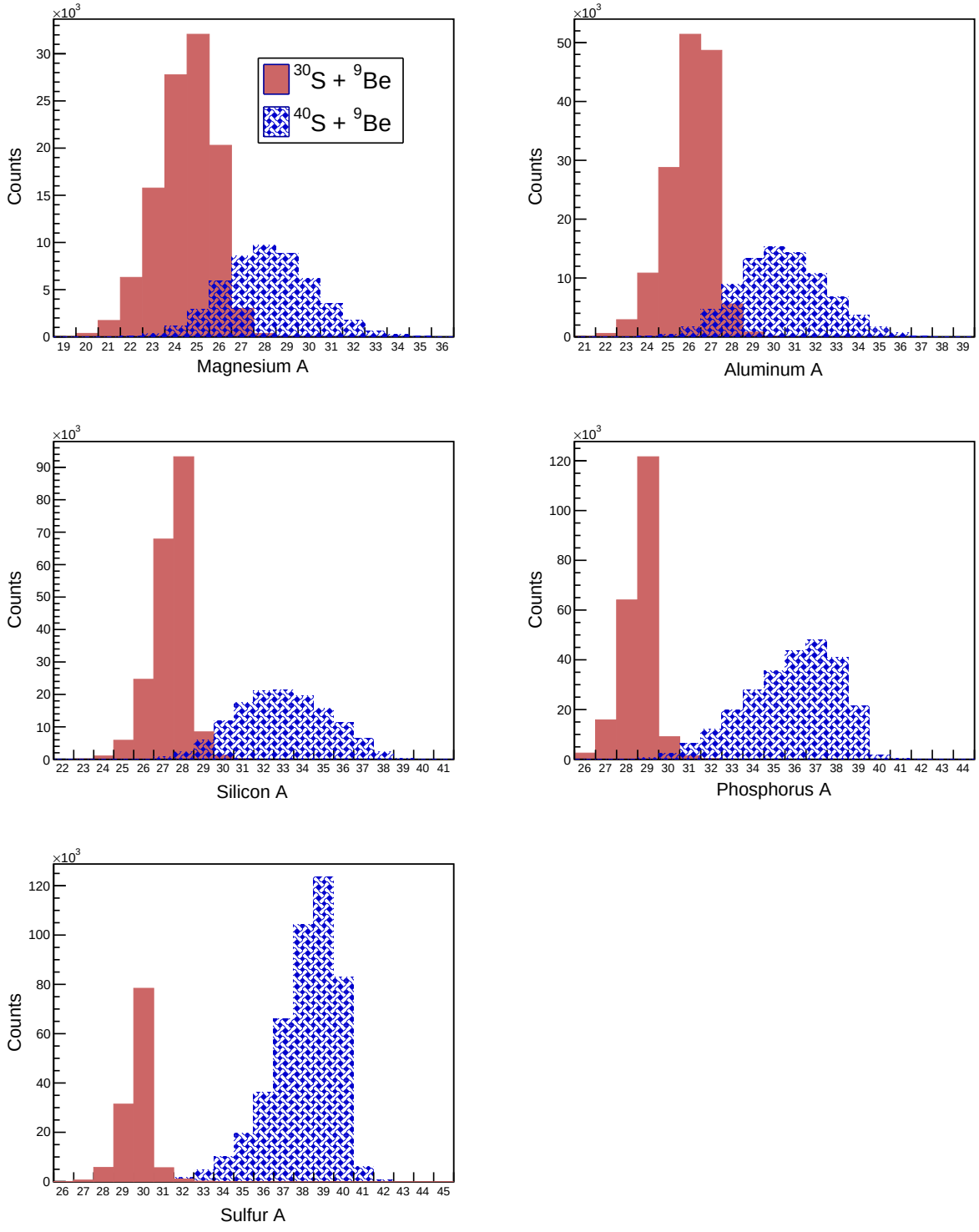

Figure 2.2: Inclusive isotope distributions from the stiff-2 CoMD + GEMINI++ simulations for elements $Z = 12 - 16$.

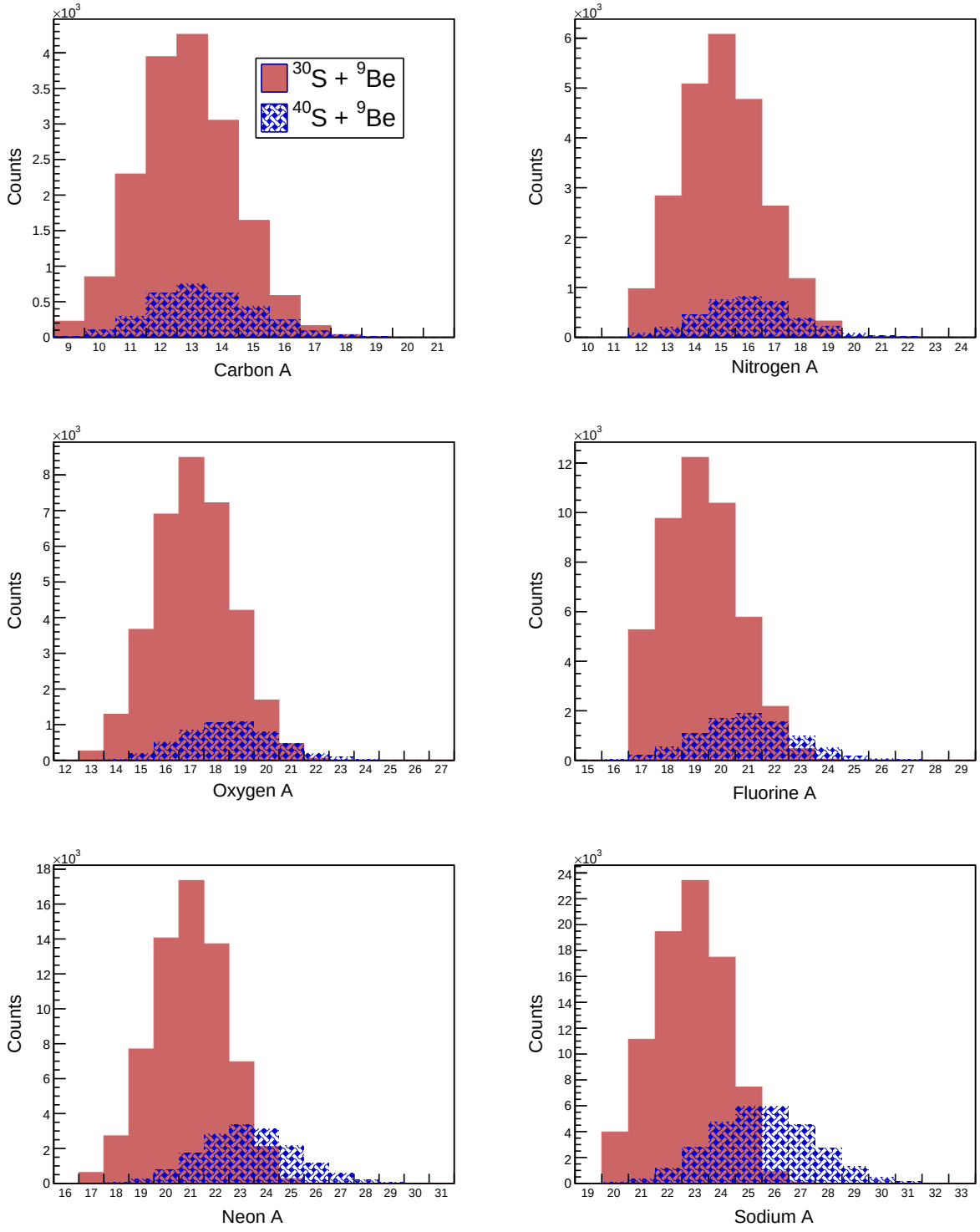

Figure 2.3: Inclusive isotope distributions from the stiff-1 CoMD + GEMINI++ simulations for elements $Z = 6 - 11$.

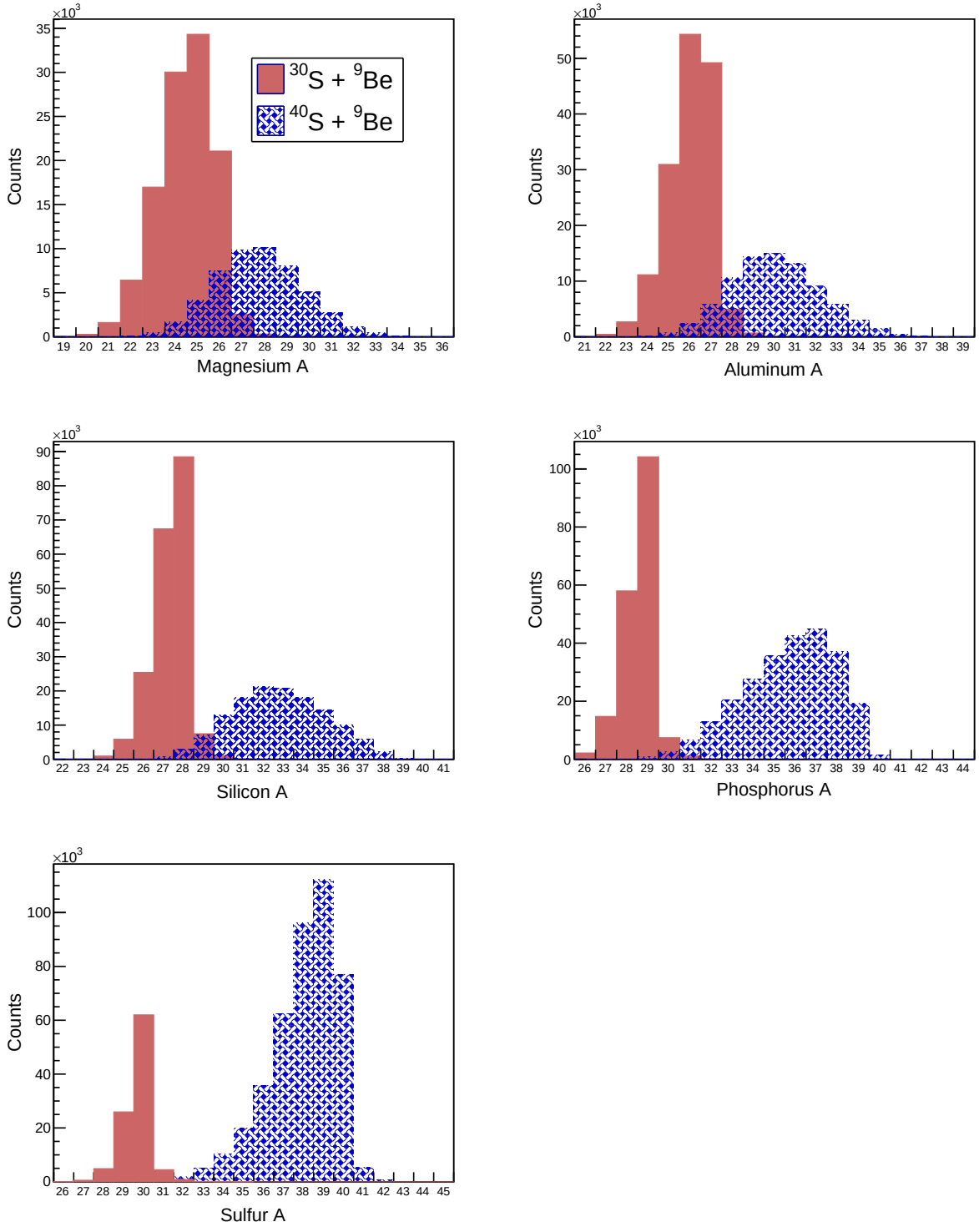

Figure 2.4: Inclusive isotope distributions from the stiff-1 CoMD + GEMINI++ simulations for elements $Z = 12 - 16$.

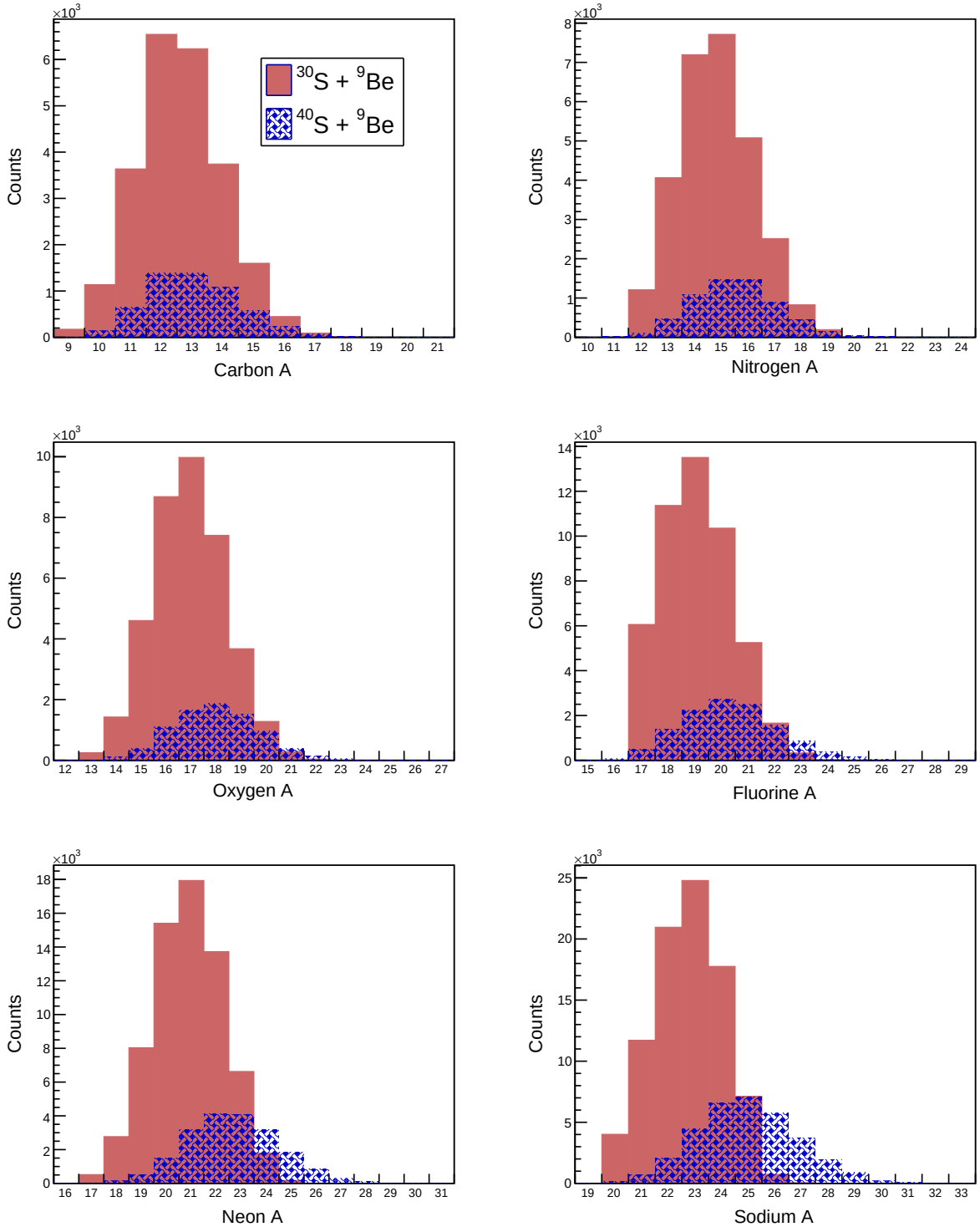

Figure 2.5: Inclusive isotope distributions from the soft CoMD + GEMINI++ simulations for elements $Z = 6 - 11$.

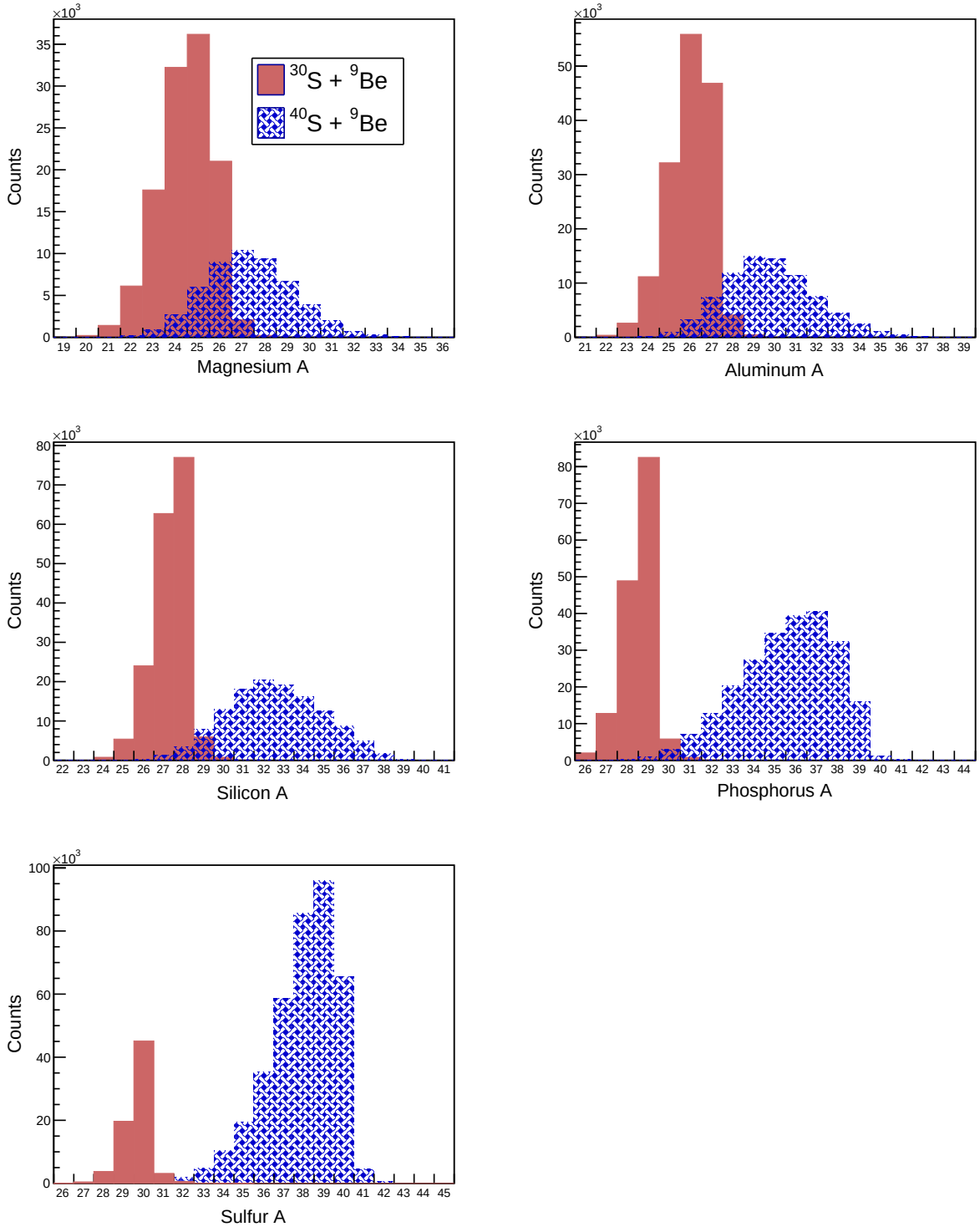

Figure 2.6: Inclusive isotope distributions from the soft CoMD + GEMINI++ simulations for elements $Z = 12 - 16$.

contains support for nucleon, pion, and composite projectiles. An object-oriented C++ version of the code, INCL++ [84, 85], is equivalent to the INCL4.6 release for nucleon and pion induced reactions. Unlike INCL4.6, INCL++ contains support for light-ion projectiles with masses up to 18. Note that the target in the present case is ^{9}Be and falls within the bounds of the supported projectile masses and can be used as the "projectile" in an inverse-kinematics option available to INCL++ and described later in this section.

INCL++ has been described as a time-like intranuclear cascade model. In the first stage, all nucleons are distributed appropriately in phase space. Target nucleons are given positions and momenta at random in agreement with Saxon-Woods and Fermi sphere distributions, respectively. The projectile particle is given the appropriate energy and an impact parameter is assigned at random. Once the parameters are defined, the projectile moves toward the target and initiates an avalanche of binary collisions within the target nucleus. Resulting particles are individually tracked, with emission of nucleons, pions, and light clusters following. Light clusters are produced by a dynamical phase-space coalescence algorithm. In cases of binary particle-particle collisions, nucleons are restricted by Pauli blocking. When the fast particles escape the nuclei and the remnant nucleus shows signs of thermalization, the cascade step stops.

Predictions from the standard version of the model, INCL4.2, have been tested against a large body of experimental data from reactions in the range of 200 MeV/u to 2 GeV/u. INCL4.2 was found to be in good agreement with experimental total reaction cross sections, particle multiplicities, residue mass and charge distributions, residue recoil velocity distributions, and neutron, proton, pion, and composite double differential cross sections [86].

INCL4.6 (and, by extension, INCL++) incorporated several new features to improve the standard version of INCL. New features introduced to INCL4.6 included cluster produc-

tion through a dynamical phase space coalescence model, Coulomb deflection for entering and exiting charged particles, experimental threshold values for particle emission, and improved treatment of Pauli blocking [83]. The new features were found to improve the model predictions [83, 87, 88].

INCL++ simulates the intranuclear-cascade or fast part of the reaction. After this step, the remaining nucleus, or cascade remnant, still holds excitation energy and may de-excite through fission, multifragmentation, or the emission particles such as nucleons, light nuclei, or photons. Coupling INCL++ to a de-excitation code is necessary to produce the distributions of the final (observed) fragments and neutrons, similar to the CoMD code. The INCL codes can interface with a few de-excitation models (including the previously described GEMINI++), however the ABLA07 code [89] is the default option selected by the authors of INCL++.

2.2.2 ABLA07

To de-excite the cascade remnant, information on the fragment is passed to a separate statistical de-excitation code. In this case the INCL++ package includes the ABLA07 code.

ABLA07 is a semiclassical code that describes the de-excitation of a hot fragment through comparison of the relative probabilities of simultaneous break-up, particle emission, and fission. Simultaneous break-up occurs when a hot fragment fractures into several fragments due to thermal instability. Particle evaporation is based on the Weisskopf-Ewing formalism, and the fission decay width is calculated by taking into account dynamical effects. An analytical approximation to the solution of the Fokker-Planck equation for the time dependent fission width is included, allowing ABLA07 to become a more dynamical code as compared to a purely statistical model. Earlier versions of the ABLA code focused on the emission

of neutrons, light charged particles ($Z < 3$), and gamma-rays, while ABLA07 included the emission of intermediate-mass fragments ($Z > 2$) [89]. While ABLA07 was originally created for describing the de-excitation stage of heavy-ion collisions and spallation reactions at relativistic energies, it has been coupled to INCL++ to handle the de-excitation step in nuclear reactions [83].

2.2.3 Limitations of the INCL Model

The INCL4.6 and INCL++ models have been well tested for projectiles up to mass 18, target nuclei close to stability, and reaction energies from around 10 MeV/u to 20 GeV/u [83, 84]. The upper limit of the projectile mass number is based on the validity of the physical approximations and testing. Heavier projectiles may be simulated in the code, but the outputs remain untested by the authors. To accommodate reactions with projectiles above a mass of 18 with a light target, INCL++ comes with the ability to introduce an inverse-kinematic transformation [84]. The initial set of variables are calculated in the direct-kinematics frame, with the input projectile moving at the given velocity along the positive Z-axis with the target at rest. In the inverse-kinematic frame, the target moves at the given velocity along the positive Z-axis with the projectile at rest. The calculation of the interaction is then followed as normal and the reaction products are boosted back to the laboratory frame at the end of the simulation.

While intranuclear-cascade style models are generally not used for reactions below 150 MeV/u, the INCL codes have shown reasonable agreement to experimental data down to a few tens of MeV per nucleon [83]. Reactions that fall below a few MeV do not reproduce inelastic events well. Low-energy reactions induced by neutral or negative particles have not

been tested. The upper energy limit for the INCL codes falls around 20 GeV/u and is not relevant to the present work.

2.2.4 INCL++ Model Parameters

Because the projectiles for this experiment had masses above 18, INCL++ was run in the inverse-kinematics mode for this analysis. The INCL++ collisions were run with the projectile ^{9}Be and targets ^{30}S and ^{40}S. The fragments were then transformed into the inverse-kinematics frame to give fragment output from the measured 55 MeV/u ^{30,40}S + ^{9}Be reactions. The de-excitation of the cascade remnants was carried out by ABLA07, the default recommended option in the INCL++ package. Unlike the CoMD model, INCL++ does not contain adjustable symmetry energy parameters and thus has not been used in symmetry energy research.

2.2.5 Isotope Production Output

The inclusive or total isotopic distributions of produced fragments from INCL++ are shown in Figures 2.7 and 2.8. Similar to the previously described fragments from the CoMD + GEMINI++ model, the fragment distributions presented here do not have an experimental filter. Simulated INCL++ fragments and neutrons were filtered through an experimental set-up as described in Chapter 4 to be compared to experimental data. Filtered results from these calculations are also described in Chapter 5.

Note that the final fragment distributions are very different for the two projectiles, as expected, except for the light fragments. The predictions from the two models are, in fact,

relatively similar, except that the INCL++ model has a large odd-even staggering for the products from the ^{40}S beam.

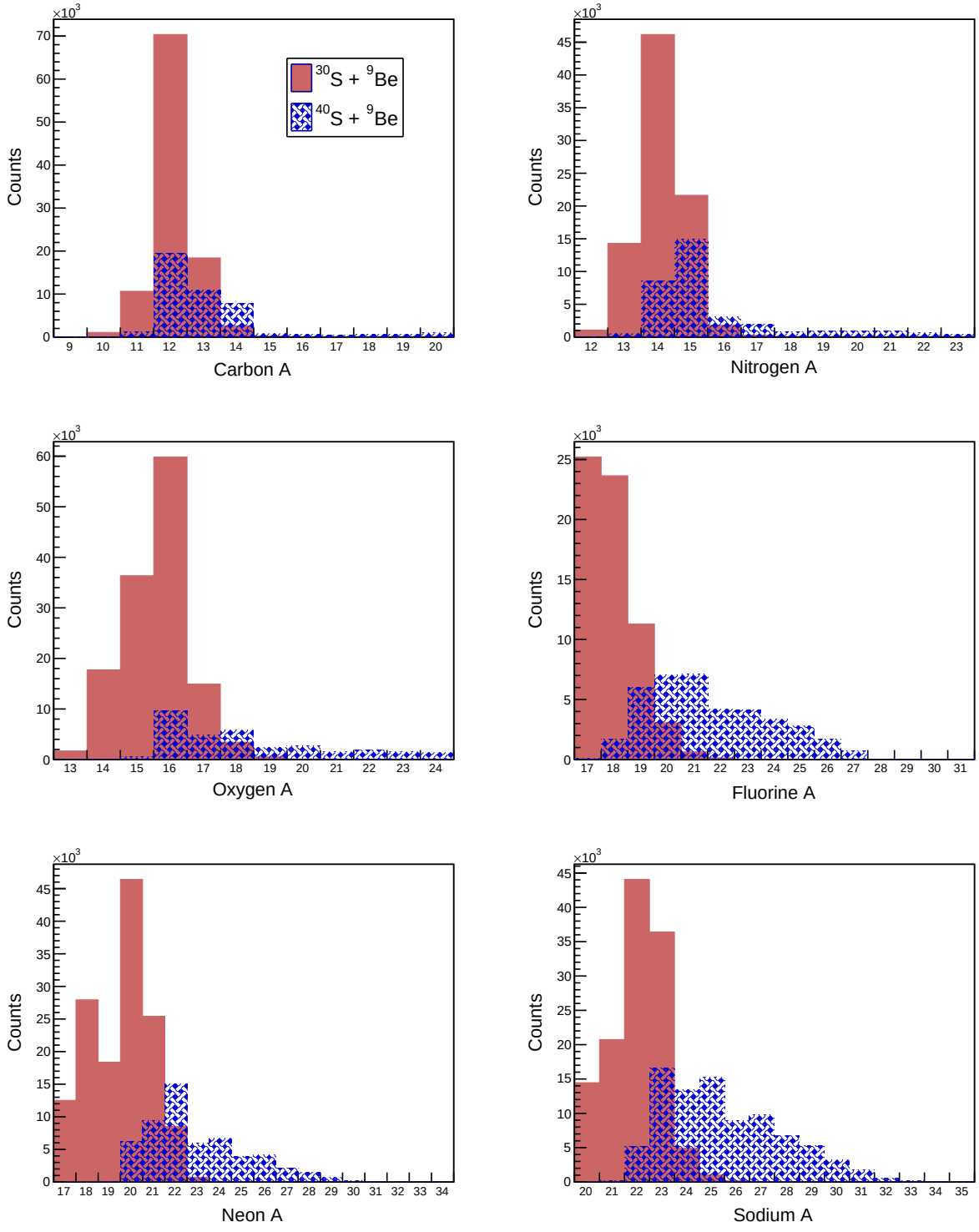

Figure 2.7: Inclusive isotope distributions from INCL++ simulations for elements $Z = 6-11$.

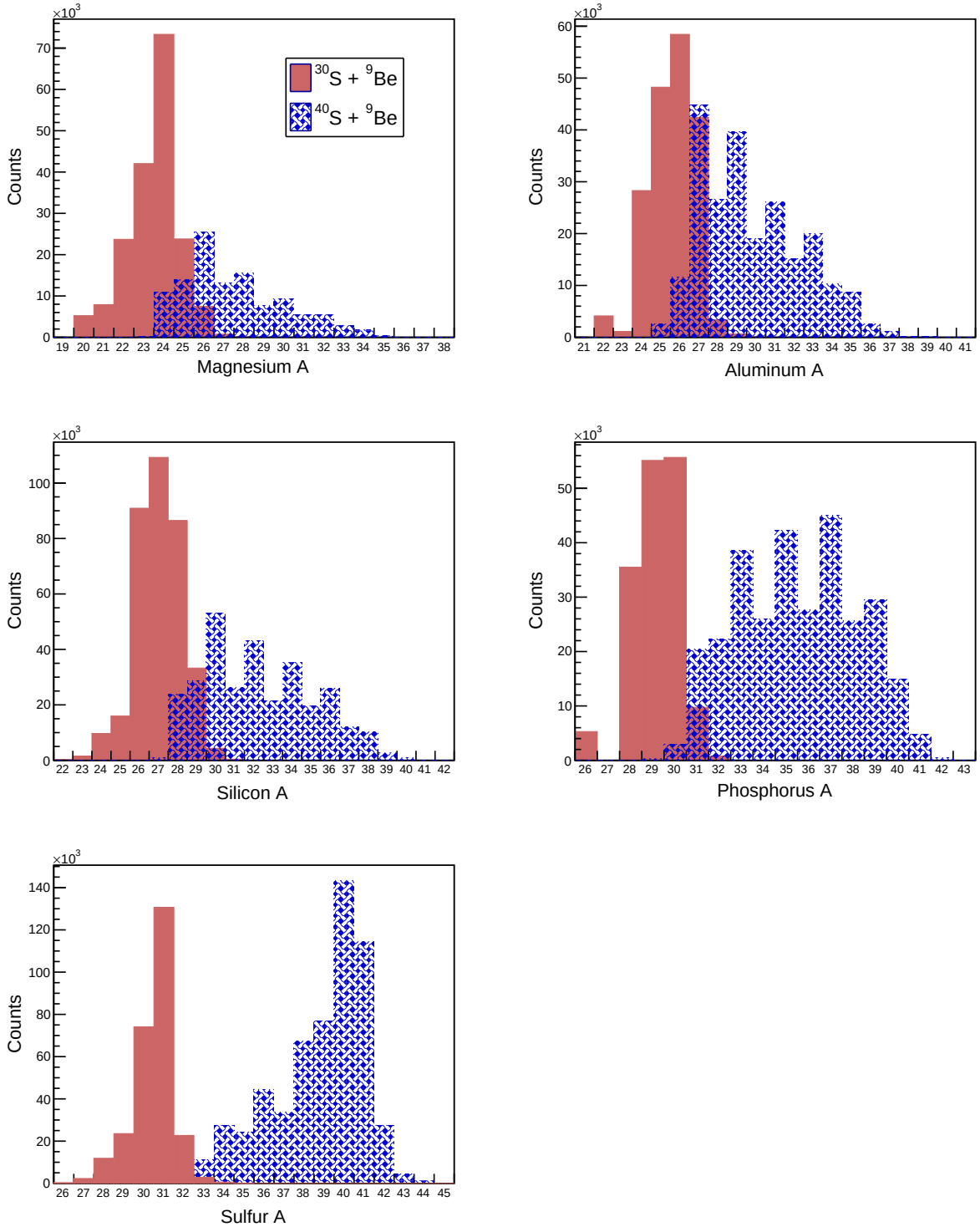

Figure 2.8: Inclusive isotope distributions from INCL++ simulations for elements $Z = 12 - 16$.

Chapter 3

Experimental Techniques

Two projectile fragmentation beams, ^{30}S and ^{40}S, were produced at the National Superconducting Cyclotron Laboratory for this work. The fragments and neutrons resulting from collisions with a ^{9}Be target placed in front of the Sweeper magnet were measured with the MoNA LISA-Sweeper experimental set-up [66–68]. This system used a very large area of plastic scintillators to detect neutrons in coincidence with a series of charged particle detectors to characterize the fragments. The details of the experimental configuration are given in this chapter. Calibrations, measurements, and data analysis are described in Chapter 4.

3.1 Beam Production

The experiment was performed at the National Superconducting Cyclotron Laboratory (NSCL) at Michigan State University. Beams of ^{30}S and ^{40}S were used to provide proton-rich and neutron-rich projectiles on either side of stability, as shown in Figure 3.1, thus allowing a wide range of fragment isospin.

The ^{30}S and ^{40}S beams were produced by projectile fragmentation of stable beams [90] that were accelerated by the Coupled Cyclotron Facility (CCF) [91]. The stable fragments impinged on a ^{9}Be target and resulting fragments were filtered by the A1900 Fragment Separator [92]. A schematic diagram of the CCF and A1900 Fragment Separator is displayed in Figure 3.2.

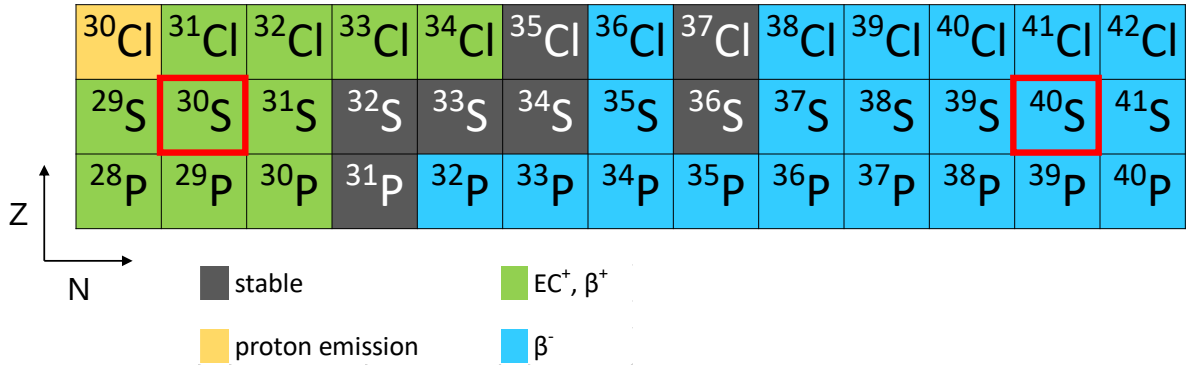

Figure 3.1: A section of the chart of the nuclei showing the isotopes of sulfur. Gray boxes represent stable isotopes, while yellow, green, and blue boxes represent isotopes that decay by proton emission, electron capture or β^+ decay, or β^- decay, respectively. The ^{30}S and ^{40}S isotopes highlighted in the red boxes are the projectiles used in the experiment.

3.1.1 ^{30}S Beam Production

To produce the ^{30}S beam, a primary beam of ^{36}Ar was ionized by an electron cyclotron resonance (ECR) ion source. The resulting $^{36}Ar^{7+}$ ions were injected into the K500 cyclotron and accelerated to 13.06 MeV/u. The ions were sent to the K1200 cyclotron, where they were passed through a stripper foil to remove the remaining electrons. The K1200 cyclotron accelerated the fully ionized $^{36}Ar^{18+}$ to 150 MeV/u.

Upon leaving the K1200 cyclotron, the ^{36}Ar ions were impinged on a beryllium production target with a thickness of 940 mg/cm^2. Collisions in the target induced the projectile fragmentation process and a wide variety of nuclei were produced. To filter out the desired ^{30}S fragments, the produced nuclei were sent through the A1900 Fragment Separator, a 35-meter long device which uses magnetic selection and energy loss in a solid wedge degrader to select individual isotopes. The A1900 Fragment Separator is composed of four dipoles that sort fragmentation products based on their momentum-to-charge ratio, or rigidity ($B\rho = p/q$). Quadrupole magnets placed between the dipole segments refocused the beam.

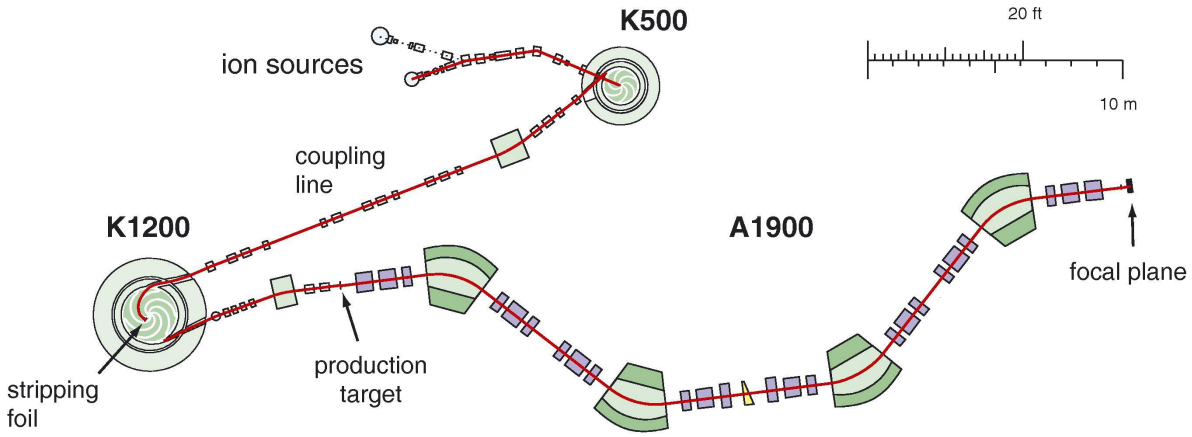

Figure 3.2: Schematic layout of the Coupled Cyclotron Facility and A1900 Fragment Separator. Figure reproduced from [93].

An aluminum wedge with a thickness of 855 mg/cm^2 was placed between the second and third dipoles to separate the isotopes with the same magnetic rigidity. As the different elemental fragments passed through the wedge, they lost energy in proportion to Z^2 [94]. Different element fragments with the same rigidity before the wedge had different rigidities after passing through the wedge. This allowed a second stage of separation in the second half of the separator.

Momentum slits were used to tune the acceptance of the A1900 Fragment Separator. These slits were set to 0.5% momentum acceptance for this experiment. After passing through the A1900 Fragment Separator, the secondary beam fragments were delivered to the experimental vault. Only 32% of the secondary beam was composed of ^{30}S fragments. Major contaminants included ^{29}P and ^{28}Si. These contaminants were excluded from analysis in a procedure described in Chapter 4. The ^{30}S fragments were delivered to the experimental vault at an energy of 55.5 MeV/u and a magnetic rigidity of 2.0403 Tm.

3.1.2 ^{40}S Beam Production

The ^{40}S secondary beam was produced in a similar manner to the ^{30}S secondary beam. A ^{48}Ca source was ionized to produce $^{48}Ca^{8+}$ ions, which were accelerated in the K500 cyclotron to 12.28 MeV/u. Passing through the stripper foil again to remove the remaining electrons, the ions were accelerated in the K1200 cyclotron to 140 MeV/u. The fully stripped ^{48}Ca ions were then impinged on a beryllium production target with a thickness of 1151 mg/cm^2.

Resulting fragments were sent through the A1900 fragment separator, where the dipole magnets, quadrupole magnets, and an aluminum wedge with a thickness of 765 mg/cm^2 were used to filter out unwanted fragments and send the desired ^{40}S fragments to the experimental vault at energy of 55.5 MeV/u and a magnetic rigidity of 2.7201 Tm. The A1900 Fragment Separator momentum slits were set to 0.5% momentum acceptance. While the ^{30}S fragments were accompanied by major contaminants, the ^{40}S beam had a purity of around 98%.

3.2 A1900 and Target Scintillators

A timing scintillator made of 0.125 mm thick BC-404 plastic optically coupled to a photo-multiplier tube (PMT) was placed at the end of the A1900 Fragment Separator to provide a time-of-flight reference signal. After passing through the A1900 fragment scintillator, the ^{30}S and ^{40}S secondary beams were delivered to the experimental vault. A three-dimensional concept drawing of of the experimental equipment is displayed in Figure 3.3 and a top-down view is shown in Figure 3.4. Both figures show the locations of the target scintillator, reaction target, sweeper magnet, and charged particle detectors.

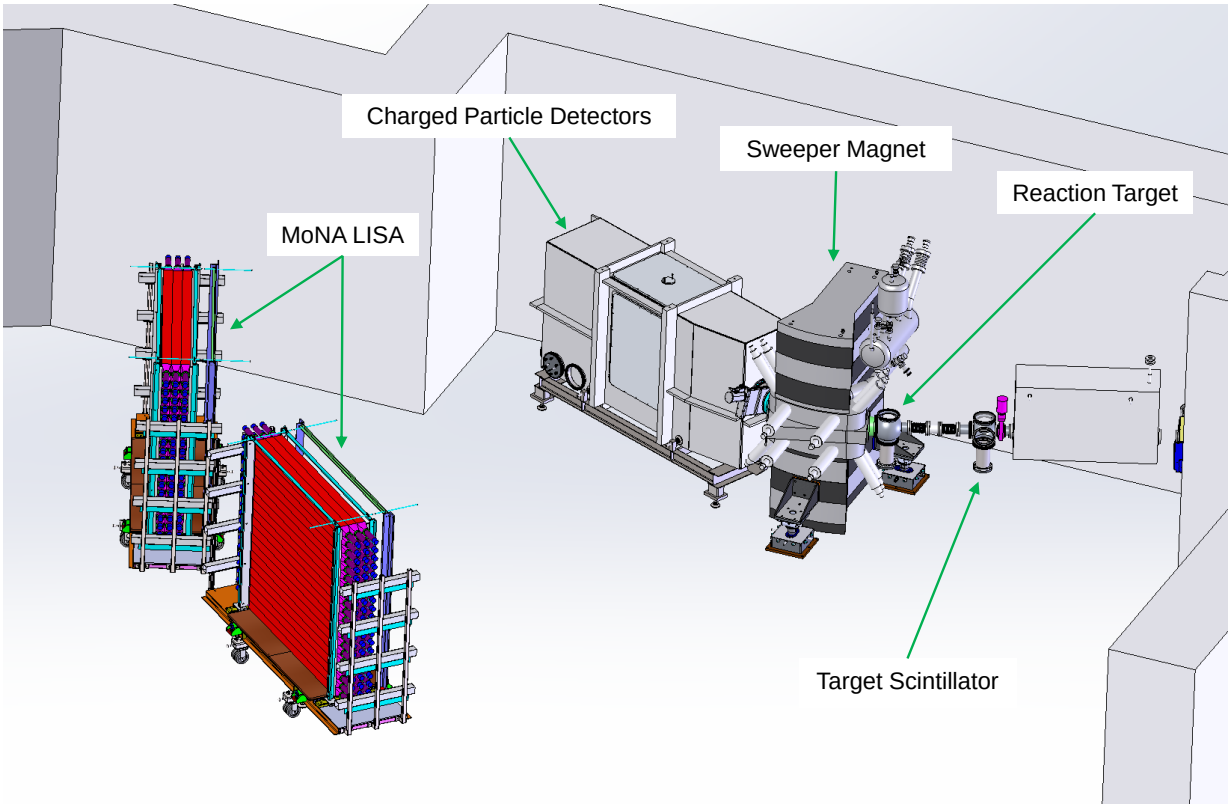

Figure 3.3: Concept mechanical drawing of the MoNA LISA-Sweeper experimental equipment in the vault. Note that only some of the MoNA LISA bars are displayed. Drawing provided by Craig Snow.

Once the beams entered the experimental vault, the beams again passed through a thin plastic timing scintillator referred to as the target scintillator to provide another time-of-flight reference. The target scintillator, placed 1.15 meters before the target, was a 0.254 mm thick BC-404 plastic foil and coupled to a PMT. The secondary beams then entered the target chamber, in which the ^{30}S and ^{40}S fragments were reacted in a 47 mg/cm^2 beryllium target.

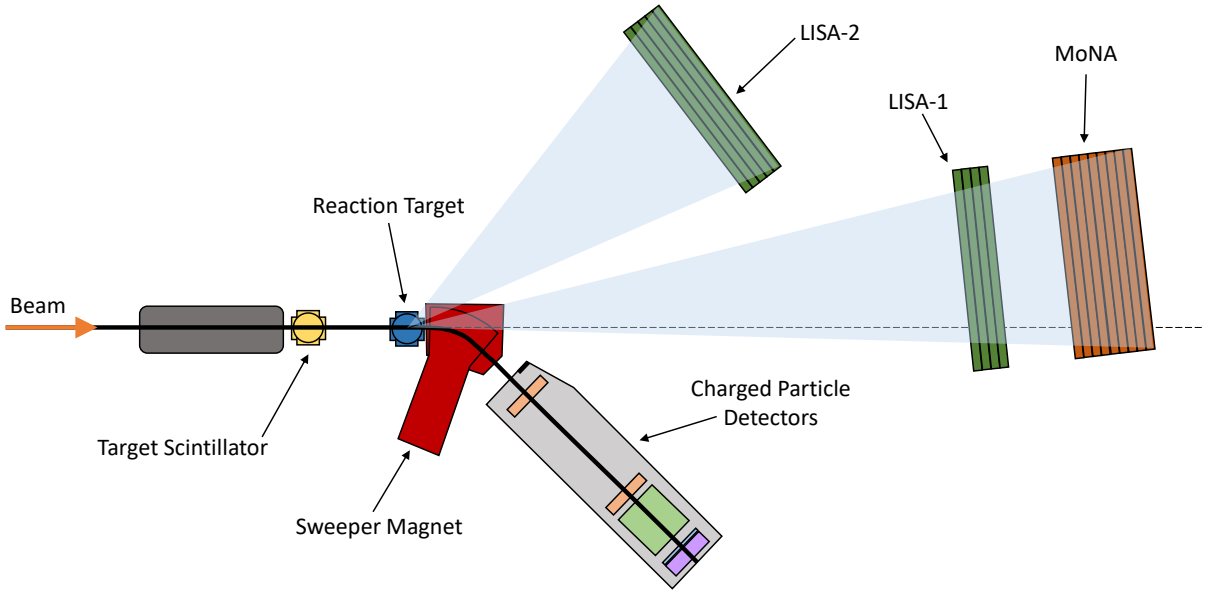

Figure 3.4: Schematic of the MoNA LISA-Sweeper experimental equipment in the vault. See text for details.

3.3 Sweeper Magnet

Charged particle fragments and neutrons from the secondary fragmentation reactions, as well as unreacted beam particles, left the target chamber and entered the Sweeper magnet [68], a large-gap dipole magnet with a bending angle of 43.3 degrees and a bend radius of 1 meter. The Sweeper magnet was designed to bend the trajectories of the unreacted ions and charged reaction fragments away from the original beam axis into a series of charged particle detectors. The neutrons, which were unaffected by the magnetic field produced by the Sweeper, then passed through a 14 cm vertical gap and a 6.4 mm thick steel plate placed at zero degrees before flying towards the MoNA LISA neutron detectors. The steel plate was necessary to maintain vacuum in the magnet gap.

A Hall probe was used to measure the magnetic field strength, which had been previously mapped [95]. During the production runs of this experiment, the magnetic rigidity of the

Sweeper magnet was set to bend the unreacted beam away from the center of the charged particle detectors. This prevented the high beam rate from damaging the charged particle detectors.

To accept a variety of fragments from each secondary beam reaction, two magnet settings were chosen for each secondary beam. For the ^{30}S + ^{9}Be reaction, the Sweeper magnet was set to 1.51 and 2.25 Tm. For the ^{40}S + ^{9}Be reaction, the Sweeper magnet was set to 2.01 and 2.27 Tm. Reaction products falling outside of the Sweeper acceptance, including products with the same rigidities as the unreacted beam, were not measured. After passing through the 47 mg/cm^2 beryllium target, unreacted ^{30}S and ^{40}S beams had rigidities of 1.97 Tm and 2.65 Tm, respectively.

3.4 Charged Particle Detectors

After leaving the Sweeper magnet, the charged fragments entered a large vacuum box containing a series of detectors. The positions and angles of each charged fragment were determined with two Cathode Readout Drift Chambers (CRDCs). Energy loss was measured in an ionization chamber, and the arrival time was measured with a thin plastic timing scintillator. Figure 3.5 contains a layout schematic of the charged particle detectors following the Sweeper magnet.

3.4.1 Blocker

To prevent the unreacted beams from hitting the active area of the CRDCs, a tungsten blocker with dimensions of 24.5 cm × 13 cm × 9.5 cm was inserted at the edge of the active area of the detectors. The blocker was located at the exit of the Sweeper magnet and before

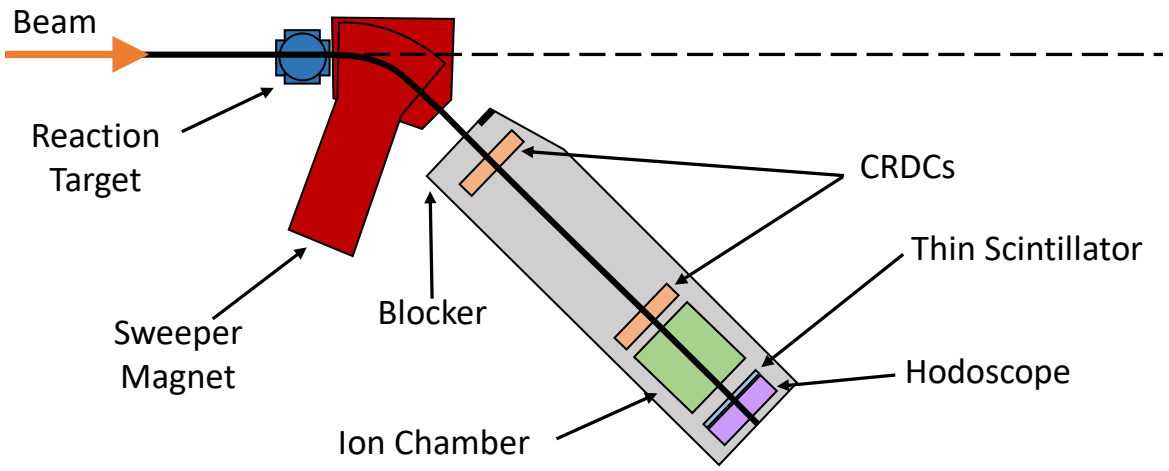

Figure 3.5: Layout schematic of the Sweeper magnet and charged particle detectors. The solid black line indicates the path of the beam. The dashed line represents the path of the unreacted beam if the Sweeper magnet was not present.

the first CRDC in the charged particle array box, as seen in Figure 3.5. The unreacted beam was stopped in the blocker.

3.4.2 Cathode Readout Drift Chambers

Two CRDCs [96] were used in this experiment to measure the X and Y positions of the fragments as they moved through the detector box. The first CRDC was placed immediately after the blocker, 1.72 m downstream from the target. The second CRDC was located 1.55 m after the first CRDC. The full active area for each CRDC was 30 cm $\times$ 30 cm in the XY-plane, though as mentioned previously, one side of the active area of the CRDCs was covered using the tungsten blocker during production runs.

Each CRDC was filled with a gas mix of 20% isobutane and 80% CF_4 at an operating pressure of 40 Torr. The CRDCs acted similarly to two-dimensional ion chambers. Charged particles passed through the detector and produced ionization pairs in the gas. A 1000 V drift voltage was applied between a plate at the top of the detector and the Frisch grid at the

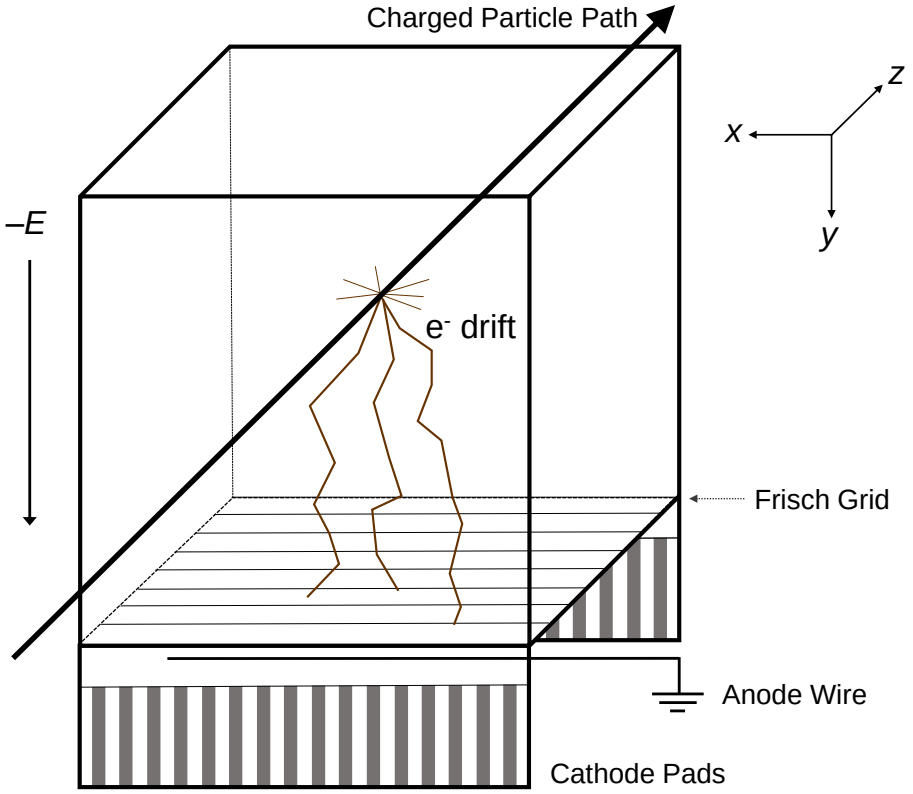

Figure 3.6: Schematic of a Cathode Readout Drift Chamber (CRDC). The Z-direction has been expanded for detail, while the field shaping wires are omitted for simplicity. Figure reproduced from [96].

bottom of the detector, creating an applied electric field and causing the ionization pairs to drift apart. Field shaping wires were placed parallel to the X-direction along the two faces of the CRDC. An anode wire ran below the Frisch grad and parallel to the X-axis. Along the Frisch grid was a series of 116 aluminum cathode pads with a pad pitch of 2.54 mm. The pads were segmented along the X-axis. A schematic diagram of a CRDC is shown in Figure 3.6.

As electrons drifted through the Frisch grid, the strong field caused by the anode wire caused an avalanche of electrons. The X-position of a particle was determined from the induced charge distribution upon the cathode pads. The charge was collected and was then

fit with a Gaussian function. The centroid of the Gaussian function was then taken to be the X-position. The Y-position of a particle was determined by the relative drift time of the electrons to the anode wire. The drift time was measured as the time difference between the thin timing scintillator near the end of the charged particle array box and the signal from the anode wire. Because there was no segmentation in the Z-direction and each CRDC had a relatively small thickness (with an interaction length of about 8.6 cm through the center of the detector), the Z-position was assumed to be the center of the each CRDC. The X and Y positions of the fragment measured in each of the CRDCs was used to determine the angle of its path.

3.4.3 Ion Chamber

Directly downstream of the CRDCs was the ion chamber [96], which was used to determine the energy loss of the charged particles. The ion chamber had an active area of 40 cm $\times$ 40 cm, a length of 65 cm, and was filled with a gas mixture of 90% argon and 10% methane at 300 Torr. The large windows were made of Kevlar filament, 12 µm PPTA, and epoxy. The windows allowed the particles to enter and exit the detector with minimal energy loss. The entrance window had an area of 30 cm $\times$ 30 cm to correspond to the active area of the second CRDC. The exit window was larger, measuring 40 cm $\times$ 40 cm, to account for beam divergence and multiple scattering. A schematic diagram of the ion chamber is shown in Figure 3.7.

Like in the CRDCs, a charged particle passing through the gas of the ion chamber created ionization pairs. The electrons drifted through the detector and passed through a Frisch grid. The electrons were collected on 16 collection pads, which were segmented in the Z-direction

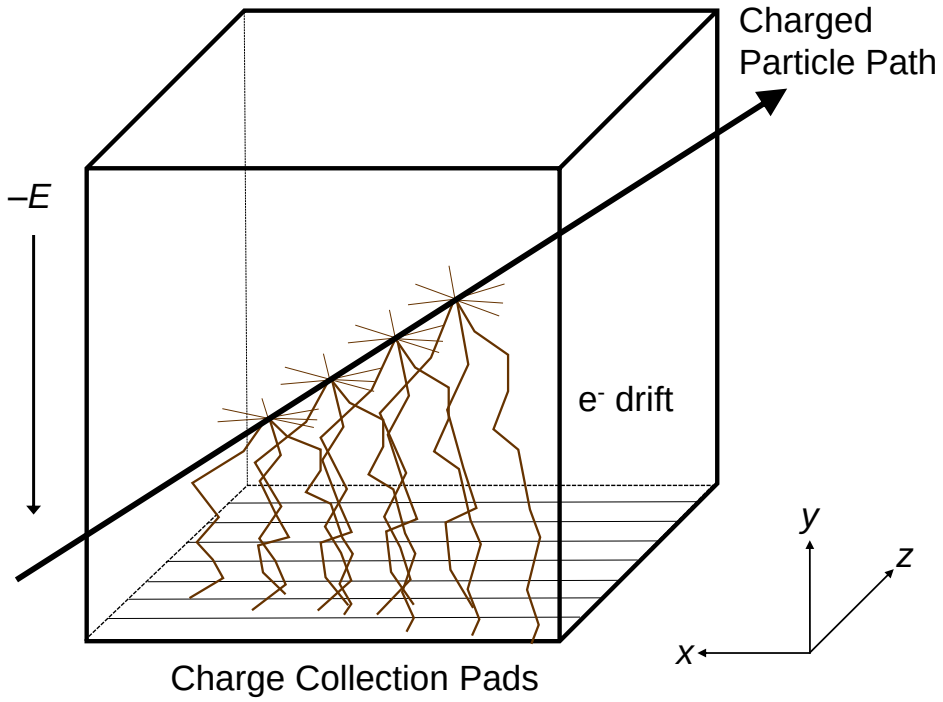

Figure 3.7: Schematic diagram of the ion chamber. Figure reproduced from [97].

and extended parallel to the X-direction. The charge collected on all 16 pads was summed and used to calculate the energy loss in the chamber.

3.4.4 Thin Timing Scintillator

A thin timing scintillator [96,97], located directly after the ion chamber, was used to measure the time-of-flight of the particles and to trigger the data acquisition system. The scintillator was made of EJ-204 plastic and measured 5 mm thick covering 55 cm $\times$ 55 cm in area. Two light guides were attached to the top of the scintillator, while another two light guides were attached to the bottom. Each light guide was optically coupled to a PMT. A schematic drawing of the thin scintillator is show in Figure 3.8.

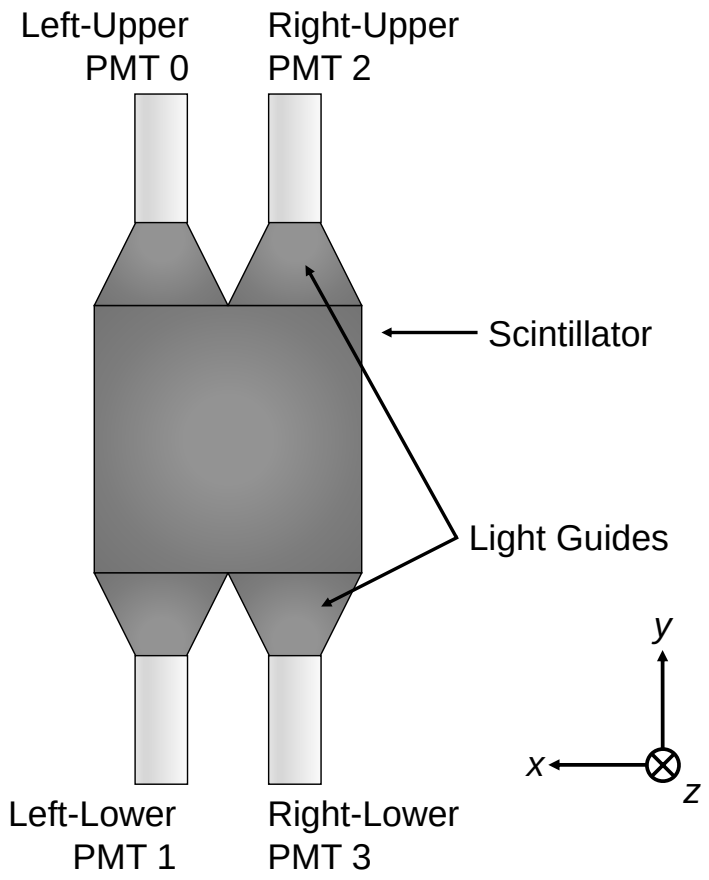

Figure 3.8: Schematic drawing of the thin scintillator while looking in the direction of the beam. Figure adapted from [95].

As a charged particle passed through the thin scintillator, it deposited energy into the organic plastic material. Organic scintillators like the thin scintillator material exploit π-electron structures of the dopant molecules in the plastic. At room temperature, most of the dopant molecules in the plastic were at the ground state. The deposited energy from the charged particle excited π electrons. Some of the highly excited molecules de-excited to the first excited singlet state through internal conversion. Any state with excess vibrational energy quickly thermalized to reach equilibrium with its neighbor. The resulting excited molecules at the first excited singlet state then de-excited to the ground state and emitted

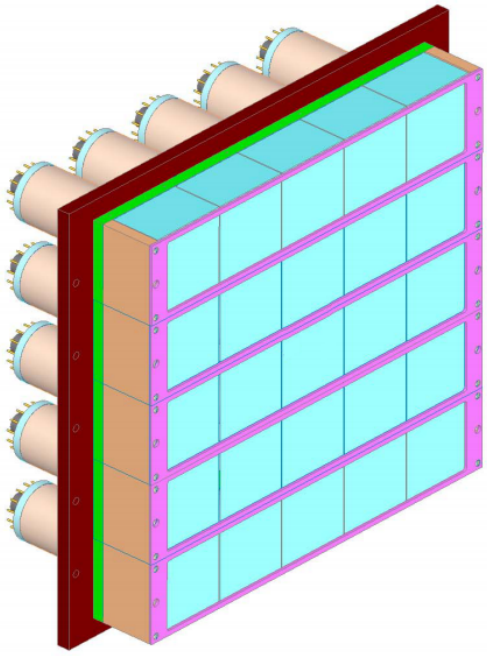

Figure 3.9: Schematic drawing of the Hodoscope CsI(Na) array. Figure taken from [97].

scintillation light. This prompt fluorescence occured with a decay constant of 1.8 ns in EJ-204 plastic. The light was then propagated to the light guides.

3.4.5 Hodoscope

The last component of the charged particle detector array was a CsI(Na) array referred to as the hodoscope [97], which was designed to stop the charged particles and measure their residual energy. The Sweeper hodoscope was similar to the hodoscope used with the S800 Spectrometer [98]. The hodoscope array was composed of twenty-five CsI(Na) crystals, each with a dimension of 3.25 in $\times$ 3.25 in $\times$ 2.16 in. The 25 crystals were arranged in a five-by-five array centered on the beam line. Each crystal was wrapped in 0.2 mm thick reflective material and was optically coupled to a Hamamatsu PMT R1307 with magnetic shielding. A mechanical drawing of the hodoscope is shown in Figure 3.9.

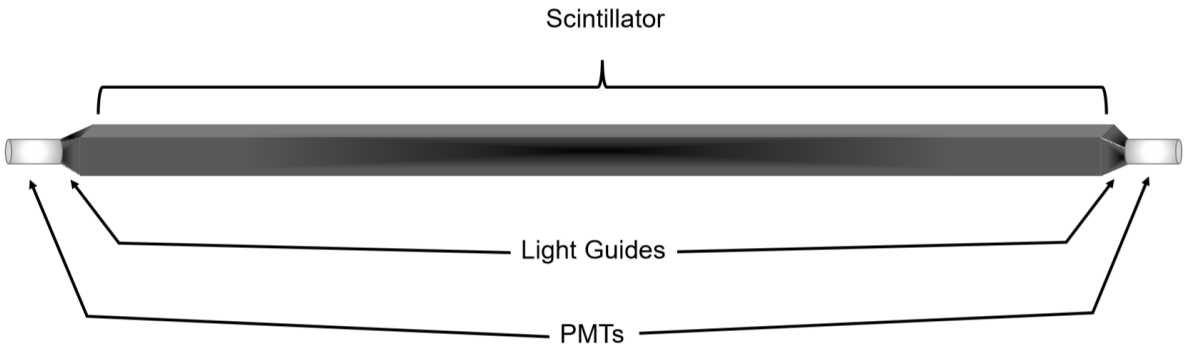

Figure 3.10: Schematic drawing of a single plastic scintillator bar in MoNA LISA.

The crystals were hygroscopic and easily damaged by moisture in the air. A four-sided gas cover was fit to surround the crystals, and a gas inlet allowed the flow of dry air along the face of the crystals when the chamber was not under vacuum. This cover was removed prior to running the experiment.

3.5 MoNA LISA

The positions and times-of-flight of neutrons was measured with the Modular Neutron Array (MoNA) and the Large-area multi-Institutional Scintillator Array (LISA) [66, 67, 99]. Both MoNA and LISA are composed of 144 plastic scintillator bars measuring 200 cm $\times$ 10 cm $\times$ 10 cm. MoNA bars were made of BC-408 plastic and LISA bars were composed of EJ-200 plastic, equivalent plastics from Bicron and Eljen, respectively. Each bar was wrapped in reflective material to reduce light lost and black plastic to prevent ambient light from inducing signals. A schematic of a single bar is shown in Figure 3.10.

As uncharged neutrons passed through the bars, the neutrons scattered on the hydrogen or carbon in the plastic, producing ionization and then scintillation light. Because the neutron-to-hydrogen mass ratio is much larger than the neutron-to-carbon mass ratio, the

recoil is much greater when the neutron interacts with a hydrogen nucleus. Thus, most of the scintillation light output came from neutron on hydrogen scattering reactions. The light was propagated to each end of the bar, where it was collected by a PMT. MoNA used Photonis XP2262/B PMTs and LISA used Hamamatsu R329-02 PMTs. The PMTs turned the light into an electronic signal for recording.

Due to the modular nature of the array, the MoNA LISA bars may be configured in a variety of settings. Bars were stacked 16-high, numbered 0 at the bottom and 15 at the top. Each stack of 16 bars formed a vertical "wall" or layer. Example layers are shown in the concept image in Figure 3.3. The assembled layers were elevated such that the layers were centered on the beam axis, with eight bars falling above and eight bars falling below the beam axis. Each layer was assigned a letter, A-R. For this experiment, the MoNA LISA bars were split among three tables named MoNA, LISA-1, and LISA-2. The MoNA bars were placed in a nine-layer arrangement (MoNA), while the LISA bars were divided into a four-layer table (LISA-1) and five-layer table (LISA-2). Thus, the location of each bar was defined by the bar's table (MoNA, LISA-1, or LISA-2), layer (A-R), and stack-height (0-15). Bar arrangements and labels for each table are shown in Figure 3.11.

The placement of the bars relative to the target is shown in Figure 3.12, where the blue shaded region indicates the acceptance angles for neutron measurement from the target. The center of the first layer of LISA-1 was placed 6.4 m from the target and offset 6 degrees from the beam axis. The MoNA table was placed directly behind the LISA-1 table at a distance of 7.6 m from the target. The LISA-2 table was placed at an angle of 38 degrees with the center of the first layer 4.1 m from the target. The full array covered angles from about -3 degrees to 51 degrees.

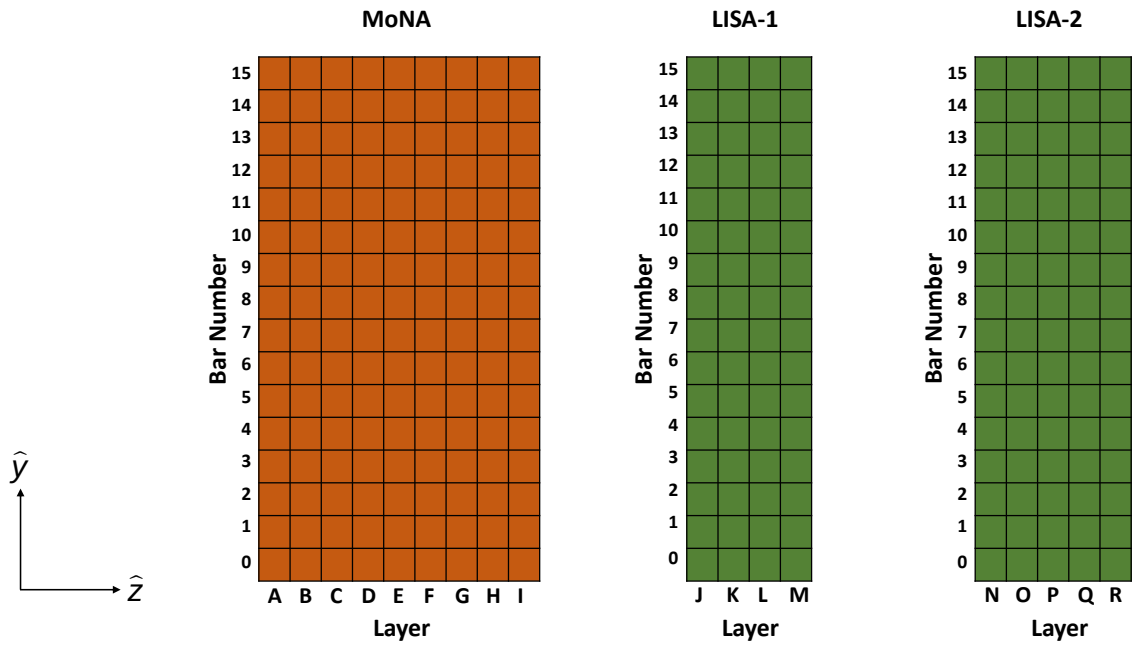

Figure 3.11: Labels for each bar in MoNA LISA as seen from the sides of each table. The front layers for the MoNA, LISA-1, and LISA-2 tables were A, J, and N, respectively.

3.6 Electronics and Data Acquisition

The electronics and data acquisition (DAQ) systems have been described in previous work [80, 95, 97, 100, 101]. A brief overview of the systems is presented here, and a condensed schematic is displayed in Figure 3.13.

MoNA, LISA, and the Sweeper particle detectors were operated as three independent DAQ subsystems. The subsystems were connected to a "Level 3" logic system that generated a system trigger and a "timestamp." The system trigger was produced upon the arrival of a signal measured in the left-upper PMT of the thin timing scintillator. The "timestamp" was a 64-bit word generated by a "clock" in the Level 3 system. The "timestamp" was simply an event tag and not a timestamp in the strict definition as the clock generating the "timestamps" did not run continuously. When the system trigger was generated, the trigger and "timestamp" were sent out to the three subsystems, which would then independently

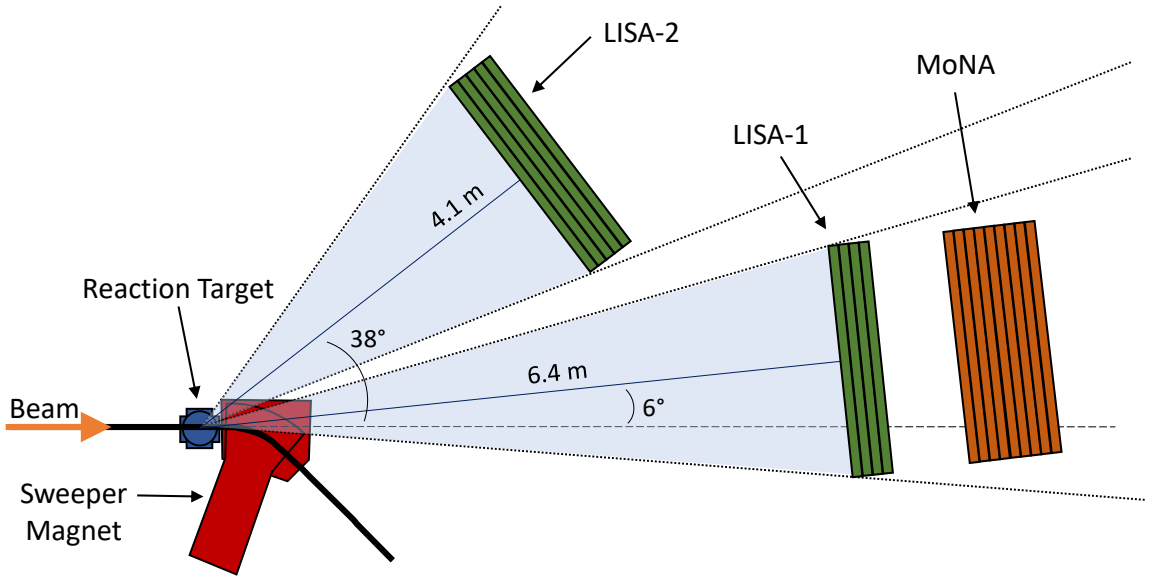

Figure 3.12: Layout schematic of the Sweeper magnet and MoNA LISA detectors. The solid black line indicates the path of the beam. The dashed line represents the path of the beam if the Sweeper magnet was not present. The shaded blue regions and dotted lines represent the acceptance ranges of the neutrons. Angles and distances from the target are given for the front of the LISA-1 and LISA-2 tables.

record the data in their system. Once the data were collected, the three separate subsystem data sets were merged offline by matching the event tag "timestamps." The present experiment was operated in a method in which the system trigger only required a valid signal from the thin scintillator, allowing charged particle fragment events to be recorded regardless of neutron signals from MoNA LISA.

The trigger logic was handled by programmable Xilinx Logic Modules (XLMs) grouped into "levels." One Level 1 module was assigned to each layer (i.e. 16 bars). The Level 1 modules collected the CFD (constant fraction discriminator) hit information for each layer and passed the information on to the Level 2 modules. There were two Level 2 modules with one assigned per array (MoNA and LISA). Figure 3.14 presents an abbreviated schematic of how the Level 1 modules feed into the Level 2 modules for each array.

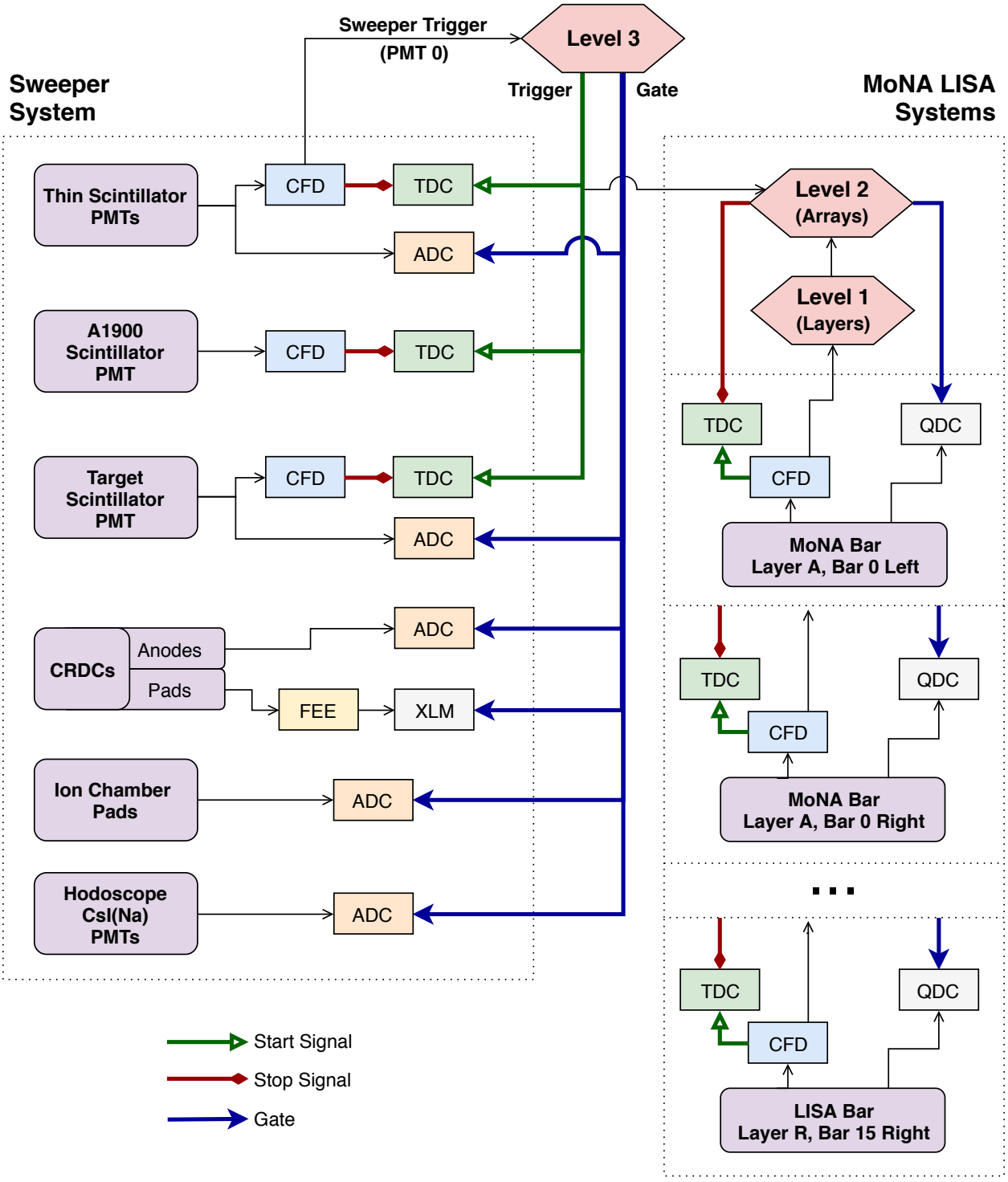

Figure 3.13: Schematic diagram of the MoNA LISA-Sweeper electronics. Start signals, stop signals, and gates are indicated by green open arrows, red closed diamonds, and blue solid arrows, respectively.

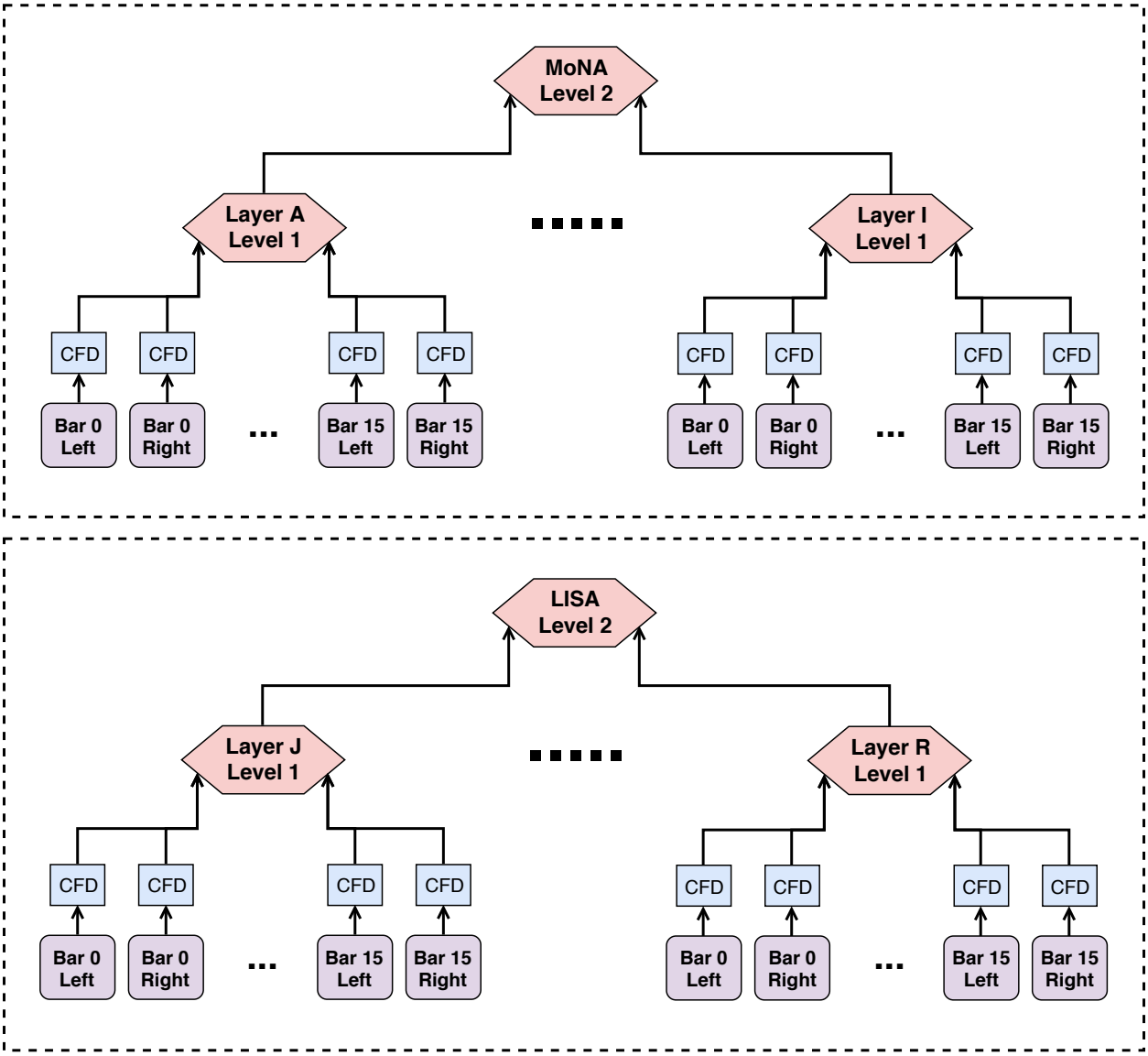

Figure 3.14: Abbreviated schematic diagram of the MoNA LISA electronics. Each Level 1 module represents one layer or layer (bars 0-15). The nine Level 1 modules for each array (A-I for MoNA and J-R for LISA) feed into Level 2 modules. TDCs and QDCs are omitted for simplicity.

The Level 2 modules determined the validity of an event in MoNA or LISA and made a decision about issuing a trigger based on the hit information. For a MoNA or LISA event to be considered valid, the system required light detection and signals in the CFD channels for both PMTs in a single bar. Level 3 held the clock for "timestamps" and handled the coincidence trigger logic between MoNA LISA and the Sweeper. When there was a system trigger, the Level 3 sent a "timestamp" to each of the subsystems and opened a coincidence gate to allow for valid signals from MoNA LISA to be recorded and all signals were read out and processed. If a valid signal was sent, each subsystem processed the event. If there was no valid MoNA LISA signal, the coincidence gate closed and only information from the Sweeper was recorded. If MoNA LISA had a valid signal but the Sweeper had not triggered, MoNA LISA performed a fast clear. Figure 3.15 shows a schematic diagram with examples for processing CFD signals for valid or invalid events.

The Sweeper data acquisition consisted of electronics for each of the CRDCs, ion chamber, timing scintillators, and hodoscope. The outputs from the A1900 timing scintillator, target scintillator, and four thin timing scintillator PMTs were each sent through a CFD and then to a TDC (time-to-digital converter). All TDCs in the Sweeper subsystem were operated in common start mode, in which the Level 3 trigger began the measurement and the timing signals from each individual PMT stopped the measurement. The CRDC pad signals were digitized with Front-End-Electronics (FEE) modules that sampled the pad pulse and sent the pulse to an XLM [96]. The signals from the ion chamber pads were sent through a shaper and then to an ADC (analog-to-digital converter). The hodoscope PMT signals were sent through shaping amplifiers into ADCs.

MoNA and LISA electronics and DAQs were separate but identical. Each PMT had two output signals. The anode signal was used for local triggering and timing. The anode was

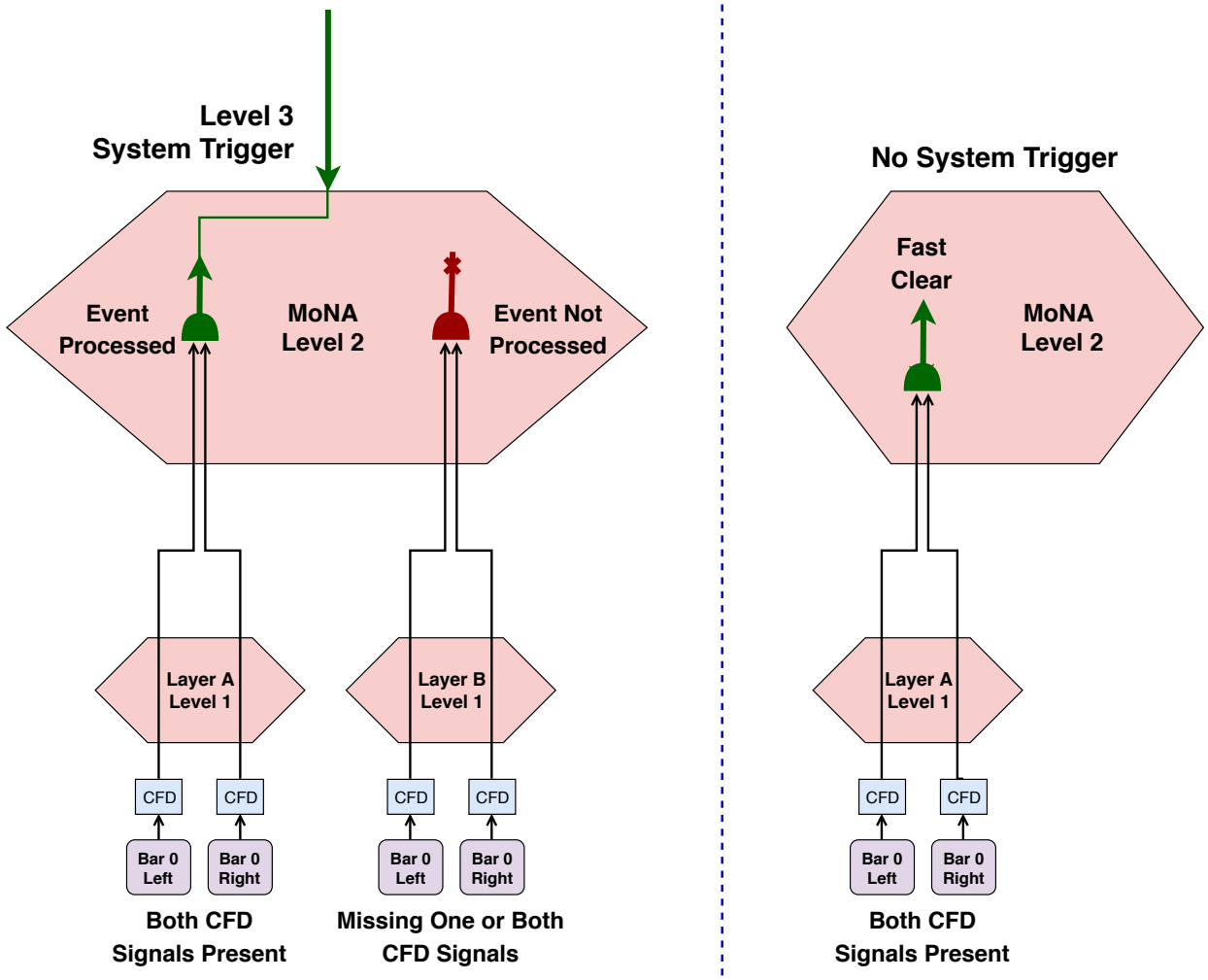

Figure 3.15: Example schematic diagram of determining valid events in the MoNA LISA electronics. Two cases involving a Level 3 system trigger are shown on the left. The first case includes two present CFD signals from one bar. The second case includes at least one missing CFD signal. The right example shows a case in which the two CFD signals are present but there is no Level 3 system trigger. TDCs and QDCs are omitted for simplicity.

sent to a CFD, which then sent outputs to a TDC and XLM. The TDCs were operated in common stop mode, in which a signal from the detector triggered the start of measurement and the Level 3 trigger ended the measurement. The dynode signal was used to measure the charge collected in each PMT. The dynode signal was passed to a charge-to-digital converter (QDC) for integration. Charge and timing information for each PMT was read out by the DAQs from the QDCs and TDCs.

Chapter 4

Data Analysis

Signals from the MoNA LISA and Sweeper charged particle detectors were processed, calibrated, and corrected for non-linear responses. Once the calibrations were completed, events were selected from the data set by isotope for analysis and comparison to the simulated reactions.

4.1 Calibrations and Corrections

4.1.1 Charged Particle Calibrations and Corrections

The detectors used for identifying each charged particle included, in sequence within the detector box, two Cathode Readout Drift Chambers (CRDCs), an ion chamber, a thin scintillator, and a hodoscope, plus the upstream A1900 and target timing scintillators.

4.1.1.1 Cathode Readout Drift Chambers

The CRDCs provided measurements of the X and Y positions of the charged fragments. As discussed in Chapter 3, the CRDC recorded the signals induced on an anode wire and cathode pads for the horizontal position and the drift time for the vertical position [96]. To obtain the actual positions of the fragments, these signals from the CRDCs had to be processed. When a charged particle was measured in one of the CRDCs, the charge read out

included the sum of the charge generated by its movement in addition to the pedestal, or the small current observed on each pad with no beam presence. The pedestal was subtracted pad by pad to determine the charge attributed directly to the detection of the particle. The pedestals were obtained in a data collection run in which no beam was sent through the Sweeper magnet. The pedestals shown in Figure 4.1 appear to have two components, one at approximately channel 250 and another at approximately half of that. However, the intensity of the lower component is less than 5%. The lower component resulted from incomplete electronic signals. The larger value of the charge collected for each pad was then fit with a Gaussian to determine the pedestal value. The pedestal subtraction is shown in Figure 4.1.

Instead of integrating the entire charge collected, each pad in the CRDCs took a number of samples, which were counted and summed to find an approximation of the total charge deposited on the given pad. The total charge on each pad could then be calculated with the following equation:

$$Q_{pad} = \frac{1}{n}\sum_{i=0}^{n} q_i - q_{ped} \tag{4.1}$$

where Q_{pad} was the total approximated charge deposited on the pad, n was the number of samples, q_i was the charge per sample, and q_{ped} was the pedestal charge.

Once the pedestal was determined and subtracted, the pads were gain matched to account for differences in charge collection among the pads. To gain match the pads, a "sweep" run was used. In a sweep run, the unreacted beam was swept across the acceptance area of the CRDCs, sequentially illuminating each pad. One pad in each CRDC was chosen as a reference, and the remaining pads were mathematically matched to that reference. The

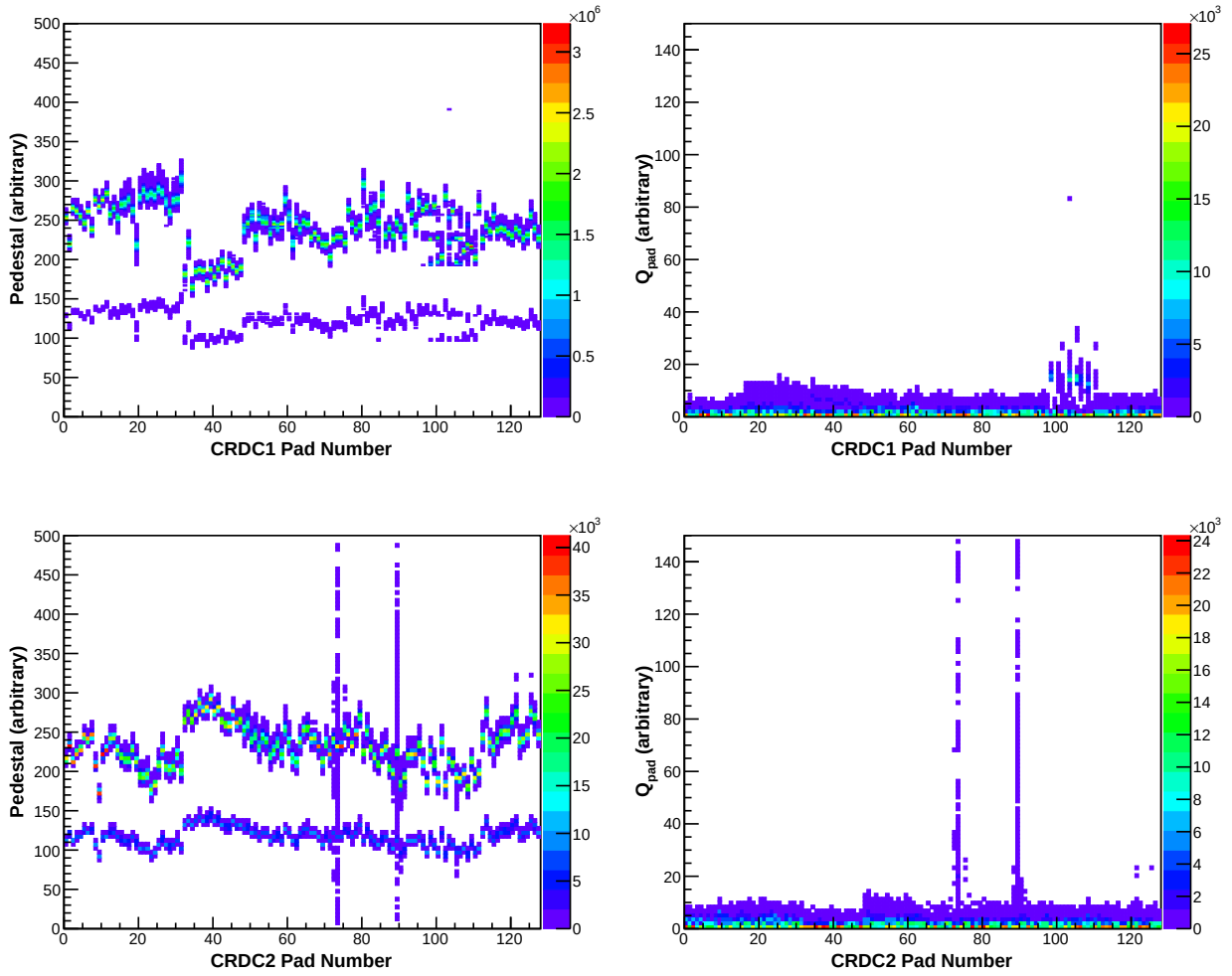

Figure 4.1: Pedestal subtraction in CRDC1 (top) and CRDC2 (bottom). The raw charge prior to pedestal subtraction is shown in the left panels, while the subtraction is shown in the right panels. Vertical lines indicate dead channels in bad pads.

total charge deposited (Q_{pad}) could then be transformed into the gain-matched charge (Q_{cal}) through the following equation:

$$Q_{cal} = \frac{\mu_{ref}}{\mu_i} \times Q_{pad} \tag{4.2}$$

where μ_{ref} was the centroid of the charge on the reference pad and μ_i was the centroid of the charge distribution on the given pad. For both CRDC1 and CRDC2, the reference pad was taken to be a central pad, number 64.

Several of the pads displayed poor response and had to be removed from analysis. These pads appeared to be overly sensitive to electronic noise, showing unusual charge collection when compared to other pads, such as the dead channels seen in Figure 4.1. For CRDC1, bad pads included 98, 100, 103, 105, 106, and 108. For CRDC2, the bad pads were 24, 73, and 89.

The X-position of the charged particle fragment was determined by the charge distribution across the pads. After the total charge collected on each pad was calculated, a Gaussian shape was fitted to each distribution of pad charge, with the centroid taken as the particle's position along the pads. The pad position was then converted to an X-position in mm in the lab frame.

The Y-position of the charged particle fragment was determined by the drift time of the electrons, specifically as the time difference between the charge collection on the anode wire and the detection of the particle in the thin scintillator. The drift time was then converted into a Y-position in mm in the lab frame.

Both the converted X and Y positions were determined through the calibration provided by a "mask." In a masked run, a tungsten mask was placed in front of the CRDC by a hydraulic drive. Each mask had a known set of lines and holes to form the specific pattern seen in Figure 4.2 [102]. The tungsten beam blocker was removed and the incoming beam was defocused and swept across the area of the CRDC mask. Only the beam particles that passed through a hole or line were detected in the CRDC. By knowing the position of the hole or line in the mask, it was possible to transform the signals measured in the CRDC into

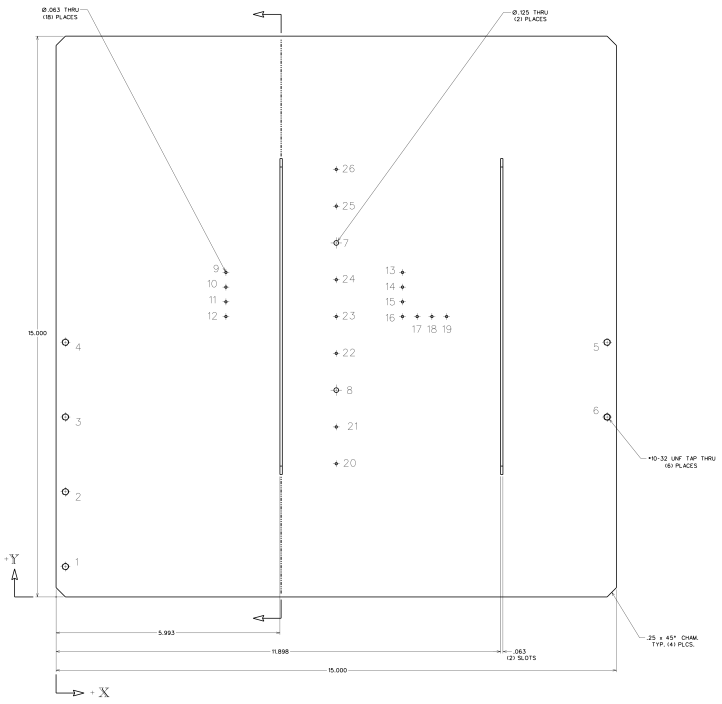

Figure 4.2: Mechanical drawing of a tungsten mask used in the experimental configuration. Each hole corresponded to a specific point in space and each line corresponded to an X-position. Drawing made by J. Honke [102].

a physical position. (The physical positions of the holes and lines and their corresponding positions in each CRDC are given in Appendix B.) An example of data from a calibrated mask run for CRDC2 is shown in Figure 4.3. Note that while the bottom of the CRDC was not fully probed and not every hole was illuminated, enough points were measured to determine the identities of the holes and lines and perform the calibration.

The offsets of the X and Y positions as well as the slope of the Y-position were determined from the linear transformation of the signals from the mask runs and are given in Tables 4.1 and 4.2. The slope for the X-position calibration was determined by the physical pad pitch of 2.54 mm. (Because of the orientations of the two CRDCs, the X-position slopes happened to have opposite signs.) The pad numbers for CRDC1 increase in the positive X-direction

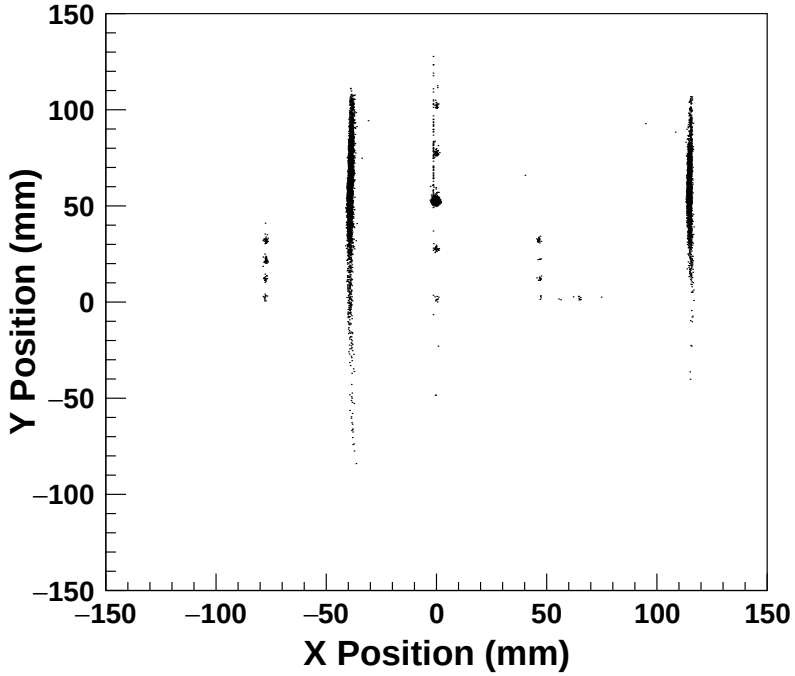

Figure 4.3: Example data from CRDC2 mask run in which the holes and lines in the mask were used to determine the slopes and offsets for the position calibration. This mask run was performed with the ^{30}S beam.

	X Slope (mm/pad)	X Offset (mm)	Y Slope (mm/pad)	Y Offset (mm)
CRDC1	2.54	-181.4	-0.1835	95.8
CRDC2	-2.54	187.2	-0.1889	98.0

Table 4.1: Results for the CRDC mask calibration slopes and offsets for the ^{30}S secondary beam.

in the lab frame, while the pad numbers for CRDC2 increase in the negative X-direction in the lab frame. The negative Y slopes are a result of the collecting electrons drifting upwards to the anodes of each detector.

The hydraulic drive was unable to fully lift the CRDC2 mask at several points during the experiment. This prevented the mask from covering the full active area of CRDC2, as shown in Figure 4.4. There was no evidence of this occurring with the CRDC1 mask. Thus, a "beam-down-center" run was used to find an additional offset in the Y-direction to place

	X Slope (mm/pad)	X Offset (mm)	Y Slope (mm/pad)	Y Offset (mm)
CRDC1	2.54	-178.3	-0.1910	95.0
CRDC2	-2.54	187.6	-0.1932	92.9

Table 4.2: Results for the CRDC mask calibration slopes and offsets for the ^{40}S secondary beam.

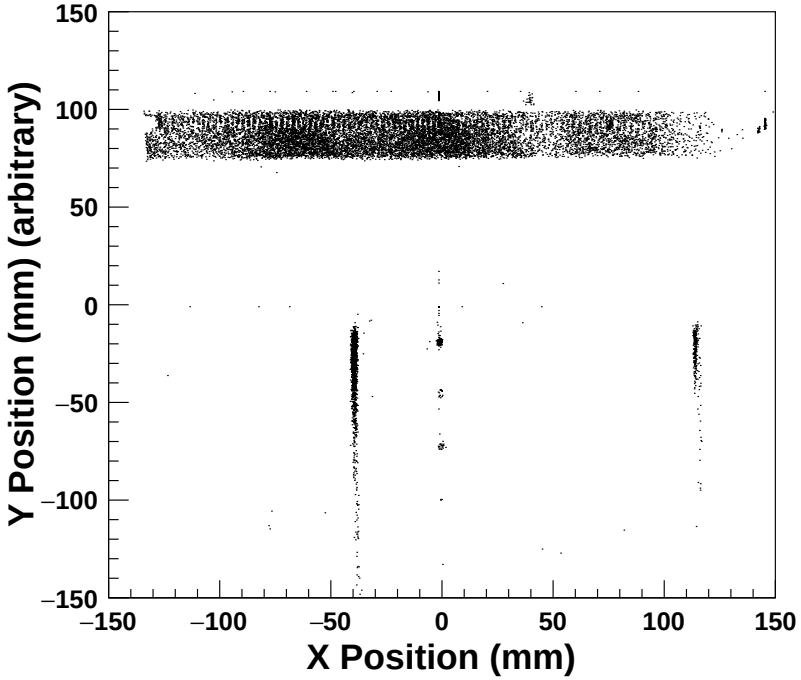

Figure 4.4: Example data from a CRDC2 mask run in which the mask did not fully insert. This mask run was performed with the ^{40}S beam.

the central path of the beam at zero on the Y-axis. Final CRDC slopes and offsets for the ^{30}S and ^{40}S secondary beams are given in Table 4.1 and Table 4.2, respectively.

4.1.1.2 Ion Chamber

The anode of the ion chamber was segmented into 16 strips along the beam path. The 16 pads (numbered 0 through 15) in the ion chamber each collected charge to determine the energy loss of the particle. The pads were gain matched with the ^{30}S and ^{40}S beams

sent through the center of the ion chamber. The calibration procedure assumes that energy loss is fairly uniform throughout the ion chamber. The energy loss in the ion chamber for each beam was calculated by approximating the detector as 65 cm of pure argon gas. The incoming ^{30}S beam lost approximately 114 MeV in the first half of the ion chamber and 121 MeV in the second half of the ion chamber. The incoming ^{40}S beam lost approximately 113 MeV in the first half of the ion chamber and 118 MeV in the second half of the ion chamber.

The charge on each pad was measured and the resulting distribution was fitted with a Gaussian shape. Pad 9 was chosen as a reference pad for comparison to the others. The centroid of the individual pad was compared to the centroid of the reference pad to determine its slope. An example of the Gaussian fits for the reference pad and another pad are shown in Figure 4.5. The calibrated charge on an individual pad was determined as in the calibration of the CRDC pads:

$$q_{cal} = \frac{\mu_{ref}}{\mu_i} \times q_{raw} \tag{4.3}$$

where μ_{ref} was the centroid of the reference pad, μ_i was the centroid of the given pad, and q_{raw} was the raw charge collected on each pad.

Results of gain matching the pads in the ion chamber are shown in Figure 4.6. After gain matching, the centroids of most pads lined up to the reference pad. The white gaps in Figure 4.6 at pads 1 and 8 indicate that the pads were inefficient. Because of their low resulting values, these pads were excluded from further analysis.

Because of unequal charge collection, the ion chamber showed a position dependence that is a variation in charge collected. To correct the observed position dependence, a sweep run was used to move the beam across the active area, illuminating all X-positions. Because

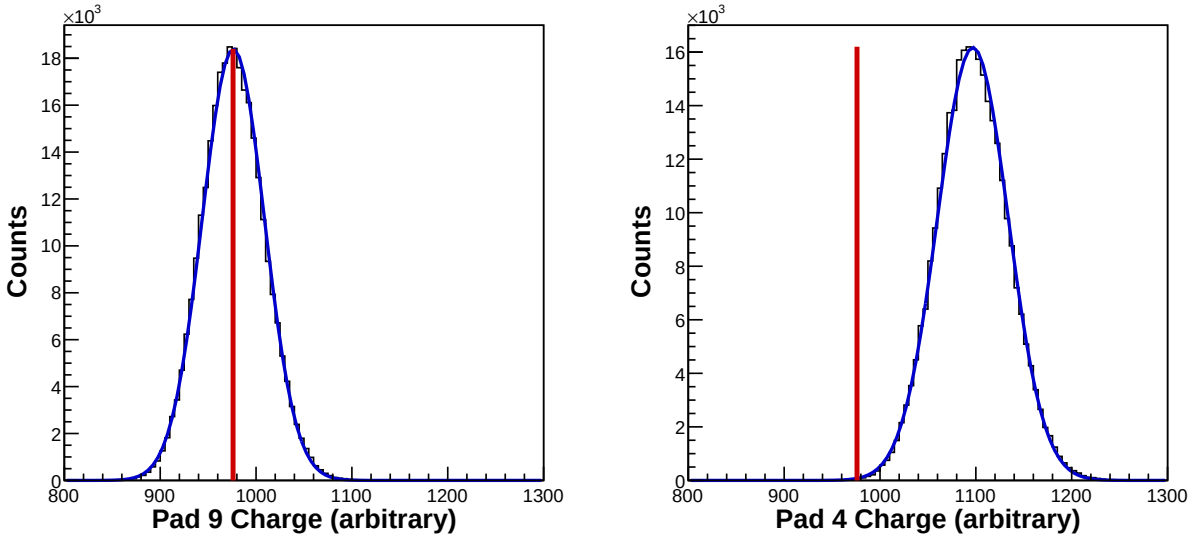

Figure 4.5: Example of the Gaussian fitting procedure used for gain matching the ion chamber. The reference pad, pad 9, is shown in the left, while the charge collected from another example pad is shown on the right. The red vertical line indicates the centroid of the reference pad. The examples were taken from the centered run with the ^{40}S beam.

the beam had the same kinetic energy despite the changing magnet setting, it deposited the same amount of charge at each X-position. The calculated energy loss was plotted against the X-position of the CRDC2 and fit with a polynomial. The dependence was corrected by calculating the position-corrected value:

$$q_{x,pos} = \frac{q_{cal}}{\sum_{i=0}^{4} a_i x^i} \tag{4.4}$$

where q_{cal} was the calibrated charge from Equation 4.3, x was the X-position, and a_i represented the polynomial coefficients for the fit on the given pad. An example of the X-position correction is shown in Figure 4.7.

A slight position-dependence was also observed in the Y-position. A similar method to removing the X-position dependence was applied for removing the Y-position dependence to find a final position-corrected value, q_{corr}:

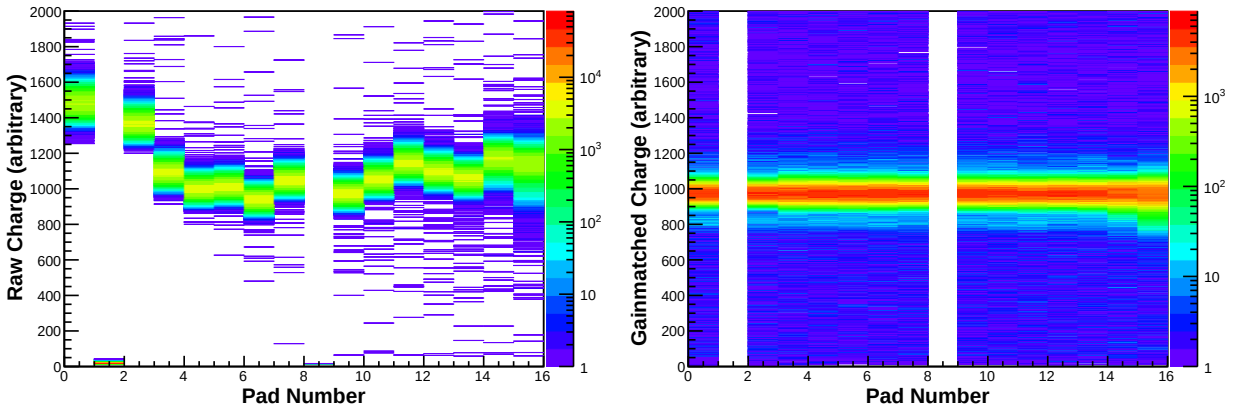

Figure 4.6: Results of gain matching the pads of the ion chamber. Values of the raw charge are displayed on the left, while calibrated charge values are shown on the right. The white gaps for pads 1 and 8 indicate the results of poor charge collection. These results were obtained with the ^{40}S beam.

$$q_{corr} = \frac{q_{x,pos}}{\sum_{i=0}^{3} a_i y^i} \tag{4.5}$$

where $q_{x,pos}$ was the X-position corrected value, y was the Y-position, and a_i represented the polynomial coefficients from the fit for the given pad. An example of the Y-position correction is shown in Figure 4.8.

Thus, once each pad had been gain matched and position-corrected, the total energy loss in the ion chamber was calculated by summing the energy loss recorded on all good pads:

$$Q_{Total} = \sum_{i=0}^{15} q_{corr,i} \tag{4.6}$$

Examples of the resulting distributions of Q_{Total}, i.e. energy loss dE, are shown later in this chapter.

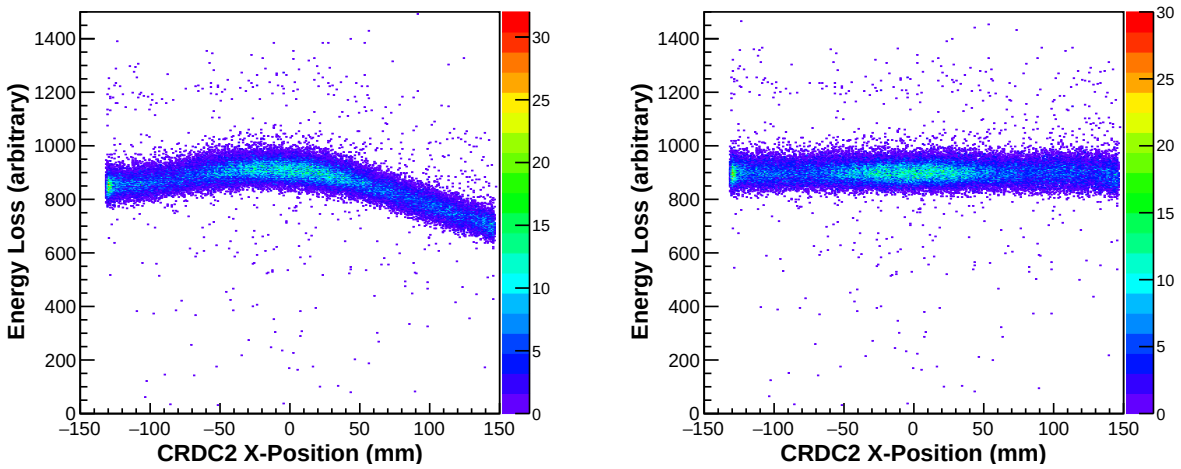

Figure 4.7: Example data for the position dependence correction in the ion chamber for pad 14. On the left is the raw signal as a function of X-position. The right panel shows the position-corrected signal. Signals were taken from the ^{30}S beam.

4.1.1.3 Thin Timing Scintillator

The thin scintillator provided an important reference for the time-of-flight of the charged particle fragments. The thin scintillator was located near the end of the beam line and was connected to four photomultiplier tubes (PMTs), with two attached to the bottom and two attached to the top. Each PMT was labeled with a number and its relative location on the thin scintillator. The PMTs measured total charge collected and the time of collection.

Signals from each PMT were gain matched and combined to create calibrated time and charge measurements. Similar to gain matching the ion chamber, a centered beam was sent through the thin scintillator. A gate on position was placed to select events measured in the center of the detector (-10 to 10 cm in the X-direction and -10 to 10 cm in the Y-direction). The position on the thin scintillator was determined by projection from positions of the CRDCs. The charge signals were fit with a Gaussian, and the slope was determined by comparing the widths of each Gaussian fit to the reference width from PMT 3. The centroids were used to calculate the offset required to place all centroids at the same charge

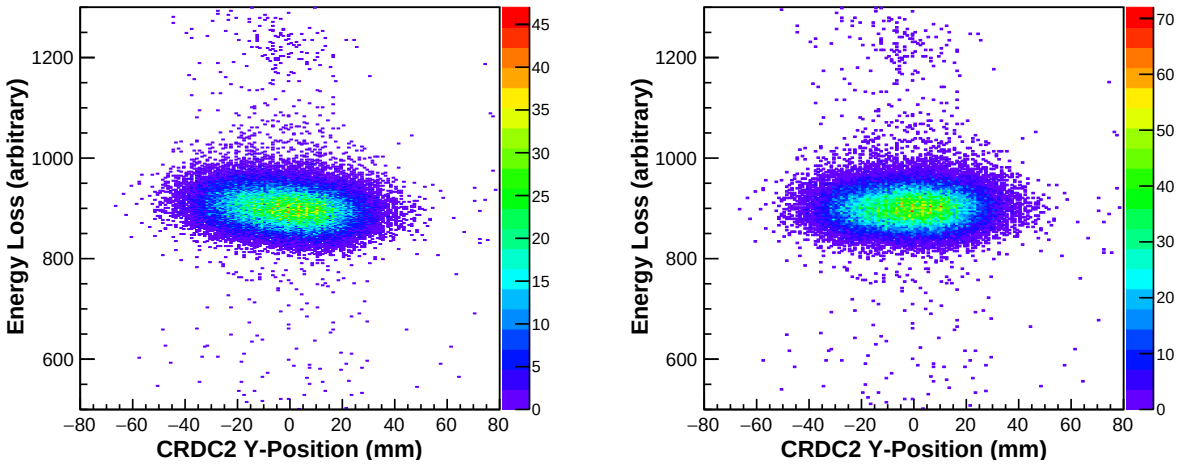

Figure 4.8: Example data for the position dependence correction in the ion chamber for pad 14. On the left is the X-position corrected energy loss as a function of Y-position. The right panel shows the position-corrected signal. Signals were taken from the ^{30}S beam.

position. The calibrated charge for the individual PMT could then be calculated with the following equation:

$$q_{cal} = \frac{\sigma_{ref}}{\sigma_i} \times q_{raw} + q_0 \tag{4.7}$$

where σ_{ref} was the Gaussian width of the reference PMT 3, σ_i was the Gaussian width of the given PMT, q_{raw} was the raw charge, and q_0 was the offset. Figure 4.9 shows the charge collected on each individual PMT before and after gain matching.

Once all four PMTs were gain matched, their signals were combined to determine the total deposited charge, q_{total}:

$$q_{top} = \frac{q_{LU} + q_{RU}}{2} \tag{4.8}$$

$$q_{bottom} = \frac{q_{LD} + q_{RD}}{2} \tag{4.9}$$

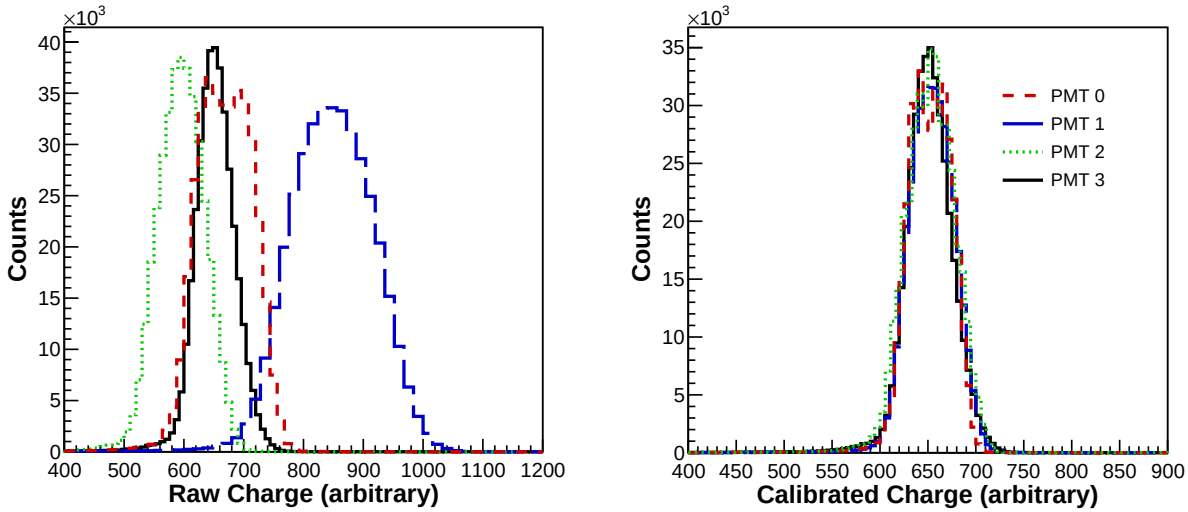

Figure 4.9: Results of gain matching the four thin scintillator PMTs. Raw charge is displayed on the left, while the gain-matched charge is shown on the right. This gain matching was performed with the ^{40}S beam.

$$q_{total} = \frac{\sqrt{q_{top}^2 + q_{bottom}^2}}{2} \tag{4.10}$$

In the above equations, q_{LU}, q_{LD}, q_{RU}, and q_{RD} represent gain-matched signals from the left-upper (PMT 0), left-lower (PMT 1), right-upper (PMT 2), and right-lower (PMT 3) PMTs, respectively.

The observed light intensity from the four PMTs depended on where the fragments interacted within the scintillator. If uncorrected, fragments with the same energy but different flight paths would be read as having different energy losses. To correct for the position dependence, the beam was swept horizontally across the active area of thin scintillator. The combined energy loss was plotted against the X-position in the thin scintillator as projected from the CRDCs and fit with a polynomial function to correct the position dependence. The final corrected total charge, q_{corr}, was calculated with the following function:

Coefficient	^{30}S	^{40}S
a_0	359.486	380.132
a_1	-0.0266998	-0.0264493
a_2	-1.33152×10^{-3}	-1.20136×10^{-3}
a_3	-4.32671×10^{-6}	-3.68012×10^{-6}
a_4	2.58745×10^{-8}	2.29955×10^{-8}

Table 4.3: Coefficients for the thin scintillator position corrections used in Equation 4.11.

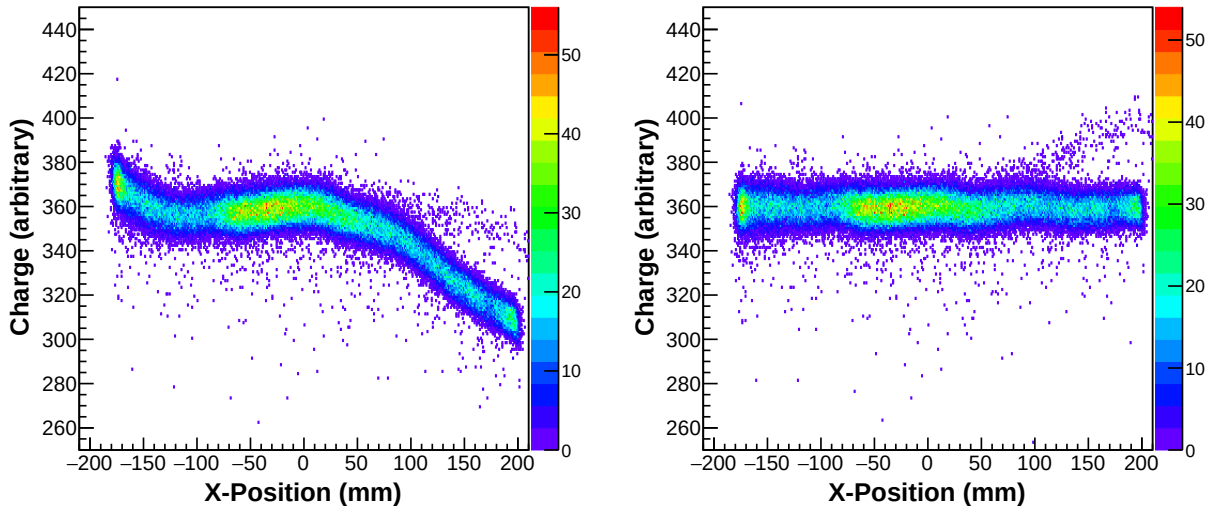

Figure 4.10: Correction of the position dependence in the thin scintillator. On the left is raw charge signal as a function of the X-position. The right panel shows the position-corrected signal. Signals were taken from the ^{30}S beam.

$$q_{corr} = \frac{q_{total}}{\sum_{i=0}^{4} a_i x^i} \tag{4.11}$$

where q_{total} was the total charge found in Equation 4.10, a_i represented the polynomial coefficients, and x was the X-position. Figure 4.10 shows the energy loss in the thin scintillator before and after the position correction for the ^{30}S beam. There was no noticeable dependence in the Y-direction when looking at the corrected charge as a function of Y-position, as shown in Figure 4.11. The coefficients for the ^{30}S and ^{40}S beams are given in Table 4.3.

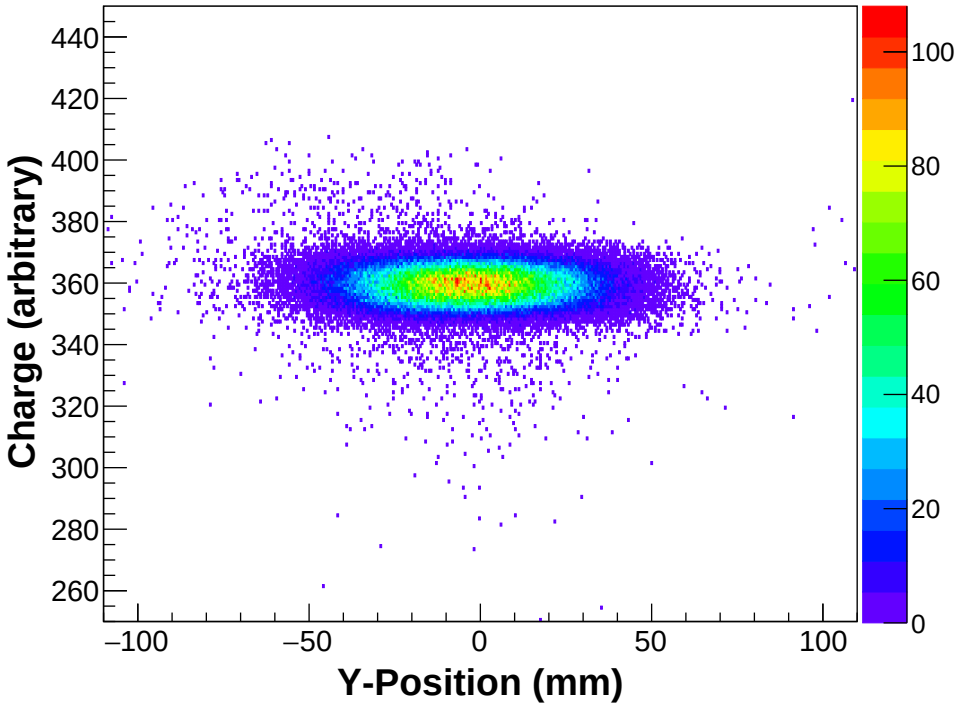

Figure 4.11: X-position-corrected signal versus the Y-position in the thin scintillator. No noticeable dependence is observed. Signals were taken from the ^{30}S beam.

Only an offset was used to calibrate the time signals from each PMT. Because the range of the TDC was fixed, with a range of 400 ns and 4096 channels, the slope of the TDC was assumed to be 0.1 ns/channel. A jitter was introduced into the TDC common stop signal by the processing in the Field Programmable Gate Array (FPGA) in the Sweeper electronics. While the jitter was around 20 ns, the exact jitter value varied by each event, requiring the jitter to be eliminated event-by-event. Because the same stop signal was used for all TDCs, the jitter was the same for each timing signal. The jitter can be eliminated by subtracting one timing signal from remaining timing signals within an event. In this experiment, the timing signal from the thin scintillator left-upper PMT was subtracted from the remaining timing signals. To allow for different TDC ranges, this subtraction was done after the slopes were applied.

Name	PMT No.	^{30}S Offset (ns)	^{40}S Offset (ns)
Left-Upper	0	42.37	42.37
Left-Lower	1	-42.854	-38.437
Right-Upper	2	-53.604	-53.537
Right Lower	3	-14.244	-13.877

Table 4.4: Thin scintillator time offsets.

The centered beam was also used with the thin scintillator to determine the time offsets for each PMT. Fragments outside the center of the scintillator were excluded for determining the time offsets. The flight-path distance from the target to the thin scintillator was 419.9 cm. The ^{30}S and ^{40}S beams had kinetic energies of 55.5 MeV/u. Thus, the calculated time-of-flight for the unreacted beams to travel from the target to the thin scintillator was 42.4 ns. The reference PMT 0 was set to this time, and all thin scintillator PMT timing signals were offset to match that value. Each offset was selected such that the centroid of each PMT aligned with the signal from the reference time-of-flight of the unreacted beam. The time calibration offsets for each PMT for each beam are listed in Table 4.4. Once the individual offsets were determined, the final calibrated timing signal for the thin scintillator was calculated from the average of each PMT:

$$t_{thin} = \frac{1}{n}\sum_{i=0}^{n} t_i \tag{4.12}$$

where n was the number of PMTs that recorded for a given event and t_i were the time signals from each PMT.

4.1.1.4 Hodoscope

The final detector in the detector box was a CsI hodoscope made up from a 5 x 5 array of crystals. The hodoscope was designed to measure the residual energy of the fragments. Prior to this experiment, it was found that the hodoscope was malfunctioning. As detailed in [101], a ^{20}O beam was swept across the faces of the crystals in the center row of the hodoscope. Each crystal in the middle row of the hodoscope displayed a non-uniform response, indicating uneven light collection and poor signal quality.

Further inspection of the crystals showed that the teflon wrapping had stuck to the crystals, possibly due to moisture condensing between the teflon and hydroscopic CsI(Na) crystals. The teflon attachment to the crystals potentially allowed light leaks, affecting signal quality in the hodoscope. Because the problems were not fixed prior to this experiment, the hodoscope was not used for this analysis.

4.1.1.5 A1900 and Target Timing Scintillators

The time offsets for two other upstream timing scintillators were also determined for each beam. The TDCs for both scintillators covered a range of 400 ns with 4096 channels, resulting in a 0.1 ns/ch fixed slope. Once the TDC channel was converted to time, the FPGA jitter was subtracted, as explained before.

To determine the offset, the secondary ^{30}S and ^{40}S beams were sent through the center of the system and the time signals were recorded. Both beams had energies of 55.5 MeV/u as determined by the magnetic rigidity in the A1900. The flight path from the A1900 scintillator to the target was 10.88 m, and the flight path from the target scintillator to the target was 1.15 m. Thus, the time-of-flight for the beams to travel from the A1900 to the target scintillator was 98.15 ns, while the time-of-flight from the target scintillator to the

Scintillator	^{30}S Offset (ns)	^{40}S Offset (ns)
A1900	-108.5	-107.9
Target	65.0	64.9

Table 4.5: Calculated timing offsets for the A1900 and target scintillators.

target was calculated to be 11.60 ns. The offsets were applied to adjust the time signals to correspond to the calibrated time at the thin scintillator. The resulting timing offsets for the A1900 and target scintillators are given in Table 4.5.

4.1.2 MoNA LISA

The MoNA LISA plastic scintillators were used to observe neutrons in coincidence with the charged particles from the reaction. The array was made up from bars of BC-408 (MoNA) and EJ-200 (LISA) scintillator that were 10 cm $\times$ 10 cm $\times$ 200 cm each with a photomultiplier tube (PMT) on each long end. Each MoNA LISA PMT gave a raw signal for charge and time based on the total light collected by the PMT and the arrival time of light. These signals were calibrated to determine the deposited charge, position of interaction in the bar, and time interaction in the bar using cosmic rays. Cosmic ray data collection was performed prior to the experiment. Cosmic ray muons traveled at a velocity close to the speed of light, depositing about 2.05 MeV per centimeter as they passed through the plastic bars [103]. The cosmic ray muons deposit approximately 20 MeVee of light into the bar, where 1 MeVee is equivalent to the light deposited by an electron with 1 MeV of kinetic energy. The known velocity of the muons was used to determine the relative timing of the bars.

4.1.2.1 Charge Calibration

Note that PMTs in general vary in sensitivity as a function of applied voltage. If one PMT is more sensitive than another, flashes of light emitted at different positions along the bar will not be detected with uniform efficiency. For example, if a weak light flash occurs near a more sensitive PMT, that PMT has a better chance of detecting the light, while a less sensitive PMT may not detect the light. Because both PMTs must detect light to accept and record an event, this non-uniformity could skew the data towards one side of the given bar. To minimize this issue and calibrate for charge signal, the PMTs were gain matched by adjusting the applied voltages to put the cosmic ray muon peaks to roughly channel 900 out of 4096. The gain-matching process was iterated until cosmic ray muon peaks aligned and voltage fluctuations in each individual PMT were below 10 V from the penultimate gain-matching run to the final gain-matching run. In this experiment, the final voltages of the PMTs ranged from around 1250 to 1930 V.

The charge signals were checked with a second set of cosmic data taken with gain-matched PMTs. A pedestal, or a small offset, was observed in every QDC channel while the electronics were running. The pedestal also caused every QDC channel to be read out for every charged particle event even if the bars did not detect a valid interaction, resulting in significant data collection dead time. To offset the pedestal so that channel 0 would correspond to 0 MeVee, a linear calibration transforming the channel number to MeVee was used to match the pedestal to 0 MeVee and the cosmic muon peak to 20 MeVee. Thus, the QDC calibrations were performed with the following relation:

$$q_{cal} = m_q \times (q_{raw} - q_{ped}) \tag{4.13}$$

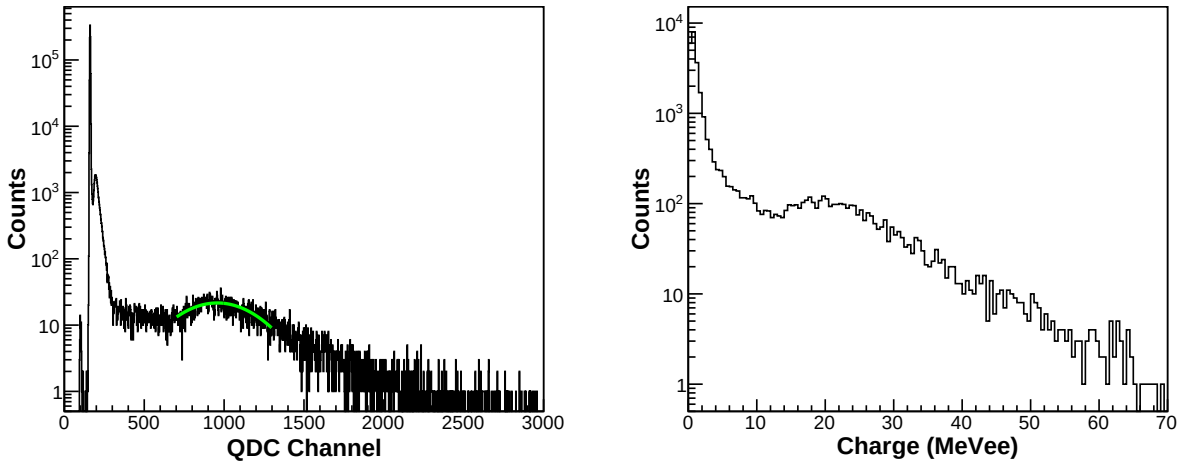

Figure 4.12: An example of the QDC calibration procedure for MoNA LISA. The data shown is from the left PMT from Layer K, Bar 8. On the left is the raw charge from each QDC channel. The cosmic peak around 1000 is fit with a Gaussian function (green). The right panel shows the calibrated charge spectrum with the pedestal subtracted.

where m_q was the QDC slope in MeVee/channel, q_{raw} was the raw QDC channel, and q_{ped} was the pedestal channel. An example of this charge calibration procedure is shown in Figure 4.12.

Furthermore, to suppress the pedestal and decrease dead time, a hardware threshold was applied slightly above the pedestal. The threshold (q_{thresh}) was calculated with the following equation:

$$q_{thresh} = \frac{q_{ped}}{16} + 2 \tag{4.14}$$

The factor of 16 was used to convert the pedestal channel from a 12 bit scale to an 8 bit scale as the pedestal and threshold were stored as 12 bit and 8 bit numbers, respectively. The addition of two ensured that the threshold was set above the pedestal. With a threshold in place, only channels with a signal greater than the threshold were included in the data. The thresholds for this experiment ranged from 0.38 to 0.85 MeVee.

4.1.2.2 Position Calibration

The MoNA LISA bars were stacked to cover a wide range of neutron emission angles in the fragment reference frame and thus had fixed spatial coordinates in two directions. The third coordinate, or the point of interaction along the length of the bar, was found by measuring the relative arrival time of the light pulse at each end of the bar. When an interaction occurred within a bar, light traveled by total internal reflection to each end of the bar and into each PMT. Because light travels at a constant speed in the plastic, the difference in arrival times can be used to calculate the position of the interaction.

The TDC channel readout was converted into a time. Since the time difference between the PMTs on a neutron detector was used to calculate the neutron position in space, the time spectrum of each bar was calibrated individually. The slope was found with a "pulser," an Ortec NIM Time Calibrator module (model 462) that pulsed the system every 40 ns over a TDC range of 350 ns. This created a "picket-fence" spectrum with a peak at every 40 ns interval, as shown for example in Figure 4.13. The first peak was assigned a time of 40 ns; the second peak was assigned a time of 80 ns; and so forth. The calculated slopes were approximately 0.085 ns/channel.

Once the TDC slopes were determined, the time difference between the two PMTs in a bar could be converted into a position along the bar. Cosmic rays interacted in the plastic along the full length of the bar. Each bar was 200 cm long, with the center of the bar marked as 0 cm and the ends defined at -100 cm and 100 cm. The edges of the time difference spectra were adjusted so that the midpoint of the fall-off landed at the ends of the bar, and a linear slope calculated from the two edges was used to find an offset to place the center of the

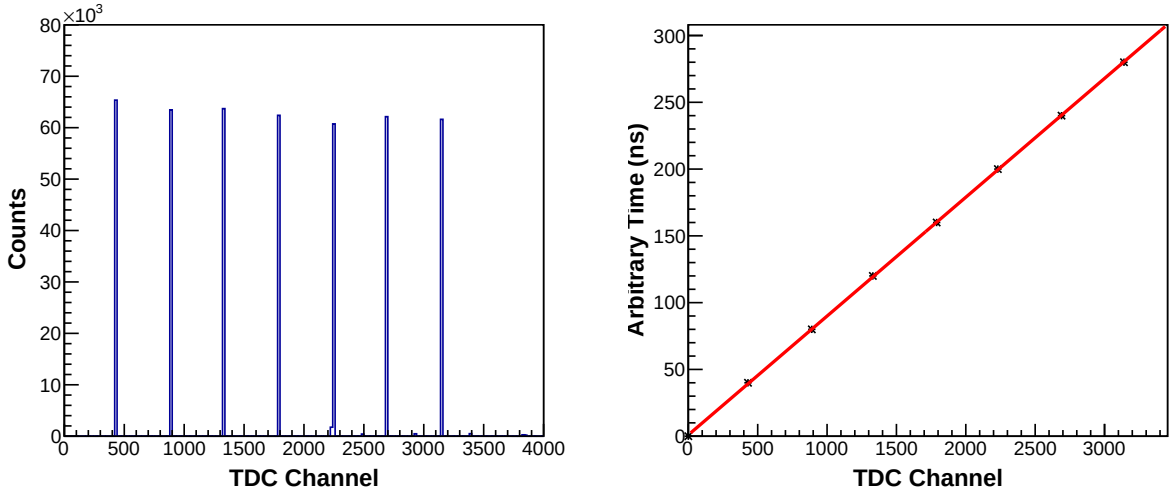

Figure 4.13: An example of the TDC calibration procedure for MoNA LISA. The data shown is the left PMT from Layer B, Bar 5. On the left is the "picket fence" spectrum created by the pulser pulsing the system every 40 ns. On the right is the relation between the TDC channel peaks and their assigned time.

bar at 0 cm within its own reference frame. Figure 4.14 shows an example of the position calibration within a bar.

4.1.2.3 Time Calibrations

The time-of-flight of an interaction in a bar was calculated by averaging the two times recorded from the two PMTs, but an offset was needed to place the time of the interaction in the bar relative to the times of other interactions within the detector array. This offset was again determined with cosmic ray muons that passed through the majority of the bars in a layer and deposited about 20 MeVee in each bar. A schematic drawing showing an example of a cosmic ray muon traveling through all bars within a single layer of MoNA LISA is displayed in the left part of Figure 4.15. Since the cosmic ray muons travel with a known velocity, it was possible to calculate the time, t, that it would take for a muon to travel from one bar to another with the following equation:

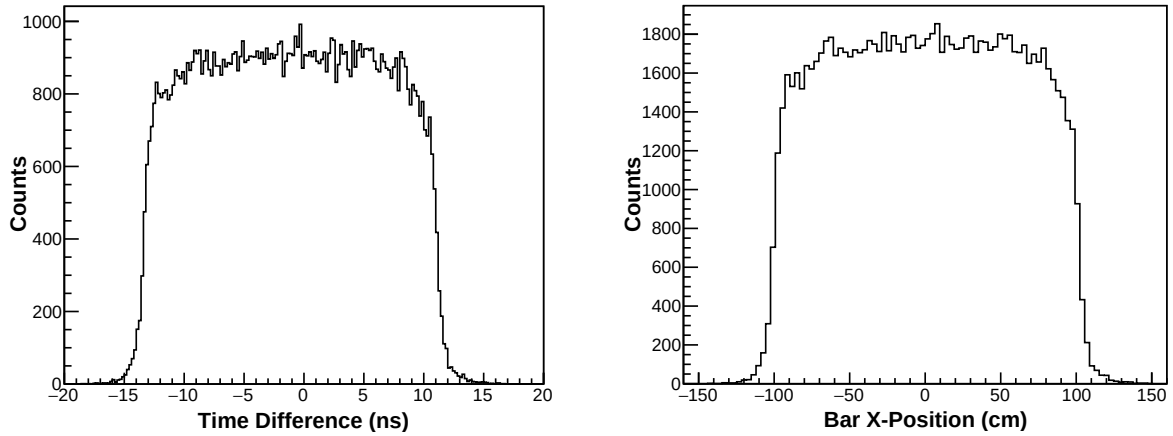

Figure 4.14: Example of the data for an X-position calibration for a bar in MoNA LISA (Layer A, Bar 8). The time difference ($t_{left} - t_{right}$) between the two PMTs is shown on the left, and the converted X-position spectrum is shown on the right.

$$t = \frac{d}{v_\mu} \tag{4.15}$$

where d was the distance between the interactions and $v_\mu = 29.8$ cm/ns, the speed of the muon. The difference between the expected travel time and the observed travel time was the time offset.

There were three "tables" (labeled MoNA, LISA-1, and LISA-2) that were supporting stacks of bars, as described in Chapter 3. Layers on the same table were linked together by cosmic ray muons passing through the top bar of every layer on the table and the bottom bar of the front layer. A schematic drawing showing example tracks of cosmic ray muons traveling through the top bar in a layer and a bottom bar in the front layer is displayed in the right part of Figure 4.15. The expected and observed times were used to calculate offsets that were then added to each bar within the layer. The result was that each table of bars was calibrated in time relative to all other bars on that table.

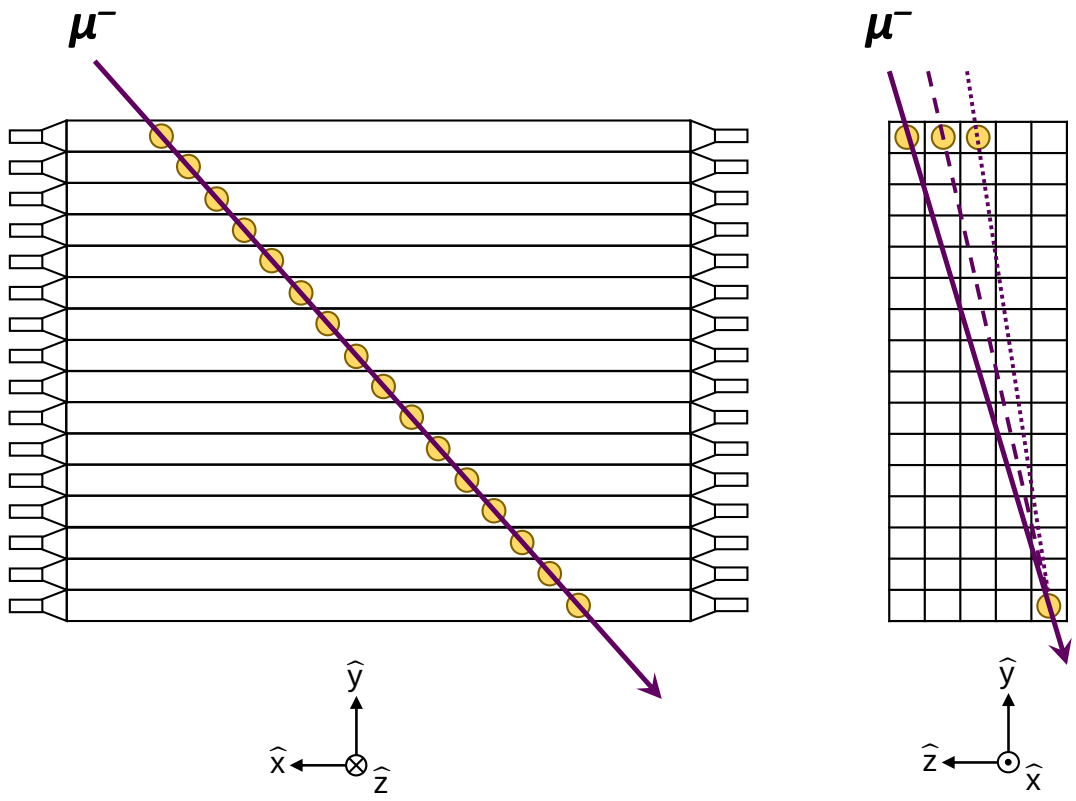

Figure 4.15: Schematic representation of cosmic ray muon paths through MoNA LISA bars. The schematic view on the left is a view from the front a table, while the view on the right of is from looking at a side view of a table.

Finally, each table had to be located in time relative to the interaction time in the target. A thick target was inserted into the beam path, and when the beam collided with the thick target, a variety of gamma rays and neutrons were produced. The known velocity of the gamma rays, $v_\gamma = 29.98$ cm/ns, was used in combination with the known physical positions of the bars to determine the final time offset to align the gamma ray peaks by their calculated times of flight. The final offsets for each table of bars were given in Table 4.6. Figure 4.16 shows the velocity spectra of all three tables with the gamma ray velocity peaks lined up with their expected values.

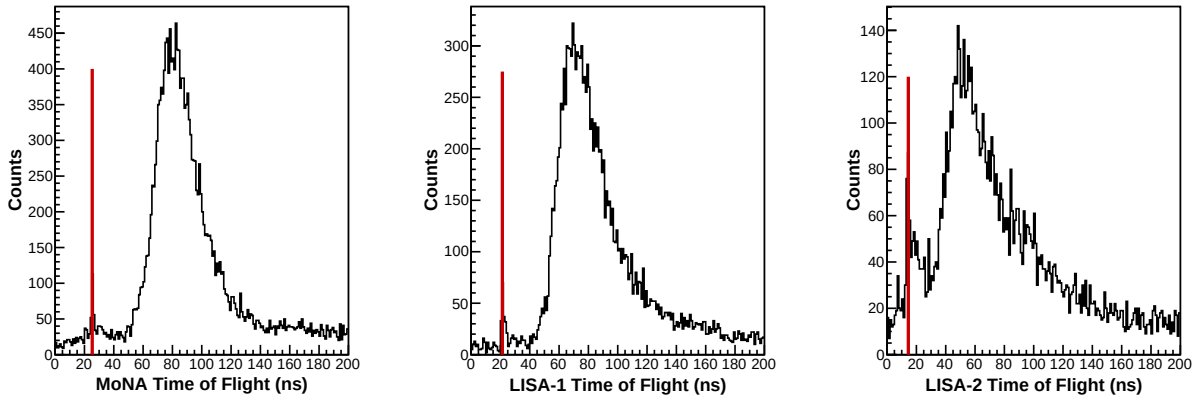

Figure 4.16: Calibrated time spectra for all detectors on each MoNA LISA table. The smaller peaks on the left of each spectra are the gamma rays, while the larger peaks are neutrons. The red vertical lines indicate the expected time for the gamma rays to arrive in each set of bars.

MoNA Offset (ns)	LISA-1 Offset (ns)	LISA-2 Offset (ns)
469.92	410.61	409.65

Table 4.6: Global time offsets for each table of MoNA-LISA.

4.2 Event Selection

While this experiment was designed to measure as many fragments as possible, many collision events had to be discarded from the final analysis. This section describes the process for selecting appropriate, complete events for the analysis.

4.2.1 Beam Identification

The A1900 Fragment Separator filters out unwanted projectile fragments and attempts to send only the desired fragments of interest to an experimental vault. However, the separation technique trades purity against rate so that contamination by unwanted products occurs in some reactions [92, 93]. Contaminants can be rejected in analysis by time-of-flight correlations. Fragments with the same magnetic rigidity but with slightly different mass-to-charge

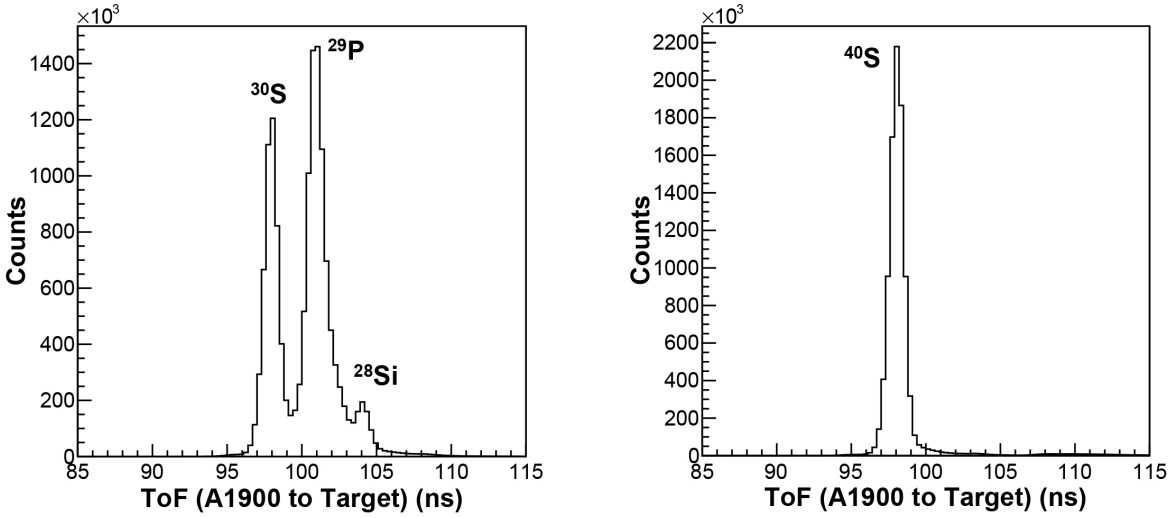

Figure 4.17: Beam component identification with flight time from the A1900 timing scintillator to the target scintillator. The ^{30}S beam and contaminants are shown on the left, while the ^{40}S beam peak is shown on the right.

ratios with different velocities will be accepted. In particular, the A1900 generally includes isotones as contaminants due to the kinetics of the separation process at approximately 100 MeV/u [92, 93, 104]. Thus, the time-of-flight from the A1900 Fragment Separator timing scintillator to the target scintillator can be used to identify the desired beam from the contaminants. Figure 4.17 shows time-of-flight spectra for both the ^{30}S beam plus contaminants and the ^{40}S beam plus contaminants.

While the ^{40}S beam was relatively pure with few contaminants, having a purity of 98%, the ^{30}S beam had a purity of only 32%. Major contaminants in the ^{30}S beam were the two isotones ^{29}P and ^{28}Si. These two contaminants arrived at different times when compared to the desired ^{30}S particles, making it relatively straightforward to exclude them from the analysis. The energy loss of the unreacted fragments in the ion chamber was examined to confirm that there were no significant contaminants with the same time-of-flights as the

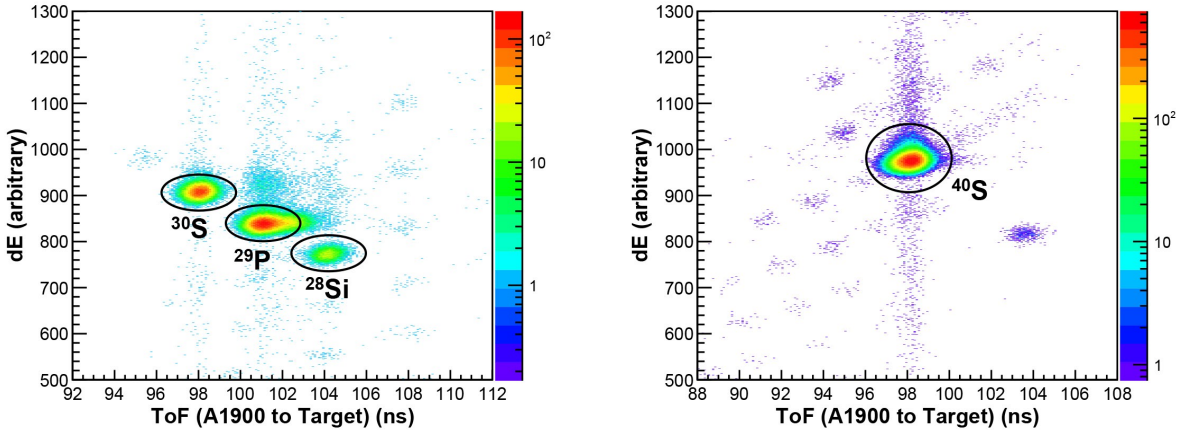

Figure 4.18: Beam component identification with flight time from the A1900 timing scintillator to the target scintillator versus the energy loss in the ion chamber. The ^{30}S beam and contaminants are shown on the left, while the ^{40}S beam and contaminants are shown on the right.

desired beams. Figure 4.18 shows the energy loss in the ion chamber versus the timing spectra from Figure 4.17.

To further improve incoming beam selection, cuts using the time-of-flight from the K1200 cyclotron to the A1900 timing scintillator were also included in the analysis. This was done by comparing the time difference between the cyclotron RF signal and the A1900 timing scintillator and the time-of-flight from the A1900 timing scintillator to the target scintillator, as displayed in Figure 4.19. The time signal from K1200 cyclotron was measured from the RF main oscillator. The multiple peaks in the time-of-flight spectra for the RF to the A1900 was due to wraparound of the RF [80]. The smaller peaks with relatively few events between the larger major peaks were likely the result of inaccurate time measurements. These "echoes" were excluded from the analysis.

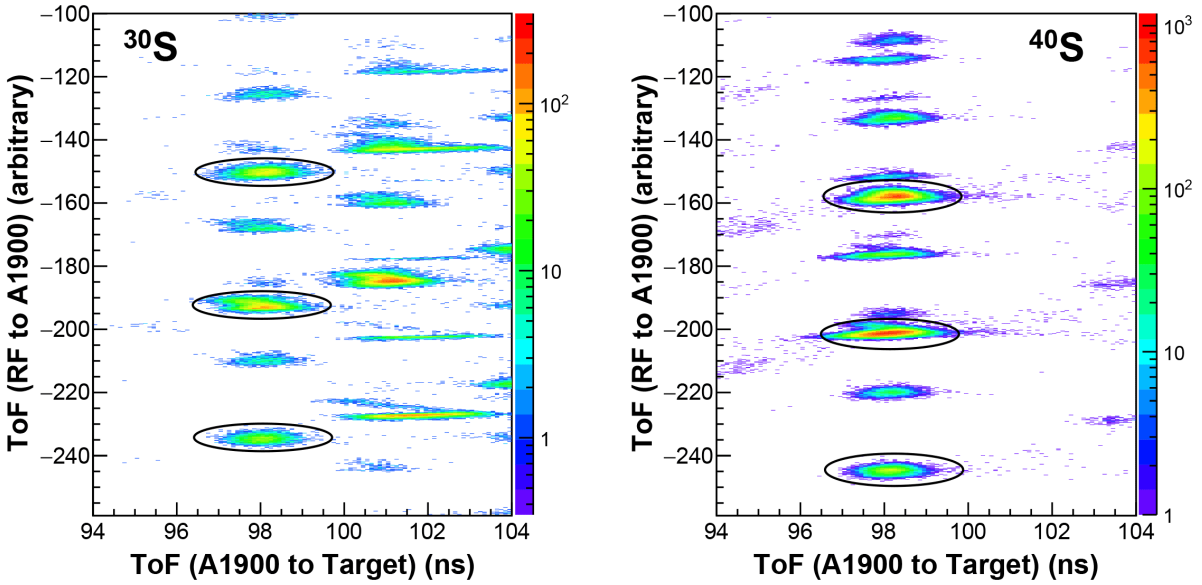

Figure 4.19: Beam component identification using the time-of-flight from the RF to the A1900 scintillator. The ^{30}S beam and contaminants are shown on the left, while the ^{40}S beam and contaminants are shown on the right. The multiple peaking in the RF to A1900 time-of-flight is due to wraparound of the RF. Beam gates were placed on the dominant packets encircled in black.

4.2.2 Event Quality Gates

Accurate position information from the CRDCs was found to be necessary to achieve identification of individual isotopes. Events in which the experimental system behaved abnormally were removed by applying "event quality gates" to the produced charged fragments in the data. In some events, the CRDCs failed to collect all charge deposited, resulting in abnormally low signals. In other events, an unusually high charge was recorded, possibly due to pile up. These events were identified by plotting the σ from the Gaussian fit for the X-position against the total charge summed over all the pads, or the pad sum. CRDC quality gates were constructed based on this relation, as shown in Figure 4.20. Furthermore, some events displayed inconsistent charge deposit from one CRDC to the other. For example, an event could deposit a high charge in CRDC1 and a low charge in CRDC2. To exclude these

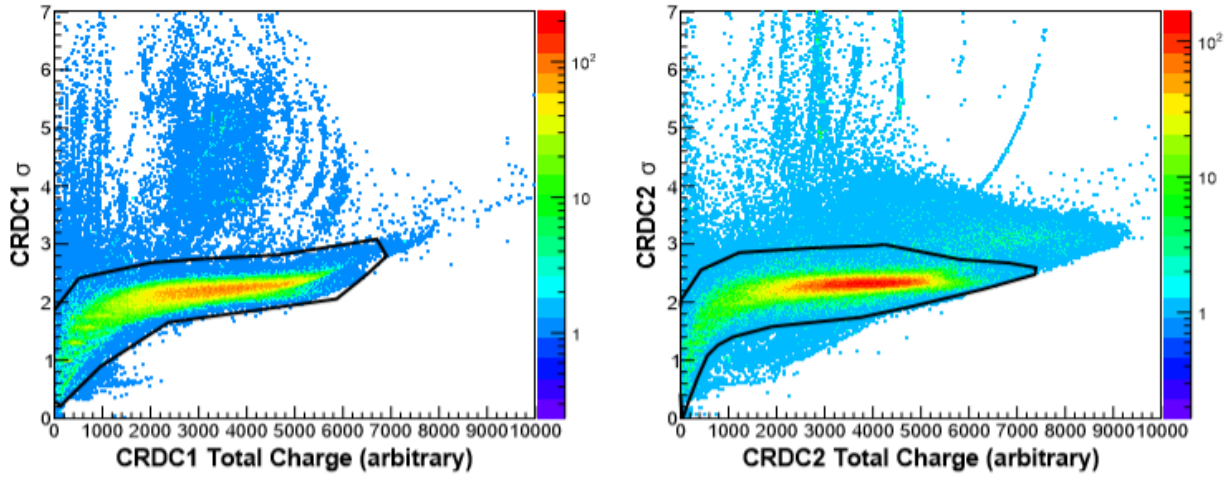

Figure 4.20: The σ of the gaussian fit as a function of total charge in the CRDCs for the ^{40}S + ^{9}Be reaction and 2.01 Tm Sweeper setting. The quality gates for each CRDC are drawn in black.

events that did not have a linear relation between the charge deposition between the two detectors, another quality gate was created, as shown in Figure 4.21. These CRDC quality gates excluded approximately 16% of events.

4.2.3 Element Identification

Two magnet settings of the Sweeper magnet were chosen for each secondary beam in order to collect data on a variety of reaction products. For the ^{30}S + ^{9}Be reaction, the Sweeper magnet was set to 1.51 Tm (115 A) and 2.25 Tm (174 A). For the ^{40}S + ^{9}Be reaction, the Sweeper magnet was set to 2.01 Tm (157 A) and 2.27 Tm (180 A).

Element separation and identification was achieved by measuring the energy loss in the ion chamber and correlating it with the time-of-flight. The Bethe-Bloch formula [5, 105] shows that energy loss in the ion chamber is related to the charge number (Z) of the incident particle and its velocity (β) in the following manner:

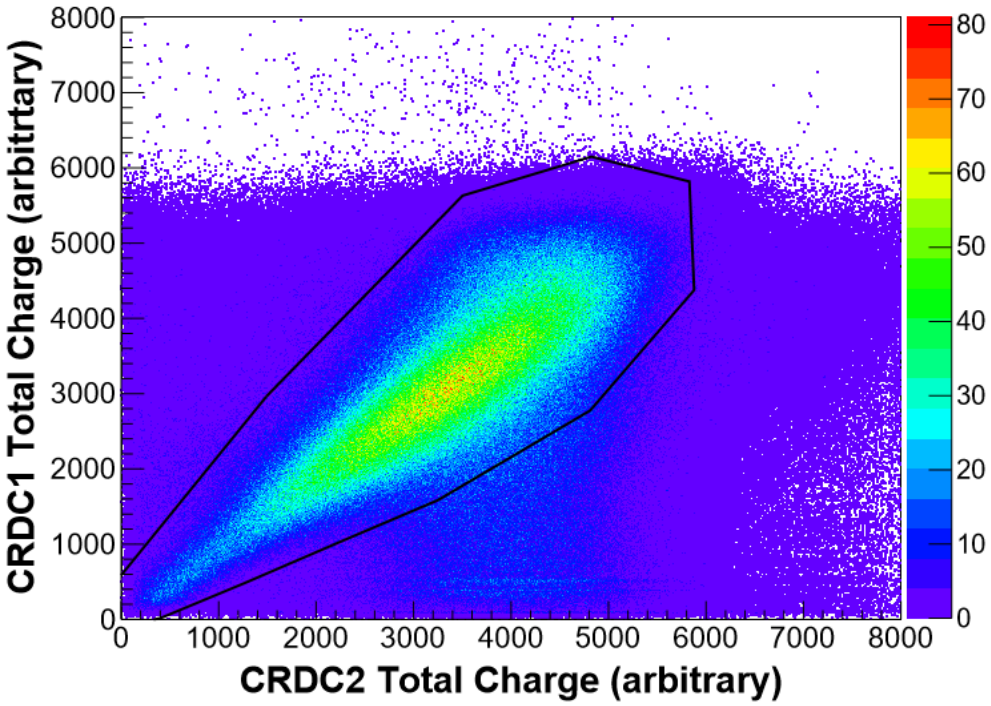

Figure 4.21: Total charge of CRDC1 plotted against the total charge of CRDC2 for the ^{40}S + ^{9}Be reaction and 2.01 Tm Sweeper setting. The quality gate (shown in black) excluded events that do not deposit charge in a linear manner in both detectors.

$$-\frac{dE}{dx} \propto \frac{Z^2}{\beta^2} \times f(\beta) \tag{4.16}$$

where $f(\beta)$ represents the other terms in the Bethe-Bloch formula. (The full formula is available in References [80, 105].)

Thus, element separation can be observed in a plot of the energy loss against a parameter tied to the velocity. The experimental configuration provided a velocity parameter through the time-of-flight from the target scintillator to the thin scintillator. Figures 4.22 and 4.23 show the element identification for products from the ^{30}S + ^{9}Be collisions and ^{40}S + ^{9}Be collisions, respectively. Each band in these figures represents products from a different element and the lines superimposed on the data indicate the sulfur ($Z = 16$) products. The

bands directly under the $Z = 16$ band contain phosphorus ($Z = 15$) products; bands under phosphorus contain silicon ($Z = 14$) products; and so forth. Gates were placed around these bands in order to make elemental cuts. Unfortunately, due to the hodoscope malfunction, no comparison could be made between the energy loss measured in the ion chamber and the total energy measured in the hodoscope.

4.2.4 Isotope Identification

Following the elemental identification of each event, the isotopic or mass number identification was necessary for the data analysis. The magnetic rigidity ($B\rho$) of a charged particle is based on its momentum to charge ratio:

$$B\rho = \frac{p}{q} = \frac{mv}{q} \tag{4.17}$$

In the present reactions at relatively high energy, light isotopes of the same element have the same number of protons and no electrons, and thus the same q. Isotopes with the same $B\rho$ and constant q could then be separated by their mass number A, as their masses are inversely proportional to their velocity:

$$v = \frac{B\rho q}{m} \propto \frac{B\rho q}{A} \tag{4.18}$$

Furthermore, because the (non-relativistic) velocity is simply distance per unit of time, the time-of-flight measured from the target to the detector and mass of a charged particle are proportional. Thus, isotopes with a lower A would arrive sooner than isotopes with the same $B\rho$ and q but higher A.

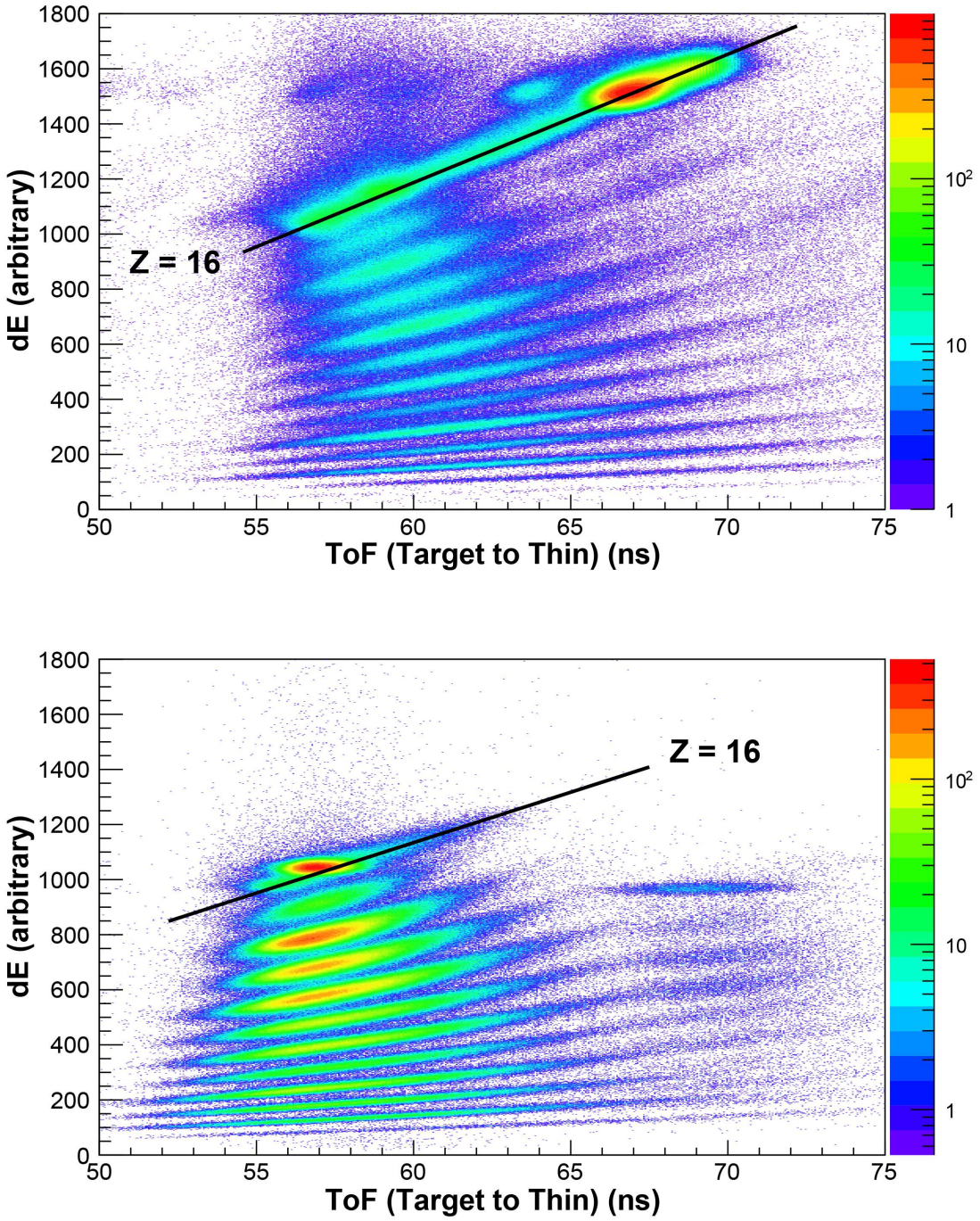

Figure 4.22: Energy loss in the ion chamber versus the time-of-flight from the target scintillator to the thin scintillator for reaction products from the ^{30}S + ^{9}Be reaction. The top panel contains products from the 1.51 Tm magnet setting. The bottom panel contains products from the 2.25 Tm magnet setting. Black lines indicate the locus of sulfur ($Z = 16$) products.

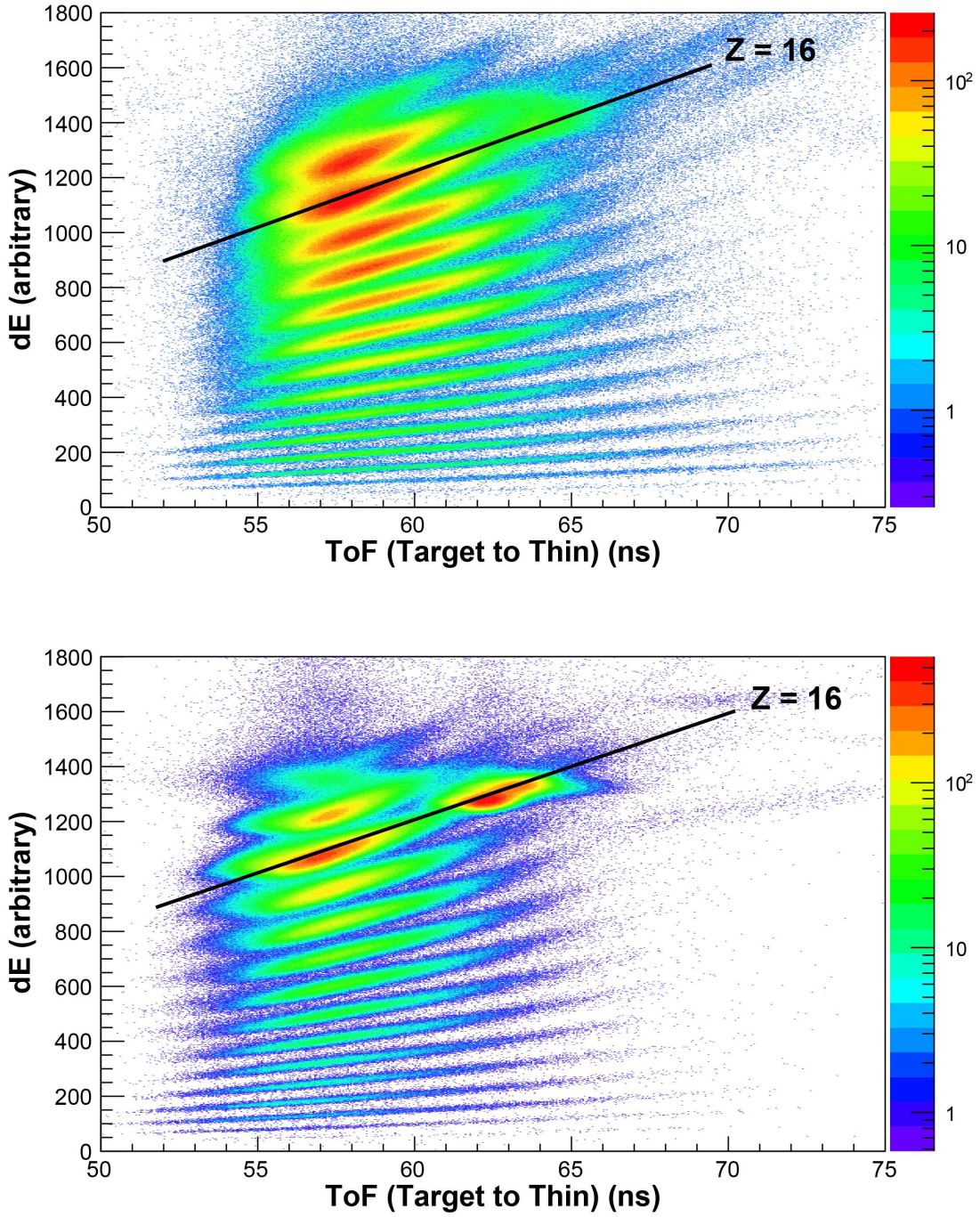

Figure 4.23: Energy loss in the ion chamber versus the time-of-flight from the target scintillator to the thin scintillator for reaction products from the ^{40}S + ^{9}Be reaction. The top panel contains products from the 2.01 Tm magnet setting. The bottom panel contains products from the 2.27 Tm magnet setting. Black lines indicate the locus of sulfur ($Z = 16$) products.

However, charged particles produced by these nuclear reactions can have a large spread in momentum. Variations in momenta lead to variations in the distance traveled in the present case, as the track of a charged particle that passes through a dipole magnet is dependent on its magnetic rigidity. Because these momenta distributions are so large and the track length varies, the times of flight of the isotopes tend to overlap one another.

Thus, the measured path was used to separate isotopes. The magnetic rigidity and path length traveled by the observed charged particles were correlated to their position and angle with the position measurements in the CRDCs and the beam spot on the target. In standard magnetic spectrometers, the fragments are highly focused in the horizontal or X-position and isotopic separation is observed in a two-dimensional plot of plane angle versus the time-of-flight [80]. However, this simple method of achieving isotopic separation was not possible with the Sweeper magnet, which was a simple dipole magnet and did not contain focusing elements such as those found in true magnetic spectrometers, such as the S800 spectrograph at the NSCL [106]. The angle and position at the "focal plane" in the Sweeper are correlated and entangle the X-position, X-angle, and time-of-flight. This correlation can be seen in a three-dimensional plot of the three parameters. An example of such a three-dimensional plot from the present work is shown in Figure 4.24.

For isotopic separation from the Sweeper magnet to be achieved, the full correlation among the X-position, X-angle, and time-of-flight must be untangled. First, the three-dimensional data for one element from one reaction was projected onto the X-position and X-angle plane, as shown for example in Figure 4.25. Contours along this plot were fit with a quadratic function:

$$f(x) = a_2 x^2 + a_1 x + c \tag{4.19}$$

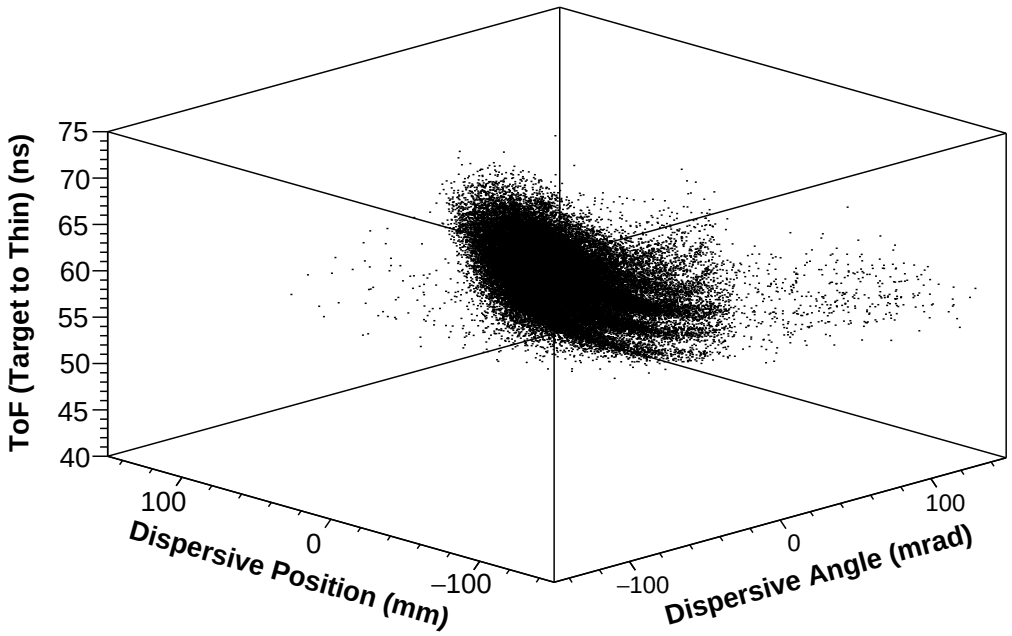

Figure 4.24: Three-dimensional plots showing the correlation among the (dispersive) X-position, X-angle, and time-of-flight for the oxygen isotopes from the ^{40}S + ^{9}Be reaction and the 2.01 Tm magnet setting. Isotope bands are visible on the right edge in the Figure but merge towards the back left side.

where x was the X-position, a_2 and a_1 were the coefficients from the quadratic fit, and c was a constant offset. Varying c only moves the curve vertically along the angle axis.

A new linearized parameter describing the position and angle for a constant time-of-flight was created. This parameter, referred to as an emittance ($e(x, \theta_x)$), was written in the following manner:

$$e(x, \theta_x) = \theta_x - (a_2 x^2 + a_1 x) \tag{4.20}$$

where θ_x was the dispersive angle. Plotting the values of this emittance parameter against the time-of-flight provided the degree of isotopic separation, shown by example in Figure 4.26, with each parallel band containing fragments from a single isotope.

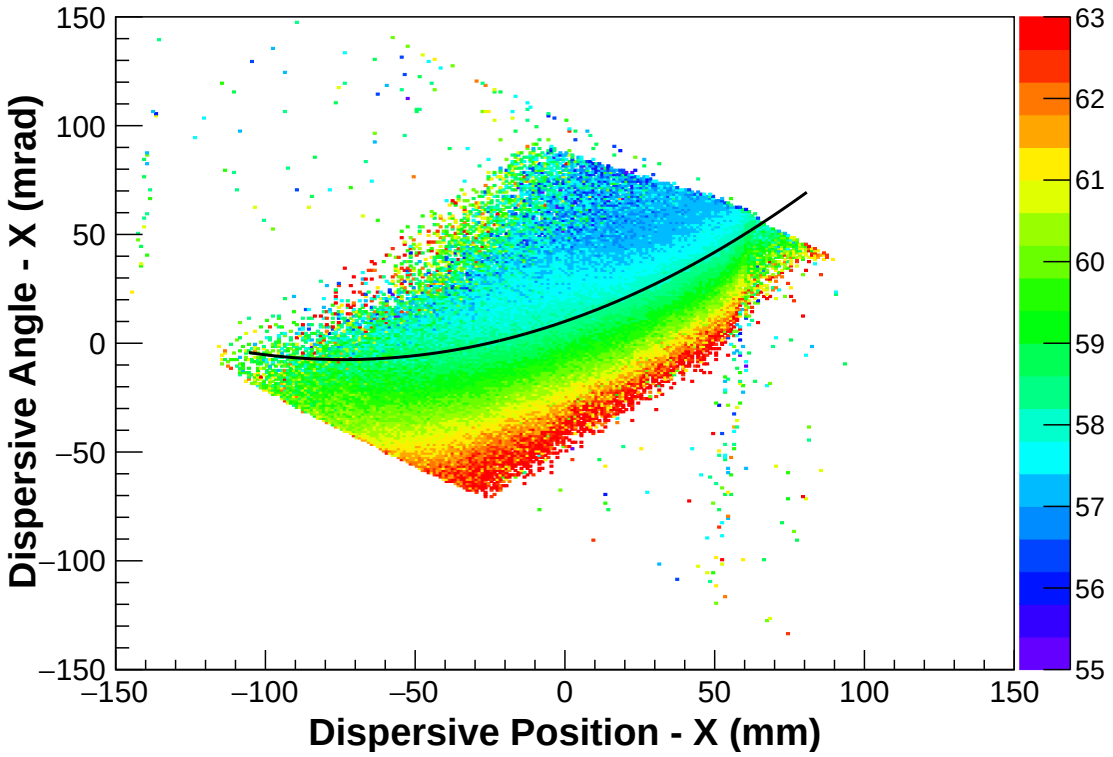

Figure 4.25: Projection of the three-dimensional plot from Figure 4.24 onto the (dispersive) X-position and X-angle plane for the oxygen isotopes from the ^{40}S + ^{9}Be reaction and the 2.01 magnet setting. A solid black line is drawn along the contours to demonstrate the quadratic function fit used in the analysis.

The isotopic separation was finally obtained by applying a linear fit to one of the isotopic bands and then projecting the data onto an axis called t_{corr}:

$$t_{corr} = m \times e(x, \theta_x) + t_{target \to thin} \tag{4.21}$$

where m was the slope of the line perpendicular to the linear fit and $t_{target \to thin}$ was the time-of-flight from the target to the thin scintillator. From another standpoint, one could say that the time-of-flight was corrected by projecting the two-dimensional figure onto the axis perpendicular to the linear fitted line.

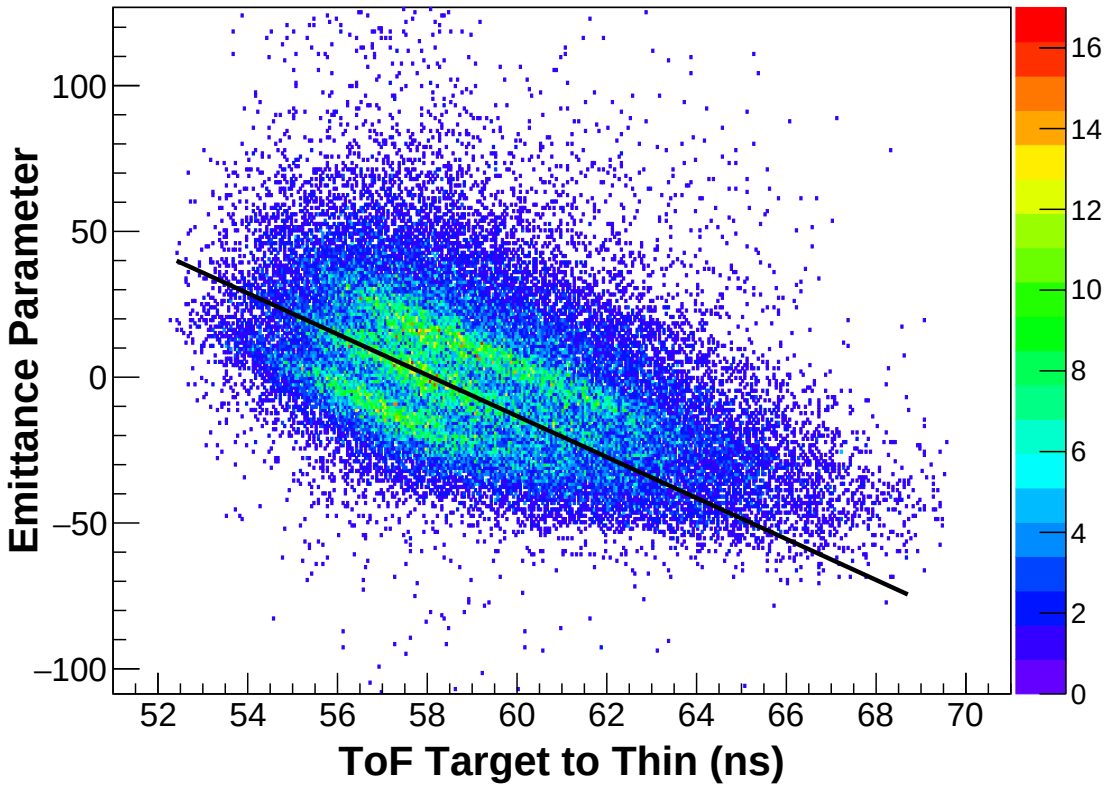

Figure 4.26: Emittance parameter from Equation 4.20 plotted against the time-of-flight from the target to the thin scintillator for the oxygen isotopes from the ^{40}S + ^{9}Be reaction and the 2.01 magnet setting. A solid black line is drawn along the contours to demonstrate the linear function fit.

Isotopic separation was further improved by plotting the corrected time-of-flight against the dispersive X-position and X-angle as well as other parameters, including the non-dispersive Y-position and Y-angle. Any observed correlations were then removed in a similar manner to the corrected time-of-flight parameter from Equation 4.21. These corrections were generally much smaller. The final time-of-flight separation parameter can be expressed in a general format:

$$t_{final} = t_{target \rightarrow thin} + \sum C_i P_i \tag{4.22}$$

where C_i were the correction coefficients and P_i were the parameters. The isotope separation procedure was carried out for the data from each element in each magnet setting for both sulfur beams. Correction coefficients and parameters for each element are summarized in Appendix C. The projected isotopic distributions are shown later in this chapter.

Once the relative distributions were constructed, the relationship between energy loss and the corrected time-of-flight was used to identify the isotopes. Energy loss is tied to Z, as demonstrated in Figures 4.22 and 4.23, in which an element with a higher Z demonstrates greater energy loss compared to an element with a lower Z.

Recall that the corrected time-of-flight is related to N/Z. The magnetic rigidity ($B\rho$) is equal to momentum divided by charge (Equation 4.17). Thus, velocity (β) can be written in terms of magnetic rigidity, charge (Z), and mass (m) in the present case because $q = Z$:

$$\beta = \frac{Z(B\rho)}{m} \tag{4.23}$$

If the magnetic rigidity is constant, the velocity will be proportional to Z/A, meaning that time-of-flight is proportional to A/Z. Thus, energy loss is comparable to Z and the corrected time-of-flight is comparable to A/Z or N/Z.

Figure 4.27 displays the expected pattern for plotting Z against N/Z in the range of 6 $\leq Z \leq$ 16 and $N/Z \leq 2$. Each point is the position of a single isotope. It is evident that isotopes with the same N/Z (or same A/Z) fall in a vertical line, such as the red diamond points representing isotopes in which $N = Z$ (or $A/Z = 2$). This pattern was compared to a plot of the energy loss versus corrected time-of-flight for each reaction in order to identify the isotopes in the data. An example of a plot of energy loss versus a corrected time-of-flight parameter is shown in Figure 4.28. While the final isotopic separation was performed

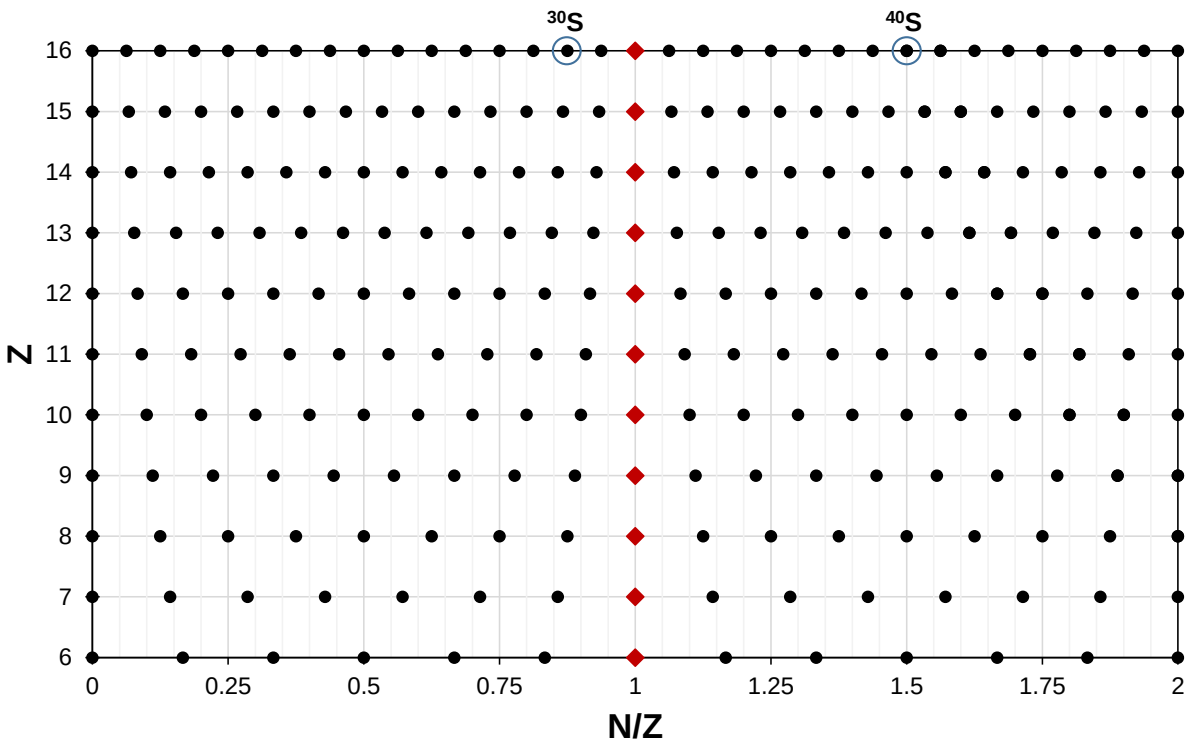

Figure 4.27: The Z versus N/Z pattern for isotopes with Z = 6-16 and $N/Z \leq 2$. Each point is a separate isotope. Some of the isotopes shown do not exist. The red diamond points represent isotopes in which $N = Z$. The two beams, ^{30}S and ^{40}S, are circled for reference.

with the correction parameters for each element, the Z and A relative pattern and isotope identification was found with the correction parameters for oxygen isotopes, which were applied to every element to create this figure. (In other words, if individual correction parameters were applied by element, the isotopes would be shifted and out of sync with each other.) The line indicating isotopes with the same "corrected" time-of-flight corresponds to the red diamond points in Figure 4.27. Those isotopes that fall along the vertical line have the same N/Z, and the remaining isotopes were identified by their relationship to the vertical line.

The final one-dimensional projections for isotope separation for fragments from the ^{30}S + ^{9}Be collision in the 1.51 Tm and 2.25 Tm Sweeper settings are shown in Figure 4.29 and

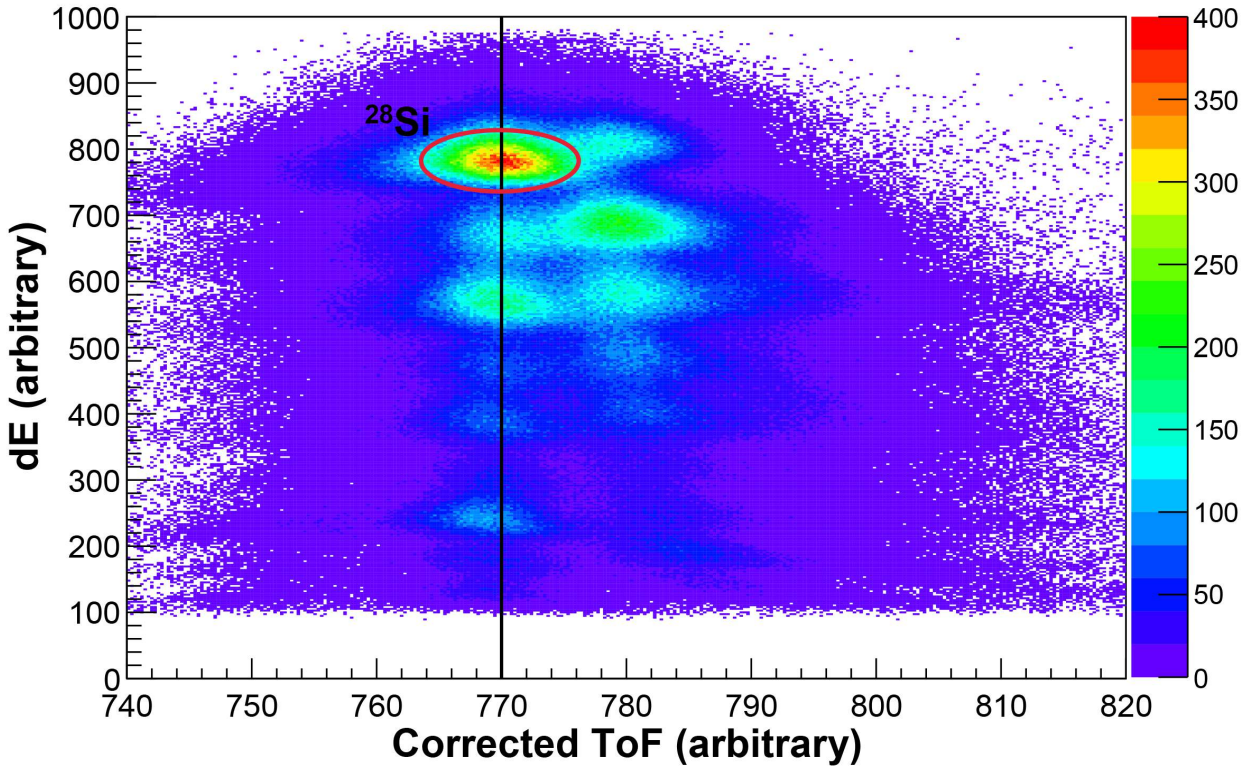

Figure 4.28: Energy loss in the ion chamber for elements $Z = 6 - 14$ using the corrected time-of-flight for oxygen isotope separation. The elements shown are from the ^{30}S + ^{9}Be reaction and the 2.25 Tm Sweeper magnet setting. A vertical line at $N/Z = 1$ is drawn for reference. This line corresponds to the red diamond points in Figure 4.27. The ^{28}Si fragments are circled in red.

Figure 4.30, respectively. Figure 4.31 and Figure 4.32 show the one-dimensional projections for isotope separation from the ^{40}S + ^{9}Be collision in the 2.01 Tm and 2.27 Tm Sweeper settings, respectively. Element gates from the energy loss in the ion chamber (as shown in Figures 4.22 and 4.23) and event quality gates were applied. The four figures indicate that separation of individual isotopes was only possible for carbon, nitrogen, oxygen, fluorine, neon, and sodium isotopes. The separation was clearest for elements with lower proton numbers, and the separation became more difficult with increasing proton number.

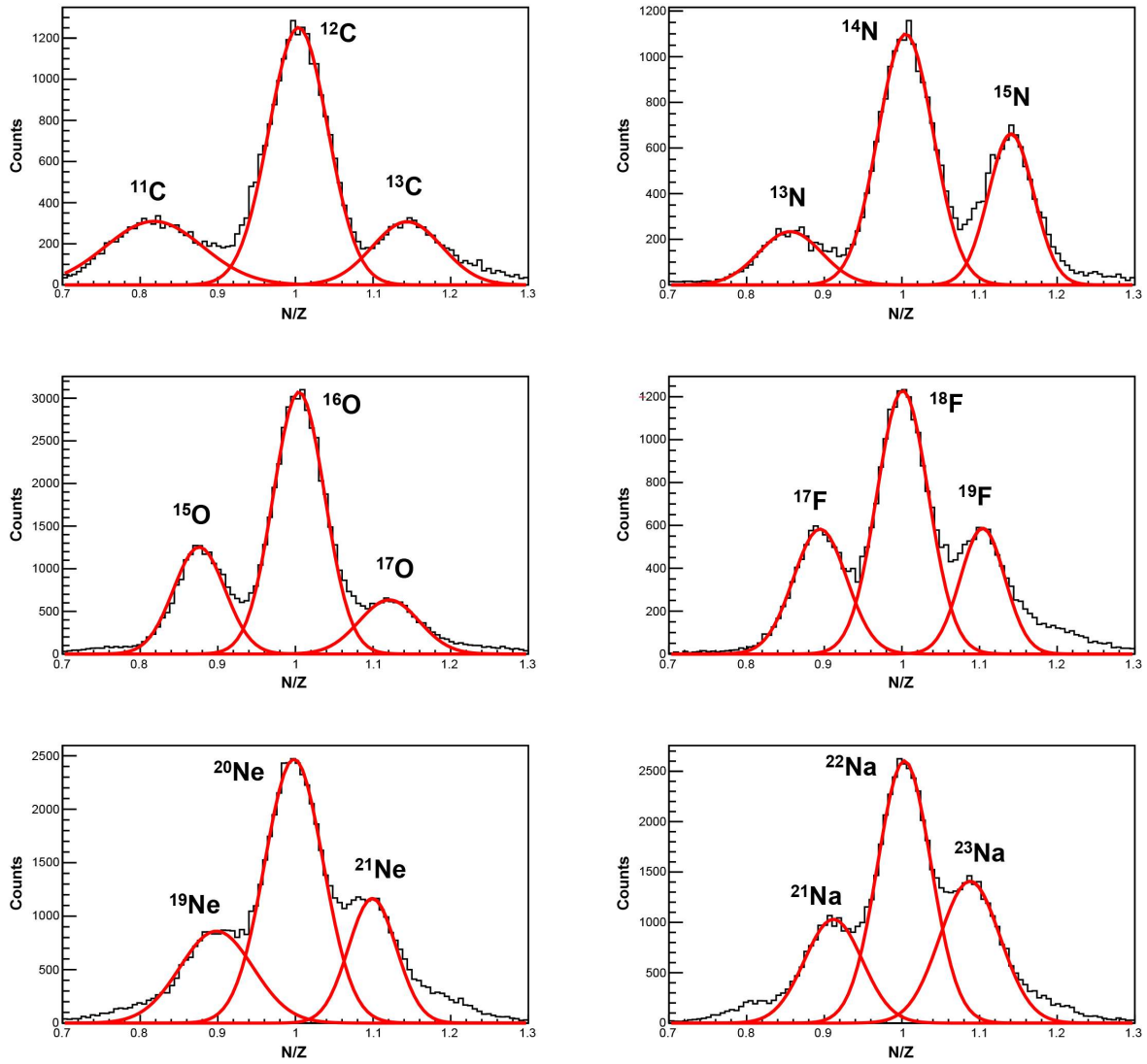

Figure 4.29: One-dimensional distributions of carbon, nitrogen, oxygen, fluorine, neon, and sodium isotopes produced from the ^{30}S + ^{9}Be reaction and the 1.51 Tm Sweeper magnet setting. Element and event quality gates were applied.

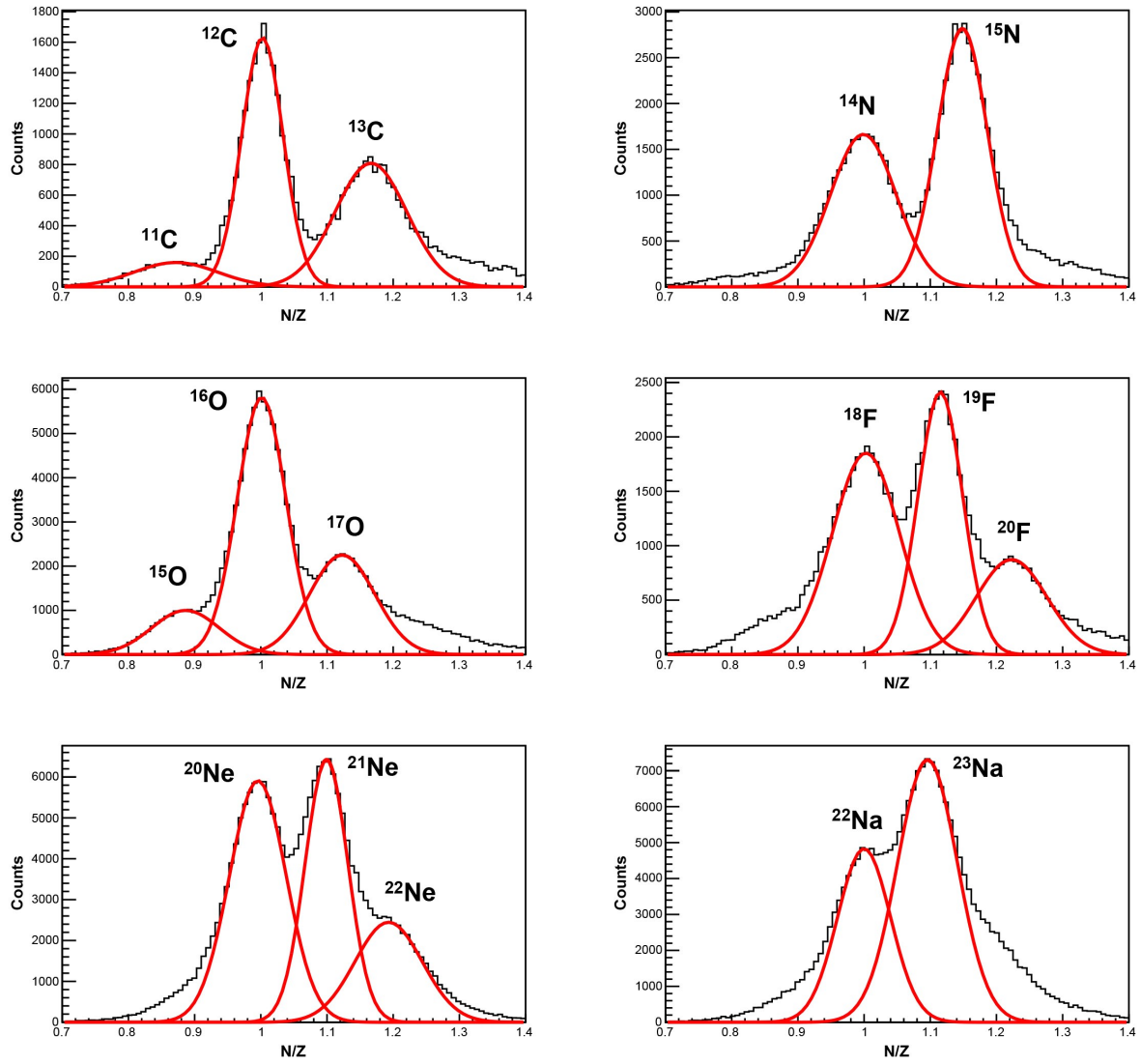

Figure 4.30: One-dimensional distributions of carbon, nitrogen, oxygen, fluorine, neon, and sodium isotopes produced from the ^{30}S + ^{9}Be reaction and the 2.25 Tm Sweeper magnet setting. Element and event quality gates were applied.

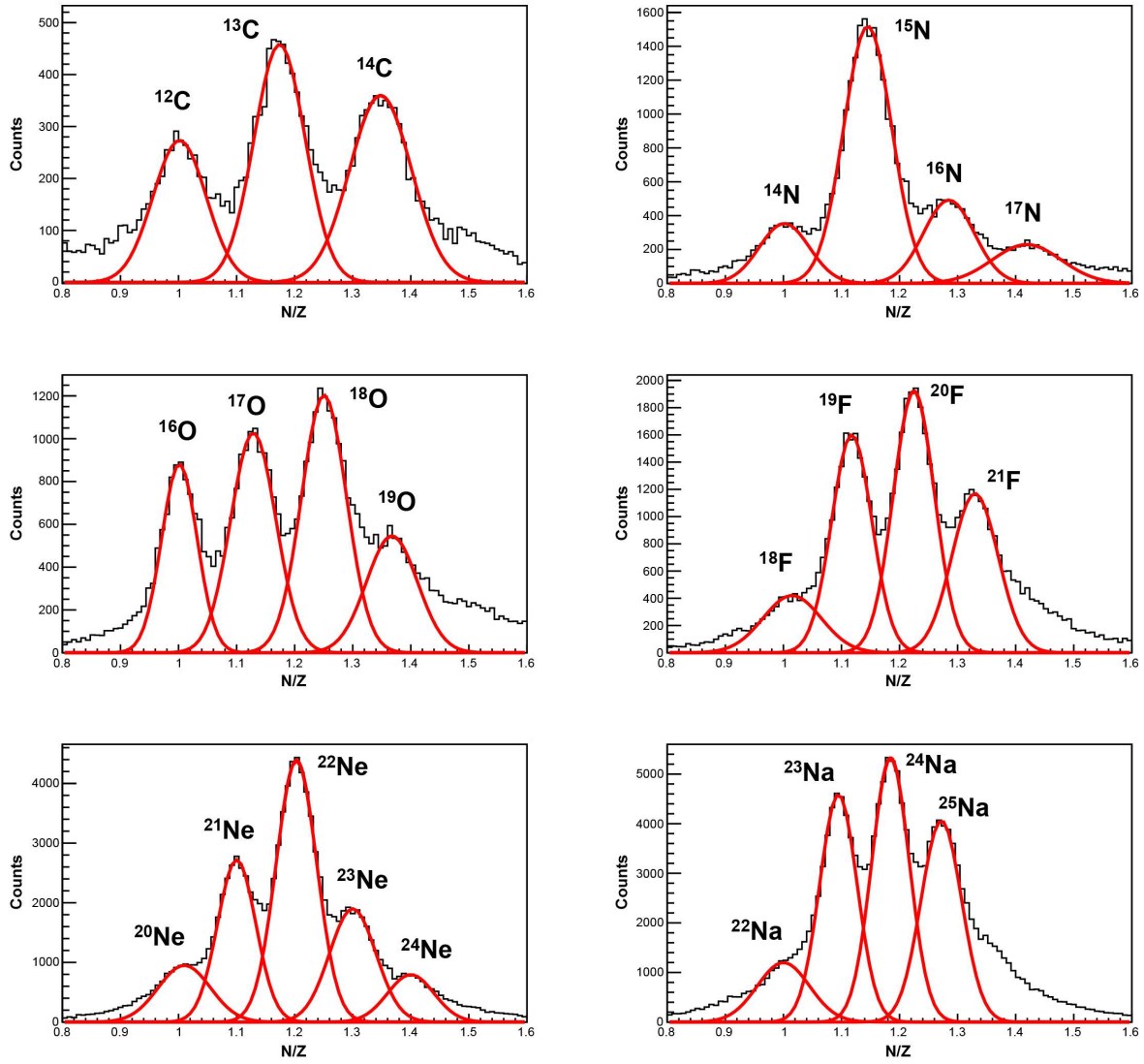

Figure 4.31: One-dimensional distributions of carbon, nitrogen, oxygen, fluorine, neon, and sodium isotopes produced from the ^{40}S + ^{9}Be reaction and the 2.01 Tm Sweeper magnet setting. Element and event quality gates were applied.

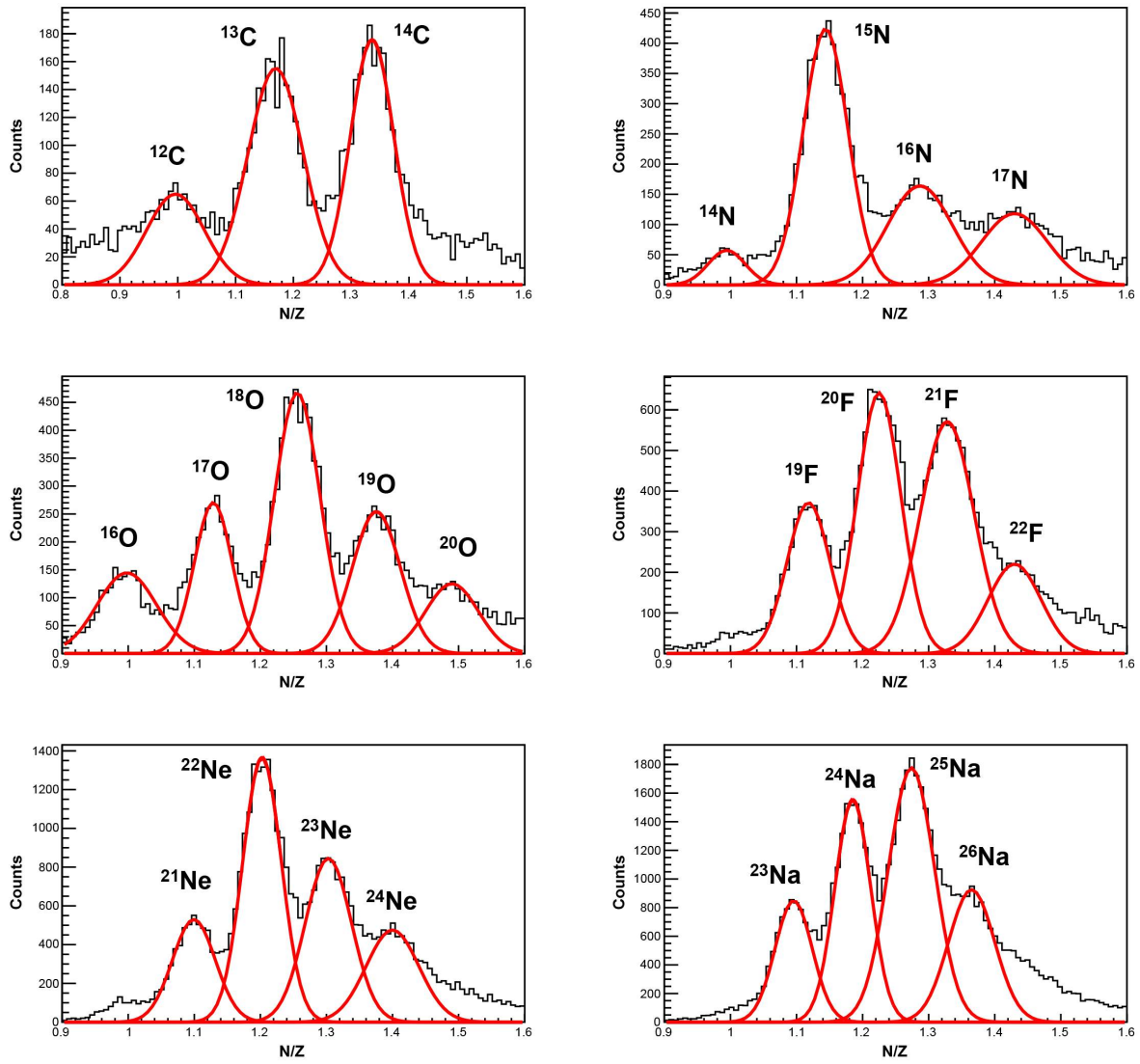

Figure 4.32: One-dimensional distributions of carbon, nitrogen, oxygen, fluorine, neon, and sodium isotopes produced from the ^{40}S + ^{9}Be reaction and the 2.27 Tm Sweeper magnet setting. Element and event quality gates were applied.

It is important to note that this experiment entered unexplored territory with the MoNA LISA and Sweeper experimental set-up. Previous experiments have focused on studying isotopes of the elements only up to magnesium ($Z = 12$) [80, 95, 97, 100, 101, 107–111]. The ^{30}S and ^{40}S ($Z = 16$) secondary beams used in this experiment were significantly higher in Z than those in the past MoNA LISA and Sweeper experiments and isotopic separation with $Z = 12 - 16$ had not been done before and was not possible here. Isotope separation results from a previous study on fluorine, neon, and sodium isotopes produced from a ^{32}Mg beam on a beryllium target already suggested that separation was difficult [110]. From Figure 4.27, elements with higher Z contain more isotopes than elements with lower Z in a given range of N/Z. For example, in the N/Z range from 0.75 to 1.25, carbon has three isotopes, while phosphorus has seven isotopes. The example isotopic separation shown in Figure 4.28 indicates this compression of the isotopes in elements with higher Z. In particular, the ^{28}Si fragments appear to be overlapping the ^{29}Si fragments in this case. Thus, the isotopes with higher Z are more overlapped and difficult to separate. Figure 4.33 demonstrates the poor one-dimensional separation for magnesium ($Z = 12$) and aluminum ($Z = 13$) isotopes from Figure 4.28. This experiment pushed the limits on the current detector configuration and the resolution was not sufficient to achieve isotope separation for the highest Z elements. However, a broad range of fragments was identified in each reaction.

Furthermore, most previous Sweeper experiments characterized isotopes produced by only one or a few nucleon removal or addition. Final fragments measured in the current experiment were produced by removing many nucleons. For example, the ^{40}S + ^{9}Be reaction produced ^{12}C, a mass change of 28 units. This wide range was not standard for the MoNA LISA and Sweeper configuration and would have to be improved for future experiments with heavier beams.

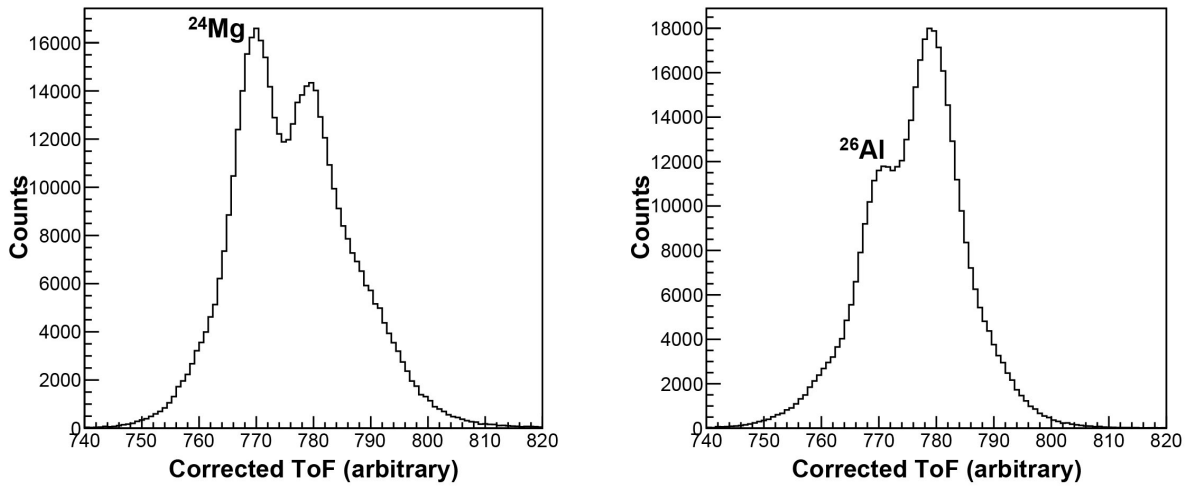

Figure 4.33: One-dimensional distributions of magnesium and aluminum isotopes produced from the ^{30}S + ^{9}Be reaction and the 2.25 Tm Sweeper magnet setting. Element and event quality gates were applied.

4.2.5 MoNA LISA Multiplicity

Charged particles were measured in coincidence with neutron hits in the MoNA LISA detectors. The kinetic energy spectrum of observed neutrons in MoNA LISA measured in coincidence with fragments from the ^{40}S + ^{9}Be reaction and the 2.01 Tm Sweeper setting is shown in Figure 4.34. The distribution peaks around beam energy, indicating that most of the detected neutrons were generated the subsequent de-excitation process. Neutrons stripped from the projectile by the target would have a kinetic energy around half the kinetic energy of the beam. The kinetic energy of a nucleon removed directly from the projectile by the target would be equal to the energy of the center-of-mass. Because the target is stationary, the stripped neutron would have half the kinetic energy.

As previously described in Chapter 3, an interaction in MoNA LISA is only considered valid if there were good timing signals in the CFD channels for both PMTs within a single bar. A valid interaction is referred to as a "hit" in MoNA LISA. The number of hits in

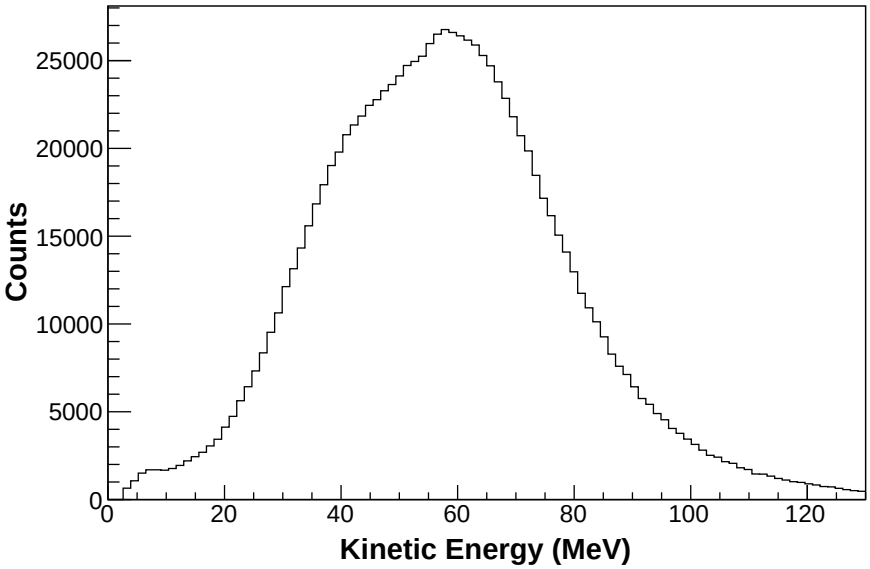

Figure 4.34: Kinetic energy of neutrons detected in MoNA LISA for all fragments measured with the ^{40}S + ^{9}Be reaction and the 2.01 Tm Sweeper setting.

MoNA LISA is called the hit multiplicity and its relation to the actual neutron multiplicity have to be obtained from comparisons to detailed simulations.

The number of hits in MoNA LISA does not directly measure the true neutron multiplicity for an event due to neutrons scattering multiple times within the full array and dark scattering. In dark scattering, neutrons scatter on carbon nuclei in the plastic scintillator material. Due to the short range of the carbon recoil, insufficient scintillation light is produced for a valid measurement. Thus, the measured hit multiplicity is not the true neutron multiplicity. Despite this, as the number of neutrons emitted increases, the number of valid neutron events recorded also can be expected to increase, leading to a higher hit multiplicity.

The hit multiplicities were extracted for comparison to the simulations discussed in the following section, Section 4.3. All of the extracted hit multiplicity distributions and the comparisons to simulations are shown in Chapter 5, but two examples of these experimental hit multiplicity distributions are shown in Figure 4.35. The distributions are shown as a

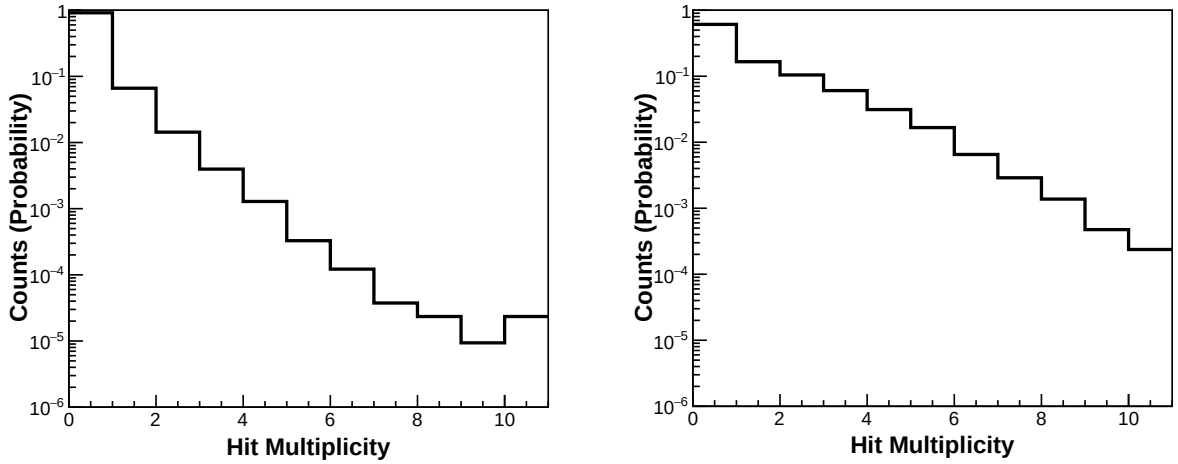

Figure 4.35: Examples of the hit multiplicity distributions for all neon fragments from the ^{30}S + ^{9}Be reaction with the 2.25 Tm Sweeper magnet setting (left) and the ^{40}S + ^{9}Be reaction with the 2.27 Tm Sweeper magnet setting (right). Distributions are presented in terms of a normalized probability.

normalized "probability" in which the distributions were normalized relative to the total number of observed hits for each fragment measured in the magnet setting. Most charged particles were measured with zero hits, or a hit multiplicity of zero, so the distributions are shown on a log scale to better highlight differences among the distributions.

From the hit multiplicity distribution examples shown in Figure 4.35, it is evident that the fragments produced from the ^{40}S reaction were in coincidence with significantly higher numbers of hits in MoNA LISA than the fragments produced from the ^{30}S reaction. Because ^{30}S contains ten less neutrons than ^{40}S, there are fewer neutrons available for reactions. Thus, fragments produced from the ^{40}S collision could be more neutron rich as well as have higher neutron multiplicities, leading to a higher number of valid hits in MoNA LISA.

4.3 Experimental Simulation and Gates

As discussed in Chapter 2, the two nuclear reactions were simulated using two different models: the Liège Intranuclear Cascade (INCL++) and the Constrained Molecular Dynamics (CoMD) model. INCL++ contained the ABLA07 code for the de-excitation of hot fragments created from the fast stage of the reactions. For CoMD simulations, GEMINI++ was used as an evaporation or "afterburner" code to decay remaining hot fragments from the dynamical model. Once the correlated distributions of fragments and neutrons from INCL++ and CoMD + GEMINI++ were obtained, the results were filtered through a model of the detection efficiency developed in the GEANT4 code. The filtering is discussed next and the results of the comparisons between the simulations and experimental data are presented in Chapter 5.

4.3.1 Fragment Gates

To mimic the physical configuration of the detectors measuring the charged particles, fragments from the CoMD + GEMINI++ and INCL++ simulations were filtered according to the magnetic rigidity and angular acceptances of the experimental setup.

The Sweeper had an acceptance range of approximately $\pm 10\%$ in momentum. To determine the acceptance range for each beam, the unreacted beam was sent through the Sweeper magnet in a series of regular momentum intervals. These step sweep runs were used to characterize the beam as it moved horizontally across the faces of the charged particle detectors as discussed above. Each step sweep run had an associated magnet setting and position in the detectors at which the beam appeared. The limits on each side of the central magnet

setting could then be deduced and used to determine the actual magnetic rigidity acceptance and active detector area.

The magnetic rigidities and trajectories exiting the target of the final simulated charged particle fragments were determined based on the results of the CoMD + GEMINI++ and INCL++ simulations. Gates were placed on the simulated data to accept or reject the fragments based on whether the fragments would pass through the acceptance ranges of the charged particle detectors to create sets of "accepted" events and the correlated neutrons.

4.3.2 Neutron Gates

The GEANT4 code is a well-known simulation package using Monte Carlo methods to model the passage of particles through detectors [112, 113]. GEANT4 has been used to simulate the interactions of the neutrons in MoNA LISA in the past [97, 101, 110, 111] and also in this work.

The neutron momentum vector in the laboratory frame and energy from the neutrons in the accepted events were used to determine the neutron's interaction in the plastic scintillator material. Text files containing the neutron four-vector information were created from INCL++ and each version of CoMD + GEMINI++ for each reaction. Each neutron was tagged with an event number to connect it back to the collision event that produced it from CoMD + GEMINI++ or INCL++. The text files were then passed to GEANT4.

In GEANT4, the neutrons were propagated through the Sweeper magnet steel because MoNA LISA was configured to cover angles ranging from -3 degrees to 51 degrees relative to the target. Interactions of the neutrons in the steel plate material in the Sweeper magnet were incorporated into the GEANT4 package. The steel Sweeper material was approximated with the neutron scattering cross section of iron [110].

The neutrons were then propagated forward towards the MoNA LISA bars. The location of the bars relative to the target was matched to the physical location of the bars within the experimental configuration. Figure 4.36 shows a top-down view of the simulated hit interactions in the bars from INCL++ and the second symmetry option for CoMD + GEMINI++. The angles of the neutron interaction relative to the target are shown in Figure 4.37. As seen in both Figures 4.36 and 4.37, the angular distribution of neutrons from the CoMD + GEMINI++ model was somewhat broader, with slightly more neutrons measured in the LISA-2 table relative to the number of neutrons measured in the LISA-2 table for INCL++. Neutron interaction cross sections in the hydrocarbon plastic bars were taken from the MENATE_R package [114], which includes neutron interaction cross sections for both carbon and hydrogen for neutrons. The MENATE_R package has been previously shown to have better agreement with experimental data taken with MoNA LISA compared to simulations run with the stock GEANT4 physics processes [115]. The GEANT4 code required a threshold to mimic the QDC hardware threshold gate of the physical detectors. In this analysis, only hits above 0.9 MeVee were counted towards hit multiplicity, so the simulated threshold for the MoNA LISA PMTs was set to 0.9 MeVee.

The neutron interaction information output from GEANT4 was matched back with the event number in CoMD + GEMINI++ or INCL++ to create a simulated hit multiplicity for each single collision determined by counting the number of simulated valid neutron hits within each event. The normalized probability distributions were then constructed for each isotope and are shown in Chapter 5.

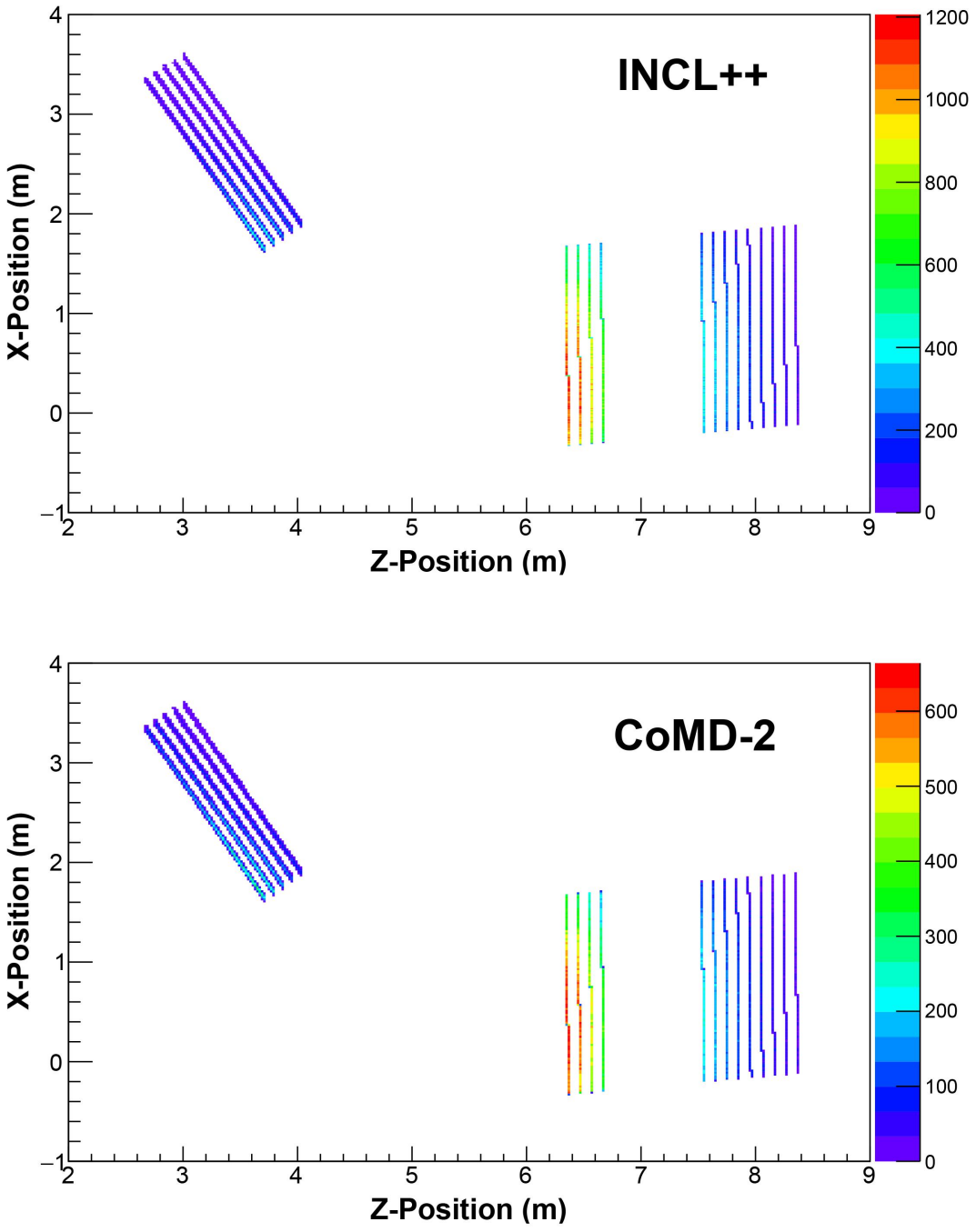

Figure 4.36: Simulated hit interactions in MoNA LISA bars for neutrons from the ^{40}S + ^{9}Be reaction. The top panel shows interactions from the INCL++ model, while the bottom panel (CoMD-2) shows interactions from the CoMD + GEMINI++ for the second symmetry energy option (stiff-1).

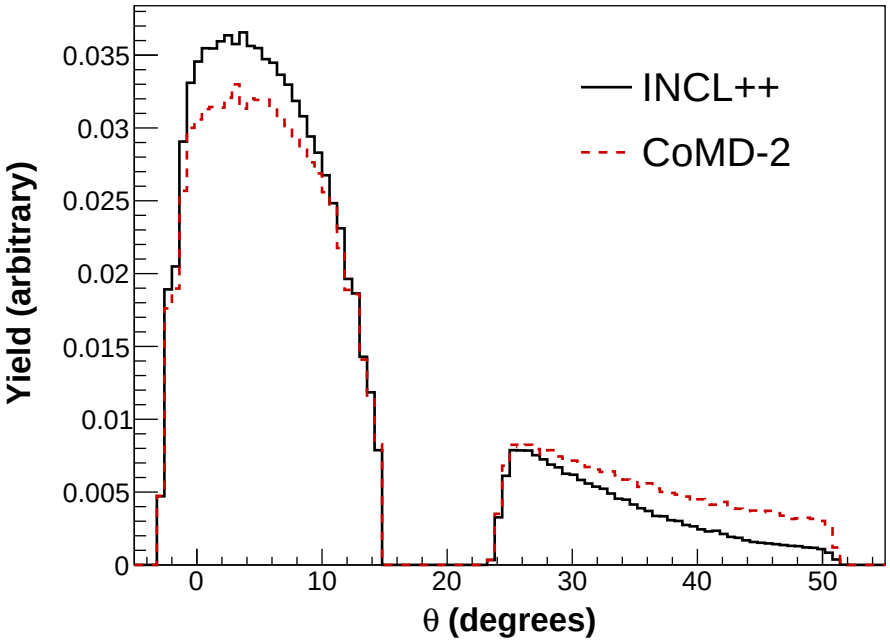

Figure 4.37: Simulated hit interaction angles in MoNA LISA bars for neutrons from the ^{40}S + ^{9}Be reaction. INCL++ and the second symmetry energy option (stiff-1, labeled here as CoMD-2) for CoMD + GEMINI++ are shown. The neutrons with angles of around -3 to 15 degrees were measured in MoNA and LISA-1, while the neutrons with angles of around 24 to 53 degrees were measured in LISA-2.

Chapter 5

Results and Discussion

After the calibrations were completed and fragment-neutron coincidence events were selected from the data set for analysis, the experimental data set was then compared to the results of the two reaction simulations. As previously discussed in Chapter 2, the two simulation data sets involved in this work were the Liège Intranuclear Cascade model (INCL++) and the combined Constrained Molecular Dynamics model and GEMINI++ (CoMD + GEMINI++). The CoMD model contained three options for the symmetry energy: stiff-2, stiff-1, and soft, which are referred to as CoMD-1, CoMD-2, and CoMD-3, respectively, in this work. As described in Chapter 4, each simulation data set was passed through a GEANT4 model of the neutron interactions with the detectors.

A summary of the isotopic fragments identified in the experimental data for each reaction is given in Figure 5.1. Note that many other isotopes than those shown in the figure were produced from the reaction, but not all produced fragments traveled through the acceptance gates of the Sweeper magnet and the charged particle detectors. Furthermore, as discussed previously in Chapter 4, no isotope identification was achieved for elements above sodium. Thus, those element rows in the figure are left blank.

As Figure 5.1 shows, several isotopes were produced and identified in both the ^{30}S + ^{9}Be and ^{40}S + ^{9}Be reactions. These shared isotopes included symmetric nulcei ($N = Z$).

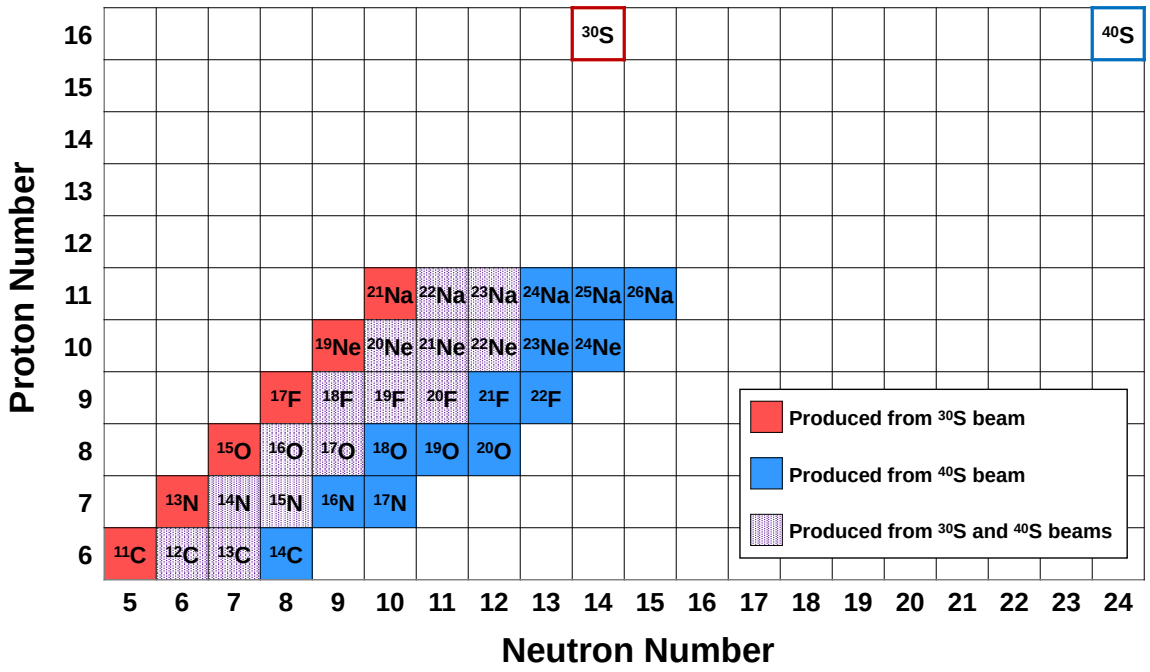

Figure 5.1: Isotopic fragments identified the experimental data. Red boxes indicate isotopes only identified from the ^{30}S + ^{9}Be reaction, blue boxes indicate isotopes only identified from the ^{40}S + ^{9}Be reaction, and purple dotted boxes indicate isotopes identified from both reactions. For comparison, the ^{30}S and ^{40}S incident beams are outlined in red and blue, respectively.

Additional fragments identified from the ^{40}S beam were neutron-rich, while some fragments identified from the ^{30}S beam were proton-rich.

5.1 Hit Multiplicities

Hit multiplicity distributions were used to compare the experimental hits measured in MoNA LISA in coincidence with fragments to the simulated hits from the reaction models. An example of hit multiplicity distributions containing experimental data and simulated data is shown in Figure 5.2. The example distribution shows the hit multiplicity distribution for

^{16}O fragments from the ^{30}S + ^{9}Be reaction with the 1.51 Tm Sweeper magnet setting. The other comparisons of the hit multiplicity distributions are shown later in this chapter.

The hit multiplicity distributions are shown in terms of "probability," in which the distributions were normalized relative to the total number of observed hits for each fragment measured in a given magnet setting. A hit multiplicity of zero indicated a fragment that did not coincide with any measured hits in MoNA LISA; a hit multiplicity of one indicated a fragment that coincided with one hit in MoNA LISA; and so forth. The probabilities of the distributions were plotted on log scales to better display differences among hit multiplicities as the hit multiplicity of zero dominates the distributions.

A consistent representation of the distributions is used in this chapter. Solid black squares represent experimental data; open pink squares represent INCL++ simulations; and open blue diamonds, open up-pointing red triangles, and open down-pointing green triangles represent CoMD + GEMINI++ simulations with the CoMD-1 (stiff-2), CoMD-2 (stiff-1), and CoMD-3 (soft) options, respectively. The data points for the simulations were slightly offset in hit multiplicity to prevent symbols from completely overlapping. The INCL++, CoMD-1, CoMD-2, and CoMD-3 points were offset in the horizontal direction by -0.1, 0.1, 0.15, and 0.2, respectively, relative to the experimental data points.

The relative uncertainty or error was calculated with the following equation:

$$E_i = \frac{P_i}{\sqrt{C_i}} \tag{5.1}$$

where i was the hit multiplicity value (bin number), P_i was the probability value of the multiplicity, and C_i was the number of counts in the multiplicity.

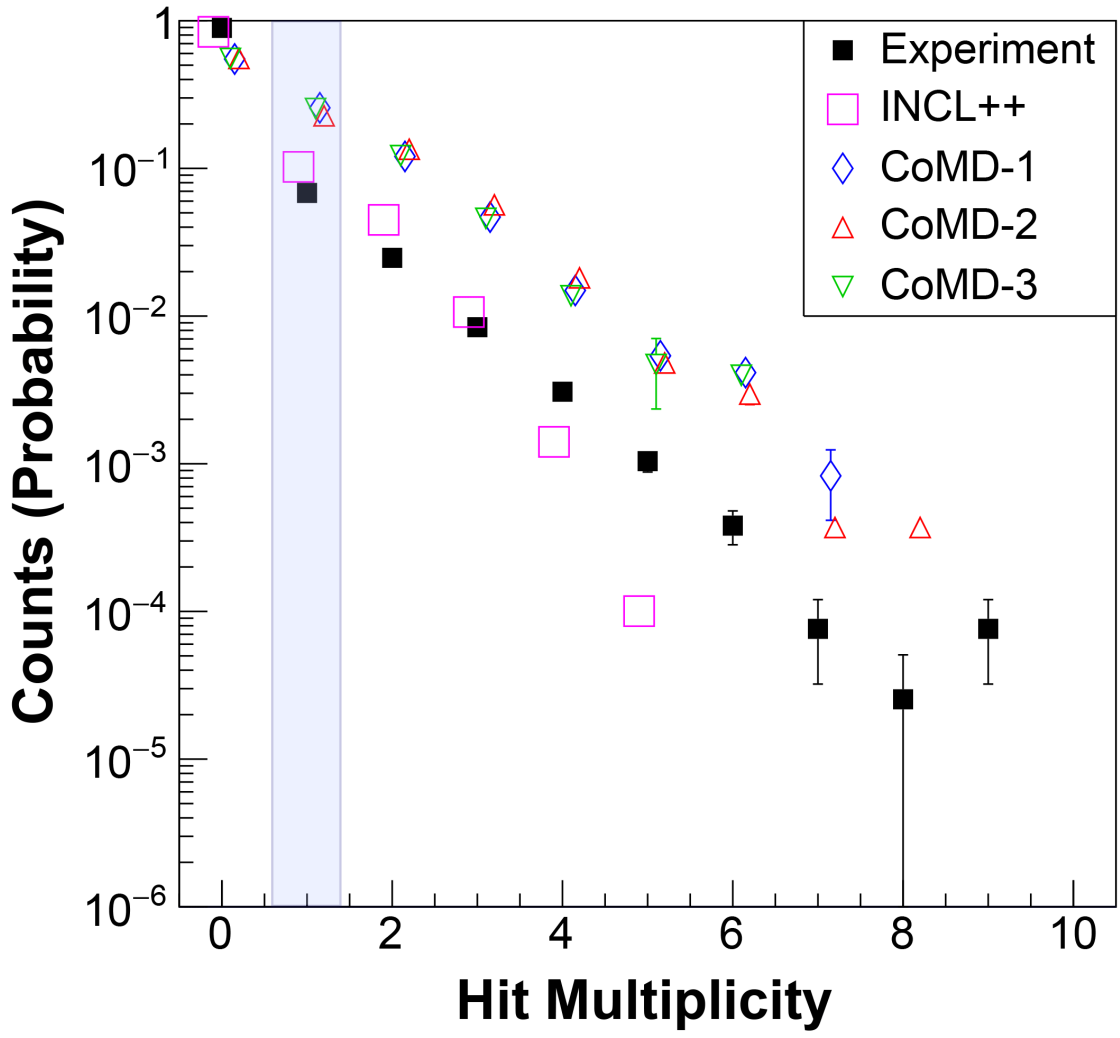

Figure 5.2: Hit multiplicity distributions for ^{16}O fragments from the ^{30}S + ^{9}Be reaction with the 1.51 Tm Sweeper magnet setting. Distributions are presented in terms of probability (see the text for details). Solid black squares represent experimental data; open pink squares represent INCL++ simulations; and open blue diamonds, open up-pointing red triangles, and open down-pointing green triangles represent CoMD + GEMINI++ simulations with the CoMD-1, CoMD-2, and CoMD-3 options, respectively. For clarity and to avoid overlap, the INCL++, CoMD-1, CoMD-2, and CoMD-3 points were offset in hit multiplicity by -0.1, 0.1, 0.15, and 0.2, respectively. Points representing a hit multiplicity of one are highlighted in shaded blue to demonstrate grouping.

5.1.1 Hit Multiplicities by Element

The hit multiplicity distributions were constructed for each element by summing over the isotopes to have an overall sense of how the distributions behaved. Figure 5.3 shows the hit multiplicities for all carbon fragments. No isotopic gates were applied to obtain the data in this figure. Similar to Figure 4.35 in Chapter 4, these results demonstrate that the fragments produced from the ^{40}S reaction were, not surprisingly, in coincidence with significantly higher numbers of hits in MoNA LISA than the fragments produced from the ^{30}S reaction in the experimental data. While the difference between the two reactions is clear in the experimental data, the simulations show a more subtle difference between the ^{30}S and ^{40}S reactions. Furthermore, it is evident that the majority of experimentally detected charged particles were measured with a hit multiplicity of zero. While INCL++ results appear to replicate the high percentage of fragments with a hit multiplicity of zero, the results of the CoMD + GEMINI++ simulations noticeably under-predict the percentage of fragments with a hit multiplicity of zero. The hit multiplicity distributions for individual carbon isotopes are further explored in Section 5.1.2.

Because no isotopic separation was achieved for elements above sodium, only the elemental hit multiplicity distributions could be extracted for comparison. Figures 5.4, 5.5, 5.6, and 5.7 show the experimental and simulated hit multiplicities for all magnesium, aluminum, silicon, and phosphorus fragments. (While sulfur fragments were also detected, measured, and simulated, comparisons are not shown here due to unreacted beam contamination in some of the magnet settings.) No isotopic gates were applied to these element hit multiplicity distributions.

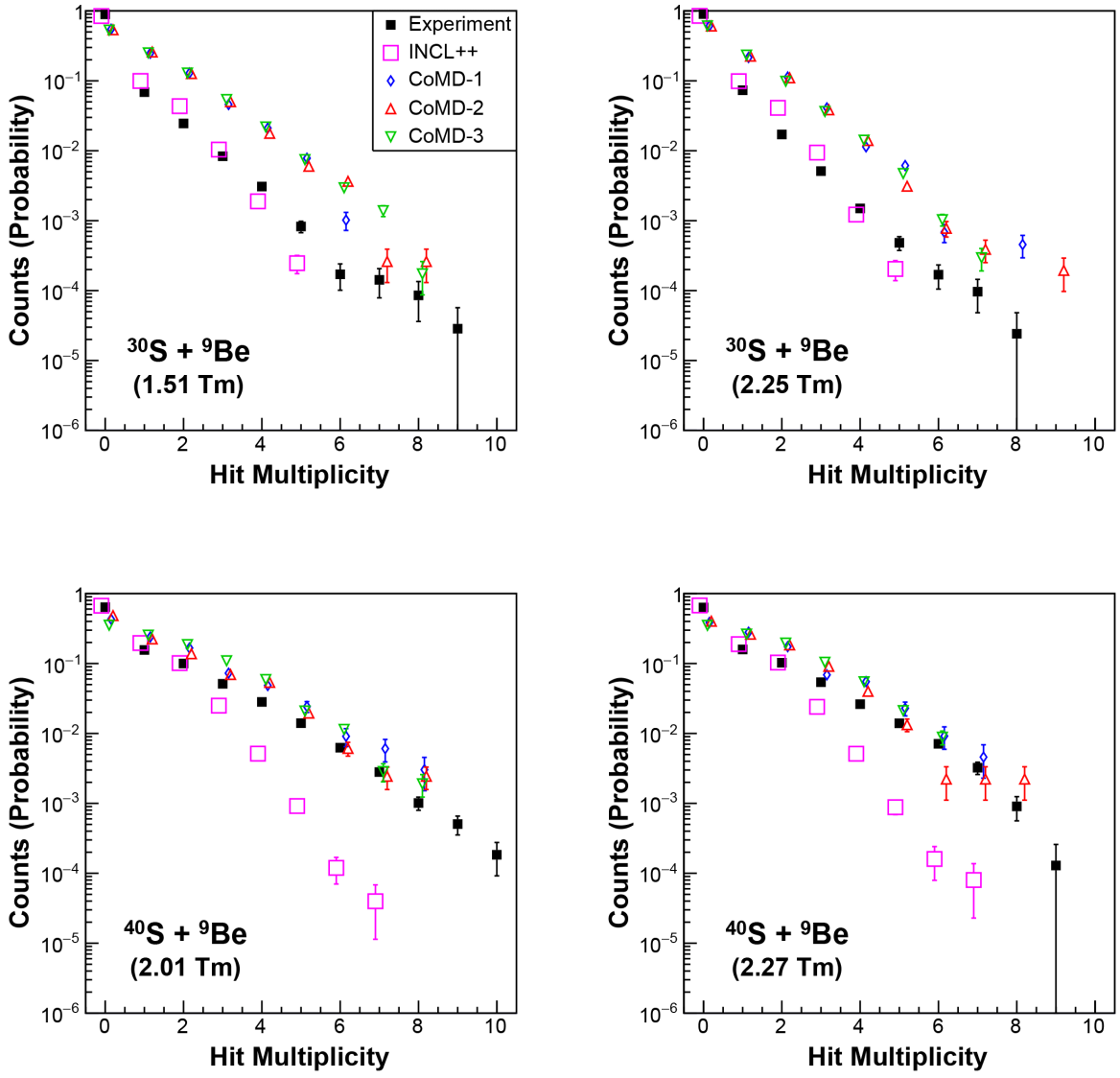

Figure 5.3: Hit multiplicity distribution for all carbon fragments produced in each beam setting for the ^{30}S + ^{9}Be and ^{40}S + ^{9}Be reactions. See text and Figure 5.2 for details. Sweeper acceptance gates were used, but no isotopic gates were applied.

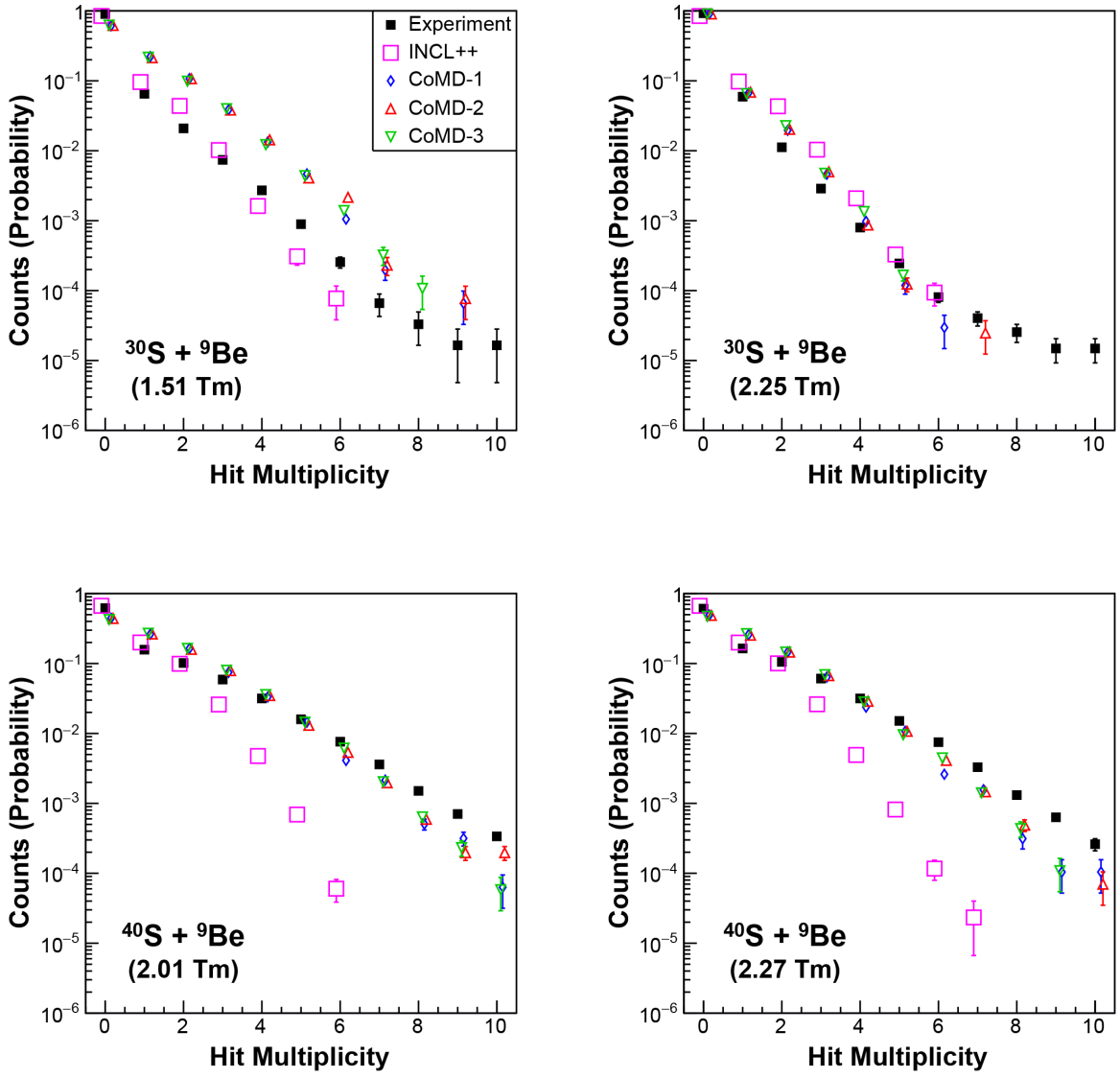

Figure 5.4: Hit multiplicity distribution for all magnesium fragments produced in each beam setting for the ^{30}S + ^{9}Be and ^{40}S + ^{9}Be reactions. See text and Figure 5.2 for details. Sweeper acceptance gates were used, but no isotopic gates were applied.

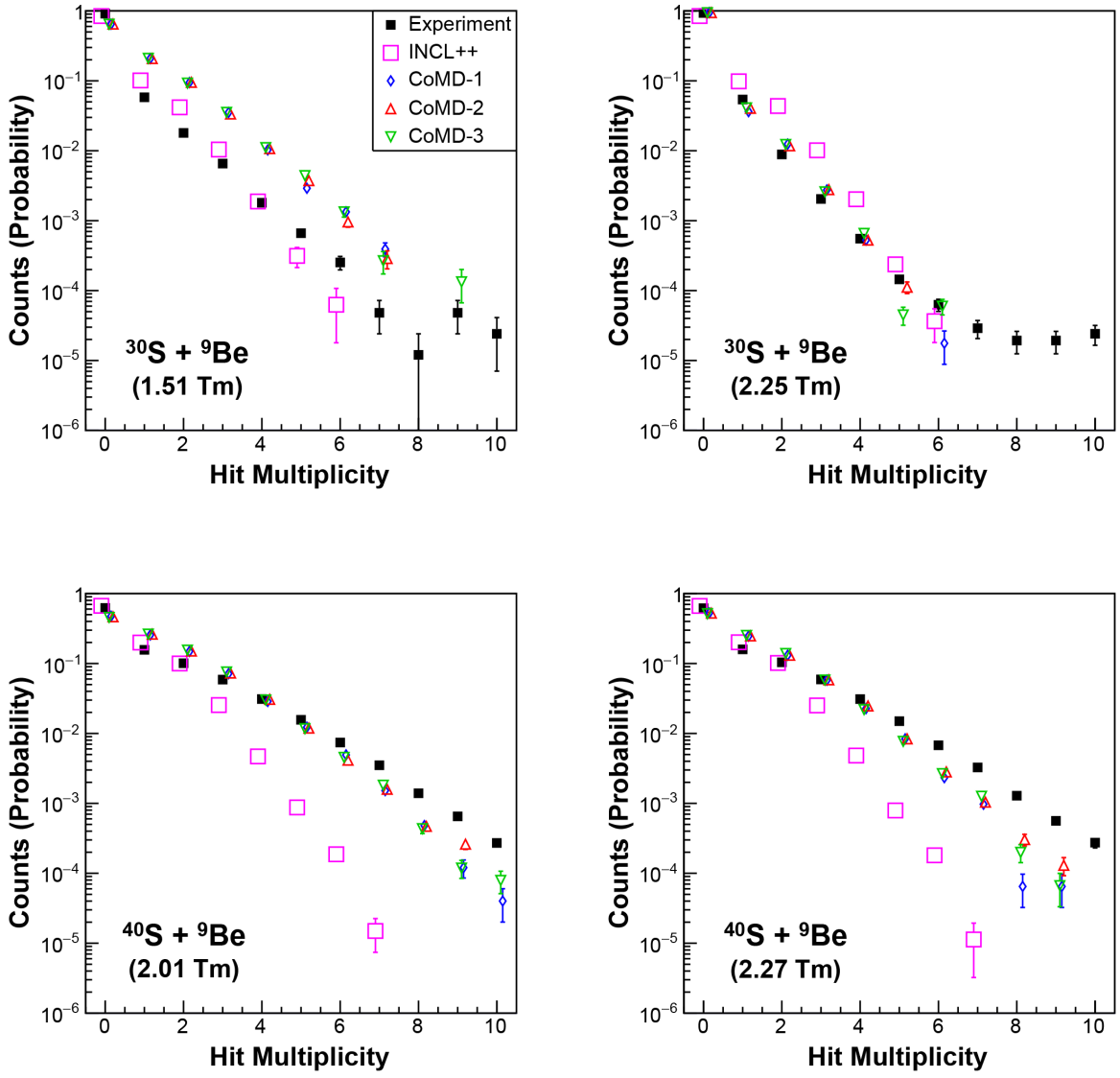

Figure 5.5: Hit multiplicity distribution for all aluminum fragments produced in each beam setting for the ^{30}S + ^{9}Be and ^{40}S + ^{9}Be reactions. See text and Figure 5.2 for details. Sweeper acceptance gates were used, but no isotopic gates were applied.

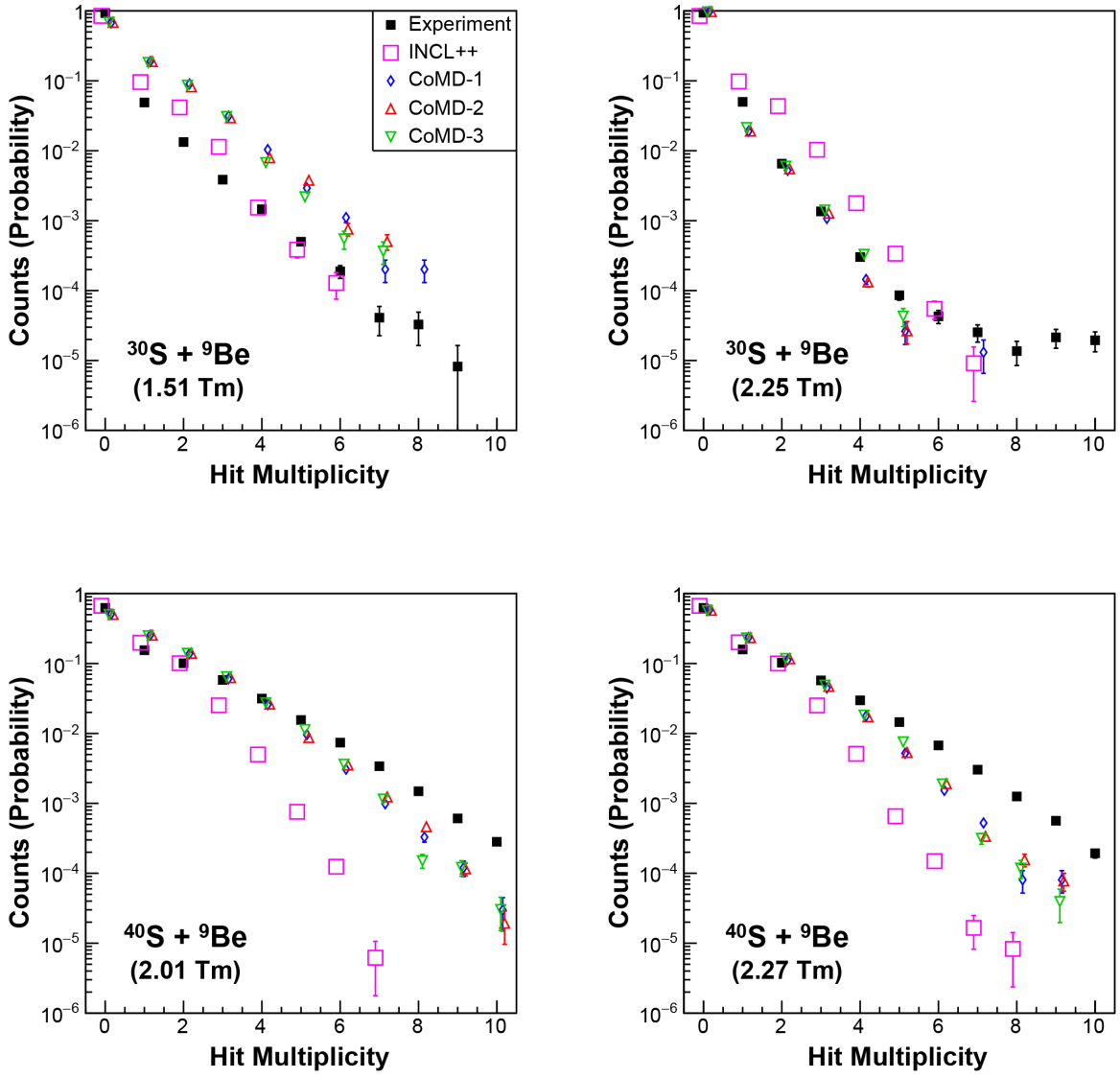

Figure 5.6: Hit multiplicity distribution for all silicon fragments produced in each beam setting for the ^{30}S + ^{9}Be and ^{40}S + ^{9}Be reactions. See text and Figure 5.2 for details. Sweeper acceptance gates were used, but no isotopic gates were applied.

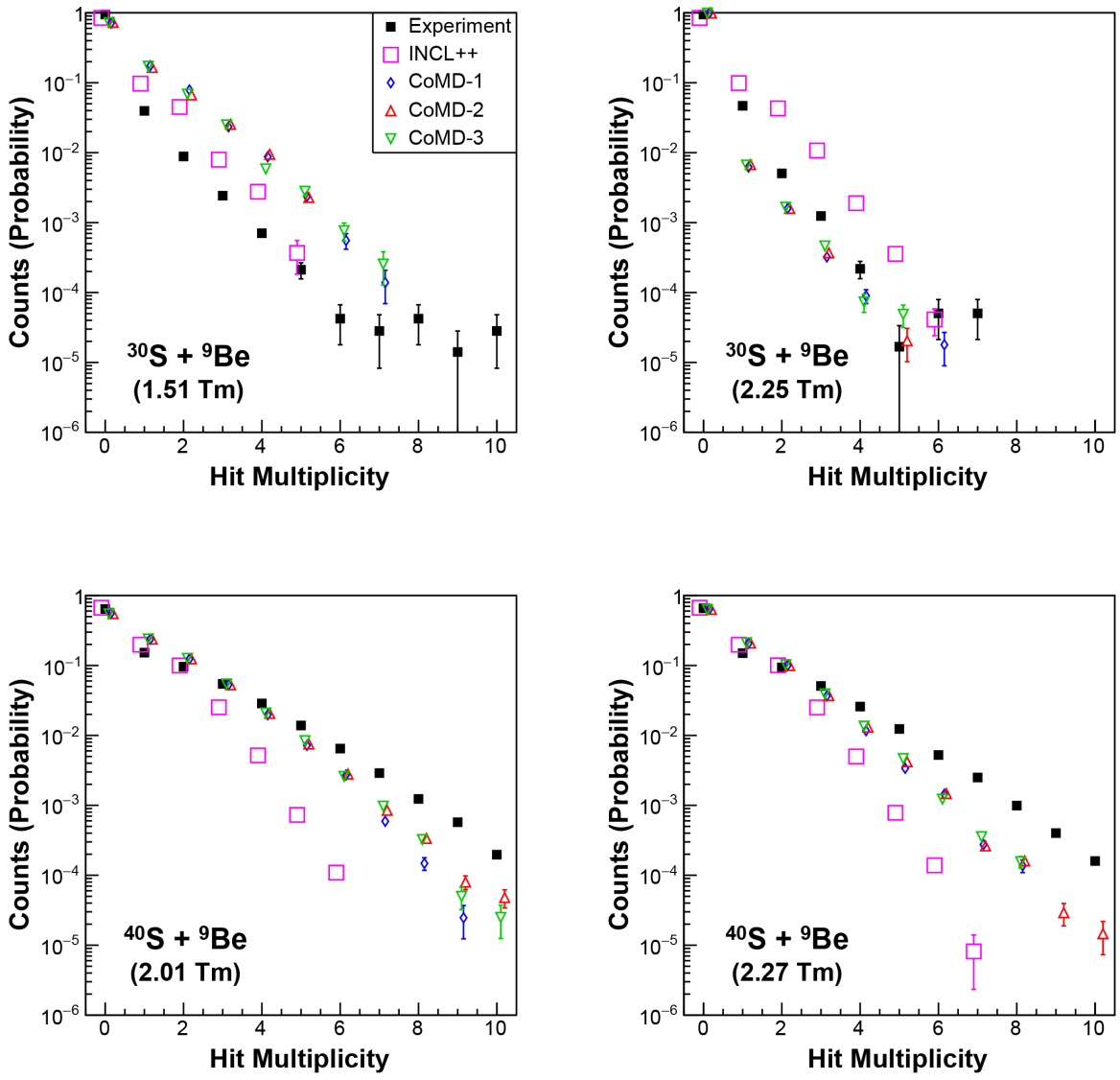

Figure 5.7: Hit multiplicity distribution for all phosphorus fragments produced in each beam setting for the ^{30}S + ^{9}Be and ^{40}S + ^{9}Be reactions. See text and Figure 5.2 for details. Sweeper acceptance gates were used, but no isotopic gates were applied.

These comparisons provided a method to look at elemental fragments that could not be identified by isotope. Overall a consistent pattern can be seen. It appears that for elements with Z values closer to the beam, CoMD + GEMINI++ results begin to match more closely with the data, particularly in results from the ^{30}S reaction with the 2.25 Tm magnet setting. This suggests that CoMD + GEMINI++ could be better at reproducing fragments that have a smaller proton and mass loss from the projectile.

However, no isotopic comparisons can be made at these higher elements in the present data set. Experiments designed to accomplish higher element isotopic separation may be able to examine this effect more closely. This could be done with set-ups that already provide better isotopic separation at higher proton numbers or with upgrades to the Sweeper magnet and its associated charged particle detectors.

5.1.2 Hit Multiplicities by Isotope

Isotopic hit multiplicity distributions were generated by applying isotopic gates to the experimental data and simulations. Figures 5.8, 5.9, 5.10, 5.11, 5.12, and 5.13 show the hit multiplicity distributions for carbon, nitrogen, oxygen, fluorine, neon, and sodium isotopic fragments, respectively.

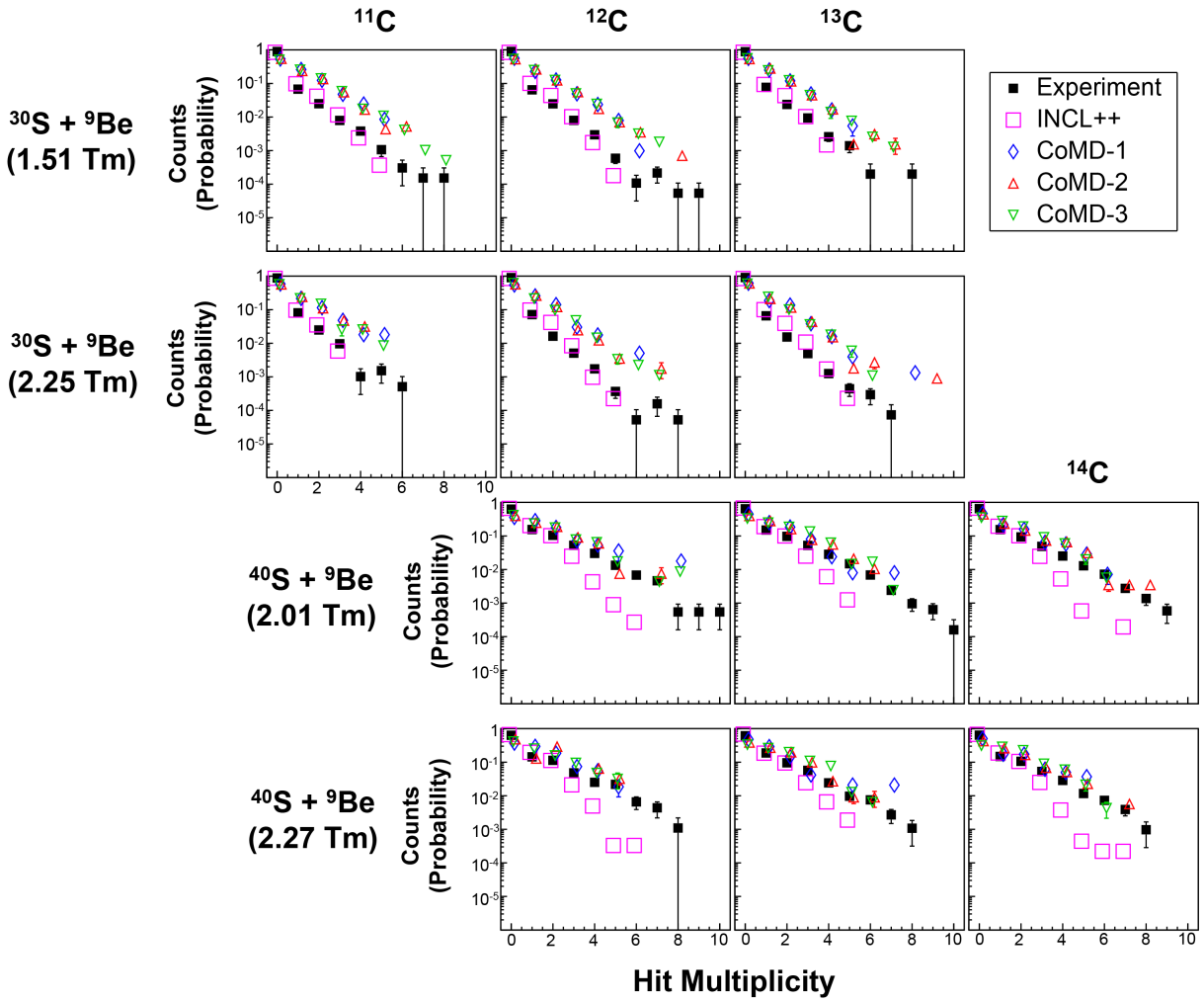

Figure 5.8: Hit multiplicity distribution for carbon isotopes produced in each beam setting for the ^{30}S + ^{9}Be and ^{40}S + ^{9}Be reactions. See the text and Figure 5.2 for details of the display.

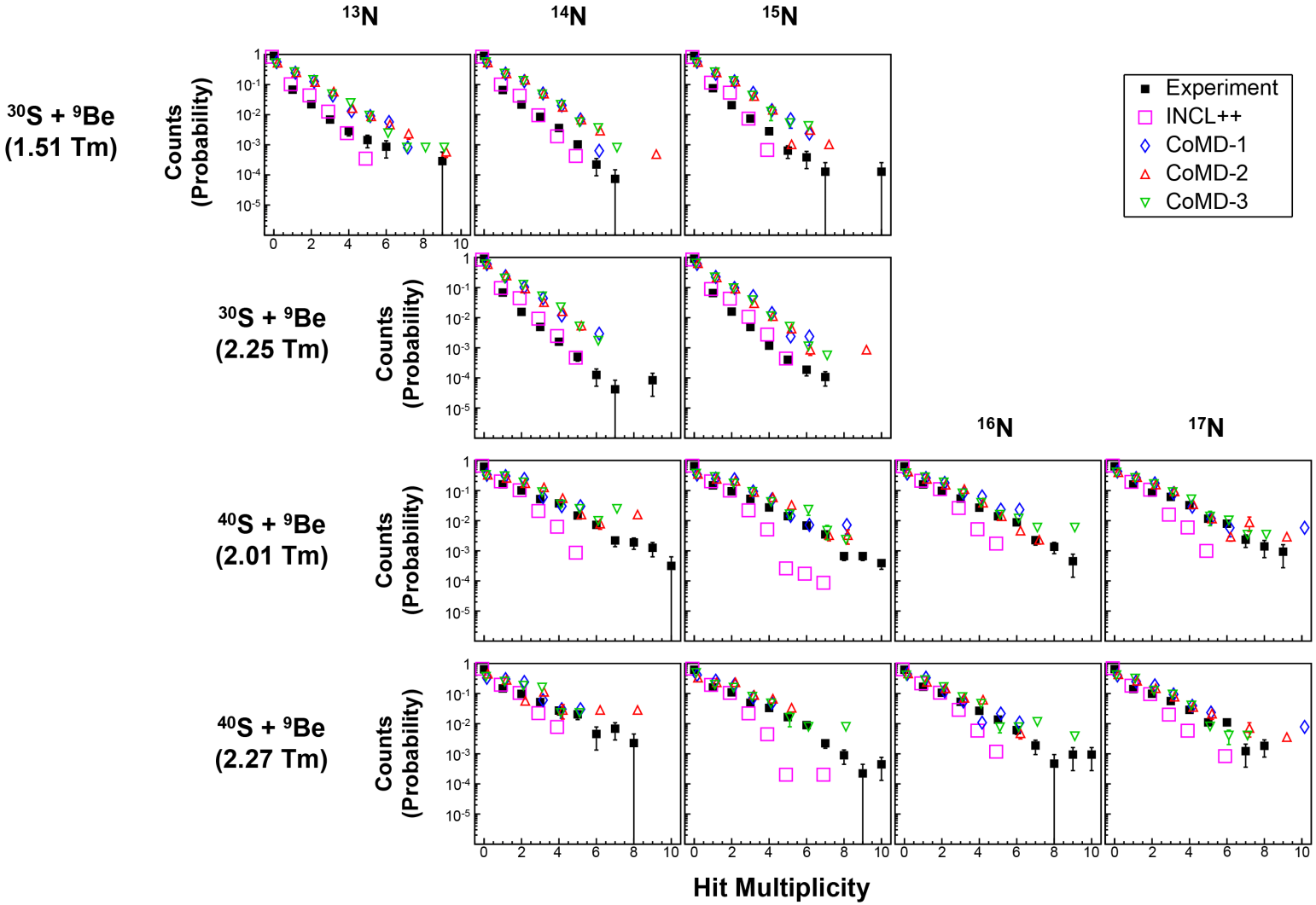

Figure 5.9: Hit multiplicity distribution for nitrogen isotopes produced in each beam setting for the ^{30}S + ^{9}Be and ^{40}S + ^{9}Be reactions. See the text and Figure 5.2 for details of the display.

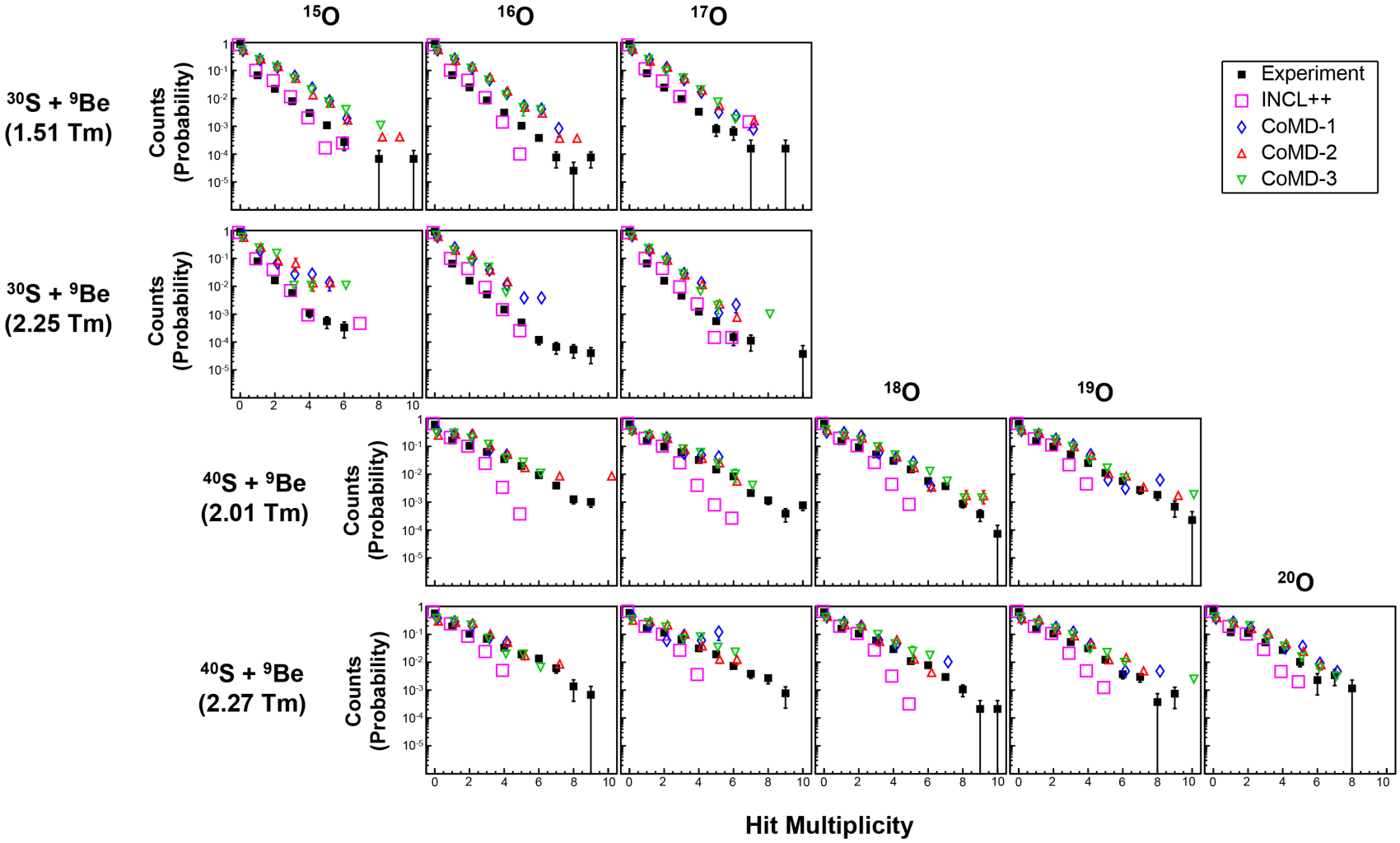

Figure 5.10: Hit multiplicity distribution for oxygen isotopes produced in each beam setting for the ^{30}S + ^{9}Be and ^{40}S + ^{9}Be reactions. See the text and Figure 5.2 for details of the display.

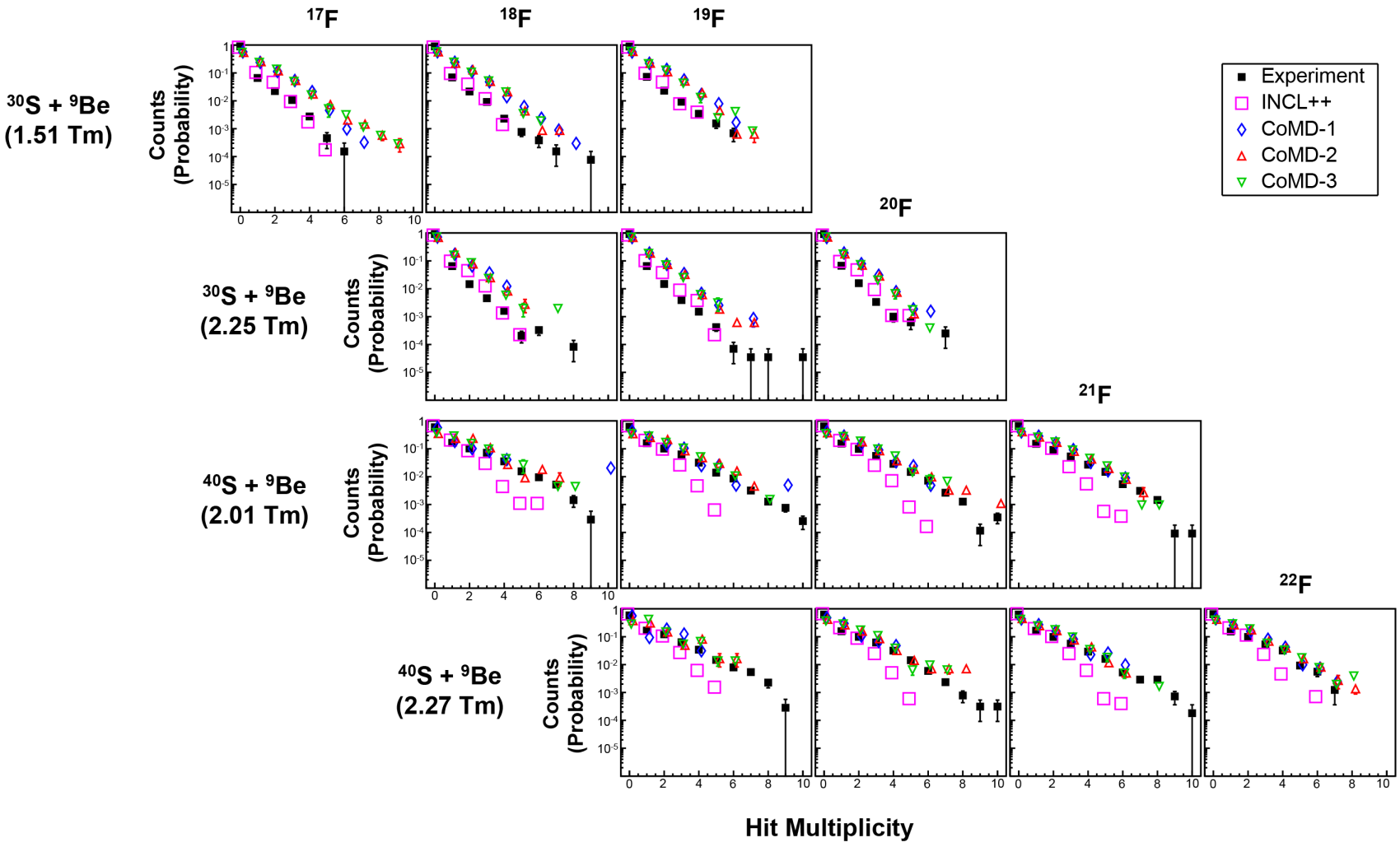

Figure 5.11: Hit multiplicity distribution for fluorine isotopes produced in each beam setting for the ^{30}S + ^{9}Be and ^{40}S + ^{9}Be reactions. See the text and Figure 5.2 for details of the display.

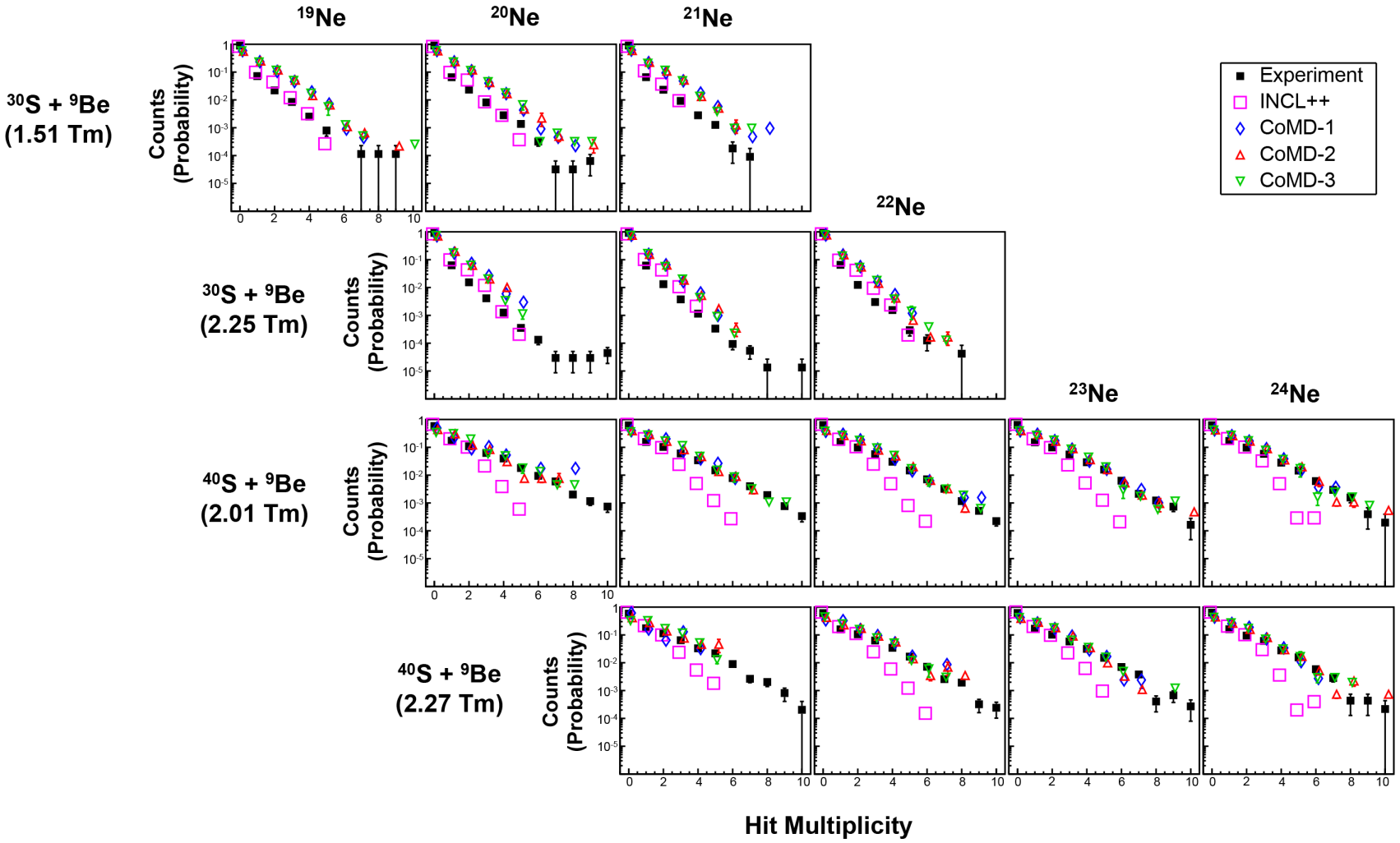

Figure 5.12: Hit multiplicity distribution for neon isotopes produced in each beam setting for the ^{30}S + ^{9}Be and ^{40}S + ^{9}Be reactions. See the text and Figure 5.2 for details of the display.

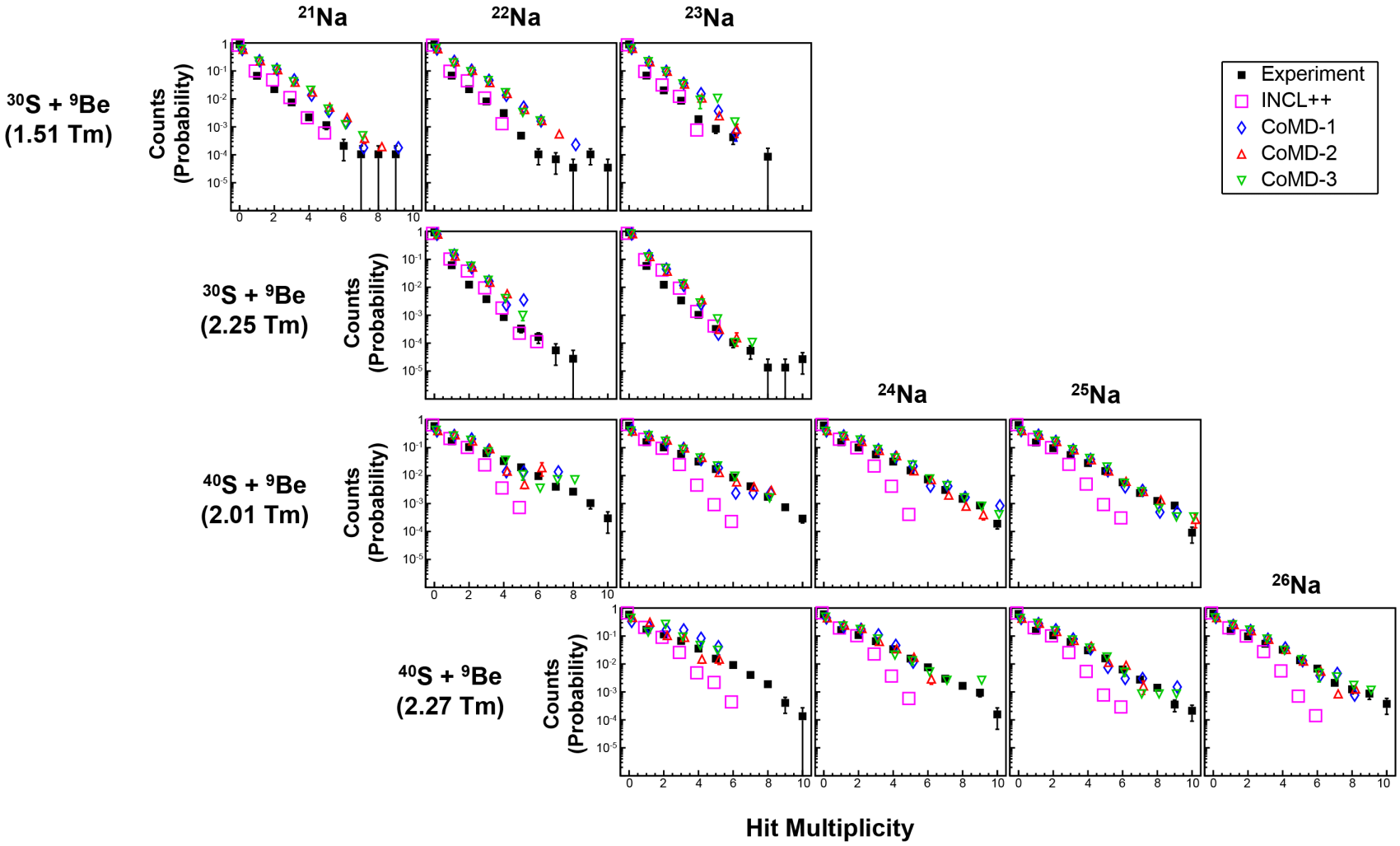

Figure 5.13: Hit multiplicity distribution for sodium isotopes produced in each beam setting for the ^{30}S + ^{9}Be and ^{40}S + ^{9}Be reactions. See the text and Figure 5.2 for details of the display.

Each of the six figures contains a panel for one isotope and they follow a standard format. The top row contains fragments measured from the ^{30}S + ^{9}Be reaction and 1.51 Tm Sweeper magnet setting, the second row contains fragments measured from the ^{30}S + ^{9}Be reaction and 2.25 Tm Sweeper magnet setting, the third row contains fragments measured from the ^{40}S + ^{9}Be reaction and 2.01 Tm Sweeper magnet setting, and the bottom row contains fragments measured from the ^{40}S + ^{9}Be reaction and 2.27 Tm Sweeper magnet setting. The isotopes identified in common to these reactions are lined up in columns. The symbols for the individual hit multiplicity distributions follow the description given in Figure 5.2.

These comparisons of the hit multiplicity distributions display several trends. When comparing isotopes produced from both reactions, such as ^{12}C in Figure 5.8 or ^{15}N in Figure 5.9, it is apparent, again not surprisingly, that those fragments produced from the ^{30}S reaction are predicted to be in coincidence with fewer hits in MoNA LISA compared to fragments produced from the ^{40}S reaction. This was shown as well in Figure 4.35 from Chapter 4 and Figure 5.3, though the previous figures did not involve any isotopic identification.

For isotopes produced from the ^{30}S + ^{9}Be reaction, each of the CoMD + GEMINI++ versions tended to under-predict the proportion of fragments measured with zero hits while over-predicting the proportion of fragments measured with one or more hit. The INCL++ results, on the other hand, matched the experimental data points more closely. While INCL++ did fail to replicate the higher hit multiplicity values present in the data, it is important to note that these higher multiplicity values contain a very small proportion of counts, sometimes representing fewer than 10 counts per bin.

Results from the ^{40}S + ^{9}Be reaction do not match the trends apparent in the ^{30}S + ^{9}Be reaction. While each of the three CoMD + GEMINI++ versions still under-predicted the proportion of fragments measured with zero hits, the overall hit multiplicity trend follows

the data more closely, with a more gentle slope downwards as multiplicity increases. The INCL++ simulation does not appear to follow the trend in the experimental data. Instead, INCL++ results display a much steeper slope in the hit multiplicity distributions due to under-prediction of the number of fragments measured in coincidence with higher numbers of hits.

For a quantitative comparison, a χ^2 statistic was calculated with the following equation:

$$\chi^2 = \sum_{i=0}^{n} \frac{(P_i^{data} - P_i^{sim})^2}{(E_i^{data})^2} \tag{5.2}$$

where i was the hit multiplicity value (bin number), P_i^{data} was the probability value of the experimental data, P_i^{sim} was the probability value of the simulation set (INCL++, CoMD-1, CoMD-2, or CoMD-3), and E_i^{data} was the uncertainty in the data.

A reduced χ_v^2 was used to compare the models to the experimental data. The inclusion of hit multiplicity values or bins with very few events could skew the comparison by placing more importance on those few events. In order to minimize this effect, only hit multiplicity values with more than five events were included. The reduced χ_v^2 was found with following equation:

$$\chi_v^2 = \frac{\chi^2}{ndf} \tag{5.3}$$

where *ndf* was the number of degrees of freedom. As usual, if the given simulation matched the data within the experimental uncertainties, the χ_v^2 value would be one. The larger the χ_v^2 value, the worse the fit. These χ_v^2 values are shown in Appendix D.

In general, the χ_v^2 values demonstrate the features observed in the previous figures, but are dominated by the lowest hit bins. Overall, the INCL++ simulations were closer in

predicting the hit multiplicity zero bin than the CoMD + GEMINI++ simulations. Because the majority of identified fragments coincided with zero hits, the χ^2_v values for the INCL++ predictions were lower (with typical χ^2_v values in the tens and hundreds) than those of the CoMD + GEMINI++ simulations (with typical χ^2_v values in the hundreds and thousands). The CoMD + GEMINI++ simulations greatly under-predicted the number of fragments produced with zero hits, leading to larger χ^2_v values.

The makers of the CoMD model acknowledged that the earliest iteration was over-producing hydrogen and helium fragments from their test collisions (symmetric reactions of ^{40}Ca + ^{40}Ca at 35 MeV/u and ^{197}Au + ^{197}Au at 35 MeV/u) [69]. The authors believed that this was due to the occupation density limitation, which randomly changes the momenta of the neighboring particles if the Pauli principle is violated and may be under-producing intermediate-mass fragments through break-up or fission. While CoMD has been modified since the earliest iteration, it appears that more attention is needed on neutron yields.

It is important to note that while INCL++ did a better job, it is still not a perfect match. In particular, INCL++ fails to generate enough events with higher hit counts in MoNA LISA.

5.2 Symmetry Energy

The CoMD model provides a dynamical description of the evolution of the many-body system. One of the advantages of the CoMD model is the inclusion of three different symmetry energy parameterizations. Each parameter gives a distinct mathematical form of the symmetry energy. If the three options produce different results, the experimental data could be

compared to the simulations to determine which of the three versions fits the experimental data best.

In this work, the three CoMD + GEMINI++ options do not appear to produce significant differences in the hit multiplicity distributions as shown in Figures 5.3-5.13. Instead, the CoMD + GEMINI++ points on these figures generally overlap. This indicates that neutron multiplicity distributions from the intermediate-energy heavy-ion collisions are not a good method for constraining the symmetry energy term in the nuclear equation of state. Thus, no constraint on the symmetry energy was attempted using this experimental data set.

5.3 Fragment Production

5.3.1 Isotope Production

While this project focused on the exclusive measurement of neutrons measured in coincidence with charged particle fragments, it was possible to examine the isotope production distributions for the experimental data and simulations. The isotope production distributions for the for the ^{30}S + ^{9}Be reaction and 1.51 Tm and 2.25 Tm magnet settings are shown in Figures 5.14 and 5.15, respectively. The isotope production distributions for the for the ^{40}S + ^{9}Be reaction and 2.01 Tm and 2.27 Tm magnet settings are shown in Figures 5.16 and 5.17, respectively. For all four distributions, the counts were normalized relative to the total number of observed fragments within the given element for that magnet setting. The stiff-2, stiff-1, and soft options for CoMD + GEMINI++ are referred to as CoMD-1, CoMD-2, and CoMD-3, respectively. The model distributions were filtered with fragment gates as described in Section 4.3.

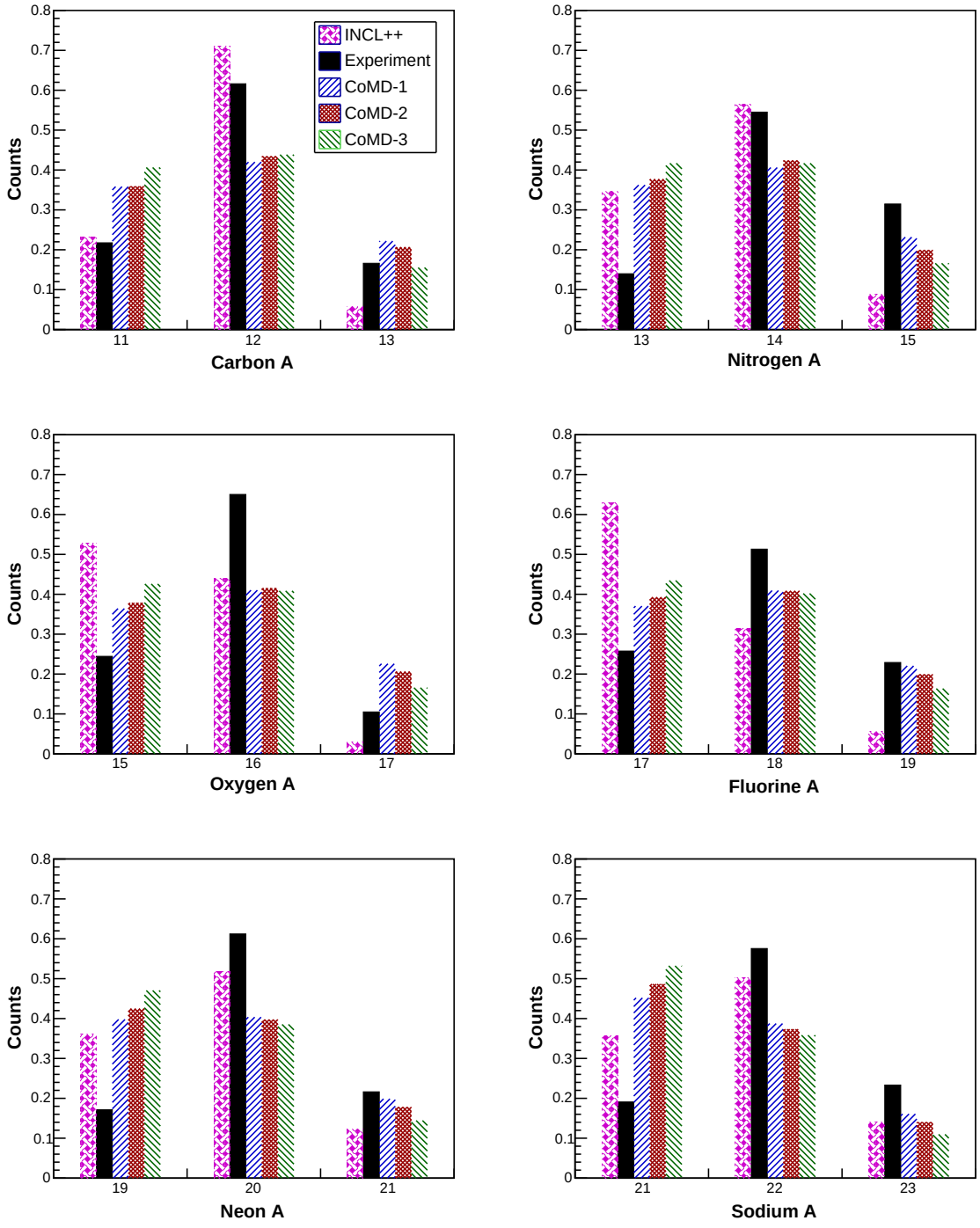

Figure 5.14: Isotope production distributions for the ^{30}S + ^{9}Be reaction and the 1.51 Tm magnet setting. Counts are given in terms of probability normalized relative to the total number of observed fragments within the given element. The CoMD + GEMINI++ model stiff-2, stiff-1, and soft options are referred to as CoMD-1, CoMD-2, and CoMD-3, respectively.

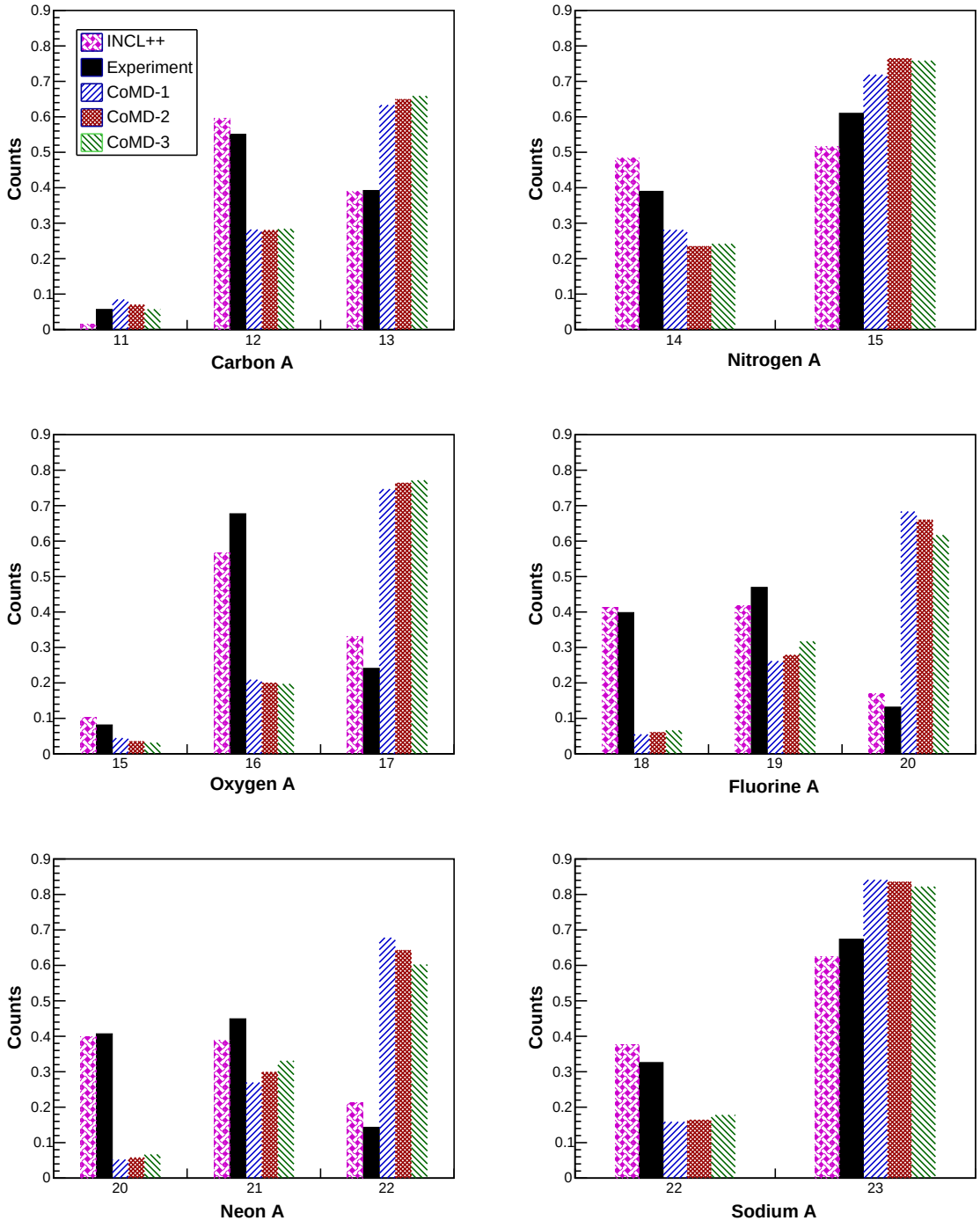

Figure 5.15: Isotope production distributions for the ^{30}S + ^{9}Be reaction and the 2.25 Tm magnet setting. Counts are given in terms of probability normalized relative to the total number of observed fragments within the given element. The CoMD + GEMINI++ model stiff-2, stiff-1, and soft options are referred to as CoMD-1, CoMD-2, and CoMD-3, respectively.

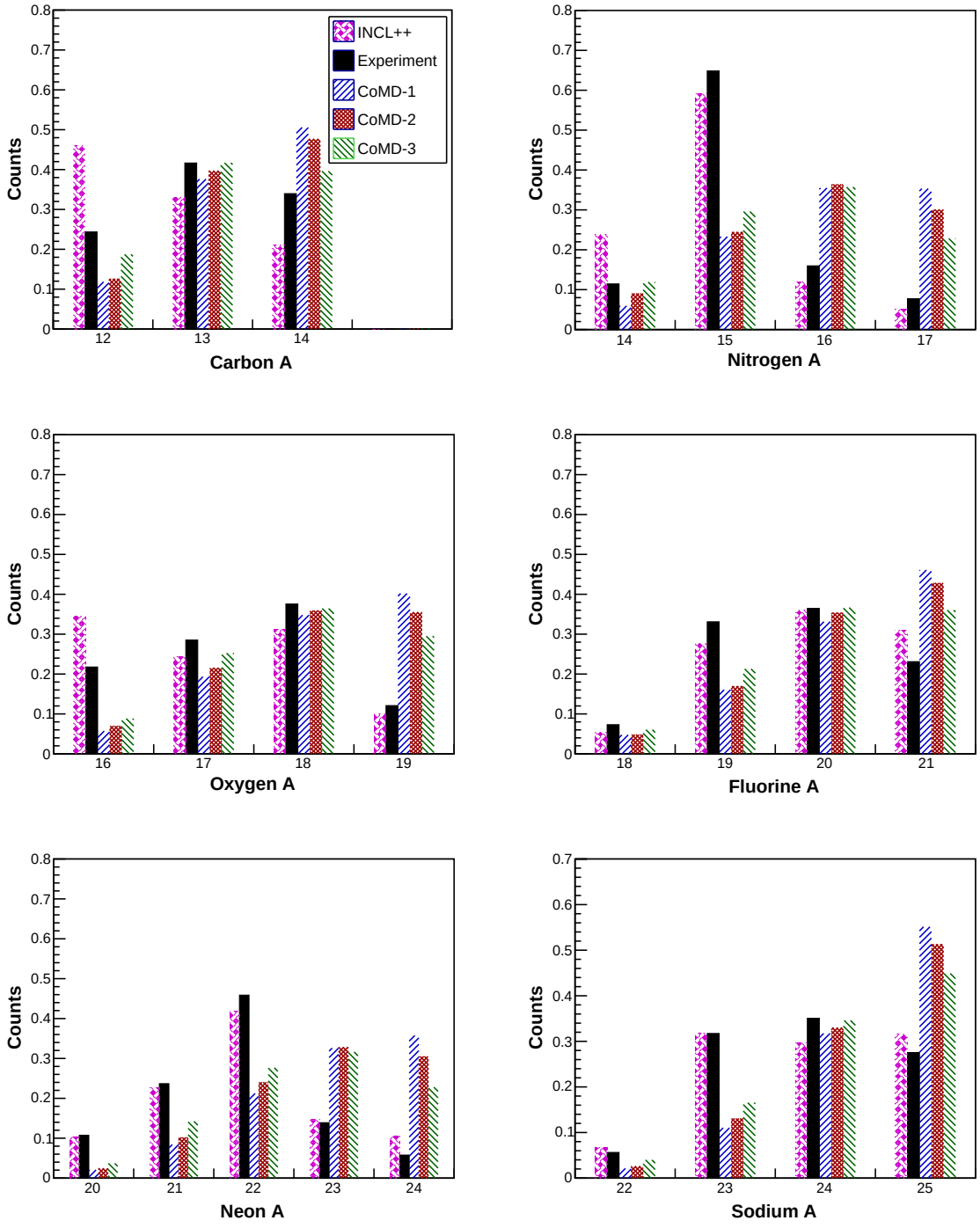

Figure 5.16: Isotope production distributions for the ^{40}S + ^{9}Be reaction and the 2.01 Tm magnet setting. Counts are given in terms of probability normalized relative to the total number of observed fragments within the given element. The CoMD + GEMINI++ model stiff-2, stiff-1, and soft options are referred to as CoMD-1, CoMD-2, and CoMD-3, respectively.

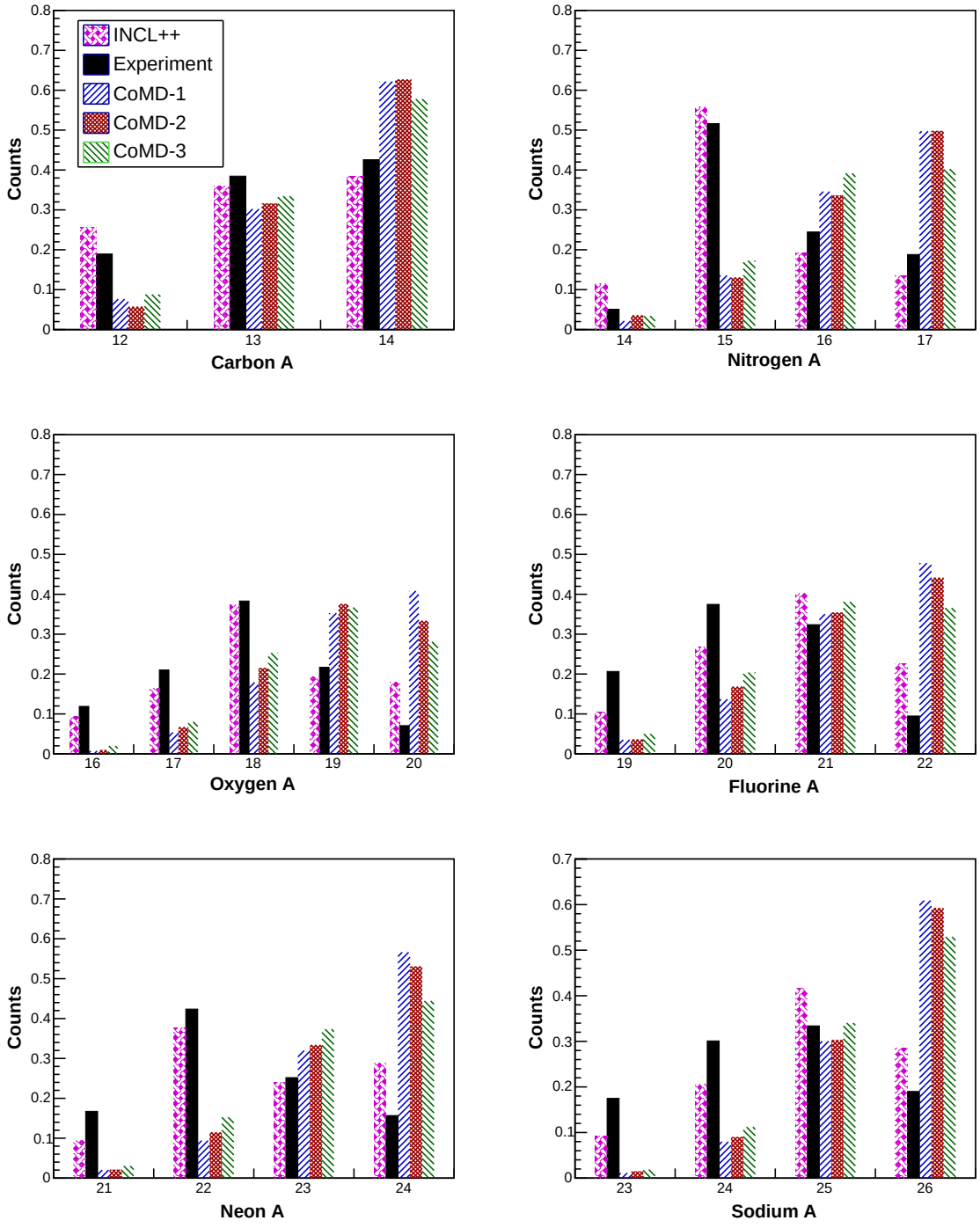

Figure 5.17: Isotope production distributions for the ^{40}S + ^{9}Be reaction and the 2.27 Tm magnet setting. Counts are given in terms of probability normalized relative to the total number of observed fragments within the given element. The CoMD + GEMINI++ model stiff-2, stiff-1, and soft options are referred to as CoMD-1, CoMD-2, and CoMD-3, respectively.

The experimental data isotope distributions follow the one-dimensional distributions from Figures 4.29-4.32 in Chapter 4. As a whole, the INCL++ simulations follow the trends of the data, with a few notable suggestions. In the oxygen and fluorine isotope distributions for the ^{30}S + ^{9}Be reaction and the 1.51 Tm magnet setting, INCL++ skews towards the more neutron-deficient isotopes. For the ^{40}S + ^{9}Be reaction and the 2.01 Tm magnet setting, INCL++ displayed a stronger preference for production of the even-even ^{12}C and ^{16}O isotopes. Each of the three CoMD + GEMINI++ options skewed neutron-rich in many of the isotope distributions. The three CoMD + GEMINI++ options were relatively similar to each other, though the stiffest option (CoMD-1) did skew to slightly higher mass (and thus more neutron-rich) isotopes relative to the softest option (CoMD-3). This follows the fully inclusive distributions shown in Figures 2.1-2.6 from Chapter 2.

5.3.2 Time Evolution in CoMD

In the present work, the CoMD heavy-ion collisions were propagated up to 2000 fm/c (about 7×10^{-21} s), allowing the system to evolve dynamically and become relatively cool. The previously presented hit multiplicity distributions were taken from the reaction products at 2000 fm/c from CoMD that were passed through GEMINI++ and then the neutrons that were passed through GEANT4. However, output from the CoMD simulations included information of precursor fragments at earlier time steps. This allowed examination of the time evolution of fragments within the simulations.

Figures 5.18 and 5.19 show the time evolution of fragments in the ^{30}S + ^{9}Be and ^{40}S + ^{9}Be reactions, respectively, from the CoMD model with the stiff-1 option. The time steps shown are 20, 40, 80, 200, 1000, and 2000 fm/c. (Other time steps were recorded but are not represented in the figures since only an overview of the time evolution is important here.)

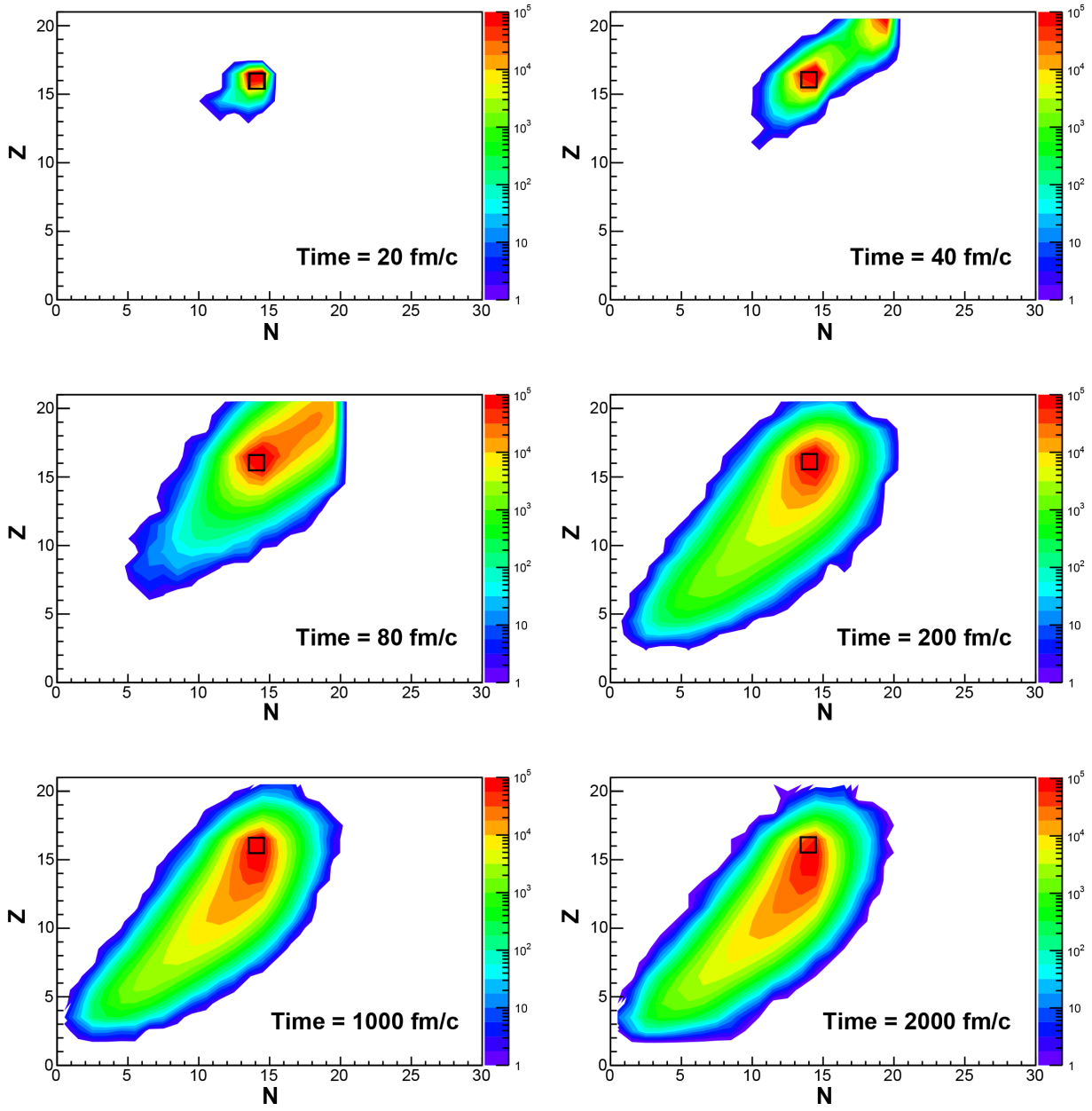

Figure 5.18: Contours in the N-Z plane of the fragment distribution showing the time evolution of fragments in the ^{30}S + ^{9}Be reaction from the CoMD model with the stiff-1 option. Only the heaviest fragments are shown. The boxes indicate the N-Z of the beam.

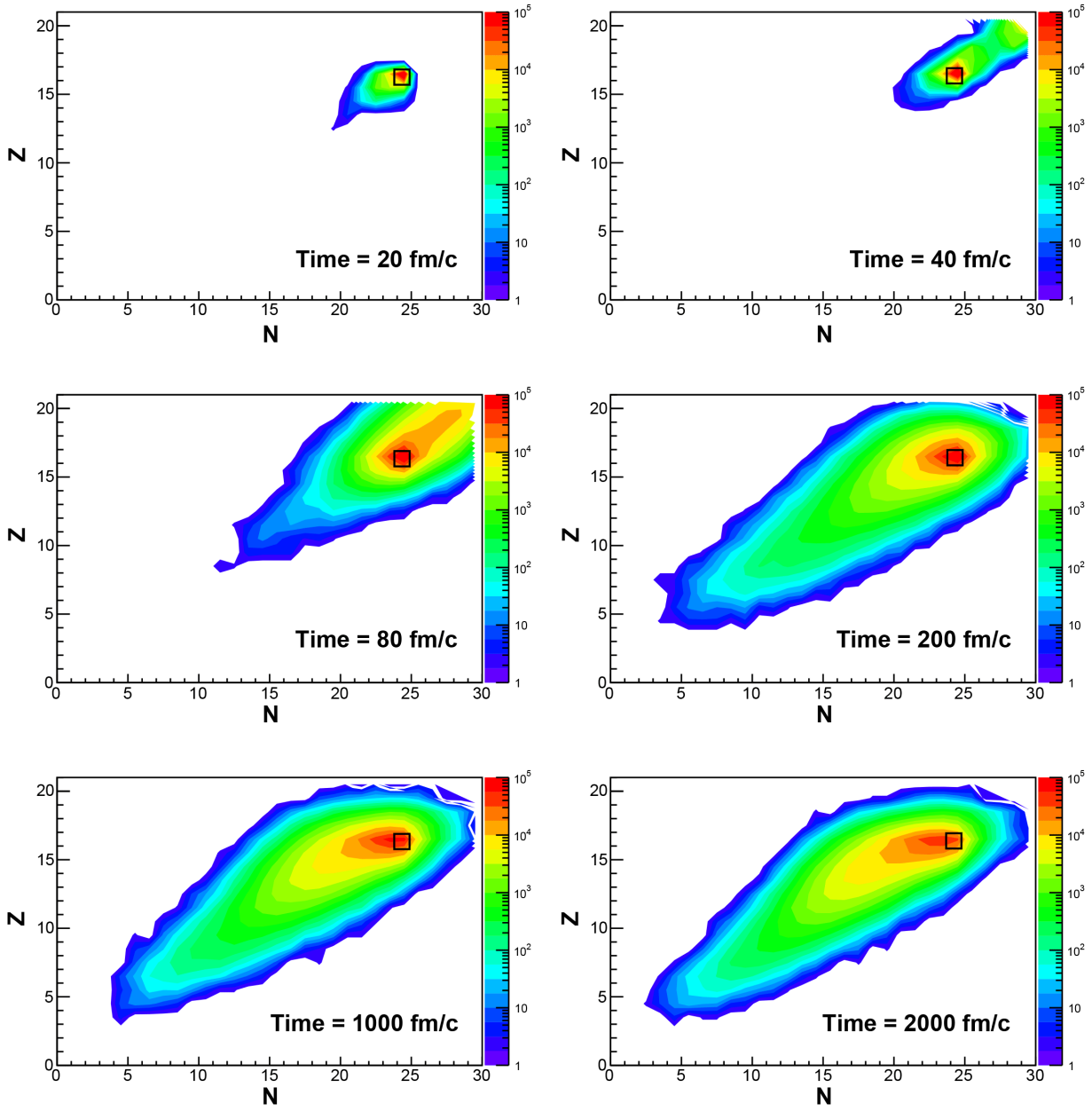

Figure 5.19: Contours in the N-Z plane of the fragment distribution showing the time evolution of fragments in the ^{40}S + ^{9}Be reaction from the CoMD model with the stiff-1 option. Only the heaviest fragments are shown. The boxes indicate the N-Z of the beam.

At 0 fm/c, the projectile (^{30}S or ^{40}S) approaches the target. The 20 fm/c panel shows the early encounter with little change in the projectile. By 40 fm/c, the projectile has interacted with the target, displaying some pick-up of protons and neutrons. In the ^{30}S + ^{9}Be reaction, two very distinct peaks appear, corresponding to fragments around ^{30}S and ^{39}Ca. (^{39}Ca represents the full combination of the ^{30}S projectile and ^{9}Be target.) This phenomenon is less pronounced in the ^{40}S + ^{9}Be reaction, but the effect is still visible. (The full combination of the ^{40}S projectile and ^{9}Be target would produce ^{49}Ca.) Sharp edges in the top and right edges of the distributions indicate the physical limitation in the number of protons and neutrons available when combining the projectile and target in the given reaction system.

At 80 fm/c, the earlier precursor fragments have started to break up. The fragments at this stage begin to reach downward in Z and N as the heaviest fragments shed mass. By 200 fm/c, a general form of the fragment distribution is apparent. At 1000 fm/c, the heavier fragments shed more nucleons, creating more fragments with lower numbers of protons and neutrons. While there is some change from 1000 to 2000 fm/c, the general form is preserved, indicating that the evolution of fragments had stabilized.

In both CoMD reaction simulations, the final fragments are concentrated around the original projectile fragments. The shape of this central concentration demonstrates the direction in which fragments evolved. For example, fragments from the ^{40}S reactions were allowed to evolve more "horizontally" in the N-Z plane, losing neutrons while at higher elements before drifting downwards as Z decreased. Fragments from the ^{30}S evolved more "diagonally" due to the ten fewer neutrons in the system and the proximity to the proton drip line.

In the final time step panels, it is evident that the ^{30}S + ^{9}Be reaction is predicted to produce more proton-rich (or neutron-deficient) isotopes relative to the ^{40}S + ^{9}Be reaction. In the opposite manner, the ^{40}S + ^{9}Be reaction is predicted to produce more neutron-rich isotopes relative to the ^{30}S + ^{9}Be reaction. While not all produced fragments were measured in the experimental data, this qualitative trend from CoMD clearly matches the observed isotopes that were identified from the experimental data set.

5.3.3 Precursor Fragments in INCL++

As described in Chapter 2, INCL++ uses two discrete steps to simulate the nuclear reaction [83–85]. The first step represents the fast part of the reaction to create an excited remnant, or intermediate precursor fragment. The remnant then "cools" through a statistical de-excitation to its final state. In the present work, the statistical de-excitation code ABLA07 was used [89].

It was possible to track the precursor fragment channels that led directly to the final de-excited fragments in such a simulation. Three isotopes were chosen to demonstrate this tracking process. The intermediate precursor fragments that led to final ^{13}C, ^{16}O, and ^{23}Na fragments from INCL++ are shown in Figures 5.20, 5.21, and 5.22, respectively. These fragments were chosen as examples because they were found in each magnet setting for both beams. (For comparison to the CoMD model, the INCL++ precursor fragments would align to CoMD precursor fragments early in the reaction, such as those around 40 fm/c.)

The magnet settings of the Sweeper magnet selected on a slice of fragments within a given range of magnetic rigidity. Changing the magnet setting then changed what slice of fragments was measured. The magnetic rigidity is equal to momentum to charge ratio ($B\rho = p/q = mv/q$) of the fragments. When a specific isotope is selected, the proton

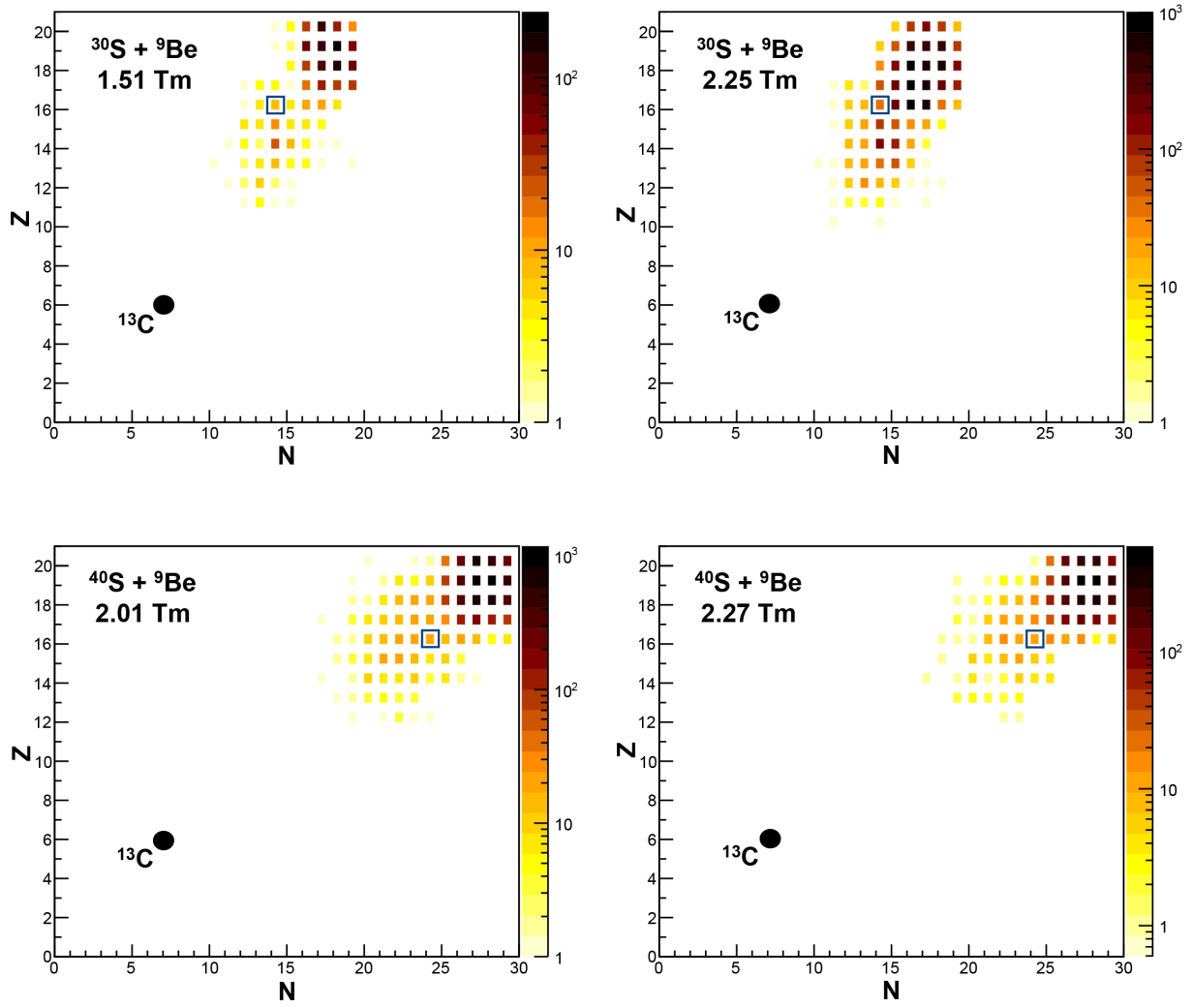

Figure 5.20: Distribution of the intermediate precursor fragments in the N-Z plane from INCL++ for final ^{13}C fragments produced in each beam setting for the ^{30}S + ^{9}Be and ^{40}S + ^{9}Be reactions. The intermediate precursor fragments are represented by the solid boxes. Open squares representing the beams (^{30}S or ^{40}S) and solid black circles representing the position of ^{13}C are displayed for comparison.

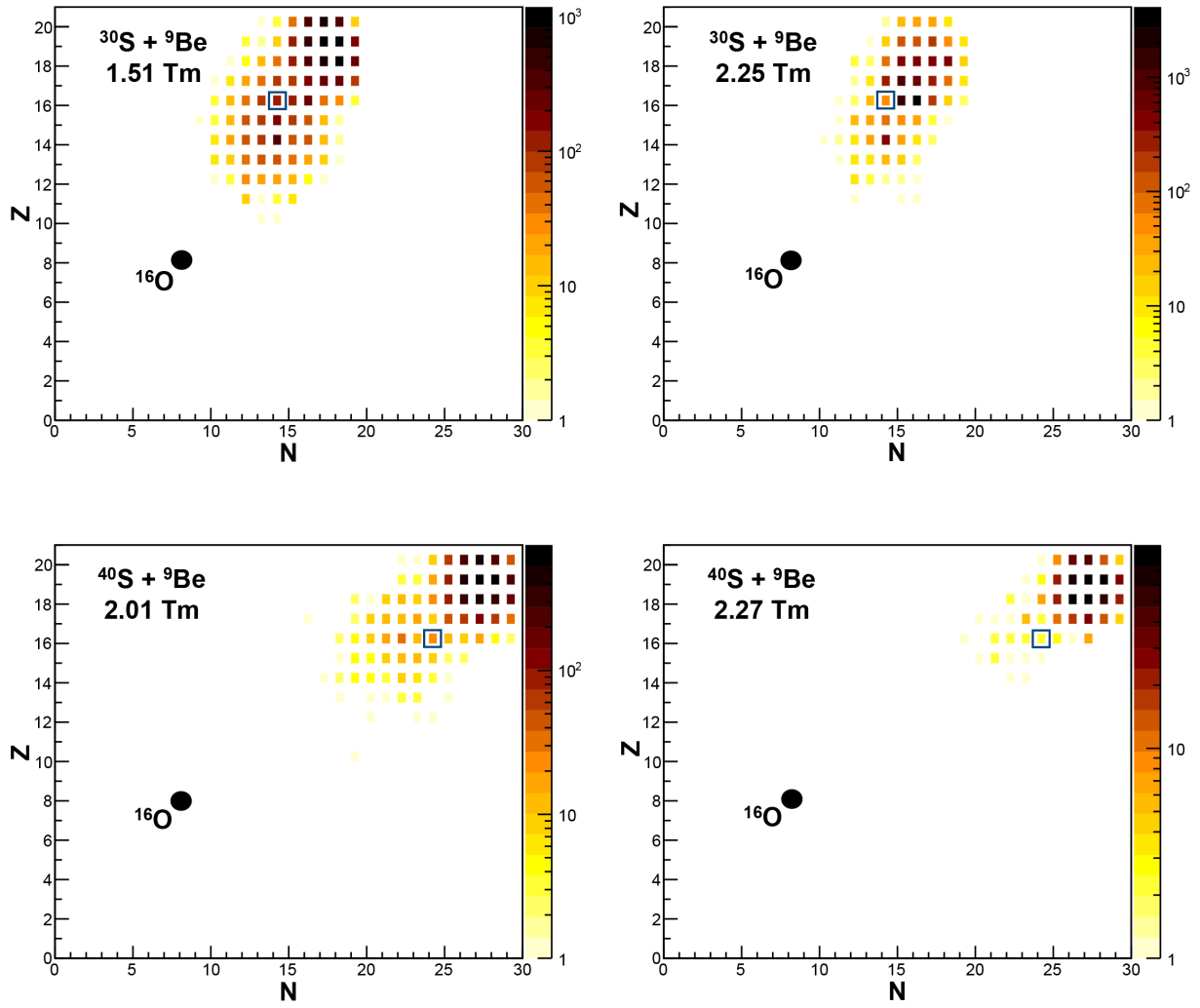

Figure 5.21: Distribution of the intermediate precursor fragments in the N-Z plane from INCL++ for final ^{16}O fragments produced in each beam setting for the ^{30}S + ^{9}Be and ^{40}S + ^{9}Be reactions. The intermediate precursor fragments are represented by the solid boxes. Open squares representing the beams (^{30}S or ^{40}S) and solid black circles representing the position of ^{16}O are displayed for comparison.

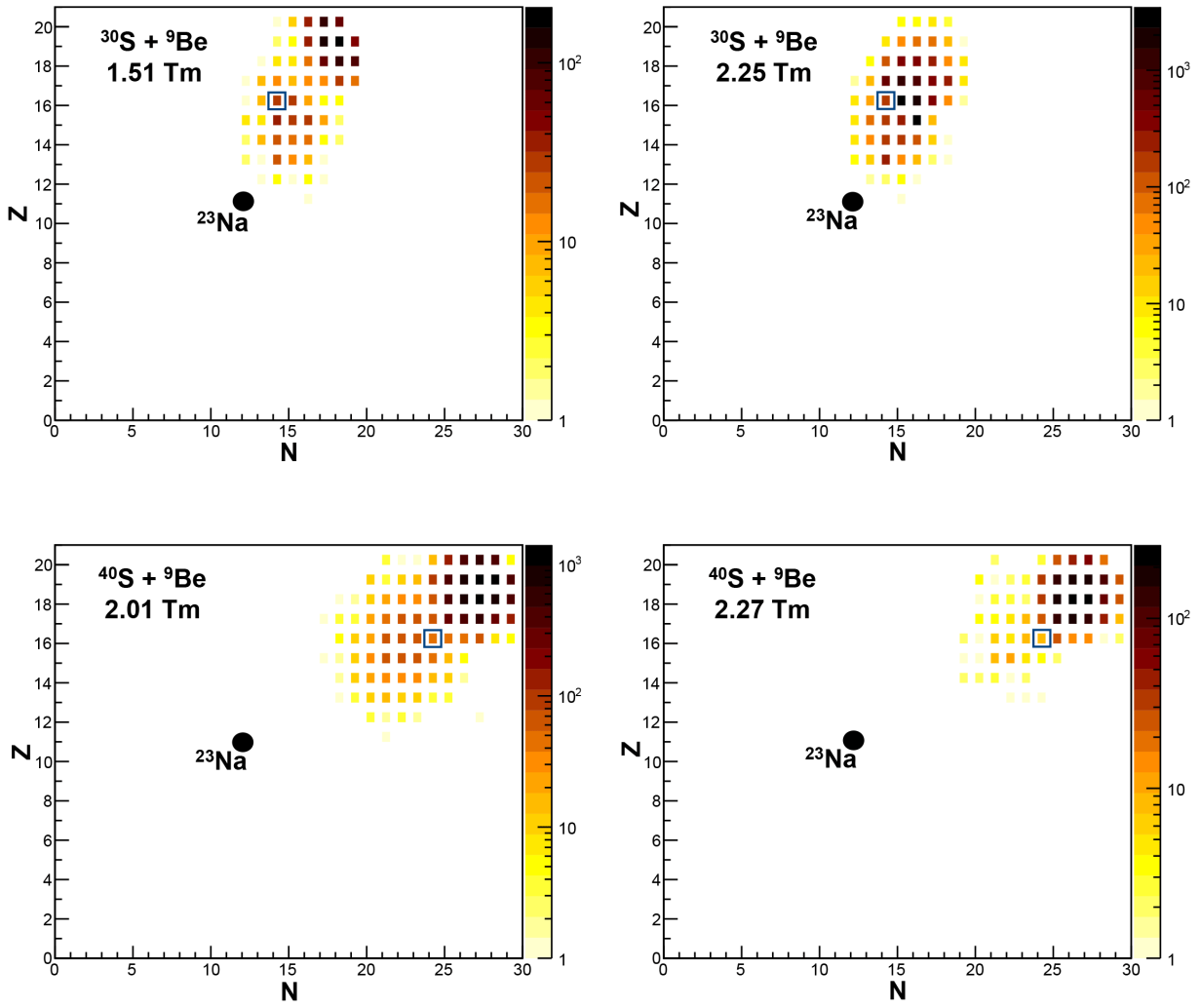

Figure 5.22: Distribution of the intermediate precursor fragments in the N-Z plane from INCL++ for final ^{23}Na fragments produced in each beam setting for the ^{30}S + ^{9}Be and ^{40}S + ^{9}Be reactions. The intermediate precursor fragments are represented by the solid boxes. Open squares representing the beams (^{30}S or ^{40}S) and solid black circles representing the position of ^{23}Na are displayed for comparison.

number and mass remains constant. Thus, fragments of the same isotope that are measured in different magnet settings must have different velocities.

In each of the three examples, the INCL++ precursor fragment distributions were found to be quite similar for the two magnet settings for the ^{40}S + ^{9}Be reaction. Recall that the two magnet settings chosen for the ^{40}S reaction (2.01 and 2.27 Tm) were both below that of the unreacted ^{40}S beam (2.65 Tm). Because of the acceptance range in the Sweeper magnet, these two settings overlapped and many of the fragments were measured in both settings. This was seen in Figures 4.31 and 4.32 from Chapter 4, which showed only a small shift of the isotopic distribution with higher numbers of neutrons in the higher magnet setting. On the other hand, the INCL++ precursor fragment examples show a broader range of precursor fragments for the lower magnet setting in the ^{40}S reaction. This effect is most apparent in the precursor fragments of ^{23}Na shown in Figure 5.22. Thus, ^{23}Na fragments that are observed with higher velocities are predicted to be produced from a somewhat narrower distribution of precursor fragments that are mainly heavier than the beam.

The INCL++ precursor fragment distributions for the two magnet settings for the ^{30}S + ^{9}Be reaction can also be seen to be somewhat different and follow a similar pattern. For example, in Figure 5.22, the precursor fragments of ^{23}Na appear to perhaps have two separate concentrated regions of precursor fragments in the lower magnet setting. Meanwhile, the precursor fragments for the higher magnet setting are more uniformly distributed around a central spot at ^{35}Cl. For reference, recall that the unreacted ^{30}S beam had a rigidity of 1.97 Tm. The Sweeper magnet settings chosen for the ^{30}S reaction fell at 1.51 Tm and 2.25 Tm, below and above the unreacted beam rigidity, respectively. Thus, different precursor fragment distributions for one fragment are associated with different final velocities.

Interestingly, in every case, many of the precursor fragments contained more nucleons than the given projectile, indicating nucleon pick-up or merging of the target and projectile. This suggests that the beam did not simply interact with an inert target in the INCL++ and CoMD simulations.

It should be noted that some degree of nucleon pick-up was present in the experiment. As Figure 4.23 in Chapter 4 showed, bands of the element chlorine were observed above the sulfur element bands for the ^{40}S + ^{9}Be reaction. The proton in these chlorine fragments would have to have come from the beryllium target, of course.

Chapter 6

Summary and Conclusions

Filling out the nuclear landscape by studying rare isotopes is a major objective in the field of nuclear science. While a small percentage of known nuclei are stable, most of the landscape is composed of unstable nuclei that decay. Some of the more exotic nuclei have half-lives of less than a second, creating challenges in producing, separating, and detecting these nuclei in a very short time frame. To produce these rare and short-lived nuclei for study, a technique called projectile fragmentation has been used for a number of years at a variety of isotope production beam facilities such as the National Superconducting Cyclotron Laboratory. This reaction is also the foundation for the next generation of these facilities.

In projectile fragmentation reactions, a high-energy beam of large nuclei is impinged in a relatively thin and low-Z target. Projectile fragmentation reactions have often been described as a two-step process. In the first step, the projectile rapidly collides and passes by the target and the overlapping area is rapidly removed. The collision produces two excited precursors, a projectile-like fragment and a target-like fragment, which enter the second, slower de-excitation process. The excited precursors release nucleons, other light particles, and energy before becoming "cold" nuclear residues. These residues encompass the broadest range of nuclei, which is the reason the reaction mechanism is so useful.

Exclusive measurements of the final fragments from projectile fragmentation reactions can provide more insight into the process by comparing to models that simulate collisions and

reactions on nuclei, but relatively few such measurements have been made. The present work used exclusive measurements of projectile fragmentations products to explore the predictions from two very different nuclear reaction models.

This work was performed at the National Superconducting Cyclotron Laboratory (NSCL), where two intermediate-energy (55.5 MeV/u) projectile fragmentation beams were produced and delivered for reaction with beryllium targets. Beams of ^{30}S and ^{40}S nuclei were chosen to provide proton-rich and neutron-rich projectiles, allowing a wide range of fragment isospin. The resulting heavy residue fragments were measured with the Sweeper magnet charged particle detectors and neutrons were detected in coincidence using the Modular Neutron Array and Large-area multi-Institutional Scintillator Array (MoNA LISA) detectors [66–68, 96].

Signals from the MoNA LISA and Sweeper charged particle detectors were processed, calibrated, and corrected for non-linear responses. Once the calibrations were completed, events were selected from the data set by isotope for analysis. This experiment was found to exceed the limits of the current detector configuration. The resolution was not sufficient to achieve isotope separation for the highest Z elements ($Z = 12 - 17$) observed in the detectors. However, a broad range of fragments was identified in each reaction for elements with $Z = 6 - 11$. The hit multiplicity distributions observed in MoNA LISA for the summed elemental and individual isotopic products were compared to simulations from two nuclear reaction models.

The two fragmentation reactions were simulated with two very different models to describe the fragment and neutron distributions from projectile fragmentation reactions. In one approach, the Liège Intranuclear Cascade (INCL++) model [83–85] uses a microscopic model and Monte Carlo based code that considers the reaction to be a two-step process with collisions between individual nucleons followed by a de-excitation process of the intermedi-

ate and highly excited residue. The de-excitation process was carried out by ABLA07, the default option selected by the authors of the INCL++ code. In the second approach, the Constrained Molecular Dynamics (CoMD) model [69, 70] uses a more quantum mechanical and global approach that follows dynamical nuclear processes using the nuclear equation of state with three options for the symmetry energy term. While most fragments were cool by the end of the CoMD calculations, the GEMINI++ code [73, 74] was used as an "after-burner" code with CoMD to decay the small percentage of remaining hot fragments. The results from both models were passed through the GEANT4 code to model the neutron detection efficiency of the MoNA LISA array.

The hit multiplicity distributions were compared to the experimental data hits measured in MoNA LISA. The fragments produced from the ^{40}S reaction were found to be in coincidence with significantly higher numbers of hits in MoNA LISA compared to fragments produced from the ^{30}S reaction as expected, given that ^{40}S has ten more neutrons than ^{30}S, leading to more neutrons available in the reaction. Furthermore, with more neutrons in the reaction, more neutron-rich final fragments could be produced. Because ^{30}S has relatively few neutrons, the distribution of fragments is limited by the proton drip line.

The majority of identified fragments were measured with no neutron hits. The CoMD + GEMINI++ simulations greatly under-predicted the number of fragments produced with zero hits. Because the INCL++ model was closer in predicting the hit multiplicity zero bin than the CoMD + GEMINI++ simulations, INCL++ was found to do a better job overall at predicting isotopic hit multiplicity distributions. The CoMD + GEMINI++ model was able to produce events with higher hit multiplicities seen in the ^{40}S data, unlike the INCL++ model.

The CoMD model has been an important part of symmetry energy research. Determining the form of the symmetry energy remains a major objective in understanding nuclear properties, astrophysical processes, and the fundamental nucleon-nucleon interaction. While the form has been constrained in a variety of methods, it is important to continue to test the predictions by experimentally constraining the form of the symmetry energy and establishing tighter and consistent constraints. In the present experiment, the hit multiplicity distributions were examined to determine if a constraint could be made. However, because the three CoMD + GEMINI++ options do not appear to produce noticeably different hit multiplicity distributions, no constraint on the symmetry energy was made from this experimental data set.

The distributions of precursor fragments in both the INCL++ and CoMD models were also examined in this work. Many of the precursor fragments contained more nucleons than the projectile. The projectile was predicted to pick up nucleons from the target, something that is different from common descriptions of these reactions. Experimental data confirmed that nucleon pick-up occurred as chlorine fragments were detected from the ^{40}S + ^{9}Be reaction. Thus, the beam did not simply fragment on an inert target.

APPENDICES

Appendix A

Deriving the Nuclear Equation of State and the Symmetry Energy

This appendix describes the connection between the nuclear equation of state for infinite nuclear matter and the Bethe-Weizsäcker formula [6] for finite matter. Some of the derivation below can be found in [14], but intermediate steps are included here for clarity.

Part 1: Nuclear Equation of State

To derive the nuclear equation of state, it is helpful to start with the Bethe-Weizsäcker formula written in the semi-empirical mass formula:

$$BE(Z,N) = a_V A - a_S A^{(2/3)} - a_C \frac{Z^2}{A^{(1/3)}} - a_A \frac{(N-Z)^2}{A} \pm \delta_{pairing} \tag{A.1}$$

where the binding energy, BE, is calculated with a volume term (a_V), a surface term (a_S), a Coulomb term (a_C), an asymmetry term (a_A), and a pairing term ($\delta_{pairing}$). The coefficients of these terms have been determined by fitting the equation to experimentally known masses [6]. The formula can be rewritten to show binding energy per nucleon:

$$\frac{BE(Z,N)}{A} = a_V - \frac{a_S}{A^{(1/3)}} - a_C \frac{Z^2}{A^{(4/3)}} - a_A \frac{(N-Z)^2}{A^2} \pm \frac{\delta_{pairing}}{A} \tag{A.2}$$

The Bethe-Weizsäcker formula is for finite matter. For "infinite matter," A approaches infinity. The surface term drops out, as the denominator leads to infinity and the numerator remains the same, pushing the term to zero. (Furthermore, there would be no surface in infinite matter.) The Coulomb term is removed per standard practice of defining the nuclear equation of state with symmetry energy. Some infinite nuclear matter studies exclude the term as including Coulomb forces makes the liquid drop unstable in this form. Finally, the pairing term is dropped because of its negligible contribution. This leaves the volume term and the asymmetry term.

$$\left.\frac{BE(Z,N)}{A}\right|_{A\to\infty} = a_V - a_A\frac{(N-Z)^2}{A^2} \approx a_V - a_A\delta^2 \tag{A.3}$$

In the above function, δ is the isospin asymmetry, which is given as

$$\delta = \frac{(\rho_n - \rho_p)}{\rho_{\rho_n+\rho_p}} \approx \frac{(N-Z)}{A} \tag{A.4}$$

where ρ_n is the neutron density and ρ_p is the proton density of the matter.

The asymmetry term can be broken into volume (a_A^v) and surface (a_A^s) terms.

$$a_A\delta^2 = \left(a_A^v + \frac{a_A^s}{A^{1/3}}\right)\delta^2 \tag{A.5}$$

Substituting the above relation into Equation A.3. giving the binding energy per nucleon as the following:

$$\left.\frac{BE(Z,N)}{A}\right|_{A\to\infty} \approx a_V - \left(a_A^v + \frac{a_A^s}{A^{1/3}}\right)\delta^2 \tag{A.6}$$

Similar to before, the surface asymmetry term is dropped. This leaves only a few terms left in the equation:

$$\left.\frac{BE(Z,N)}{A}\right|_{A\to\infty} \approx a_V - a_A^v\delta^2 \tag{A.7}$$

Consider the above as two parts: the symmetric ($N = Z$) part and the asymmetric ($N \neq Z$) part. For symmetric matter, $\delta = 0$. If $\delta = 0$ is substituted into Equation A.7, only the volume term a_V remains:

$$\left.\frac{BE(Z,N)}{A}\right|_{A\to\infty} \approx a_V - a_A^v(0)^2 = a_V = E(\rho,0) \tag{A.8}$$

The volume terms (a_V) then represents the symmetric part of the nuclear equation of state ($E(\rho,0)$). Thus, $a_A^v\delta^2$ becomes the asymmetric term (when $N \neq Z$).

$$a_A^v\delta^2 = E_{sym}(\rho)\delta^2 \tag{A.9}$$

The symmetry energy term is written as $E_{sym}(\rho,\delta)$. Thus the nuclear equation of state is written in its common form.

$$\left.\frac{BE(Z,N)}{A}\right|_{A\to\infty} \approx E(\rho,\delta) = E(\rho,0) + E_{sym}(\rho)\delta^2 \tag{A.10}$$

Part 2: The Symmetry Energy

The symmetry energy term is expanded using a Taylor expansion characterizing the departure of symmetry energy from its value at saturation density. The Taylor expansion generic form [116] is given as the following:

$$f(x_0) + \frac{f'(x_0)}{1!}(x - x_0) + \frac{f''(x_0)}{2!}(x - x_0)^2 + ... \tag{A.11}$$

The symmetry energy has been defined [14] in the following relation:

$$E_{sym}(\rho) = \frac{1}{2}\frac{\partial^2}{\partial\delta^2}E(\rho, \delta)\Big|_{\delta=0} \tag{A.12}$$

For the Taylor expansion formula, the $(x - x_0)$ value is based on the difference of the density from the saturation density. The difference is often written as the following equation:

$$(x - x_0) = z = \frac{\rho - \rho_0}{3\rho_0} \tag{A.13}$$

where ρ is the density and ρ_0 is the saturation density.

Due to the small contribution of the latter terms, only the first three terms in the expansion are considered. Let J, K, and L represent magnitude, slope, and curvature, respectively. The form of the symmetry energy can be given as:

$$E_{sym}(\rho) = J + Lz + \frac{1}{2}Kz^2 \tag{A.14}$$

with the magnitude parameter, the slope parameter, and the curvature parameter written as the below Equations A.15, A.16, and A.17, respectively.

$$J = E_{sym}(\rho_0) \tag{A.15}$$

$$Lz = \frac{d}{d\rho}E_{sym}(\rho)\Big(\frac{\rho - \rho_0}{3\rho_0}\Big) = \frac{L_{sym}}{3}\Big(\frac{\rho - \rho_0}{\rho_0}\Big) \tag{A.16}$$

$$Kz^2 = \frac{1}{2}\frac{d^2}{d\rho^2}E_{sym}(\rho)\Big(\frac{\rho - \rho_0}{3\rho_0}\Big)^2 = \frac{K_{sym}}{18}\Big(\frac{\rho - \rho_0}{\rho_0}\Big)^2 \tag{A.17}$$

Adding the terms together gives the total expansion of the symmetry energy term in magnitude, slope, and curvature.

$$E_{sym}(\rho) = E_{sym}(\rho_0) + \frac{L_{sym}}{3}\left(\frac{\rho - \rho_0}{\rho_0}\right) + \frac{K_{sym}}{18}\left(\frac{\rho - \rho_0}{\rho_0}\right)^2 \tag{A.18}$$

Appendix B

CRDC Mask Positions

As Chapter 4 explained, to determine the XY-positions of particles in the CRDCs, the pad position (labeled in the data as "gravity" or pad number) was converted to an X-position in mm in the lab frame and the drift time of the electrons (TAC) was converted into a Y-position in mm in the lab frame. Figure B.1 shows how the "raw" signals in each CRDC appeared before they were transformed into the correct XY-positions.

Both the converted X and Y positions were determined through the calibration provided by tungsten masks. The mask was placed in front of the CRDC by a hydraulic drives. Each mask had a known set of lines and holes forming a specific pattern, as shown in Figure B.2 [102]. The incoming beam was defocused and swept across the area of the CRDC mask, and only the beam particles that passed through a hole or line were detected in the CRDC. Because the positions of the holes and lines in the mask were know, it was possible to convert the CRDC raw signals into physical positions.

Table B.1 gives the XY-positions of the holes and the X-positions of the lines in the masks. The physical coordinates of the holes and lines in the mask were converted to the corresponding coordinates for CRDC1 and CRDC2.

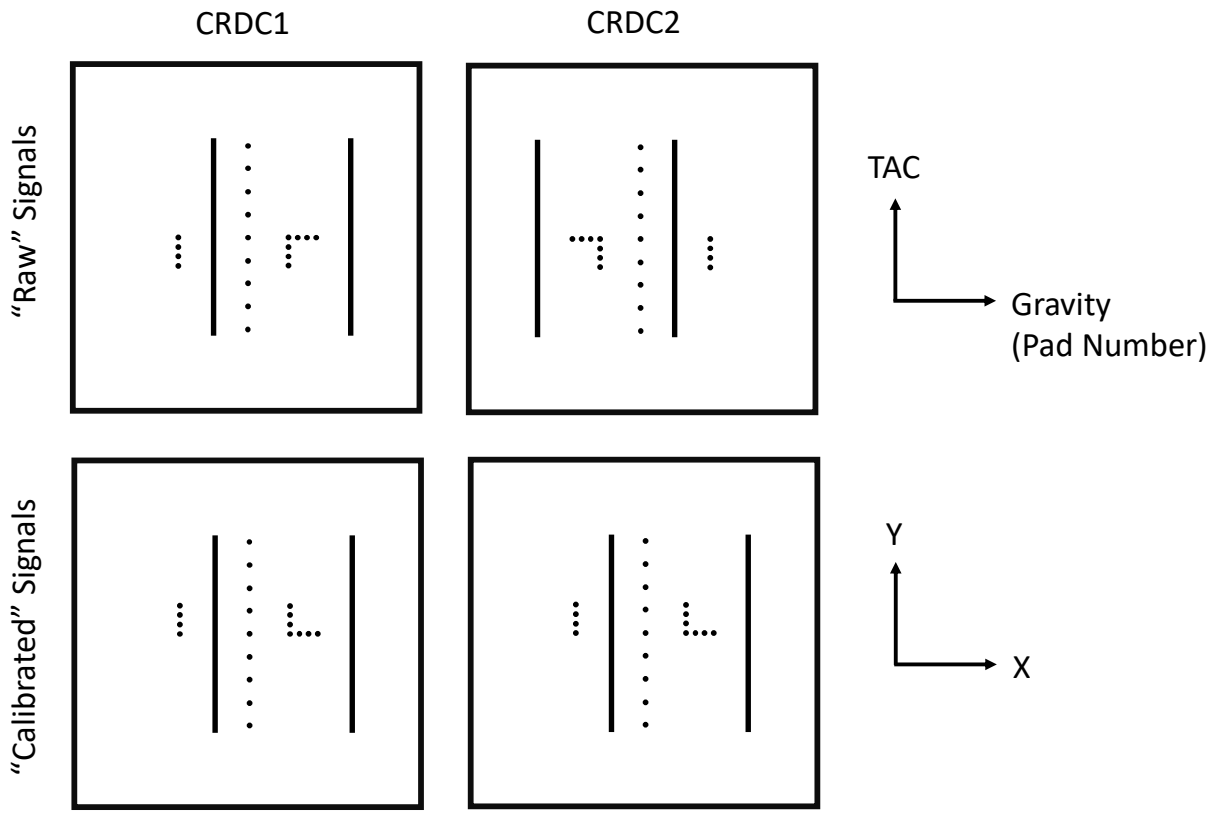

Figure B.1: Schematic demonstrating the orientation of the raw signals TAC and gravity (or pad number) in CRDC1 and CRDC2 and their transformed and calibrated XY-positions.

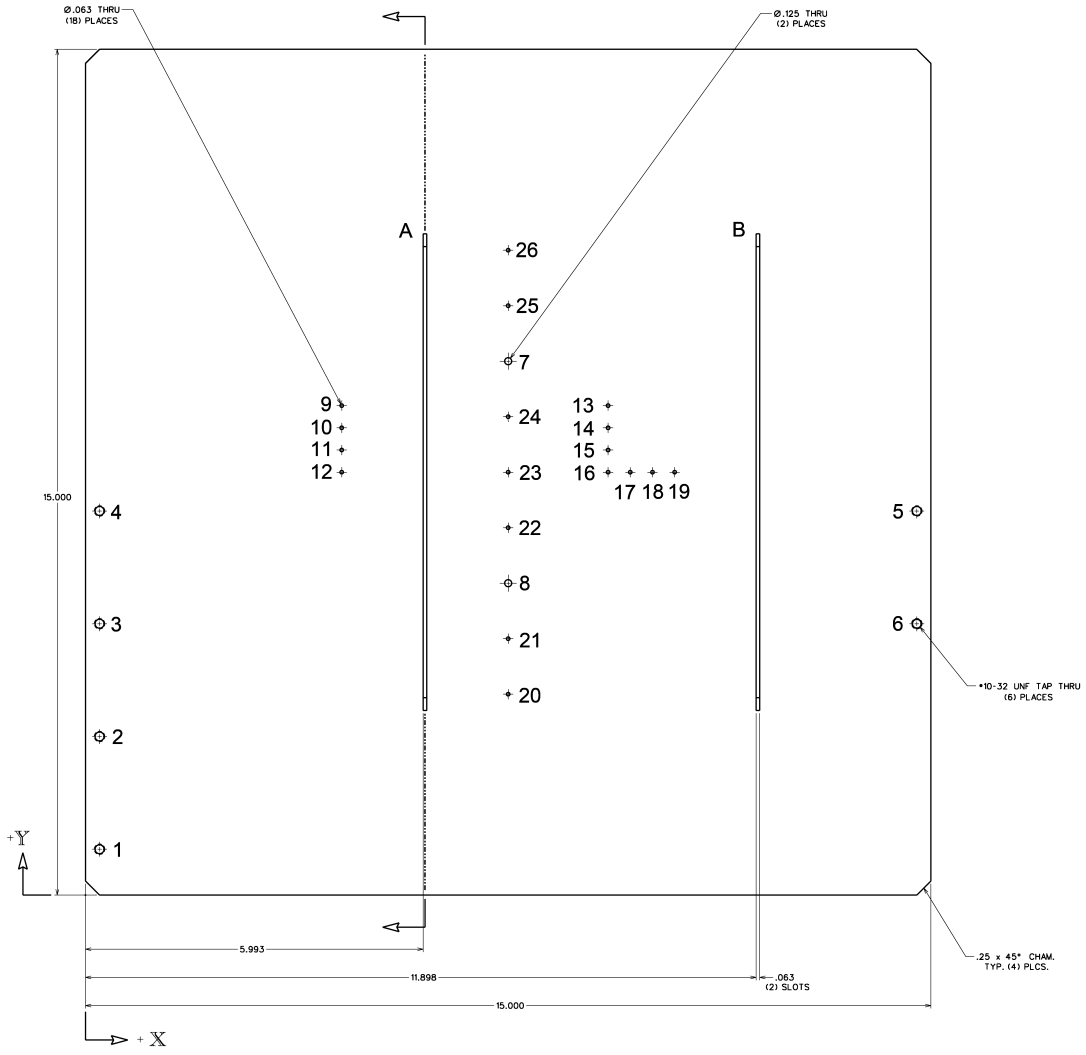

Figure B.2: Mechanical drawing of a tungsten mask used in the experimental configuration. Each hole (1-26) and line (A and B) corresponded to a specific point in space. Adapted from a drawing made by J. Honke [102].

	Diagram				CRCD1		CRDC2	
Label	X (in.)	Y (in.)	X (mm)	Y (mm)	X (mm)	Y (mm)	X (mm)	Y (mm)
1	0.25	0.81	6.35	20.65	-181.15	-169.85	-184.15	-166.85
2	0.25	2.81	6.35	71.45	-181.15	-119.05	-184.15	-116.05
3	0.25	4.81	6.35	122.25	-181.15	-68.25	-184.15	-65.25
4	0.25	6.81	6.35	173.05	-181.15	-17.45	-184.15	-14.45
5	14.75	6.81	374.65	173.05	187.15	-17.45	184.15	-14.45
6	14.75	4.81	374.65	122.25	187.15	-68.25	184.15	-65.25
7	7.50	9.47	190.50	240.51	3.00	50.01	0.00	53.01
8	7.50	5.53	190.50	140.51	3.00	-49.99	0.00	-46.99
9	4.55	8.68	115.47	220.50	-72.03	30.00	-75.03	33.00
10	4.55	8.29	115.47	210.49	-72.03	19.99	-75.03	22.99
11	4.55	7.89	115.47	200.51	-72.03	10.01	-75.03	13.01
12	4.55	7.50	115.47	190.50	-72.03	0.00	-75.03	3.00
13	9.27	8.68	235.53	220.50	48.03	30.00	45.03	33.00
14	9.27	8.29	235.53	210.49	48.03	19.99	45.03	22.99
15	9.27	7.89	235.53	200.51	48.03	10.01	45.03	13.01
16	9.27	7.50	235.53	190.50	48.03	0.00	45.03	3.00
17	9.67	7.50	245.52	190.50	58.02	0.00	55.02	3.00
18	10.06	7.50	255.52	190.50	68.02	0.00	65.02	3.00
19	10.45	7.50	265.53	190.50	78.03	0.00	75.03	3.00
20	7.50	3.56	190.50	90.50	3.00	-100.00	0.00	-97.00
21	7.50	4.55	190.50	115.49	3.00	-75.01	0.00	-72.01
22	7.50	6.52	190.50	165.51	3.00	-24.99	0.00	-21.99
23	7.50	7.50	190.50	190.50	3.00	0.00	0.00	3.00
24	7.50	8.48	190.50	215.49	3.00	24.99	0.00	27.99
25	7.50	10.45	190.50	265.51	3.00	75.01	0.00	78.01
26	7.50	11.44	190.50	290.50	3.00	100.00	0.00	103.00
A	5.99	-	152.22	-	-35.28	-	-38.28	-
B	11.90	-	302.21	-	114.71	-	111.71	-

Table B.1: The XY coordinates for the holes and lines in the CRDC masks. The coordinates from the diagram were converted to their corresponding locations on CRDC1 and CRDC2.

Appendix C

Isotope Separation Parameters and Corrections

Chapter 4 describes the isotope separation procedure. The isotope separation procedure was carried out for the data from each element in each magnet setting for both the ^{30}S and ^{40}S beams. The corrections and parameters for each element are summarized in the following tables. The numbers in the right columns were multiplied by the parameters in the far left columns. The values were then summed to construct the final corrected time-of-flight in the following equation:

$$t_{final} = t_{target \rightarrow thin} + \sum C_i P_i \tag{C.1}$$

where C_i were the correction coefficients (the right columns) and P_i were the parameters (the left column). Isotope separation was found by applying these corrections to the appropriate element fragments.

Tables C.1 and C.2 provide the parameters and coefficients for fragments produced from the ^{30}S + ^{9}Be reaction and the 1.51 Tm and 2.25 Tm Sweeper magnet settings, respectively. Tables C.3 and C.4 provide the parameters and coefficients for fragments produced from the ^{40}S + ^{9}Be reaction and the 2.01 Tm and 2.27 Tm Sweeper magnet settings, respectively.

An example that of the calculation of Equation C.1 for the carbon fragments produced from the ^{30}S + ^{9}Be reaction and the 1.51 Tm Sweeper magnet setting is shown below.

$$\begin{aligned} t_{final}^{carbon} =& t_{target\rightarrow thin} + (-4.21014 \times 10^{-1})x + (-3.51953 \times 10^{-3})x^2 + (1.12644)\theta_x \\ &+ (4.29741 \times 10^{-3})\theta_x^2 + (1.42990 \times 10^{-1})y + (4.53751 \times 10^{-3})y^2 \\ &+ (-1.18388 \times 10^{-3})\theta_y + (-7.28025 \times 10^{-3})\theta_y^2 + (4.13360 \times 10^{-3})x\theta_x \\ &+ (-1.70214 \times 10^{-6})x^2\theta_x^2 + (9.25063)t_{target\rightarrow thin} \end{aligned} \tag{C.2}$$

	Carbon	Nitrogen	Oxygen	Fluorine	Neon	Sodium
x	-4.21014 $\times 10^{-1}$	-3.76333 $\times 10^{-1}$	-2.91627 $\times 10^{-1}$	-2.91884 $\times 10^{-1}$	-3.54995 $\times 10^{-1}$	-3.02621 $\times 10^{-1}$
x^2	-3.51953 $\times 10^{-3}$	-2.16416 $\times 10^{-3}$	-2.74075 $\times 10^{-3}$	-2.82947 $\times 10^{-3}$	-2.07933 $\times 10^{-3}$	4.03140 $\times 10^{-4}$
x^3	-	-4.32900 $\times 10^{-5}$	-5.15389 $\times 10^{-5}$	-4.22475 $\times 10^{-5}$	-3.82195 $\times 10^{-5}$	-6.08871 $\times 10^{-5}$
θ_x	1.12644	9.77349 $\times 10^{-1}$	1.04316	1.04248	1.05602	1.07408
θ_x^2	4.29741 $\times 10^{-3}$	5.32203 $\times 10^{-4}$	-	-	-	-
y	1.42990 $\times 10^{-1}$	1.29525 $\times 10^{-1}$	1.28582 $\times 10^{-1}$	1.26766 $\times 10^{-1}$	9.29421 $\times 10^{-2}$	1.17116 $\times 10^{-1}$
y^2	4.53751 $\times 10^{-3}$	3.92893 $\times 10^{-3}$	3.76369 $\times 10^{-3}$	3.79120 $\times 10^{-3}$	3.40481 $\times 10^{-3}$	3.61254 $\times 10^{-3}$
θ_y	-1.18388 $\times 10^{-3}$	4.29734 $\times 10^{-2}$	-1.16298 $\times 10^{-2}$	-1.12000 $\times 10^{-2}$	3.61747 $\times 10^{-2}$	1.36818 $\times 10^{-2}$
θ_y^2	-7.28025 $\times 10^{-3}$	-1.52684 $\times 10^{-3}$	-5.00950 $\times 10^{-3}$	-	-	-
$x\theta_x$	4.13360 $\times 10^{-3}$	-2.15249 $\times 10^{-3}$	-1.39708 $\times 10^{-3}$	-2.22464 $\times 10^{-3}$	7.80569 $\times 10^{-5}$	5.85587 $\times 10^{-4}$
$x^2\theta_x^2$	-1.70214 $\times 10^{-6}$	-1.77161 $\times 10^{-6}$	-2.82452 $\times 10^{-6}$	6.33964 $\times 10^{-7}$	-6.89200 $\times 10^{-7}$	-2.58906 $\times 10^{-7}$
$x^3\theta_x^3$	-	-4.09191 $\times 10^{-10}$	-7.69764 $\times 10^{-10}$	-	-	-
ToF^*	8.25063	7.77247	6.45237	6.21714	6.90080	5.98684
ΔE_{IC}	-	-	-	1.54680 $\times 10^{-2}$	-2.44056 $\times 10^{-2}$	9.95481 $\times 10^{-3}$

$^*ToF_{target \rightarrow thin}$

Table C.1: Final correction factors used for isotope separation for fragments produced from the ^{30}S + ^{9}Be reaction and the 1.51 Sweeper magnet setting.

	Carbon	Nitrogen	Oxygen	Fluorine	Neon	Sodium
x	-6.31523 $\times 10^{-1}$	-6.05760 $\times 10^{-1}$	-6.90426 $\times 10^{-1}$	-5.97753 $\times 10^{-1}$	-6.85592 $\times 10^{-1}$	-6.42464 $\times 10^{-1}$
x^2	-2.28293 $\times 10^{-3}$	-2.55234 $\times 10^{-3}$	-1.37997 $\times 10^{-3}$	-1.75521 $\times 10^{-3}$	-2.73203 $\times 10^{-3}$	-1.87090 $\times 10^{-3}$
x^3	-	-8.37146 $\times 10^{-6}$	-	-	-1.16694 $\times 10^{-5}$	-8.33033 $\times 10^{-6}$
θ_x	9.72445 $\times 10^{-1}$	1.014035	9.75722 $\times 10^{-1}$	1.002234	1.14073	9.37767 $\times 10^{-1}$
θ_x^2	1.83028 $\times 10^{-3}$	1.88481 $\times 10^{-3}$	-2.14629 $\times 10^{-4}$	1.10371 $\times 10^{-3}$	-6.57750 $\times 10^{-4}$	2.01998 $\times 10^{-3}$
θ_x^3	-	-	-9.31887 $\times 10^{-6}$	-	-5.89717 $\times 10^{-5}$	-
y	1.65249 $\times 10^{-1}$	1.29125 $\times 10^{-1}$	9.51435 $\times 10^{-2}$	1.00653 $\times 10^{-1}$	1.02590 $\times 10^{-1}$	1.24917 $\times 10^{-1}$
y^2	5.15829 $\times 10^{-3}$	6.07290 $\times 10^{-3}$	4.01068 $\times 10^{-3}$	4.96386 $\times 10^{-3}$	4.23464 $\times 10^{-3}$	4.47153 $\times 10^{-3}$
θ_y	3.74497 $\times 10^{-2}$	2.06325 $\times 10^{-2}$	2.87760 $\times 10^{-2}$	3.58381 $\times 10^{-2}$	4.39263 $\times 10^{-2}$	-
θ_y^2	1.67589 $\times 10^{-3}$	2.56012 $\times 10^{-3}$	1.96523 $\times 10^{-3}$	-	-	-
$x\theta_x$	-	-9.83607 $\times 10^{-4}$	-8.01858 $\times 10^{-4}$	-7.91037 $\times 10^{-4}$	-1.79488 $\times 10^{-3}$	-2.07703 $\times 10^{-3}$
$x^2\theta_x^2$	-	-	-	-	-4.22700 $\times 10^{-7}$	-9.36356 $\times 10^{-7}$
$x^3\theta_x^3$	-	-	-	-	-	-
ToF^*	3.42879 $\times 10^{1}$	3.47553 $\times 10^{1}$	2.66472 $\times 10^{1}$	3.37634 $\times 10^{1}$	3.63524 $\times 10^{1}$	2.86306 $\times 10^{1}$
ΔE_{IC}	-	-	-	-2.43065 $\times 10^{-1}$	3.58891 $\times 10^{-2}$	-3.05655 $\times 10^{-1}$
ΔE_{IC}^2	-	-	-	3.33372 $\times 10^{-4}$	-	-2.66471 $\times 10^{-4}$

$^*ToF_{target \rightarrow thin}$

Table C.2: Final correction factors used for isotope separation for fragments produced from the ^{30}S + ^{9}Be reaction and the 2.25 Sweeper magnet setting.

	Carbon	Nitrogen	Oxygen	Fluorine	Neon	Sodium
x	-1.29621	-1.21297	-1.19580	-8.72480×10^{-1}	-1.14109	-1.17800
x^2	-3.89795×10^{-3}	1.42778×10^{-3}	5.47301×10^{-3}	-2.57488×10^{-4}	1.41042×10^{-4}	-1.19571×10^{-3}
x^3	-7.14639×10^{-4}	-1.08579×10^{-3}	-9.00213×10^{-4}	-9.98858×10^{-4}	-9.86415×10^{-4}	-1.01516×10^{-3}
θ_x	8.00033×10^{-1}	8.18146×10^{-1}	8.75322×10^{-1}	9.1623×10^{-1}	9.17048×10^{-1}	9.16177×10^{-1}
θ_x^2	1.22943×10^{-1}	1.23215×10^{-1}	1.28244×10^{-2}	1.27262×10^{-1}	1.27342×10^{-1}	1.26905×10^{-1}
θ_x^3	1.24519×10^{-1}	1.24508×10^{-1}	-3.09585×10^{-4}	1.24630×10^{-1}	1.24635×10^{-1}	1.24589×10^{-1}
y	1.83709×10^{-1}	1.22695×10^{-1}	1.51930×10^{-1}	1.14758×10^{-1}	1.14595×10^{-1}	1.07479×10^{-1}
y^2	1.26645×10^{-1}	1.25725×10^{-1}	-5.61972×10^{-3}	1.27029×10^{-1}	1.28281×10^{-1}	1.25565×10^{-1}
θ_y	-2.29830×10^{-4}	-1.72589×10^{-4}	-2.67244×10^{-4}	-3.20693×10^{-4}	-2.43192×10^{-4}	-2.88624×10^{-4}
θ_y^2	-1.01731×10^{-2}	-9.38943×10^{-3}	-1.10577×10^{-2}	-1.07260×10^{-2}	-1.02837×10^{-2}	-2.13894×10^{-2}
$x\theta_x$	-5.72727×10^{-3}	-4.63388×10^{-3}	-5.20661×10^{-3}	-4.94628×10^{-3}	-4.99835×10^{-3}	-5.42562×10^{-3}
$x^2\theta_x^2$	-2.56692×10^{-6}	-1.74465×10^{-6}	-2.13910×10^{-6}	-2.11771×10^{-6}	-2.99474×10^{-6}	-1.90380×10^{-6}
ToF^*	6.64998	6.73078	6.17817	8.33772	7.45735	7.65281
ΔE_{IC}	2.49880	1.23366	1.03563	9.90138×10^{-1}	8.26615×10^{-1}	7.98638×10^{-1}
ΔE_{IC}^2	-7.88068×10^{-3}	-2.82654×10^{-3}	-1.56647×10^{-3}	-1.24955×10^{-3}	-8.64823×10^{-4}	-6.77071×10^{-4}

$^*ToF_{target \rightarrow thin}$

Table C.3: Final correction factors used for isotope separation for fragments produced from the ^{40}S + ^{9}Be reaction and the 2.01 Sweeper magnet setting.

	Carbon	Nitrogen	Oxygen	Fluorine	Neon	Sodium
x	-1.19777	-1.26471	-1.18715	-1.33243	-1.35075	-1.40206
x^2	-1.55306×10^{-2}	5.47301×10^{-3}	5.57342×10^{-3}	-9.30528×10^{-4}	-1.76240×10^{-3}	-3.76194×10^{-3}
x^3	-1.00078×10^{-3}	-9.58920×10^{-4}	-8.99616×10^{-4}	-8.98881×10^{-4}	-8.70187×10^{-4}	-9.24366×10^{-4}
θ_x	8.84322×10^{-1}	9.34056×10^{-1}	9.19855×10^{-1}	8.96637×10^{-1}	9.57798×10^{-1}	0.912594×10^{-1}
θ_x^2	-4.82437×10^{-3}	-1.23330×10^{-2}	-1.00328×10^{-2}	-1.84343×10^{-2}	-9.92907×10^{-3}	-9.34532×10^{-3}
θ_x^3	-3.09585×10^{-4}	-5.06380×10^{-4}	-4.82665×10^{-4}	-6.23105×10^{-4}	-5.01209×10^{-4}	-4.94422×10^{-4}
y	2.09501×10^{-1}	4.53709×10^{-1}	6.31530×10^{-1}	1.89120×10^{-1}	1.99088×10^{-1}	3.71123×10^{-1}
y^2	-5.90194×10^{-3}	-6.21424×10^{-3}	-5.85912×10^{-3}	-5.68960×10^{-3}	-5.78834×10^{-3}	-6.28356×10^{-3}
θ_y	-3.28330×10^{-4}	-1.91054×10^{-4}	-2.67334×10^{-4}	-2.66530×10^{-4}	-1.85992×10^{-4}	-2.87112×10^{-4}
θ_y^2	-1.09471×10^{-2}	-1.21635×10^{-2}	-1.16106×10^{-2}	-1.06154×10^{-2}	-9.84135×10^{-3}	-1.13894×10^{-2}
$x\theta_x$	-4.99835×10^{-3}	-5.15454×10^{-3}	-5.83140×10^{-3}	-5.46694×10^{-3}	-4.99835×10^{-3}	-4.89421×10^{-3}
$x^2\theta_x^2$	-2.03215×10^{-6}	-2.78083×10^{-6}	-2.18188×10^{-6}	-2.26745×10^{-6}	-2.09632×10^{-6}	-1.71128×10^{-6}
ToF^*	7.57671	8.53880	6.24597	7.44467	7.09218	7.18210
ΔE_{IC}	6.93957×10^{-2}	1.28058	9.21870×10^{-2}	1.09720×10^{-1}	9.22175×10^{-2}	4.12172×10^{-1}
ΔE_{IC}^2	-	-2.97914×10^{-3}	-	-	-1.56005×10^{-3}	-2.75234×10^{-4}

$^*ToF_{target \rightarrow thin}$

Table C.4: Final correction factors used for isotope separation for fragments produced from the ^{40}S + ^{9}Be reaction and the 2.27 Sweeper magnet setting.

Appendix D

χ_v^2 Values

As described in Chapter 5, χ_v^2 values were calculated for a quantitative comparison to the simulated models. As a brief reminder, the models used in this analysis were INCL++ and the three versions of CoMD + GEMINI++ (labeled here as CoMD-1, CoMD-2, and CoMD-3).

First, χ^2 values were calculated for each hit multiplicity value with the following equation:

$$\chi^2 = \sum_{i=0}^{n} \frac{(P_i^{data} - P_i^{sim})^2}{(E_i^{data})^2} \tag{D.1}$$

where i was the hit multiplicity value (bin number), P_i^{data} was the probability value of the experimental data, P_i^{sim} was the probability value of the simulation set, and E_i^{data} was the uncertainty in the data.

A reduced χ_v^2 was used to compare models with different numbers of parameters. The inclusion of hit multiplicity values or bins with very few events could skew the comparison by placing more importance on those few events. In order to minimize this effect, only hit multiplicity values with more than five events were included. The reduced χ_v^2 was found with the following equation:

$$\chi_v^2 = \frac{\chi^2}{ndf} \tag{D.2}$$

where *ndf* was the degrees of freedom (the number of bins subtract one). If the given simulation matched the data within the experimental uncertainties, the χ^2_v value would be one. The larger the χ^2_v value, the worse the fit.

The χ^2_v values are given in the following tables. Tables D.1 and D.2 provide the calculated χ^2_v Values for isotope hit multiplicity distributions produced by the ^{30}S + ^{9}Be reaction and the 1.51 Tm and 2.25 Tm Sweeper magnet settings, respectively. Tables D.3 and D.4 provide the calculated χ^2_v values for isotope hit multiplicity distributions produced by the ^{40}S + ^{9}Be reaction and the 2.01 Tm and 2.27 Tm Sweeper magnet settings, respectively. The average given in the tables is the total of the χ^2_v values of a simulation divided by the number of isotopes in that setting.

Isotope	COMD-1	COMD-2	COMD-3	INCL
^{11}C	1898.47	1835.89	2252.20	39.10
^{12}C	5251.70	5962.74	5799.37	147.66
^{13}C	1154.09	1260.59	1142.56	23.39
^{13}N	955.09	1129.78	1266.93	33.57
^{14}N	3829.17	4276.70	3871.57	117.59
^{15}N	2158.96	2004.40	2214.18	128.27
^{15}O	5157.21	4794.39	4833.07	131.27
^{16}O	8545.54	8972.88	8329.43	256.99
^{17}O	1417.42	1392.30	1307.27	46.63
^{17}F	2050.41	2245.29	2295.02	87.18
^{18}F	2617.99	2931.60	2717.69	65.67
^{19}F	1498.47	1185.19	1148.44	44.30
^{19}Ne	1980.14	2295.78	2092.33	65.46
^{20}Ne	5571.36	6191.00	6031.88	293.89
^{21}Ne	2059.19	2322.77	2207.63	102.27
^{21}Na	2258.28	2143.88	2226.45	97.75
^{22}Na	5916.04	5171.33	4583.89	235.18
^{23}Na	1612.18	1552.83	1730.95	44.62
Average	3107.32	3203.85	3113.94	108.93

Table D.1: Calculated χ^2_v values for isotope hit multiplicity distributions produced by the ^{30}S + ^{9}Be reaction and the 1.51 Sweeper magnet setting.

Isotope	COMD-1	COMD-2	COMD-3	INCL
^{11}C	564.48	607.85	692.62	6.08
^{12}C	7178.11	5655.27	4882.24	212.58
^{13}C	4662.11	4237.77	4214.36	182.72
^{14}N	6691.34	6311.20	9005.17	350.54
^{15}N	9573.68	6509.68	7525.17	414.74
^{15}O	2523.50	3284.80	3049.19	73.39
^{16}O	14570.80	16537.37	10277.38	792.90
^{17}O	5477.91	4705.06	4959.60	419.38
^{18}F	2827.75	2940.24	2569.97	400.14
^{19}F	4700.76	4363.91	3622.98	410.74
^{20}F	1298.89	1037.52	879.28	148.08
^{20}Ne	6978.30	6895.98	5139.13	1034.15
^{21}Ne	5619.90	5587.73	5472.99	1402.53
^{22}Ne	1702.93	1537.72	1473.48	491.18
^{22}Na	1925.52	1752.52	2429.46	586.41
^{23}Na	2822.84	2198.50	2642.74	1385.43
Average	4944.93	4635.19	4302.24	519.44

Table D.2: Calculated χ^2_v values for isotope hit multiplicity distributions produced by the ^{30}S + ^{9}Be reaction and the 2.25 Sweeper magnet setting.

Isotope	COMD-1	COMD-2	COMD-3	INCL
^{12}C	191.27	143.47	118.74	39.76
^{13}C	188.71	228.55	384.26	51.87
^{14}C	122.09	163.37	274.88	39.78
^{14}N	191.69	250.08	234.00	32.87
^{15}N	1098.27	865.57	771.21	163.00
^{16}N	190.14	120.40	167.40	40.76
^{17}N	72.16	83.06	77.42	27.83
^{16}O	340.15	572.82	358.37	93.62
^{17}O	380.88	363.63	411.01	108.21
^{18}O	829.47	543.53	428.19	111.24
^{19}O	218.29	176.09	186.32	35.99
^{18}F	16.47	144.97	108.54	44.98
^{19}F	338.46	599.31	543.64	152.97
^{20}F	545.30	691.20	796.32	156.19
^{21}F	416.27	371.60	430.89	101.43
^{20}Ne	231.54	167.62	304.36	120.87
^{21}Ne	603.47	562.76	690.89	213.42
^{22}Ne	1480.82	1054.62	1300.17	344.24
^{23}Ne	419.85	387.05	388.59	107.52
^{24}Ne	119.42	116.89	125.73	41.00
^{22}Na	211.06	177.85	139.63	78.60
^{23}Na	718.42	1006.32	975.37	388.00
^{24}Na	1107.80	1006.23	1195.65	418.50
^{25}Na	984.19	956.06	1044.62	263.00
Average	459.01	448.05	477.34	132.32

Table D.3: Calculated χ^2_v values for isotope hit multiplicity distributions produced by the ^{40}S + ^{9}Be reaction and the 2.01 Sweeper magnet setting.

Isotope	COMD-1	COMD-2	COMD-3	INCL
^{12}C	56.09	65.16	38.50	11.84
^{13}C	75.00	69.51	114.68	15.01
^{14}C	45.86	67.46	148.02	20.63
^{14}N	45.49	27.99	41.29	5.92
^{15}N	162.84	259.94	53.82	50.95
^{16}N	83.42	55.51	75.62	21.18
^{17}N	4.26	7.27	8.86	24.85
^{16}O	51.20	82.27	54.44	25.33
^{17}O	215.13	114.53	107.58	32.16
^{18}O	153.72	126.50	131.82	44.58
^{19}O	138.73	152.40	96.72	27.45
^{20}O	81.14	67.02	55.92	14.02
^{19}F	69.21	129.16	261.02	39.93
^{20}F	153.53	291.97	253.90	71.37
^{21}F	132.24	111.17	144.13	48.96
^{22}F	49.83	63.93	85.78	20.37
^{21}Ne	76.84	98.68	207.95	62.89
^{22}Ne	568.53	267.92	214.98	134.24
^{23}Ne	196.46	259.81	209.59	82.80
^{24}Ne	145.86	112.79	139.10	49.30
^{23}Na	382.39	172.23	255.96	96.00
^{24}Na	210.46	200.99	145.33	138.49
^{26}Na	331.13	300.74	307.03	130.05
^{25}Na	134.08	150.52	161.07	63.70
Average	148.48	135.64	138.05	51.33

Table D.4: Calculated χ^2_v values for isotope hit multiplicity distributions produced by the ^{40}S + ^{9}Be reaction and the 2.27 Sweeper magnet setting.

BIBLIOGRAPHY

BIBLIOGRAPHY

[1] J. Erler, N. Birge, M. Kortelainen, W. Nazarewicz, E. Olsen, A. M. Perhac, and M. Stoitsov. The limits of the nuclear landscape. *Nature*, 486:509512, Jun 2012.

[2] E. O'Donnell. Chart of nuclei. https://www.flickr.com/photos/nsclmedia/16247725170/in/album-72157622074745816/, 2015. Accessed: 2018-05-30.

[3] J. D. Bowman, W. J. Swiatecki, and C. F. Tsang. Abrasion and ablation of heavy ions. Technical Report LBL-2908, Lawrence Berkeley National Laboratory, July 1973.

[4] A. S. Goldhaber and H. H. Heckman. High energy interactions of nuclei. *Annual Review of Nuclear and Particle Science*, 28(1):161–205, 1978.

[5] W. Loveland, D. J. Morrissey, and G. T. Seaborg. *Modern Nuclear Chemistry*. John Wiley & Sons, Inc., Hoboken, NJ, 2006.

[6] H. A. Bethe and R. F. Bacher. Nuclear physics A. Stationary states of nuclei. *Rev. Mod. Phys.*, 8:82–229, Apr 1936.

[7] L. Satpathy and R. Nayak. Generalized Hugenholtz-Van Hove theorem and a new mass relation for finite nuclei. *Phys. Rev. Lett.*, 51:1243–1246, Oct 1983.

[8] R. D. Mattuck. *A Guide to Feynman Diagrams in the Many-body Problem*. Dover Publications, 2nd edition, 1992.

[9] J. D. Walecka. *Theoretical Nuclear and Subnuclear Physics*. Imperial College Press and World Scientific, Hackensack, NJ, 2nd edition, 2004.

[10] B. A. Li, L. W. Chen, and C. M. Ko. Recent progress and new challenges in isospin physics with heavy-ion reactions. *Physics Reports*, 464(4):113 – 281, 2008.

[11] L. W. Chen, B. J. Cai, C. M. Ko, B. A. Li, C. Shen, and J. Xu. Higher-order effects on the incompressibility of isospin asymmetric nuclear matter. *Phys. Rev. C*, 80:014322, Jul 2009.

[12] P. Danielewicz and J. Lee. Symmetry energy I: Semi-infinite matter. *Nuclear Physics A*, 818(1):36 – 96, 2009.

[13] G. Giuliani, H. Zheng, and A. Bonasera. The many facets of the (non-relativistic) nuclear equation of state. *Progress in Particle and Nuclear Physics*, 76:116 – 164, 2014.

[14] S. Typel, H. H. Wolter, G. Röpke, and D. Blaschke. Effects of the liquid-gas phase transition and cluster formation on the symmetry energy. *Eur. Phys. J. A*, 50(2):17, 2014.

[15] R. Wang and L. W. Chen. Empirical information on nuclear matter fourth-order symmetry energy from an extended nuclear mass formula. *Physics Letters B*, 773:62 – 67, 2017.

[16] B. A. Li and U. Schroder. *Isospin Physics in Heavy-Ion Collisions at Intermediate Energies*. Nova Science Publishers, Inc., Huntington, NY, 2001.

[17] C. Fuchs and H. H. Wolter. Modelization of the EOS. *The European Physical Journal A - Hadrons and Nuclei*, 30(1):5–21, Oct 2006.

[18] S. D. Gupta and G. D. Westfall. Probing dense nuclear matter in the laboratory. *Physics Today*, 46:34, 1993.

[19] W. Reisdorf and H.G. Ritter. Collective flow in heavy-ion collisions. *Annual Review of Nuclear and Particle Science*, 47(1):663–709, 1997.

[20] N. Herrmann, J. P. Wessels, and T. Wienold. Collective flow in heavy-ion collisions. *Annual Review of Nuclear and Particle Science*, 49(1):581–632, 1999.

[21] D. J. Magestro, W. Bauer, and G. D. Westfall. Isolation of the nuclear compressibility with the balance energy. *Phys. Rev. C*, 62:041603, Sep 2000.

[22] P. Danielewicz, R. Lacey, and W. G. Lynch. Determination of the equation of state of dense matter. *Science*, 298(5598):1592–1596, 2002.

[23] S. Shlomo, V. M. Kolomietz, and G. Colò. Deducing the nuclear-matter incompressibility coefficient from data on isoscalar compression modes. *The European Physical Journal A - Hadrons and Nuclei*, 30(1):23–30, Oct 2006.

[24] D. D. S. Coupland, W. G. Lynch, M. B. Tsang, P. Danielewicz, and Y. Zhang. Influence of transport variables on isospin transport ratios. *Phys. Rev. C*, 84:054603, Nov 2011.

[25] M. B. Tsang, J. R. Stone, F. Camera, P. Danielewicz, S. Gandolfi, K. Hebeler, C. J. Horowitz, Jenny Lee, W. G. Lynch, Z. Kohley, R. Lemmon, P. Möller, T. Murakami, S. Riordan, X. Roca-Maza, F. Sammarruca, A. W. Steiner, I. Vidaña, and S. J. Yennello. Constraints on the symmetry energy and neutron skins from experiments and theory. *Phys. Rev. C*, 86:015803, Jul 2012.

[26] R. J. Furnstahl. Neutron radii in mean-field models. *Nuclear Physics A*, 706(1):85 – 110, 2002.

[27] B. A. Li. High density behaviour of nuclear symmetry energy and high energy heavy-ion collisions. *Nuclear Physics A*, 708(3):365 – 390, 2002.

[28] Bao-An Li. Probing the high density behavior of the nuclear symmetry energy with high energy heavy-ion collisions. *Phys. Rev. Lett.*, 88:192701, Apr 2002.

[29] J. M. Lattimer and M. Prakash. The physics of neutron stars. *Science*, 304(5670):536–542, 2004.

[30] V. Baran, M. Colonna, V. Greco, and M. Di Toro. Reaction dynamics with exotic nuclei. *Physics Reports*, 410(5):335 – 466, 2005.

[31] L. W. Chen, C. M. Ko, and B. A. Li. Determination of the stiffness of the nuclear symmetry energy from isospin diffusion. *Phys. Rev. Lett.*, 94:032701, Jan 2005.

[32] T. Klähn, D. Blaschke, S. Typel, E. N. E. van Dalen, A. Faessler, C. Fuchs, T. Gaitanos, H. Grigorian, A. Ho, E. E. Kolomeitsev, M. C. Miller, G. Röpke, J. Trümper, D. N. Voskresensky, F. Weber, and H. H. Wolter. Constraints on the high-density nuclear equation of state from the phenomenology of compact stars and heavy-ion collisions. *Phys. Rev. C*, 74:035802, Sep 2006.

[33] P. G. Krastev and B. A. Li. Constraining a possible time variation of the gravitational constant G with terrestrial nuclear laboratory data. *Phys. Rev. C*, 76:055804, Nov 2007.

[34] A. W. Steiner, M. Prakash, J. M. Lattimer, and P. J. Ellis. Isospin asymmetry in nuclei and neutron stars. *Physics Reports*, 411(6):325 – 375, 2005.

[35] H.-Th. Janka, K. Langanke, A. Marek, G. Martnez-Pinedo, and B. Mller. Theory of core-collapse supernovae. *Physics Reports*, 442(1):38 – 74, 2007. The Hans Bethe Centennial Volume 1906-2006.

[36] D. V. Shetty, S. J. Yennello, and G. A. Souliotis. Density dependence of the symmetry energy and the nuclear equation of state: A dynamical and statistical model perspective. *Phys. Rev. C*, 76:024606, Aug 2007.

[37] T. Fischer, M. Hempel, I. Sagert, Y. Suwa, and J. Schaffner-Bielich. Symmetry energy impact in simulations of core-collapse supernovae. *The European Physical Journal A*, 50(2):46, Feb 2014.

[38] J. M. Lattimer and A.W. Steiner. Constraints on the symmetry energy using the mass-radius relation of neutron stars. *The European Physical Journal A*, 50(2):40, Feb 2014.

[39] M. Duer, O. Hen, E. Piasetzky, H. Hakobyan, L. B. Weinstein, M. Braverman, E. O. Cohen, D. Higinbotham, K. P. Adhikari, S. Adhikari, M. J. Amaryan, J. Arrington, A. Ashkenazi, J. Ball, I. Balossino, L. Barion, M. Battaglieri, V. Batourine, A. Beck, I. Bedlinskiy, A. S. Biselli, S. Boiarinov, W. J. Briscoe, W. K. Brooks, S. Bueltmann, D. Bulumulla, V. D. Burkert, F. Cao, D. S. Carman, A. Celentano, G. Charles, T. Chetry, G. Ciullo, L. Clark, B. A. Clary, P. L. Cole, M. Contalbrigo, O. Cortes, V. Crede, R. Cruz-Torres, A. D'Angelo, N. Dashyan, R. De Vita, E. De Sanctis, M. Defurne, A. Deur, C. Djalali, G. Dodge, R. Dupre, H. Egiyan, A. El Alaoui, L. El Fassi, P. Eugenio, R. Fersch, A. Filippi, T. A. Forest, G. Gavalian, Y. Ghandilyan, S. Gilad, G. P. Gilfoyle, K. L. Giovanetti, F. X. Girod, E. Golovatch, R. W. Gothe, K. A. Griffoen, L. Guo, N. Harrison, M. Hattawy, F. Hauenstein, K. Hafidi, K. Hicks, M. Holtrop, C. E. Hyde, Y. Ilieva, D. G. Ireland, B. S. Ishkhanov, E. L. Isupov, K. Joo, M. L. Kabir, D. Keller, G. Khachatryan, M. Khachatryan, M. Khandaker, A. Kim, W. Kim, A. Klein, F. J. Klein, I. Korover, S. E. Kuhn, L. Lanza, G. Laskaris, P. Lenisa, K. Livingston, I. J. D. MacGregor, C. Marchand, N. Markov, B. McKinnon, S. Mey-Tal Beck, T. Mineeva, M. Mirazita, V. Mokeev, R. A. Montgomery, A. Movsisyan, C. Munoz-Camacho, B. Mustapha, S. Nadeeshani, P. Nadel-Turonski, S. Niccolai, G. Niculescu, M. Osipenko, A. I. Ostrovidov, M. Paolone, E. Pasyuk, M. Patsyuk, A. Papadopoulou, K. Park, D. Payette, W. Phelps, O. Pogorelko, J. Poudel, J. W. Price, S. Procureur, Y. Prok, D. Protopopescu, M. Ripani, A. Rizzo, G. Rosner, P. Rossi, F. Sabatié, A. Schmidt, C. Salgado, B. A. Schmookler, R. A. Schumacher, E. P. Segarra, Y. G. Sharabian, G. D. Smith, D. Sokhan, N. Sparveris, S. Stepanyan, S. Strauch, M. Taiuti, J. A. Tan, M. Ungaro, H. Voskanyan, E. Voutier, D. P. Watts, X. Wei, N. Zachariou, J. Zhang, X. Zheng, Z. W. Zhao, and The CLAS Collaboration. Probing high-momentum protons and neutrons in neutron-rich nuclei. *Nature*, 560(7720):617–621, 2018.

[40] J. M. Lattimer and M. Prakash. Neutron star structure and the equation of state. *The Astrophysical Journal*, 550(1):426, 2001.

[41] J. Rikovska Stone, J. C. Miller, R. Koncewicz, P. D. Stevenson, and M. R. Strayer. Nuclear matter and neutron-star properties calculated with the Skyrme interaction. *Phys. Rev. C*, 68:034324, Sep 2003.

[42] B. A. Li and A. W. Steiner. Constraining the radii of neutron stars with terrestrial nuclear laboratory data. *Physics Letters B*, 642(5):436 – 440, 2006.

[43] A. W. Steiner, J. M. Lattimer, and E. F. Brown. The equation of state from observed masses and radii of neutron stars. *The Astrophysical Journal*, 722(1):33, 2010.

[44] A. W. Steiner, J. M. Lattimer, and E. F. Brown. The neutron star mass-radius relation and the equation of state of dense matter. *The Astrophysical Journal Letters*, 765(1):L5, 2013.

[45] J. Erler, C. J. Horowitz, W. Nazarewicz, M. Rafalski, and P. G. Reinhard. Energy density functional for nuclei and neutron stars. *Phys. Rev. C*, 87:044320, Apr 2013.

[46] I. Tews, T. Krüger, K. Hebeler, and A. Schwenk. Neutron matter at next-to-next-to-next-to-leading order in chiral effective field theory. *Phys. Rev. Lett.*, 110:032504, Jan 2013.

[47] K. Stiefel, Z. Kohley, R. T. deSouza, S. Hudan, and K. Hammerton. Symmetry energy dependence of long-timescale isospin transport. *Phys. Rev. C*, 90:061605, Dec 2014.

[48] T. Li, U. Garg, Y. Liu, R. Marks, B. K. Nayak, P. V. Madhusudhana Rao, M. Fujiwara, H. Hashimoto, K. Kawase, K. Nakanishi, S. Okumura, M. Yosoi, M. Itoh, M. Ichikawa, R. Matsuo, T. Terazono, M. Uchida, T. Kawabata, H. Akimune, Y. Iwao, T. Murakami, H. Sakaguchi, S. Terashima, Y. Yasuda, J. Zenihiro, and M. N. Harakeh. Isotopic dependence of the giant monopole resonance in the even-A $^{112-124}$Sn isotopes and the asymmetry term in nuclear incompressibility. *Phys. Rev. Lett.*, 99:162503, Oct 2007.

[49] L. W. Chen, C. M. Ko, B. A. Li, and J. Xu. Density slope of the nuclear symmetry energy from the neutron skin thickness of heavy nuclei. *Phys. Rev. C*, 82:024321, Aug 2010.

[50] P. Möller, W. D. Myers, H. Sagawa, and S. Yoshida. New finite-range droplet mass model and equation-of-state parameters. *Phys. Rev. Lett.*, 108:052501, Jan 2012.

[51] A. Tamii, I. Poltoratska, P. von Neumann-Cosel, Y. Fujita, T. Adachi, C. A. Bertulani, J. Carter, M. Dozono, H. Fujita, K. Fujita, K. Hatanaka, D. Ishikawa, M. Itoh, T. Kawabata, Y. Kalmykov, A. M. Krumbholz, E. Litvinova, H. Matsubara, K. Nakanishi, R. Neveling, H. Okamura, H. J. Ong, B. Özel-Tashenov, V. Yu. Ponomarev, A. Richter, B. Rubio, H. Sakaguchi, Y. Sakemi, Y. Sasamoto, Y. Shimbara, Y. Shimizu, F. D. Smit, T. Suzuki, Y. Tameshige, J. Wambach, R. Yamada, M. Yosoi, and J. Zenihiro. Complete electric dipole response and the neutron skin in ^{208}Pb. *Phys. Rev. Lett.*, 107:062502, Aug 2011.

[52] X. Roca-Maza, M. Brenna, G. Colò, M. Centelles, X. Viñas, B. K. Agrawal, N. Paar, D. Vretenar, and J. Piekarewicz. Electric dipole polarizability in ^{208}Pb: Insights from the droplet model. *Phys. Rev. C*, 88:024316, Aug 2013.

[53] L. Trippa, G. Colò, and E. Vigezzi. Giant dipole resonance as a quantitative constraint on the symmetry energy. *Phys. Rev. C*, 77:061304, Jun 2008.

[54] M. B. Tsang, Y. Zhang, P. Danielewicz, M. Famiano, Z. Li, W. G. Lynch, and A. W. Steiner. Constraints on the density dependence of the symmetry energy. *Phys. Rev. Lett.*, 102:122701, Mar 2009.

[55] P. Danielewicz and J. Lee. Symmetry energy II: Isobaric analog states. *Nuclear Physics A*, 922:1 – 70, 2014.

[56] M. Kortelainen, T. Lesinski, J. Moré, W. Nazarewicz, J. Sarich, N. Schunck, M. V. Stoitsov, and S. Wild. Nuclear energy density optimization. *Phys. Rev. C*, 82:024313, Aug 2010.

[57] S. Gandolfi, J. Carlson, and S. Reddy. Maximum mass and radius of neutron stars, and the nuclear symmetry energy. *Phys. Rev. C*, 85:032801, Mar 2012.

[58] K. Hebeler, J. M. Lattimer, C. J. Pethick, and A. Schwenk. Constraints on neutron star radii based on chiral effective field theory interactions. *Phys. Rev. Lett.*, 105:161102, Oct 2010.

[59] Z. Kohley and S. J. Yennello. Heavy-ion collisions: Direct and indirect probes of the density and temperature dependence of E_{sym}. *The European Physical Journal A*, 50(2):31, Feb 2014.

[60] Z. Kohley, G. Christian, T. Baumann, P. A. DeYoung, J. E. Finck, N. Frank, M. Jones, J. K. Smith, J. Snyder, A. Spyrou, and M. Thoennessen. Exploiting neutron-rich radioactive ion beams to constrain the symmetry energy. *Phys. Rev. C*, 88:041601, Oct 2013.

[61] Z. Kohley, L. W. May, S. Wuenschel, A. Bonasera, K. Hagel, R. Tripathi, R. Wada, G. A. Souliotis, D. V. Shetty, S. Galanopoulos, M. Mehlman, W. B. Smith, S. N. Soisson, B. C. Stein, and S. J. Yennello. Investigation of transverse collective flow of intermediate mass fragments. *Phys. Rev. C*, 82:064601, Dec 2010.

[62] P. Russotto, P. Z. Wu, M. Zoric, M. Chartier, Y. Leifels, R. C. Lemmon, Q. Li, J. Łukasik, A. Pagano, P. Pawowski, and W. Trautmann. Symmetry energy from elliptic flow in ^{197}Au+^{197}Au. *Physics Letters B*, 697(5):471 – 476, 2011.

[63] M. Colonna, A. Ono, and J. Rizzo. Fragmentation paths in dynamical models. *Phys. Rev. C*, 82:054613, Nov 2010.

[64] A. Ono. Antisymmetrized molecular dynamics with quantum branching processes for collisions of heavy nuclei. *Phys. Rev. C*, 59:853–864, Feb 1999.

[65] J. Rizzo, M. Colonna, M. Di Toro, and V. Greco. Transport properties of isospin effective mass splitting. *Nuclear Physics A*, 732:202 – 217, 2004.

[66] B. Luther, T. Baumann, M. Thoennessen, J. Brown, P. DeYoung, J. Finck, J. Hinnefeld, R. Howes, K. Kemper, P. Pancella, G. Peaslee, W. Rogers, and S. Tabor. Mona the modular neutron array. *Nuclear Instruments and Methods in Physics Research Section A: Accelerators, Spectrometers, Detectors and Associated Equipment*, 505(1):33 –

35, 2003. Proceedings of the tenth Symposium on Radiation Measurements and Applications.

[67] T. Baumann, J. Boike, J. Brown, M. Bullinger, J. P. Bychoswki, S. Clark, K. Daum, P. A. DeYoung, J. V. Evans, J. Finck, N. Frank, A. Grant, J. Hinnefeld, G. W. Hitt, R. H. Howes, B. Isselhardt, K. W. Kemper, J. Longacre, Y. Lu, B. Luther, S. T. Marley, D. McCollum, E. McDonald, U. Onwuemene, P. V. Pancella, G. F. Peaslee, W. A. Peters, M. Rajabali, J. Robertson, W. F. Rogers, S. L. Tabor, M. Thoennessen, E. Tryggestad, R. E. Turner, P. J. VanWylen, and N. Walker. Construction of a modular large-area neutron detector for the NSCL. *Nuclear Instruments and Methods in Physics Research Section A: Accelerators, Spectrometers, Detectors and Associated Equipment*, 543(2):517 – 527, 2005.

[68] M. D. Bird, S. J. Kenney, J. Toth, H. W. Weijers, J. C. DeKamp, M. Thoennessen, and A. F. Zeller. System testing and installation of the NHMFL/NSCL sweeper magnet. *IEEE Transactions on Applied Superconductivity*, 15(2):1252–1254, Jun 2005.

[69] M. Papa, T. Maruyama, and A. Bonasera. Constrained molecular dynamics approach to fermionic systems. *Phys. Rev. C*, 64:024612, Jul 2001.

[70] M. Papa, G. Giuliani, and A. Bonasera. Constrained molecular dynamics II: An N-body approach to nuclear systems. *Journal of Computational Physics*, 208(2):403 – 415, 2005.

[71] A. Ono and H. Horiuchi. Antisymmetrized molecular dynamics for heavy ion collisions. *Progress in Particle and Nuclear Physics*, 53(2):501 – 581, 2004.

[72] Z. Kohley. *Transverse Collective Flow and Emission Order of Mid-Rapidity Fragments in Fermi Energy Heavy Ion Collisions*. PhD thesis, Texas A&M University, 2010.

[73] R. J. Charity, M. A. McMahan, G. J. Wozniak, R. J. McDonald, L. G. Moretto, D. G. Sarantites, L. G. Sobotka, G. Guarino, A. Pantaleo, L. Fiore, A. Gobbi, and K. D. Hildenbrand. Systematics of complex fragment emission in niobium-induced reactions. *Nuclear Physics A*, 483(2):371 – 405, 1988.

[74] R. J. Charity. In *Joint ICTP-AIEA Advanced Workshop on Model Codes for Spallation Reactions*, Report INDC(NDS)-0530, IAEA, Vienna, February 2008.

[75] M. Mocko, M. B. Tsang, D. Lacroix, A. Ono, P. Danielewicz, W. G. Lynch, and R. J. Charity. Transport model simulations of projectile fragmentation reactions at 140 MeV/nucleon. *Phys. Rev. C*, 78:024612, Aug 2008.

[76] G. Cardella, G. Giuliani, I. Lombardo, M. Papa, L. Acosta, C. Agodi, F. Amorini, A. Anzalone, L. Auditore, I. Berceanu, S. Cavallaro, M. B. Chatterjee, E. De Filippo, E. Geraci, L. Grassi, J. Han, E. La Guidara, D. Loria, G. Lanzalone, C. Maiolino,

T. Minniti, A. Pagano, S. Pirrone, G. Politi, F. Porto, F. Rizzo, P. Russotto, S. Santoro, A. Trifirò, M. Trimarchi, G. Verde, and M. Vigilante. Effects of neutron richness on the behavior of nuclear systems at intermediate energies. *Phys. Rev. C*, 85:064609, Jun 2012.

[77] M. Papa, I. Berceanu, L. Acosta, F. Amorini, C. Agodi, A. Anzalone, L. Auditore, G. Cardella, S. Cavallaro, M. B. Chatterjee, E. De Filippo, L. Francalanza, E. Geraci, L. Grassi, B. Gnoffo, J. Han, E. La Guidara, G. Lanzalone, I. Lombardo, C. Maiolino, T. Minniti, A. Pagano, E. V. Pagano, S. Pirrone, G. Politi, F. Porto, L. Quattrocchi, F. Rizzo, E. Rosato, P. Russotto, A. Trifirò, M. Trimarchi, G. Verde, and M. Vigilante. Dipolar degrees of freedom and isospin equilibration processes in heavy ion collisions. *Phys. Rev. C*, 91:041601, Apr 2015.

[78] C. Y. Qiao, H. L. Wei, C. W. Ma, Y. L. Zhang, and S. S. Wang. Isobaric yield ratio difference between the 140A MeV ^{58}Ni +^{9} Be and ^{64}Ni + ^{9}Be reactions studied by the antisymmetric molecular dynamics model. *Phys. Rev. C*, 92:014612, Jul 2015.

[79] R. Wada, T. Keutgen, K. Hagel, Y. G. Ma, J. Wang, M. Murray, L. Qin, P. Smith, J. B. Natowitz, R. Alfarro, J. Cibor, M. Cinausero, Y. El Masri, D. Fabris, E. Fioretto, A. Keksis, S. Kowalski, M. Lunardon, A. Makeev, N. Marie, E. Martin, Z. Majka, A. Martinez-Davalos, A. Menchaca-Rocha, G. Nebbia, G. Prete, V. Rizzi, A. Ruangma, D. V. Shetty, G. Souliotis, P. Staszel, M. Veselsky, G. Viesti, E. M. Winchester, S. J. Yennello, W. Zipper, and A. Ono. Reaction dynamics and multifragmentation in fermi energy heavy ion reactions. *Phys. Rev. C*, 69:044610, Apr 2004.

[80] G. Christian. *Spectroscopy of Neutron-Unbound Fluorine*. PhD thesis, Michigan State University, 2011.

[81] G. Christian, N. Frank, S. Ash, T. Baumann, P. A. DeYoung, J. E. Finck, A. Gade, G. F. Grinyer, B. Luther, M. Mosby, S. Mosby, J. K. Smith, J. Snyder, A. Spyrou, M. J. Strongman, M. Thoennessen, M. Warren, D. Weisshaar, and A. Wersal. Spectroscopy of neutron-unbound ^{27,28}F. *Phys. Rev. C*, 85:034327, Mar 2012.

[82] D. Weisshaar, A. Gade, T. Glasmacher, G. F. Grinyer, D. Bazin, P. Adrich, T. Baugher, J. M. Cook, C. Aa. Diget, S. McDaniel, A. Ratkiewicz, K. P. Siwek, and K. A. Walsh. CAESAR- A high-efficiency CsI(Na) scintillator array for in-beam γray spectroscopy with fast rare-isotope beams. *Nuclear Instruments and Methods in Physics Research Section A: Accelerators, Spectrometers, Detectors and Associated Equipment*, 624(3):615 – 623, 2010.

[83] A. Boudard, J. Cugnon, J.-C. David, S. Leray, and D. Mancusi. New potentialities of the Liège intranuclear cascade model for reactions induced by nucleons and light charged particles. *Phys. Rev. C*, 87:014606, Jan 2013.

[84] S. Leray, D. Mancusi, P. Kaitaniemi, J.-C. David, A. Boudard, B. Braunn, and J. Cugnon. Extension of the Lige Intra Nuclear Cascade model to light ion-induced collisions for medical and space applications. *Journal of Physics: Conference Series*, 420(1):012065, 2013.

[85] D. Mancusi, A. Boudard, J. Cugnon, J.-C. David, P. Kaitaniemi, and S. Leray. Extension of the Liège intranuclear-cascade model to reactions induced by light nuclei. *Phys. Rev. C*, 90:054602, Nov 2014.

[86] A. Boudard, J. Cugnon, S. Leray, and C. Volant. Intranuclear cascade model for a comprehensive description of spallation reaction data. *Phys. Rev. C*, 66:044615, Oct 2002.

[87] J.-C. David, D. Filges, F. Gallmeier, M. Khandaker, A. Konobeyev, S. Leray, G. Mank, A. Mengoni, R. Michel, N. Otuka, and Y. Yariv. Benchmark of spallation models. *Progress in NUCLEAR SCIENCE and TECHNOLOGY*, 2:942–947, Oct 2011.

[88] J.-C. David. Spallation reactions: A successful interplay between modeling and applications. *The European Physical Journal A*, 51(6):68, Jun 2015.

[89] A. Kelić, M. V. Ricciardi, and K.-H. Schmidt. In *Joint ICTP-AIEA Advanced Workshop on Model Codes for Spallation Reactions*, Report INDC(NDS)-0530, IAEA, Vienna, February 2008.

[90] I. Tanihata. Radioactive beam facilities and their physics program. *Nuclear Physics A*, 553:361 – 372, 1993.

[91] F. Marti, P. Miller, D. Poe, M. Steiner, J. Stetson, and X. Y. Wu. Commissioning of the Coupled Cyclotron system at NSCL. *AIP Conference Proceedings*, 600(1):64–68, 2001.

[92] D. J. Morrissey, B. M. Sherrill, M. Steiner, A. Stolz, and I. Wiedenhoever. Commissioning the A1900 projectile fragment separator. *Nuclear Instruments and Methods in Physics Research Section B: Beam Interactions with Materials and Atoms*, 204:90 – 96, 2003. 14th International Conference on Electromagnetic Isotope Separators and Techniques Related to their Applications.

[93] A. Stolz, T. Baumann, T. N. Ginter, D. J. Morrissey, M. Portillo, B. M. Sherrill, M. Steiner, and J. W. Stetson. Production of rare isotope beams with the NSCL fragment separator. *Nuclear Instruments and Methods in Physics Research Section B: Beam Interactions with Materials and Atoms*, 241(1):858 – 861, 2005. The Application of Accelerators in Research and Industry.

[94] K.-H. Schmidt, E. Hanelt, H. Geissel, G. Mnzenberg, and J. P. Dufour. The momentum-loss achromat - A new method for the isotopical separation of relativis-

tic heavy ions. *Nuclear Instruments and Methods in Physics Research Section A: Accelerators, Spectrometers, Detectors and Associated Equipment*, 260(2):287 – 303, 1987.

[95] N. Frank. *Spectroscopy of Neutron Unbound States in Neutron Rich Oxygen Isotopes*. PhD thesis, Michigan State University, 2006.

[96] C. Freigang. Building the Sweeper magnet focal plane detector. Master's thesis, Michigan State University, 2001.

[97] J. K. Smith. *Unbound States in the Lightest Island of Inversion: Neutron Decay Measurements of ^{11}Li, ^{10}Li, and ^{12}Be*. PhD thesis, Michigan State University, 2014.

[98] K. Meierbachtol. *Parallel and Perpendicular Momentum Distributions in Projectile Fragmentation Reactions*. PhD thesis, Michigan State University, 2012.

[99] T. Baumann, A. Spyrou, and M. Thoennessen. Nuclear structure experiments along the neutron drip line. *Reports on Progress in Physics*, 75(3):036301, 2012.

[100] W. Peters. *Study of Neutron Unbound States Using the Modular Neutron Array (MoNA)*. PhD thesis, Michigan State University, 2007.

[101] M. D. Jones. *Spectroscopy of Neutron Unbound States in ^{24}O and ^{23}N*. PhD thesis, Michigan State University, 2015.

[102] J. Honke. Sweeper Magnet Focal Plane Det.: CRDC Mask & Drive. National Superconducting Cyclotron Laboratory Drawing Number 7-SWF-4-6-D, Rev. A, 6 2001.

[103] J. M. Paul. The density effect and rate of energy loss in common plastic scintillators. *Nuclear Instruments and Methods*, 96(1):51 – 59, 1971.

[104] A. Stolz, T. Baumann, N. H. Frank, T. N. Ginter, G. W. Hitt, E. Kwan, M. Mocko, W. Peters, A. Schiller, C. S. Sumithrarachchi, and M. Thoennessen. First observation of ^{60}Ge and ^{64}Se. *Physics Letters B*, 627(1):32 – 37, 2005.

[105] G. F. Knoll. *Radiation Detection and Measurement*. John Wiley & Sons, Inc., New York, NY, 3rd edition, 2000.

[106] D. Bazin, J. A. Caggiano, B. M. Sherrill, J. Yurkon, and A. Zeller. The S800 spectrograph. *Nuclear Instruments and Methods in Physics Research Section B: Beam Interactions with Materials and Atoms*, 204:629 – 633, 2003. 14th International Conference on Electromagnetic Isotope Separators and Techniques Related to their Applications.

[107] C. Hoffman. *Investigation of the Neutron-Rich Oxygen Isotopes at the Drop Line*. PhD thesis, Florida State University, 2009.

[108] M. Strongman. Neutron spectroscopy of ^{22}N and the disappearance of the N=14 shell. Master's thesis, Michigan State University, 2011.

[109] S. Mosby. *Spectroscopy of Neutron Unbound States in Neutron Rich Carbon.* PhD thesis, Michigan State University, 2012.

[110] M. Mosby. *Measurement of Excitation Energy of Neutron-Rich Precursor Fragments.* PhD thesis, Michigan State University, 2013.

[111] J. Snyder. *Spectroscopy of ^{15}Be.* PhD thesis, Michigan State University, 2014.

[112] S. Agostinelli, J. Allison, K. Amako, J. Apostolakis, H. Araujo, P. Arce, M. Asai, D. Axen, S. Banerjee, G. Barrand, F. Behner, L. Bellagamba, J. Boudreau, L. Broglia, A. Brunengo, H. Burkhardt, S. Chauvie, J. Chuma, R. Chytracek, G. Cooperman, G. Cosmo, P. Degtyarenko, A. Dell'Acqua, G. Depaola, D. Dietrich, R. Enami, A. Feliciello, C. Ferguson, H. Fesefeldt, G. Folger, F. Foppiano, A. Forti, S. Garelli, S. Giani, R. Giannitrapani, D. Gibin, J. J. Gmez Cadenas, I. Gonzlez, G. Gracia Abril, G. Greeniaus, W. Greiner, V. Grichine, A. Grossheim, S. Guatelli, P. Gumplinger, R. Hamatsu, K. Hashimoto, H. Hasui, A. Heikkinen, A. Howard, V. Ivanchenko, A. Johnson, F.W. Jones, J. Kallenbach, N. Kanaya, M. Kawabata, Y. Kawabata, M. Kawaguti, S. Kelner, P. Kent, A. Kimura, T. Kodama, R. Kokoulin, M. Kossov, H. Kurashige, E. Lamanna, T. Lampn, V. Lara, V. Lefebure, F. Lei, M. Liendl, W. Lockman, F. Longo, S. Magni, M. Maire, E. Medernach, K. Minamimoto, P. Mora de Freitas, Y. Morita, K. Murakami, M. Nagamatu, R. Nartallo, P. Nieminen, T. Nishimura, K. Ohtsubo, M. Okamura, S. O'Neale, Y. Oohata, K. Paech, J. Perl, A. Pfeiffer, M. G. Pia, F. Ranjard, A. Rybin, S. Sadilov, E. Di Salvo, G. Santin, T. Sasaki, N. Savvas, Y. Sawada, S. Scherer, S. Sei, V. Sirotenko, D. Smith, N. Starkov, H. Stoecker, J. Sulkimo, M. Takahata, S. Tanaka, E. Tcherniaev, E. Safai Tehrani, M. Tropeano, P. Truscott, H. Uno, L. Urban, P. Urban, M. Verderi, A. Walkden, W. Wander, H. Weber, J. P. Wellisch, T. Wenaus, D. C. Williams, D. Wright, T. Yamada, H. Yoshida, and D. Zschiesche. Geant4 a simulation toolkit. *Nuclear Instruments and Methods in Physics Research Section A: Accelerators, Spectrometers, Detectors and Associated Equipment*, 506(3):250 – 303, 2003.

[113] J. Allison, K. Amako, J. Apostolakis, H. Araujo, P. Arce Dubois, M. Asai, G. Barrand, R. Capra, S. Chauvie, R. Chytracek, G. A. P. Cirrone, G. Cooperman, G. Cosmo, G. Cuttone, G. G. Daquino, M. Donszelmann, M. Dressel, G. Folger, F. Foppiano, J. Generowicz, V. Grichine, S. Guatelli, P. Gumplinger, A. Heikkinen, I. Hrivnacova, A. Howard, S. Incerti, V. Ivanchenko, T. Johnson, F. Jones, T. Koi, R. Kokoulin, M. Kossov, H. Kurashige, V. Lara, S. Larsson, F. Lei, O. Link, F. Longo, M. Maire, A. Mantero, B. Mascialino, I. McLaren, P. Mendez Lorenzo, K. Minamimoto, K. Murakami, P. Nieminen, L. Pandola, S. Parlati, L. Peralta, J. Perl, A. Pfeiffer, M. G. Pia, A. Ribon, P. Rodrigues, G. Russo, S. Sadilov, G. Santin, T. Sasaki, D. Smith, N. Starkov, S. Tanaka, E. Tcherniaev, B. Tome, A. Trindade, P. Truscott, L. Urban, M. Verderi, A. Walkden, J. P. Wellisch, D. C. Williams, D. Wright, and

H. Yoshida. Geant4 developments and applications. *IEEE Transactions on Nuclear Science*, 53(1):270–278, Feb 2006.

[114] B. Roeder. In-beam validation of the recoil separator design concept for EURISOL. EURISOL Design Study, Oct 2008. Accessed: 2018-05-30.

[115] Z. Kohley, E. Lunderberg, P.A. DeYoung, B. T. Roeder, T. Baumann, G. Christian, S. Mosby, J. K. Smith, J. Snyder, A. Spyrou, and M. Thoennessen. Modeling interactions of intermediate-energy neutrons in a plastic scintillator array with Geant4. *Nuclear Instruments and Methods in Physics Research Section A: Accelerators, Spectrometers, Detectors and Associated Equipment*, 682:59 – 65, 2012.

[116] H. Anton, I. Bivens, and S. Davis. *Calculus: Early Transcendentals*. John Wiley & Sons, Inc., Hoboken, NJ, 8th edition, 2005.